Stabilité et contrôle latéral d'un aéronef à petite dérive par utilisation différentielle des systèmes de poussée. Utilisation de méthodes de co-design

Eric Nguyen Van

THÈSE

En vue de l'obtention du

DOCTORAT DE L'UNIVERSITÉ DE TOULOUSE

Délivré par : *l'Institut Supérieur de l'Aéronautique et de l'Espace (ISAE)*

Présentée et soutenue le *23 Octobre 2020* **par :**

ERIC NGUYEN VAN

Stabilité et contrôle latéral d'un aéronef à petite dérive par utilisation différentielle des systèmes de poussée. Utilisation de méthodes de co-design.

Lateral stability and control of an aircraft equipped with a small vertical tail by differential use of the propulsion systems. Use of co-design methods.

JURY

M. ISABELLE FANTONI	Directrice de Recherche	Examinatrice
M. MARK LOWENBERG	Professeur des Universités	Rapporteur
M. FRANCK CAZAURANG	Professeur des Universités	Président du jury, rapporteur
M. PHILIPPE PASTOR	Enseignant Chercheur	Encadrant de thèse
M. CARSTEN DÖLL	Ingénieur de Recherche	Co-Directeur de thèse
M. DANIEL ALAZARD	Enseignant Chercheur	Directeur de thèse

École doctorale et spécialité :
EDSYS : Automatique 4200046

Unité de Recherche :
ONERA - The French Aerospace Lab - Traitement de l'Information et Systèmes
ISAE-SUPAERO Institut Supérieur de l'Aéronautique et de l'Espace - Département Conception et Conduite des véhicules Aéronautiques et Spatiaux

Directeur(s) de Thèse :
M. DANIEL ALAZARD, *M.* CARSTEN DÖLL et *M.* PHILIPPE PASTOR

Rapporteurs :
M. MARK LOWENBERG et *M.* FRANCK CAZAURANG

English resume

The possibility to increase the performance of a transport aircraft through a relaxation of the directional static stability, also called weathercock stability, is studied in this thesis. A change of paradigm brought by the concept of distributed electric propulsion allows the consideration of an active use of differential thrust. This additional means of flight control and the reduction of the vertical tail are the main ideas explored in this work. In a first part, the directional static stability and controllability of an aircraft are evaluated to find the sizing flight conditions for the vertical tail. The contribution here is to take into account the specificities of the unconventional propulsion system. Mathematical tools are developed to trim the aircraft using differential thrust as a mean of directional control and aerodynamic tools are constructed to describe the variable vertical tail size and the aero-propulsive interactions taking place between a propeller and a wing. This analysis isolates a sizing flight condition, particularly the case of engine failure at take-off, for the vertical tail and leads to a significant reduction in surface area. It is also shown that the rudder control surface could be removed and replaced by differential thrust. In a second part, the flight dynamic aspects of an aircraft with a small vertical tail and differential thrust as the only means of directional control are studied. A methodology is proposed to answer the question of how should the vertical tail and propulsion system be designed to satisfy a set of prescribed flight handling qualities ? An automatic control architecture and co-design methodology relying on structured H_∞ control design and non convex optimisation tools are utilized and developed to manage the trade off between vertical tail size and engine bandwidth. This framework is used in the flight conditions defined in the first part and notably in presence of engine failures. In a last part, a means of experimental research is developed to contribute to an effort to produce experimental data on distributed electric propulsion. This flight demonstrator is specifically oriented toward the study of the lateral flight mechanics of an aircraft having a large portion of the wing embedded in the propeller slipstream. It was possible to identify the aerodynamic derivatives and their dependence on the thrust from the flight data to illustrate the particularity of flight dynamics with distributed propulsion and blown wing.

Résumé en français

Cette thèse étudie la possibilité d'améliorer les performances d'un avion de transport à travers un relâchement de la stabilité de route et une réduction de l'empennage vertical. L'idée principale est l'utilisation active de la poussée différentielle, rendue

possible grâce au changement de paradigme apporté par la propulsion électrique distribuée. Ce moyen de contrôle supplémentaire et la réduction de l'empennage vertical sont étudiés en trois axes principaux. L'objectif de la première partie est l'évaluation de la stabilité de route ainsi que la contrôlabilité directionnelle de l'avion afin d'identifier les conditions de vol dimensionnant l'empennage vertical. Une contribution est apportée afin de prendre en compte l'aspect non-conventionnelle de la propulsion électrique distribuée. Des outils mathématiques sont développés pour trimmer l'avion utilisant la poussée différentielle comme moyen de contrôle et des outils aérodynamiques sont développés afin de modéliser un empennage vertical de taille variable ainsi que les interactions aéro-propulsives apparaissant sur une voilure soufflée par des hélices. Cette analyse permet d'isoler des conditions dimensionnantes, particulièrement en cas de pannes moteur au décollage et conduit à une réduction significative de la taille de l'empennage pour des cas statiques. De plus, il est montré que la gouverne de direction peut être remplacée par la poussée différentielle. Dans une seconde partie, les aspects dynamiques d'un avion utilisant la poussée différentielle à la place d'une gouverne de direction sont abordés. Une méthode est proposée afin de répondre au questionnement suivant : comment l'empennage vertical et les systèmes de propulsion devraient être dimensionnés afin de satisfaire un ensemble de qualités de vol imposées ? Une architecture de contrôle automatique et une méthode de co-design se basant sur la synthèse H_∞ structurée et sur des outils d'optimisation non convexe sont utilisés pour gérer le compromis entre la taille de l'empennage vertical et la bande passante des moteurs. Cet ensemble d'outils est ensuite mis à contribution pour étudier l'avion dans les conditions définies dans la première partie et notamment en présence de pannes moteur. Dans une dernière partie, un moyen de recherche expérimentale est développé afin de contribuer à un effort de production de donnée sur la propulsion électrique distribuée. Ce démonstrateur de vol est spécifiquement orienté vers l'étude de la mécanique de vol latérale d'un avion possédant une aile soufflée. Il a été possible d'identifier depuis les mesures réalisées en vol, les dérivées aérodynamiques de l'avion ainsi que leur dépendance à la poussée. Cela a ensuite permis d'illustrer les particularités de la dynamique de vol d'un avion à propulsion distribuée et aile soufflée.

Remerciements

Trois années de labeur ont fini par aboutir à ce manuscrit qui compile l'ensemble de mon travail de thèse. Ces quelques centaines de pages me paraissent quelque peu réductives par rapport aux efforts qui y ont été investi par moi mais aussi par un ensemble de personnes formidables.

Il me faut d'abord remercier mes établissements et équipes d'accueil qui m'ont permis d'effectuer ce doctorant en mobilisant les fonds nécessaires. Il s'agit de l'équipe IDCO de l'ONERA, du laboratoire DCAS de l'ISAE et de la chair CEDAR portée par Airbus.

Vient ensuite une profonde reconnaissance pour mon directeur de thèse Daniel Alazard, mon co-directeur Carsten Döll et mon superviseur à l'ISAE Philippe Pastor qui ont très rapidement cru en moi, m'ont accordé une large autonomie ainsi qu'une grande confiance.

J'aimerais remercier Dr. Isabelle Fantoni, Prof. Dr.-Ing. Mark Lowenberg et Prof. Dr. Franck Cazaurang qui ont accepté de former mon jury de thèse et d'évaluer ce travail.

Un résultat scientifique n'est aujourd'hui que rarement le fruit du travail d'une seule personne et c'est particulièrement vrai avec cette thèse qui a mobilisé une petite armée de contributeurs pour la partie expérimentale. Merci à Emmanuel Benard qui m'a donné sa confiance et les moyens pour développer un démonstrateur et réaliser une campagne de vols. Merci à Eric Poquillon et Dominique Bernard pour leur aide, leur patience et nos désaccords qui ont renforcé le projet et m'ont à la fois beaucoup appris.

Les équipes techniques de l'ISAE ont été un véritable pilier de ce projet, Daniel Gagneux et Xavier Foulquier pour la fabrication, Marc Grellet qui m'a généreusement aidé à construire la sphere cinq trous. L'ensemble des membres des équipes techniques du DCAS et du DISC pour leur travail acharné sur la maquette mais fort heureusement récompensé par une raclette valaisanne mémorable.

Une pensée spéciale pour Marie Faure qui a toujours été là pour m'aider dans toutes les démarches administratives et Thierry Faure qui a accueilli et soutenu notre projet à l'InnovSpace.

A l'ONERA, il y a bien sûr Jean Hermetz, Peter Schmollgruber et Clément Toussaint qui m'ont fait bénéficier de leur grande expérience pratique des tests sur modèles réduits et m'ont donné de précieux conseils.

Il ne faut pas non plus négliger le travail des étudiants et stagiaires qui ont

apporté une aide importante au projet, en particulier Cedra Al-Nahhas et Fernando Varra-Rabar qui ont largement contribué à l'identification.

Heureusement, une bonne ambiance de travail était assurée grâce à Louis et Thibault, oscillant entre sessions de câblage drônistique, café météo et rando-parapente. Mais aussi Joël et Stéphanie pour votre gentillesse et passions partagées pour l'Aviation, la Montagne et l'Espace.

Il me faut remercier "ct'équipe" que j'ai laissé en Suisse et en Haute Savoie et qui ne m'oublie pas. Mon frère que j'admire, c'est toujours plus facile d'évoluer dans la vie lorsque quelqu'un nous montre la voie.

Enfin, par les conditions spéciales qu'a créé un charmant virus du nom de SARS-CoV-2, la thèse s'est écrite en majeure partie confiné chez Maman et sa jambe cassée. Cela a donné lieu à un beau soutien mutuel dans nos épreuves respectives. Merci à toi et à Papa de m'avoir soutenu sans faille depuis le début de ce long parcours universitaire.

Contents

List of Figures

List of Tables

Acronyms

CCV Control Configured Vehicle.

CFD Computation Fluid Dynamics.

CG Center of Gravity.

DECOL DEmonstrateur COntrol Latéral, (Lateral Control Demonstrator).

DEP Distributed Electric Propulsion.

DT Differential Thrust.

DTC Direct Torque Control.

ESC Electronic Speed Controller.

GNSS Global Navigation Satellite System.

IMU Inertial Measurement Unit.

LFR Linear Fractional Representation.

LL Lifting Line.

LMIs Linear Matrix Inequalities.

MDO Multi-Disciplinary Optimization.

MIMO Multiple Input Multiple Output.

NED North East Down.

OEI One Engine Inoperational.

ONERA Office National d'Études et de Recherches Aérospatiales.

PCA Propulsion Control Aircraft.

PIV Particle Image Velocimetry.

PWM Pulse Width Modulation.

RANS Reynolds-Averaged Navier-Stokes.

RC Remote Controlled.

ROS Robotic Operating System.

SISO Single Input Single Output.

STOL Short Take Off and Landing.

UAV Unmanned Aerial Vehicle.

V/STOL Vertical/Short Take Off and Landing.

VeDSC Vertical tail Design, Stability and Control.

VLM Vortex Lattice Method.

VT Vertical Tail.

Part I

Introduction

0.1 Context

The pursuit of efficient flight for transport aircraft can lead to question the rule stating that an aircraft must be statically stable. Latest civilian transport aircraft like the A380 and A350 are designed to reduced longitudinal static stability. Though requiring an automatic stability augmentation system and an emergency back-up controller, it leads to a smaller horizontal stabilizer, a reduced wetted surface area and a lower empty mass [Abzug 2005]. However, the same logic cannot be applied for the directional stability, also called weathercock stability, because the Vertical Tail (VT) is essentially dimensioned according to the One Engine Inoperational (OEI) case illustrated by Fig 1 [Torenbeek 1982], [Raymer 1989], [Obert 2009]. This flight condition, requires a sufficiently large static stability or directional control power, to trim the aircraft with unbalanced thrust, sizing in turn the VT. Because this case happens at low speed, the vertical stabilizer remains oversized for the rest of the aircraft operation.

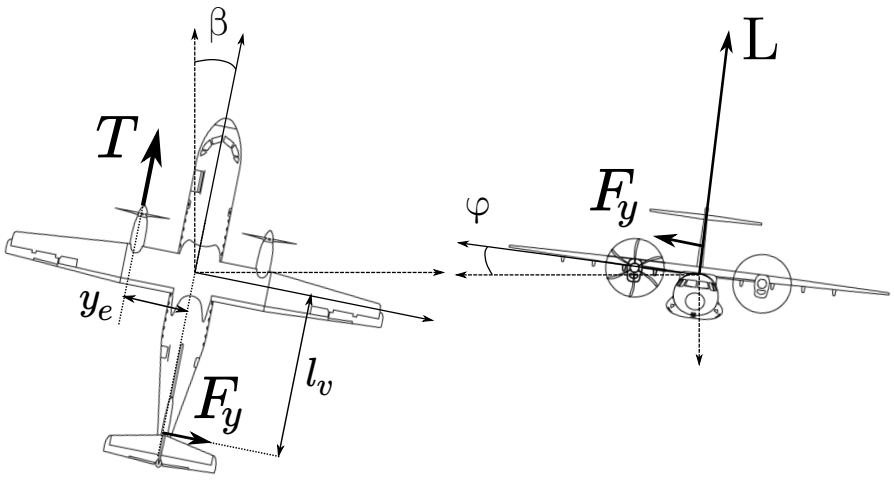

Figure 1 – Illustration of the forces at play in equilibrated One Engine Inoperational (OEI) conditions.

A change of paradigm becomes possible with the emergence of new propulsion architectures and particularly the Distributed Electric Propulsion (DEP). The idea has been suggested in the literature that DEP may unlock reduced directional stability for transport aircraft [Kim 2010]. Conventional turbo-fan engine, distributed along the wingspan in pursue of the same goal, prove to be inefficient due to their inherent low reaction time [Nguyen 2018]. With the emergence of turbo-electric, hybrid and full electric propulsive systems, this idea was regarded with a new look.

The well known rapid reaction time of electric engines combined with the possibility to easily distribute electric engines, rendered this objective possible. To this day, it was not demonstrated and no methodology has been proposed to dimension an aircraft with a relaxed directional static stability and DEP.

The objectives of this dissertation are twofold:

1 - Propose a methodology for the co-design of vertical tail and control laws answering the constraints of safety, flight qualities and actuator limitations.

2 - Flight demonstration of a small scale demonstrator using DEP and reduced lateral stability.

0.2 State of the art

It is possible to organize the multi-disciplinary subjects related to this work under two themes: directional aircraft stability in overall aircraft design and Distributed Electric Propulsion (DEP).

0.2.1 Directional stability in overall aircraft design

On a traditional tube and wing aircraft, the function of stability is provided by the tail surfaces. Directional stability is provided by the VT, which should answer the following list of requirements [Obert 2009], [Torenbeek 1982]:

1. the VT should provide static and dynamic stability and allow control of the aircraft,
2. it should handle very large angle of side slip, up to 25° without risk of stall,
3. it should provide a mean to trim the aircraft at all time, especially during thrust unbalance or side wind.

Requirement number **2** drives mainly the aspect ratio and sweep angle of the vertical tail. The aspect ratio is kept low and a high sweep angle of the order of 30° is used to avoid and delay abrupt stall. Some designs (mostly subsonic designs) include a dorsal-fin, a highly swept surface extending in front of the vertical tail having a very thin sometimes flat airfoil. This surface has the same function as the sweep angle, it does not influence the lateral side force coefficient other than delaying stall, allowing side slip angle up to 25° [Obert 2009]. A representation of all the elements previously described is given in Fig 2.

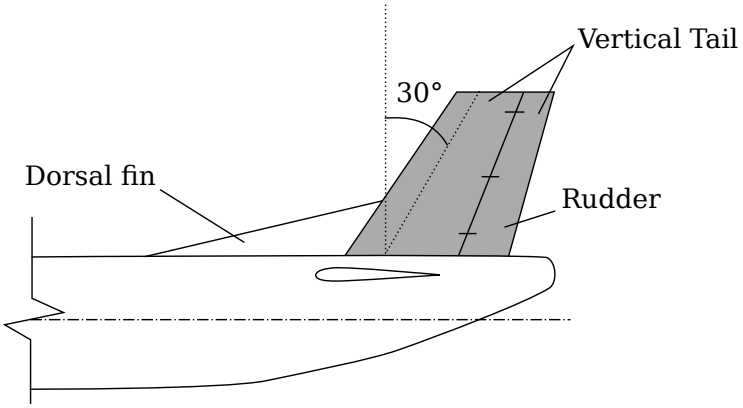

Figure 2 – Vertical tail representation.

In the literature, the definition of the VT surface area can vary. Also as a general rule for this work, the VT surface area refers to the shaded area in Fig 2. Requirements **1** and **3** follow the constraints brought by aircraft certification regulation. It is referred to the European certification CS25, amendment 20, subpart B, dealing with the flight requirements [EASA 2017] for large aircraft (heavier than 19 000 Lb or more than 19 passengers). CS25 contains a series of requirements that an aircraft should meet in order to demonstrate safety objectives for civilian use. Among the specification enacted for flight, paragraph CS25.147, CS25.149, CS25.177 and CS25.181 refer respectively to directional control, trim capability, static and dynamic stability. Among these criteria, the trim capability in presence of thrust unbalance is cited as the driving criterion for sizing the VT surface area in preliminary design [Torenbeek 1982], [Morris 2013], [Raymer 1989], [Nita 2008]. This limitation is measured by the minimum control airspeed V_{mc} which may not be larger than $1.13V_{\text{sr}}$ where V_{sr} is the 1g stall velocity.

Based on the situation depicted in Fig 1, an example of VT sizing for trim objective as recommended by aircraft design handbooks [Torenbeek 1982], [Raymer 1989] is proposed. In an OEI situation, the thrust T of the remaining engine generates a yawing moment that has to be balanced by the side force F_y produced by the VT:

$$-F_y l_v + N_{A-v} + T y_e = 0,$$

where l_v is the level arm between vertical tail quarter chord and aircraft Center of Gravity (CG), N_{A-v} is the yawing moment of the aircraft, without its VT, at non zero side slip and y_e is the level arm between the operational engine and aircraft CG. In this example, for a turbo-propeller aircraft equipped with an automatic feathering system, the failed engine is assumed to produce negligible additional drag [1]. N_{A-v} for aircraft with a wing of small dihedral and sweep angle, comes mainly from the fuselage in side-slip and is destabilizing.

The side force can be decomposed into the sum of forces produced by the VT in side slip, β and a deflection δ_R of the rudder:

$$F_y = \frac{1}{2}\rho S V_v^2 C_y \ ,$$

$$C_y = C_{y_\beta}\left((\beta - \sigma_v) + \tau_r \delta_R\right) \ ,$$

1. The same cannot be said for turbo-fan engines and an additional yawing moment produced by the dragging engine has to be taken into account

where C_{y_β} is the VT side force coefficient, $\tau_r = \frac{\partial C_{y_\beta}}{\partial \delta_R}$ is the rudder efficiency factor, S is the reference surface area, ρ is the air density, σ_v and V_v are respectively the side wash angle and the airspeed at the location of the VT.

With known rudder saturation, it is possible to deduce the required VT surface area S_v, or with l the reference length, a VT volume ratio $\frac{S_v l_v}{Sl}$ to trim the aircraft:

$$C_{y_\beta}\left((\beta - \sigma_v) + \tau_r \delta_R\right) S_v l_v = \frac{N_{A-v} + T y_e}{0.5\rho V_v^2} \ ,$$

$$S_v l_v = \frac{N_{A-v} + T \cdot y_e}{0.5\rho V_v^2 C_{y_\beta}\left((\beta - \sigma_v) + \tau_r \delta_R\right)} \ .$$

For a twin-engine aircraft with high wing position, the propeller slipstream influences the side wash σ_v depending on the direction of rotation. This is the reason why when engines are rotating in the same direction, there is one engine loss that is more critical than the other. Unless the propeller slipstream impacts directly the VT, the term V_v is close to the airspeed at infinity.

The thrust being related to the power by the relation [2]: $P = TV$, for a constant engine power and assuming $V_v = V$, one obtains:

$$S_v l_v = \frac{N_{A-v}}{0.5\rho V^2 C_{y_\beta}\left((\beta - \sigma_v) + \tau_r \delta_R\right)} + \frac{P \cdot y_e}{0.5\rho V^3 C_{y_\beta}\left((\beta - \sigma_v) + \tau_r \delta_R\right)}.$$

The term due to the thrust unbalance being divided by V^3, this relation highlights the importance of the airspeed during engine failure in the design of the VT.

In addition, the aircraft is limited by certification regulation to $\phi = 5°$ of bank angle to balance the side force F_v. In preliminary design, F_v is considered to originate entirely from the VT, neglecting the fuselage contribution at this stage:

$$F_v = L \sin\phi \approx L\phi,$$

from which one can express a constraint on the VT surface area:

$$\frac{S_v}{S} \leq \frac{V^2}{V_v^2} \frac{C_L \phi}{C_{y_\beta}\left((\beta - \sigma_v) + \tau_r \delta_R\right)}, \text{ with } \phi = \frac{5\pi}{180} \text{ rad}.$$

With C_{y_β} being fixed by requirement **2**, if this constraint is violated during preliminary design, the designer has to play with the level arm l_v or increase the minimum airspeed at which OEI is supposed to happen. Torenbeek [Torenbeek 1982] and

2. This relation is true for propeller aircraft and approximated for turbo-fan [Boiffier 1998].

Obert [Obert 2009], argue that lateral flight handling qualities may be ignored in preliminary design, only the trim criterion in OEI should be calculated. This is confirmed by Nita in [Nita 2008] as an exercise to redesign a turbo-propeller transport aircraft. It is found that the trim criterion requires a larger VT than the dynamic stability criterion. In addition, many studies [Morris 2013], [Hoerner 1985], [Ciliberti 2013] suggest that the VT is often over-dimensioned to cope with the difficulties of accurately predicting the VT aerodynamic performance. The flow impacting the VT being disturbed by other aircraft components.

These are as many reasons to size the VT with a large stability margin to cope with emergency situations and low speed operations. There are however real advantages to reduce static stability on an aircraft.

0.2.2 Reduced static stability

When reducing the tail volumes i.e stability surfaces and level arms, a significant reduction in drag can be obtained thanks to the diminution of wetted surface area, trim drag and lower structural mass. In the civilian domain, this effect is increasingly exploited due to the important flight performance increase [Rediess 1980], [Abzug 2005].

To obtain a high level of performance improvement, the aircraft design strategy must be modified so as to include a stability and control block that can act on the geometry of the aircraft. This way, the designer can take advantage of fly by wire and active control. This discipline is called Control Configured Vehicle (CCV) and is not limited to aircraft [Abzug 2005].

An example of aircraft design based on CCV principles has been described by Anderson and Mason in [Anderson 1996]. The authors introduce the main problem with CCV; the automation of control law design and flight quality assessment in order to embed the discipline in a Multi-Disciplinary Optimization (MDO). They propose a solution based on fuzzy logic to weight the risk associated with the complexity of the control design. This treatment is then integrated in an MDO framework for overall aircraft design.

In the following years Chudoba and Smith [Chudoba 2003] as well as Perez and Liu [Perez 2006], both presented a MDO framework with stability and control laws design based on stability augmentation system and pole placement technique. Welstead in [Welstead 2014], utilized a more advanced control design technique with the inclusion of optimal control into MDO. Recently, Denieul [Denieul 2016]

realized a co-design by calculation of control law and flight control surfaces with the inclusion of flight handling quality constraints and using non smooth optimization techniques.

These examples integrate automatic control tools of increasing complexity into aircraft design. They tend toward a more global approach to handle the coupling of two or more disciplines [3].

0.2.2.1 Previous attempts at VT reduction

While methods exist for designing aircraft with relaxed longitudinal stability [Cozensa 2017], reduction of directional stability remains an active field of research. Feuersanger [Feuersänger 2008] proposed a robust control design and back-up controller for a dynamically unstable blended wing body, with the integration of handling quality constraints using Linear Matrix Inequalities (LMIs) optimization. A similar approach has been used by Morris for traditional tube and wing aircraft [Morris 2013]. For both studies, the VT is reduced while ensuring satisfying handling qualities but the trim capability with OEI is solved by imposing a higher approach velocity.

This trim limitation can be overcome without modifying the approach velocity by increasing the VT efficiency using airflow control technology to delay flow separation on the rudder. This idea was successfully demonstrated in flight, eventually resulting in a reduction of 12% in VT surface area and 0.9% reduction in cruise drag [Mooney 2014], [Lin 2016].

Finally, there has been the idea to lower VT surface area without impacting the trim limitation using differential thrust with small turbo-fans distributed on the wing [Ameyugo 2006], [Nguyen 2018]. The authors underlined the following limitations for this idea:

— a lower engine efficiency due to small turbo-fans,

— the slow reaction time of turbo fans.

These limitations can be overcame by the consideration of a distributed electric propulsion.

3. Here, mainly but not limited to, flight performance and flight stability and control.

0.2.3 Distributed Propulsion

Distributed propulsion without the specific mention to electric power, has a vague meaning and can designate any aircraft which propulsive system is composed of more than one engine. This definition is too broad and can lead to misconception about the original goal of power distribution. NASA researcher Hyun Dae Kim proposed the following definition to refine the category of aircraft concerned by this technology: "*Distributed propulsion in aircraft application is the spanwise distribution of the propulsive thrust stream such that overall vehicle benefits in terms of aerodynamic, propulsive, structural, and/or other efficiencies are mutually maximized to enhance the vehicle mission*" [Kim 2010]. DEP considered in this work falls into this definition because it is the spanwise distribution of the power that should allow an enhanced directional control with differential thrust.

Restricting the review to scientific work related to DEP would be too restrictive in regard to the important scientific contribution in exploiting propulsion-airframe interference for Vertical/Short Take Off and Landing (V/STOL) applications.

Figure 3 – Breguet Br-941 in approach, reproduced from [Aerostories 2002]

The 1950s and 1960s saw a large interest in distributed propulsion to build V/STOL aircraft among which the Breguet Br-941 represented in Fig 3, is worth a presentation in the context of this work. Also known as McDonnell 188, it is representative of the blown wing concept. The Br-941 utilizes four distributed turbopropellers to obtain high-lift characteristics, rendering possible a take-off within 140m and landing within 95m. These performances are obtained by fully embedding the wing in the propeller slipstreams. Redundancy was provided by mechanically

coupling of all four propellers, making the aircraft able to maintain cruise speed with two failed power plants, without the loss of the corresponding propellers. This redundancy was a key aspect for the safety demonstration of the aircraft [Gambu 1959].

The most interesting detail, for this thesis is the variable-pitch propellers, which were used differentially for lateral control at low speed , [Noetinger 2001], [Quigley 1964]. Figure 4, shows the propeller pitch differential applied as a function of pilot inputs.

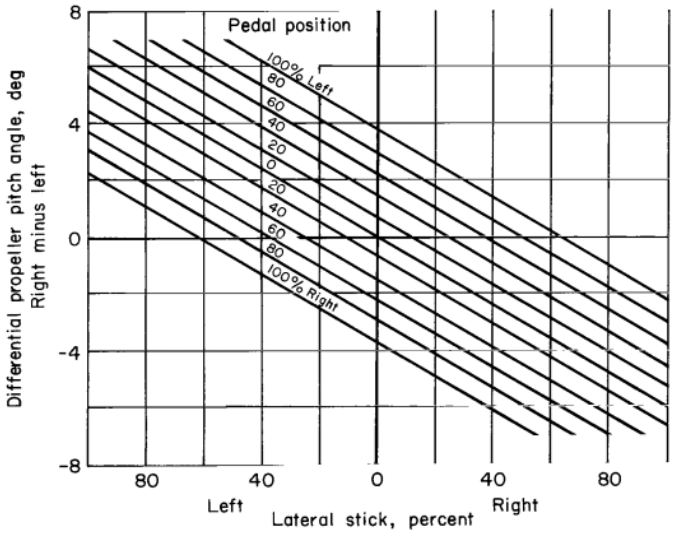

Figure 4 – Breguet Br-941 differential propeller pitch angle as function of pilot lateral (stick) and directional (pedal) inputs, reproduced from [Quigley 1964]

DT is used both for yaw and bank pilot input. The advantages brought by the use of DT is given by Quigley et al, as pilot's rating of the handling qualities. The pilot's rating for the lateral axis at landing goes from "*satisfactory in normal operations*" with DT to "*unsatisfactory in normal operation*" when DT is disabled. The pilot's comments are worth a reproduction here: "*The relatively large adverse yaw which occurred without differential propeller pitch was very objectionable.*". Although this adverse yaw comes from the large deflected ailerons in high lift configuration, DT is said to contribute in two ways to lateral control: by increasing directional control power and by lowering adverse yaw. Interestingly, the trend is reversed during cruise and the aircraft is judged too sensitive both for the lateral and the directional axis if differential thrust is activated.

In this example, the advantages obtained with the differential use of the propulsion systems are mostly associated with enhanced handling qualities. The impact

on the design is not clear but it may well have prevented the installation of a disproportionally large VT for low speed operations. The Br-941 remains the only example of differential thrust with distributed propulsion that holds an operational career (retired in 1974 [Noetinger 2001]), to the author's knowledge.

0.2.3.1 Distributed Electric Propulsion

Propulsive architectures with specific mention of distributed electric propulsion proposed by [Drum 1924] and [Kilgore 1949], are two early examples of electrical power transmission to distributed thrust providers (see the concept of Kilgore in Fig 5).

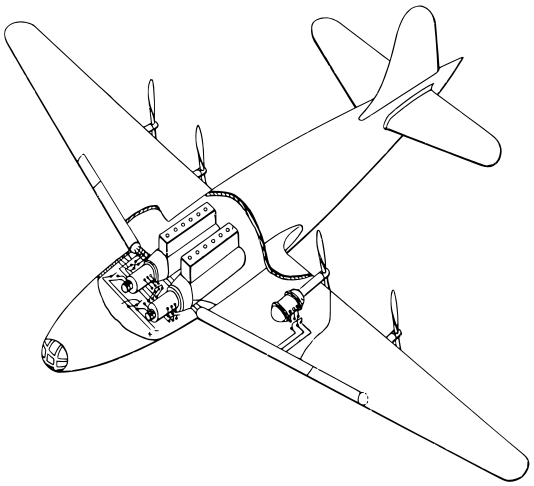

Figure 5 – Early example of distributed electric propulsion with gasoline generators, reproduced from [Kilgore 1949].

Among the advantages, [Kilgore 1949] cites better propulsion airframe integration and better propeller efficiency as the two most promising. Electric engines can be made compact enough to be buried in the airfoil and gasoline generators are installed in the fuselage, eliminating the nacelle drag. Distributing the power across many propellers allows smaller propellers with lower tip mach number and fewer blades.

If DEP is not a new idea, it gained attention in late 2010, when it became apparent that there exists a limit to the efficiency increase of turbo-fans. Whether because of airframe integration problems (example of the 737) or due to design complexity (geared turbo-fans), increasing the by-pass ratio to improve the propulsive efficiency is becoming more difficult [Felder 2009]. Distributing the power across many smaller electric fans appeared as an equally complex solution to increase the

by-pass ratio and it offers the possibility to find synergies with the advantages of electric propulsion. In [Felder 2009], the authors provide a list of potential advantages for DEP. The numerous possibilities offered by DEP means that it can be employed for multiple usage. For example, it may provide high lift, redundancy and directional control as is the case for the concept plane Ampere [Liaboeuf 2018], [Dilinger 2018].

The main reason to distribute the propulsive power is to improve the propulsive efficiency [Ko 2003] or exploit beneficial aero-propulsive interactions between the propulsion and aerodynamic surfaces. Propulsion integration favoring a synergistic airframe-propulsion interaction is the source of a large amount of studies at the moment of writing [Hermetz 2016], [Schmollgruber 2019], [Clarke 2017], [Kim 2018].

0.2.3.2 Electric motors

As mentioned before, electric motors are the key systems to unlock reduced directional stability thanks to their presumed fast reaction time and their good efficiency at small scale. These affirmations seem to make a general consensus in the literature (see [Moore 2014] and [Hepperle 2012]), although powerful high power density electric engines of the order of 100KW to a few megawatts for aviation remain to be built and flight tested. Research efforts in this way are currently undertaken to envision future electric engine technology for aircraft [Henke 2018]. Electrical engineers can rely on more than one hundred years of scientific and engineering knowledge in the domain and the work mainly resides in increasing the power density and improving thermal management. Examples of motors of a few hundreds KW were already successfully flown in experimental test programs [Aerospace-Technology 2017], [Warwick 2019], and the E-fanX experiment promises a first test in the MW class [Airbus 2019]. The interest is not to verify these affirmations, rather to quantify the awaited performance regarding future electric motors technology for aircraft, especially concerning the bandwidth one can expect from propulsive electric motor for aircraft.

Electric V/STOL relying on vertical thrust similar to drones, are examples of flight stabilization using the principal mean of propulsion systems [Angrand 2020] and [Aviation-Week 2017]. This can be regarded as an argument in favour of active flight control with electric motors. However, vertical flight requires only small thrust variation while forward flight contains flight segment with large variation of thrust due to the more important airspeed range. The same technology may not be adapted

and a small review of electric engine drive has been found beneficial for this work. The main question remains, what kind of bandwidth can be considered for future large electric engines dedicated to aircraft propulsion?

In the example of a simple DC electric motor, the mechanical time constant is a function of electrical and mechanical construction of the motor. The torque can be controlled by varying the current through the voltage applied to the motor. With this control, the reaction time can be the order of 10^{-1} s [Grellet 1996]. Modern motor drives make use of power electronics and fast processors to offer digital control of the engine. Among the possible methods, the Direct Torque Control (DTC) provides a response time for torque of the order of 10^{-3} s. Additionally, it is independent of engine electrical parameters and suitable for many types of electric motor (synchronous, asynchronous) [Casadei 2006] [Zhong 1997], [Wildi 2000]. If one considers this type of control coupled with a constant speed propeller, it is clear that the limiting component for bandwidth will be the propeller pitch control actuator and this independently of the engine size or inertia. The bandwidth to consider can therefore be restricted to classical aeronautical actuators, of the order of 2.5Hz [Denieul 2016].

0.2.3.3 Stability reduction with distributed propulsion and DEP

The last paragraph of this literature review concerns the efforts that have already been undertaken to couple stability reduction with the propulsion systems and particularly a DEP.

A special use of the propulsion system can be implemented in commercial aircraft as a back-up control system to land an aircraft that would have suffered the complete loss of hydraulic systems of the usage of the control surfaces. From a historical perspective, such a control system has been first developed by NASA and is called Propulsion Control Aircraft (PCA), [Tucker 1999]. The loss of directional stability following a damage caused to the vertical stabilizer can also be a reason to use the propulsion system differentially and studies have been done in this direction such as [Lu 2018]. However these researches aim at designing an emergency back-up controller and not at integrating the additional control power given by the propulsion system and the design of stability surfaces into preliminary design.

An example of the integration of the propulsion system into a longitudinal stability module for multidisciplinary design can be found in [Schmollgruber 2019].

Studies concerned with directional stability can be mentioned with a similar

project by Empirical System [Klunk 2018b] and [Freeman 2018]. These papers report the preparation of a flight dynamic simulation environment for DEP aircraft and the set-up of a small scale demonstrator with distributed electric fans on the wing with the goal to explore a reduction of directional stability. The study by Klunk and Freeman [Klunk 2018b] focuses on the sizing criterion for the vertical tail by taking into consideration thrust reconfiguration or active control with DEP. The application case is a 150 passenger aircraft with a hybrid-electric propulsion system consisting of distributed electric fans embedded in the wing. The authors use different failure scenarios for their design and show that a trade off has to be made between directional stability at low airspeed and the mass of the electric grid for power transmission. Their conclusions being that the weight associated with an electrical grid allowing redundancy and thrust re-configuration overcomes the weight savings associated with removal of vertical tail. The potential of active differential thrust is however underlined as it may replace the vertical tail for trim requirements expressed by flight safety regulations.

0.3 Conclusion and formulation of research paths

This review was aimed at introducing the different disciplines related to the problem of relaxing the directional static stability and using an active differential thrust for flight control. The main interest seems to remain the ability to re-allocate the thrust thanks to the high redundancy and avoid thrust unbalance. The field remains largely unexplored with a high general complexity due to the number of disciplines covered and the added degrees of freedom. A first interrogation can be formulated around the sizing flight conditions for the VT. Obviously the thrust cannot be always re-allocated, there will exist a scenario of failure for which a thrust asymmetry is inevitable and one wishes to identify this critical failure condition.

The first idea to answer this problem is explored in Part II and consists of evaluating the flight envelope of the aircraft with various engine failure scenarios and variable vertical tail size. To this end, a trimming tool adapted to aircraft with distributed electric propulsion is introduced in Chapter 1 and a model to capture the variation of the vertical tail surface area is developed in Chapter 2. A next work consists in improving the fidelity of the aircraft modelling and specifically in taking into account the aero-propulsive interactions, which are often cited as non-negligible forces at low speed. The principle, which is detailed in Chapter 3, is to adapt an

existing technique to the needs of the project and add it to the framework created in the previous chapters.

The unconventional aircraft configuration quickly questions the flight conditions explicitly mentioned by the certification regulation for safety demonstration, especially the OEI case. Rather than considering OEI, the critical failure condition is looked for by successively switching off the engines until the trim condition cannot any more be satisfied. To overcome this iterative process, an attempt is made to invert the problem and design the propulsion system and the VT for a known critical engine failure instead of looking for the critical failure. Following these two steps, detailed in Chapter 4 and 5 respectively, the sizing flight conditions are found and general sizing rules to satisfy static trim and controllability requirements are established at the end of Part II.

In Part III, the interest will be the inclusion of the static trim requirements and the sizing flight conditions in a co-design framework where the VT, the control laws and the engine bandwidth are designed considering static trim and handling quality requirements. The main principle behind co-design is the use of optimisation techniques and the inclusion of both control law gains and design parameters into the set of optimisation variables. This way, it is possible for automatic control to influence the design at an early phase. A known procedure to achieve this is to use H_∞ control design methods and multi-objective optimisation functions. The specificity of this study will be to compute a trade-off that can answer the design constraints for both nominal and asymmetric thrust conditions with only a reconfiguration of the control gains. This part is separated in three chapters where Chapter 6 introduces the co-design with H_∞, the control system and presents a preliminary design. Chapter 7 explores the sensitivity of the solution to design variables allowing the definition of additional constraint and the calculation of a design trade-off. Finally Chapter 8 deals with the inclusion of the asymmetric thrust condition alongside the nominal flight condition in the co-design.

Knowing the limitation of the diverse models and the assumptions made for the co-design architecture, a means of validation through flight tests will be considered in Part IV. For this purpose, a DEP flight demonstrator model is built, instrumented and flight tested. The model has a 2m wingspan, weights 8.25kg and has eight engines distributed along the wing leading edge. Flight data are then used to identify a model of the aircraft that reveals the influence of the thrust on the aircraft lateral motion. This experimental work is reported in Chapter 9 for the description of the

flying demonstrator and in Chapter 10 for the flight model identification.

Part II

System Modelling and Flight Envelope Studies

Chapter 1

Flight dynamics model

Contents

The determination of achievable flight envelope, static and dynamic stability suppose the calculation of flight equilibrium or quasi-equilibrium. This can be achieved with a trim algorithm. The contours of a flight envelope can then be calculated knowing the available control power. Static and dynamic stability can be assessed after linearisation around an equilibrium point and linear control theory can be used for the design of control laws.

The starting point is therefore the construction of a trimming algorithm that can handle distributed propulsion as an actuation system and may be used in combination with multiple aerodynamic models. This chapter aims at constructing the mathematical model of a general DEP aircraft and a trim algorithm that can be used for a distributed architecture.

The chapter is structured as follow, a definition of the reference frames, transformation matrices, variables and parameters used throughout the manuscript is made in sections 1.1 and 1.2. A mathematical model of distributed propulsion is then proposed and introduced in the equations of motions in section 1.3. The trim algorithm is detailed in section 1.5 and the linearisation process in section 1.6.

Hypothesis In order to obtain the flight dynamic equations used throughout this work, the following hypotheses are made:

1. The Earth is considered flat and fixed,
2. The wind field is considered uniform.

1.1 Reference Frames and variables

The frames presented in this section and their transformations are based on [Boiffier 1998].
The interest is to model the aircraft flight dynamics around equilibrium and/or pseudo-equilibrium for relatively short periods of time compared to a whole flight time. A convenient frame for this analysis is the aerodynamic frame, $\mathcal{F}_a$, referred with the subscript $_a$, that allows direct monitoring of the main variables contributing to the aerodynamic forces and propulsion. Specifically, these variables are the air velocity V_a and the aerodynamic angles: β_a for the slide slip and α_a for the angle of attack (see Fig 1.1).

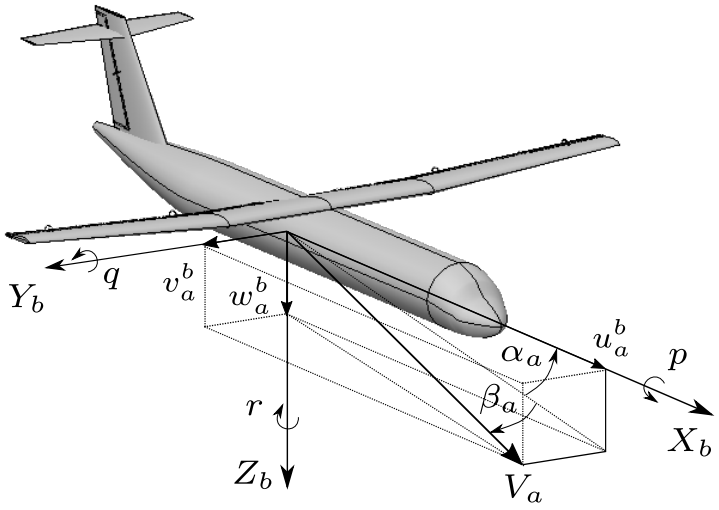

Figure 1.1 – Body $\mathcal{F}_b$ and Aerodynamic $\mathcal{F}_a$ reference frames definition.

In parallel, an experimental campaign using a flying demonstrator is planned as part of this thesis. Hence, complementary frames are defined, in which the data measured on-board the aircraft are expressed. The standard equipment observed in actual drones and that can be used to reconstruct aircraft dynamics, includes inertial and Global Navigation Satellite System (GNSS) sensors. The first delivers

measurement in body frame, $\mathcal{F}_b$ while the other delivers measurements in both the geocentric inertial frame $\mathcal{F}_I$ and the vehicle carried North East Down (NED) frame $\mathcal{F}_o$ (see Fig 1.2). All three frames are taken into consideration.

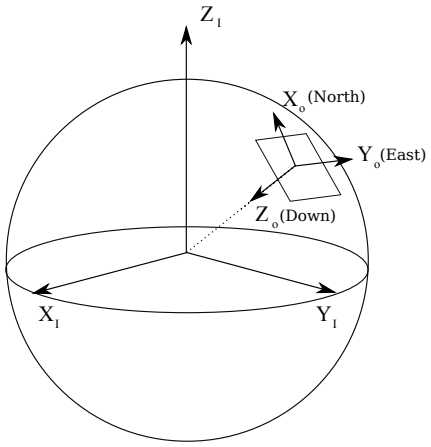

Figure 1.2 – Inertial $\mathcal{F}_i$ and local North-East-Down $\mathcal{F}_o$, reference frames definition.

The transformation from the vehicle carried NED frame to the body frame is realized using the Euler angles (see Fig 1.3):

— Azimuth angle ψ,

— Pitch angle θ,

— Bank angle ϕ.

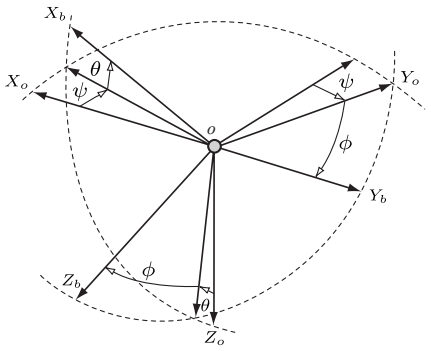

Figure 1.3 – Euler angles rotation definition.

The associated rotation matrix is given as

$$\mathbf{X}^o = \mathcal{T}_{ob}\mathbf{X}^b, \tag{1.1}$$

$$\mathcal{T}_{ob} = \begin{pmatrix} \cos\theta\cos\psi & \sin\theta\sin\phi\cos\psi - \sin\psi\cos\phi & \cos\psi\sin\theta\cos\phi + \sin\phi\sin\psi \\ \sin\psi\cos\theta & \sin\theta\sin\phi\sin\psi + \cos\psi\cos\phi & \sin\theta\cos\phi\sin\psi - \sin\phi\cos\psi \\ -\sin\theta & \cos\theta\sin\phi & \cos\theta\cos\phi \end{pmatrix}$$

The transformation from the vehicle carried NED $\mathcal{F}_o$ to the aerodynamic frame $\mathcal{F}_a$ is realized using the aerodynamic angles:

— Aerodynamic bank angle μ_a,

— Aerodynamic flight path angle γ_a,

— Aerodynamic azimuth angle χ_a.

The associated rotation matrix is given as

$$\mathbf{X}^o = \mathcal{T}^{oa}\mathbf{X}^a, \tag{1.2}$$

$$\mathcal{T}_{oa} = \begin{pmatrix} \cos\chi_a\cos\gamma_a & \cos\chi_a\sin\gamma_a\sin\mu_a - \sin\chi_a\cos\mu_a & \cos\mu_a\sin\gamma_a\cos\chi_a + \sin\chi_a\sin\mu_a \\ \sin\chi_a\cos\gamma_a & \sin\chi_a\sin\gamma_a\sin\mu_a + \cos\chi_a\cos\mu_a & \cos\mu_a\sin\chi_a\sin\gamma_a - \sin\mu_a\cos\chi_a \\ -\sin\gamma_a & \cos\gamma_a\sin\mu_a & \cos\gamma_a\cos\mu_a \end{pmatrix}$$

The transformation from the body frame $\mathcal{F}_b$ to the aerodynamic frame $\mathcal{F}_a$ is realized using the angle of attack and side slip angles:

— Angle of attack α_a,

— Side slip angle β_a,

The associated rotation matrix is given as

$$\mathbf{X}^b = \mathcal{T}_{ba}\mathbf{X}^a, \tag{1.3}$$

$$\mathcal{T}_{ba} = \begin{pmatrix} \cos\alpha_a\cos\beta_a & -\cos\alpha_a\sin\beta_a & -\sin\alpha_a \\ \sin\beta_a & \cos\beta_a & 0 \\ \sin\alpha_a\cos\beta_a & -\sin\alpha_a\sin\beta_a & \cos\alpha_a \end{pmatrix}$$

Because the previously introduced rotation matrix is orthogonal, the following property is true:

$$\mathcal{T}_{ab}^{-1} = \mathcal{T}_{ab}^{\intercal} = \mathcal{T}_{ba} \tag{1.4}$$

1.2 Variables

The variables used to model aircraft dynamics are defined here in the different reference frames when it is necessary.

The kinematic velocity of the aircraft $\mathbf{V}_k$ is defined in the vehicle carried NED frame as:

$$\mathbf{V}_k^o = \begin{pmatrix} u_k^o \\ v_k^o \\ w_k^o \end{pmatrix}. \tag{1.5}$$

Its expression in the body frame is obtained by projection:

$$\mathbf{V}_k^b = \mathcal{T}_{bo} \begin{pmatrix} u_k^o \\ v_k^o \\ w_k^o \end{pmatrix}. \tag{1.6}$$

The air velocity $\mathbf{V}_a$ is carried in the aerodynamic frame by the $\mathbf{x}_a$ axis, its expression in body frame is:

$$\mathbf{V}_a^b = \mathcal{T}_{ba} \begin{pmatrix} V_a \\ 0 \\ 0 \end{pmatrix},$$

$$\mathbf{V}_a^b = \begin{pmatrix} u_a^b \\ v_a^b \\ w_a^b \end{pmatrix} = V_a \begin{pmatrix} \cos\alpha_a \cos\beta_a \\ \sin\beta_a \\ \sin\alpha_a \cos\beta_a \end{pmatrix}. \tag{1.7}$$

Similarly, its expression in the NED frame is:

$$\mathbf{V}_a^o = \mathcal{T}_{oa} \begin{pmatrix} V_a \\ 0 \\ 0 \end{pmatrix},$$

$$\mathbf{V}_a^o = \begin{pmatrix} u_a^o \\ v_a^o \\ w_a^o \end{pmatrix} = V_a \begin{pmatrix} \cos\chi_a \cos\gamma_a \\ \sin\chi_a \cos\gamma_a \\ -\sin\gamma_a \end{pmatrix}. \tag{1.8}$$

The relationship between the kinematic velocity and the air velocity is given through the wind speed $\mathbf{V}_w$:

$$\mathbf{V}_k = \mathbf{V}_a + \mathbf{V}_w. \tag{1.9}$$

The definition of angle of attack α_a, side slip β_a and air velocity V_a can be derived from equation (1.7):

$$V_a = \sqrt{{u_a^b}^2 + {v_a^b}^2 + {w_a^b}^2}, \tag{1.10}$$

$$\beta_a = \arcsin \frac{v_a^b}{V_a}, \tag{1.11}$$

$$\alpha_a = \arctan \frac{w_a^b}{u_a^b}. \tag{1.12}$$

The aerodynamic flight path angle γ_a and azimuth angle χ_a can be derived using equation (1.8):

$$V_a = \sqrt{{u_a^o}^2 + {v_a^o}^2 + {w_a^o}^2}, \tag{1.13}$$

$$\chi_a = \arctan \frac{v_a^o}{u_a^o} \tag{1.14}$$

$$\gamma_a = \arcsin \frac{-w_a^o}{V_a}. \tag{1.15}$$

Considering hypothesis 1, the vector of rotations of the aircraft with respect to the vehicle attached earth frame is defined in the body frame as:

$$\mathbf{\Omega}_{bo} = \begin{pmatrix} p \\ q \\ r \end{pmatrix}. \tag{1.16}$$

The kinetic relationship associating the vector of rotations and angular rates is expressed as:

$$\begin{pmatrix} p \\ q \\ r \end{pmatrix} = \begin{pmatrix} 1 & 0 & -\sin\theta \\ 0 & \cos\phi & \cos\theta\sin\phi \\ 0 & -\sin\phi & \cos\theta\cos\phi \end{pmatrix} \begin{pmatrix} \dot{\phi} \\ \dot{\theta} \\ \dot{\psi} \end{pmatrix}. \tag{1.17}$$

For steady turning manoeuvres, the turn rate Ω is analogous to the angular rate $\dot{\psi}$

and is expressed by inverting equation (1.17):

$$\Omega = (q \sin\phi + r \cos\phi) \frac{1}{\cos\theta} \,. \tag{1.18}$$

In order to find the aerodynamic bank angle, μ_a one can express the transformation from NED to aerodynamic frame using an intermediate step by the body frame:

$$\mathcal{T}_{ao} = \mathcal{T}_{ab} \cdot \mathcal{T}_{bo}. \tag{1.19}$$

Retaining only the last column of $\mathcal{T}_{ao}$ and $\mathcal{T}_{bo}$:

$$\begin{pmatrix} -\sin\gamma_a \\ \cos\gamma_a \sin\mu_a \\ \cos\gamma_a \cos\mu_a \end{pmatrix} = \mathcal{T}_{ab} \begin{pmatrix} -\sin\theta \\ \cos\theta \sin\phi \\ \cos\theta \cos\phi \end{pmatrix},$$

$$\begin{pmatrix} \sin\gamma_a \\ \cos\gamma_a \sin\mu_a \\ \cos\gamma_a \cos\mu_a \end{pmatrix} = \begin{pmatrix} \cos\alpha_a \cos\beta_a \sin\theta - \sin\beta_a \sin\phi \cos\theta - \sin\alpha_a \cos\beta_a \cos\phi \cos\theta \\ \sin\theta \cos\alpha_a \sin\beta_a + \cos\beta_a \cos\theta \sin\phi - \sin\alpha_a \sin\beta_a \cos\theta \cos\phi \\ \sin\theta \sin\alpha_a + \cos\beta_a \cos\theta \cos\phi \end{pmatrix}. \tag{1.20}$$

Equation (1.20) gives an additional definition for the aerodynamic flight path angle that does not include velocity terms.

The aerodynamic forces and moments are rendered non-dimensional with the following relationships:

$$\mathbf{F}^a = \frac{1}{2}\rho S V_a^2 \begin{pmatrix} C_X^a \\ C_Y^a \\ C_Z^a \end{pmatrix} \tag{1.21}$$

$$\mathbf{M}^a = \frac{1}{2}\rho S l V_a^2 \begin{pmatrix} C_l^a \\ C_m^a \\ C_n^a \end{pmatrix} \,. \tag{1.22}$$

Here, rho is the air density, the reference surface area S corresponds to the wing surface area, while the reference length l is:

— $\bar{c}$, the mean chord for the longitudinal axis,

— b, the wingspan for the lateral axis.

C_l^a, C_m^a and C_n^a are respectively the rolling, pitching and yawing moment coefficients.

The force coefficients C_x^a, C_y^a and $C_z^a$are conveniently defined in the aerodynamic frame as:

$$\begin{pmatrix} C_X^a \\ C_Y^a \\ C_Z^a \end{pmatrix} = \begin{pmatrix} -C_D \\ C_y \\ -C_L \end{pmatrix}, \tag{1.23}$$

where one finds the traditional notation C_D for the drag coefficient, C_L for the lift coefficient and C_y for the side force coefficient. The relationship between body and aerodynamic frame being:

$$\begin{pmatrix} C_X^b \\ C_Y^b \\ C_Z^b \end{pmatrix} = \mathcal{T}_{ba} \begin{pmatrix} -C_D \\ C_y \\ -C_L \end{pmatrix}. \tag{1.24}$$

The gravity vector is defined in the NED reference frame as:

$$\mathbf{g} = \begin{pmatrix} 0 \\ 0 \\ g \end{pmatrix}. \tag{1.25}$$

The inertia matrix computed at the centre of mass of the aircraft $\mathbb{I}$ expressed in the body frame is given by:

$$\mathbb{I}^b = \begin{pmatrix} I_x & 0 & -I_{xz} \\ 0 & I_y & 0 \\ -I_{xz} & 0 & I_z \end{pmatrix}, \tag{1.26}$$

with I_x, I_y, I_z the moment of inertia around the body axis $\mathbf{X}_b$, $\mathbf{Y}_b$ and $\mathbf{Z}_b$ respectively and I_{xz} the product inertia between axis $\mathbf{X}_b$ and $\mathbf{Z}_b$.

1.3 Propulsion modelling

1.3.1 Thrust and moments with DEP

The propulsion is modelled through N_m point forces assumed symmetrically placed along the wing leading edge. The total thrust force and moments due to

point forces are calculated by summation based on the geometrical arrangement shown in Fig 1.4:

$$\mathbf{T}_x^b = \begin{pmatrix} \sum_{i=1}^{N_m} T_i \cos(i_{p_i}) \\ 0 \\ \sum_{i=1}^{N_m} T_i \sin(i_{p_i}) \end{pmatrix}, \tag{1.27}$$

$$\mathbf{M}_c^b = \sum_{i=1}^{N_m} \begin{pmatrix} x_i \\ y_i \\ z_i \end{pmatrix} \times \begin{pmatrix} T_i \cos(i_{p_i}) \\ 0 \\ T_i \sin(i_{p_i}) \end{pmatrix}, \tag{1.28}$$

where T_i is the thrust force of the i$^{\text{th}}$ motor, x_i, y_i, z_i are the level arms between the centre of gravity and the i$^{\text{th}}$ motor and i_{p_i} is the tilt angle of the i^{th} motor measured between engine axis and body $\mathbf{x}_b$ axis.

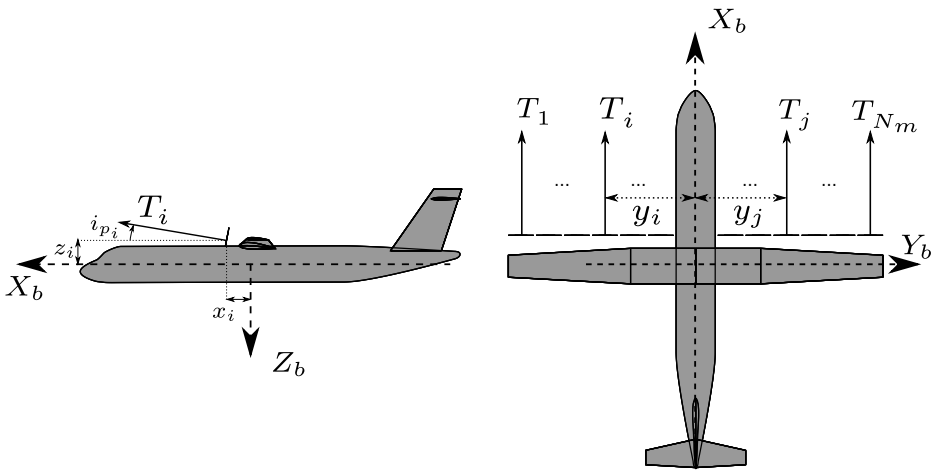

Figure 1.4 – Illustration of a symmetric thrust distribution covering the whole wing where $y_j = -y_i$, $j = N_m + 1 - i$.

Our study is limited to propulsive system based on propellers driven by electric engines. For aircraft equipped with a propeller or a fan, a common thrust model is [Sachs 2012]:

$$T = PV^{-1}\eta_p \frac{\rho}{\rho_0}\delta x, \tag{1.29}$$

where P is the engine power at sea level, V is the flight velocity, η_p is the propeller or fan efficiency, ρ the air density and δ_x the throttle command. Equation (1.29) models the loss of power of air breathing engines with the variation of the air density

with respect the air density at sea level ρ_0. Electric motors on the contrary, do not suffer from the rarefaction of air as turbo-machines, such that the following thrust model may be considered [Sachs 2012]:

$$T_i = \frac{P_E}{N_m} V^{-1} \eta_m \eta_p \delta_{x,i}, \tag{1.30}$$

with P_E being the total electrical power available from the line, N_m being the total number of engine, η_m and η_p respectively the engine and propeller efficiency (both considered constant, although η_p is affected by air density). Hence, the power is considered equally divided between each engine.

One may argue that electric propulsion will be impacted by altitude anyway. It is true in many aspects, for example:

— With increasing altitude cooling of electric engine and power electronics can become more difficult,

— Maximum rated voltage of conductors decreases with altitude due to Corona effect, [Wir 2010]

— Finally, in the case of series hybrid or turbo-electric propulsion, the turbo-machine producing the electric power remains sensitive to air rarefaction.

These limitations are either due to technological locks that can be overcome with increasing interest in electric propulsion or associated with a level of detail outside the scope of our study. For these reasons, the assumption is made that the maximum continuous power remains constant with altitude.

1.3.2 Propeller rotor term

The propeller gyroscopic effect can be significant for the control of a propeller aircraft. Sudden change of engine rotation rates or sudden manoeuvres create efforts on the aircraft through the gyroscopic effect and Newton's Third law. Gyroscopic

forces of a rotating propeller can be calculated as:

$$\mathbf{M}_g = \mathbf{\Omega} \times \sum_{i=1}^{N_{eng}} \mathcal{T}_{bp_i} \mathbf{I}_p \mathbf{h}_i^p,$$

$$\mathbf{M}_g = \begin{pmatrix} p \\ q \\ r \end{pmatrix} \times \sum_{i=1}^{N_{eng}} \begin{pmatrix} \cos i_{p_i} & 0 & \sin i_{p_i} \\ 0 & 1 & 0 \\ -\sin i_{p_i} & 0 & \cos i_{p_i} \end{pmatrix} \begin{pmatrix} I_{x,p_i} & 0 & 0 \\ 0 & I_{y,p_i} & 0 \\ 0 & 0 & I_{z,p_i} \end{pmatrix} \begin{pmatrix} \omega_{x_i} \\ 0 \\ 0 \end{pmatrix},$$

$$\mathbf{M}_g = \begin{pmatrix} p \\ q \\ r \end{pmatrix} \times \sum_{i=1}^{N_{Nm}} \begin{pmatrix} \omega_{x_i} I_{x,p_i} \cos i_{p_i} \\ 0 \\ -\omega_{x_i} I_{x,p_i} \sin i_{p_i} \end{pmatrix},$$

$$\mathbf{M}_g = \sum_{i=1}^{N_{Nm}} \omega_{x_i} I_{x,p_i} \begin{pmatrix} -q \sin i_{p_i} \\ p \sin i_{p_i} - r \cos i_{p_i} \\ -q \cos i_{p_i} \end{pmatrix} \tag{1.31}$$

With DEP, small and light propellers are likely to be used to favour reaction time. Additionally, it is possible to cancel the gyroscopic moments of propellers by alternating the direction of rotation of propellers. For these two reasons, the gyroscopic moments will be ignored for the determination of flight stability and handling qualities. It may not be so true for the evaluation of structural efforts on the wing and should be taken into account in a full multi-disciplinary design.

1.3.3 Propeller forces and moments

It is known that when a propeller disk is not aligned with the incoming airflow, a normal force and accompanying moment are created due to the asymmetric airflow angles at the blades. These efforts depend largely on the propeller geometry such as the number of blades and solidity ratio. The propeller forces and moments due to misaligned airflow are discussed in detail in chapter 3. For this part of the study, two additional terms are defined to take these forces into account: $\mathbf{F}_p^b$ and $\mathbf{M}_p^b$. The total contribution of the propulsion to forces and moments can therefore be written

as the sum of the previously introduced effects:

$$\mathbf{T}^a = \mathcal{T}_{ab}\left(\mathbf{T}_x^b + \mathbf{F}_p^b\right) \tag{1.32}$$

$$\mathbf{M}_T^b = \mathbf{M}_c^b + \mathbf{M}_p^b \tag{1.33}$$

1.4 Equations of flight

The fundamental flight dynamics equations are defined as [Boiffier 1998]:

$$m\frac{d\mathbf{V}_k^o}{dt} = m\mathbf{g}^o + \mathbf{F}^o + \mathbf{T}^o\,, \tag{1.34}$$

$$\mathbb{I}^b\dot{\mathbf{\Omega}}_{bo} + \mathbf{\Omega}_{bo} \times \mathbb{I}^b\mathbf{\Omega}_{bo} = \mathbf{M}^b + \mathbf{M}_T^b\,. \tag{1.35}$$

Equations (1.34) and (1.35) can be put in different forms depending on the reference frame in which they are expressed and the hypothesis that are made. Considering hypothesis 2 and expressing the equations in the aerodynamic frame allows to write the equations of flight in terms of α_a and β_a and V_a. To do so, the acceleration term $\frac{d\mathbf{V}_k^o}{dt}$ is expressed using equation (1.9) as:

$$\frac{d\mathbf{V}_k^o}{dt} = \frac{d\mathbf{V}_a^o}{dt} + \frac{d\mathbf{V}_w^o}{dt}. \tag{1.36}$$

Hypothesis 2 allows to set:

$$\frac{d\mathbf{V}_w^o}{dt} = 0, \tag{1.37}$$

$$\frac{d\mathbf{V}_k^o}{dt} = \frac{d\mathbf{V}_a^b}{dt} + \mathbf{\Omega}_{bo} \times \mathbf{V}_a^b, \tag{1.38}$$

$$\frac{d\mathbf{V}_k^o}{dt} = \frac{d\mathbf{V}_a^a}{dt} + \mathbf{\Omega}_{ab} \times \mathbf{V}_a^a + \mathbf{\Omega}_{bo} \times \mathbf{V}_a^b. \tag{1.39}$$

The moment equations are unchanged by the projection in the aerodynamic frame thanks to hypothesis 2. The equations can now be written:

$$m\left(\frac{d\mathbf{V}_a^a}{dt} + \mathbf{\Omega}_{ab} \times \mathbf{V}_a^a + \mathbf{\Omega}_{bo} \times \mathbf{V}_a^b\right) = m\mathbf{g}^a + \mathbf{F}^a + \mathbf{T}^a, \tag{1.40}$$

$$\mathbb{I}^b\dot{\mathbf{\Omega}}_{bo} + \mathbf{\Omega}_{bo} \times \mathbb{I}^b\mathbf{\Omega}_{bo} = \mathbf{M}^b + \mathbf{M}_T^b, \tag{1.41}$$

which after rendering the components explicit become:

$$\begin{pmatrix} m\dot{V} \\ m\left[\dot{\beta}_a V - V(p\sin\alpha_a - r\cos\alpha_a)\right] \\ m\left[\dot{\alpha_a} V\cos\beta_a + V\left(\sin\beta_a(p\cos\alpha_a + r\sin\alpha_a) - q\cos\beta_a\right)\right] \end{pmatrix} = mg \begin{pmatrix} -\sin\gamma_a \\ \cos\gamma_a\sin\mu_a \\ \cos\gamma_a\cos\mu_a \end{pmatrix}$$

$$+\mathbf{F}^a + \mathbf{T}^a \tag{1.42}$$

$$\mathbb{I}^b \begin{pmatrix} \dot{p} \\ \dot{q} \\ \dot{r} \end{pmatrix} + \begin{pmatrix} p \\ q \\ r \end{pmatrix} \times \mathbb{I}^b \begin{pmatrix} p \\ q \\ r \end{pmatrix} = \mathbf{M}^b + \mathbf{M}^b_T. \tag{1.43}$$

The complementary kinematic equations are obtained by inverting equation 1.17:

$$\begin{pmatrix} \dot{\phi} \\ \dot{\theta} \\ \dot{\psi} \end{pmatrix} = \begin{pmatrix} 1 & \sin\phi\tan\theta & \cos\phi\tan\theta \\ 0 & \cos\phi & -\sin\phi \\ 0 & \frac{\sin\phi}{\cos\theta} & \frac{\cos\phi}{\cos\theta} \end{pmatrix} \begin{pmatrix} p \\ q \\ r \end{pmatrix}. \tag{1.44}$$

1.5 Finding the trim position by minimisation

The aircraft motion is modelled with equations (1.42), (1.43), (1.44) and the first line of (1.20), representing a set of $N_e = 10$ equations.

The state vector is defined as; $\mathbf{x} = [V_a, \alpha_a, \beta_a, p, q, r, \phi, \theta]$ with $n_x = 8$ variables. The input vector corresponding to control surfaces, respectively ailerons, elevator and rudder is $\mathbf{u} = [\delta a, \delta_e, \delta_R]$ with $n_u = 3$ variables. For differential thrust, the throttle command vector $\delta_{x,i}$ is added to the control input vector such that: $\mathbf{u} = [\delta_a, \delta_e, \delta_R, \delta_{x,1}, \ldots, \delta_{x,N_m}]$. The number of input becomes : $n_u = 3 + N_m$. Finally, $n_p = 2$ additional parameters the flight path angle and the turn rateγ_a and Ω.

To find a trim position, the state time derivatives $\dot{\mathbf{x}}$ in equations (1.42), (1.43) and (1.44) are set to zero and the system of equations is solved to find the trim value of the state variables and inputs $\hat{\mathbf{x}}$ and $\hat{\mathrm{u}}$.

Similarly to what is done in [Goman 2008], a set of additional constraints N_c can be defined to condition the problem such that only one solution exists. The number of variables to determine $(n_x + n_u + n_p)$ must equal the number of equations and constraints $N_e + N_c$. In this case, considering that the number of engine varies, the

number of additional constraints to define is given by:

$$N_c = n_x + n_u + n_p - N_e,$$

$$N_c = N_m + 3.$$

If differential thrust is disabled, the additional input is $N_m = 1$, representing forward thrust or throttle level, and one must fix $N_c = 4$ additional constraints. These additional constraints are added to determine the flight condition, typically fixing the following variables: $[V_a, \beta_a, \gamma_a, \Omega]$. With differential thrust, the minimum number of additional inputs is $N_m = 2$ with two engines. Consequently, the problem becomes quickly over-determined. An infinite number of equilibrium points can exist. This can be pictured by the different possible combination of throttle levels and rudder action to satisfy a certain thrust and side slip.

For over-determined problems, it is common to use optimization methods to find a satisfying solution [Oppenheimer 2006]. Two options are possible: one may define the input vector as $[\delta_a, \delta_e, \delta_n, \delta_x]$ with δ_n being the total yaw moment input and δ_x the total thrust force such that the equilibrium problem is well conditioned and then use an optimization [1] method to find the δ_R and $\delta_{x,i}$. Or one could run the optimization on the complete set of variables. The second option has been selected for this study. This is motivated by the will of extracting the motor control power terms $\frac{\partial \delta_{x,i}}{\partial V}$ and $\frac{\partial \delta_{x,i}}{\partial r}$ at the linearized position as they are expected to vary with the airspeed.

Without loss of generality, additional higher and lower bounds are added on control inputs, angle of attack and bank angle depending on the flight phase and the aerodynamic model. For example, the bank angle is limited to $\pm 5°$ when studying engine failure at take off as stated by flight regulations [EASA 2017] and the maximum angle of attack is fixed by the aerodynamic model. These bounds are resumed in table 1.1 and are in part, dependent on the aircraft selected for the study.

The following variables are chosen to fix the flight conditions: $[V_a, \beta_a, \gamma_a, \Omega]$. The objective function to minimize is defined as the sum of the mean power level: $\mathbb{E}(\delta_{x,i})$ and the standard deviation: $\sigma(\delta_{x,i})$. Such an objective function makes sense in the point of view of the designer who looks for minimizing the power to install on the aircraft and at the same time it aims at distributing the control effort as much

1. Optimisation methods have been selected and used throughout this work to solve allocation problems. It should be prescribed that any methodology proposed in [Oppenheimer 2006] to solve allocation problem can be envisioned.

Table 1.1 – Additional bounds depending on flight phase

Flight phase	$V < 71m.s^{-1}$ (Flap out)	$V > 71m.s^{-1}$	Engine failure
$\alpha_a(^\circ)$	$-2 \leq \alpha_a \leq \alpha_{max_1}$	$-2 \leq \alpha_a \leq \alpha_{max_2}$	$-2 \leq \alpha_a \leq \alpha_{max_1}$
$\phi(^\circ)$	± 30	± 30	± 5
$\theta(^\circ)$	± 30	± 30	± 30
$\delta_e(^\circ)$	± 20	± 20	± 20
$\delta_a(^\circ)$, $\delta_R(^\circ)$	± 30	± 30	± 30
$\delta_{x,i}$	$0 < \delta_{x,i} \leq 1$	$0 < \delta_{x,i} \leq 1$	$0 < \delta_{x,i} \leq 1$

as possible. Finally, to simulate engine failure, a constraint on the throttle level of the corresponding engine is added.

The problem hence writes:

$$\widehat{\mathbf{x}}' = \arg\min_{\mathbf{x}'} \ \mathbb{E}(\delta_{x,i}) + \sigma(\delta_{x,i}), \tag{1.44}$$

$$\text{with:} \qquad \mathbf{x}' = [\alpha_a, p, q, r, \phi, \theta, \delta_a, \delta_e, \delta_R, \delta_{x,1}, \ldots, \delta_{x,N_m}],$$

Subject to:

$$\begin{pmatrix} 0 \\ -mV(p\sin\alpha_a - r\cos\alpha_a) \\ mV\left[\sin\beta_a(p\cos\alpha_a + r\sin\alpha_a) - q\cos\beta_a\right] \end{pmatrix} = mg \begin{pmatrix} -\sin\gamma_a \\ \cos\gamma_a\sin\mu_a \\ \cos\gamma_a\cos\mu_a \end{pmatrix} + \mathbf{F}^a + \mathbf{T}^a,$$

$$0 = \mathbf{M}^b + \mathbf{M}_T^b - \begin{pmatrix} p \\ q \\ r \end{pmatrix} \times \mathbf{I} \begin{pmatrix} p \\ q \\ r \end{pmatrix},$$

$$0 = p + q\sin\phi\tan\theta + r\cos\phi\tan\theta,$$

$$0 = q\cos\phi - r\sin\phi,$$

$$\Omega = (q\sin\phi + r\cos\phi)\frac{1}{\cos\theta},$$

$$\sin\gamma_a = \cos\alpha_a\cos\beta_a\sin\theta - \sin\beta_a\sin\phi\cos\theta - \sin\alpha_a\cos\beta_a\cos\phi\cos\theta,$$

$$0 = \delta_{x,1},$$

$$\vdots,$$

$$0 = \delta_{x,j}.$$

The trim algorithm is implemented in Python. A Sequential Least SQuares Programming algorithm available in SciPy, see [Kraft 1988], is used to solve the optimization problem. The tolerance on the constraints is adapted to the use, ranging from 10^{-3} for the generation of flight envelope maps to 10^{-6} before linearizing the system. When the Sequential Least SQuares Programming fails to achieve this level of tolerance, it was found a better convergence with a trust region algorithm also available in SciPy (see [Byrd 1996]) to achieve a tolerance of the order of 10^{-6} in case of thrust asymmetry with aero-propulsive interaction.

1.6 Linearisation

The system is linearised by a first order TAYLOR expansion of the system. Equations (1.42), (1.43) and (1.44) form a system of non linear equations of the form:

$$\dot{\mathbf{x}} = \mathbf{f}(\mathbf{x}, \mathbf{u}), \tag{1.45}$$

with

$$\mathbf{x} = [V_a, \beta_a, \alpha_a, p, q, r, \phi, \theta]^\intercal,$$

$$\mathbf{u} = [\delta_a, \delta_e, \delta_R, \delta_{x,1}, \ldots, \delta_{x,i}, \ldots, \delta_{x,N_m}]^\intercal.$$

The solution $\hat{\mathbf{x}}'$ of the optimization problem (1.44) and the fixed parameters $[V_a, \beta_a, \gamma_a, \Omega]$ are used to reconstruct equilibrium state and input vectors: $\hat{\mathbf{x}}$, $\hat{\mathbf{u}}$. The Jacobian of $\mathbf{f}(\mathbf{x}, \mathbf{u})$ is evaluated numerically by computing centred finite differences:

$$\dot{\widetilde{\mathbf{x}}} = \frac{\partial \mathbf{f}}{\partial \mathbf{x}} \widetilde{\mathbf{x}} + \frac{\partial \mathbf{f}}{\partial \mathbf{u}} \widetilde{\mathbf{u}} + \frac{\partial \mathbf{f}}{\partial \gamma_a} \widetilde{\gamma}_a, \tag{1.46}$$

with $\widetilde{\mathbf{x}} = \mathbf{x} - \hat{\mathbf{x}}$, $\widetilde{\mathbf{u}} = \mathbf{u} - \hat{\mathbf{u}}$ and $\widetilde{\gamma_a} = \gamma_a - \hat{\gamma}_a$.

It is of interest to introduce the flight path angle γ_a in the state space representation so as to better differentiate the short period oscillation (mainly α and q dynamics) and the phugoid (mainly V_a and γ_a dynamics). One can do so by a change of variable. Using the first line of equation (1.20):

$$\sin\gamma_a = \cos\alpha_a \cos\beta_a \sin\theta - \sin\beta_a \sin\phi \cos\theta - \sin\alpha_a \cos\beta_a \cos\phi \cos\theta,$$

under the assumption of small angles and neglecting the term of second order, γ_a can be expressed as:

$$\gamma_a = \theta - \alpha_a$$

$$\dot{\gamma}_a = \dot{\theta} - \dot{\alpha}_a.$$

Subtracting the line corresponding to $\dot{\alpha}_a$ to the line corresponding to $\dot{\theta}$ in the matrix $\left[\frac{\partial \mathbf{f}}{\partial \mathbf{x}}, \frac{\partial \mathbf{f}}{\partial \mathbf{u}}, \frac{\partial \mathbf{f}}{\partial \gamma_a}\right]$ completes the reformulation. Finally, the system is re-ordered into two linear state space representations, one for the longitudinal motion $_L$, one for the

lateral motion $_D$:

$$\dot{\mathbf{x}}_L = \mathbf{A}_L\mathbf{x}_L + \mathbf{B}_L\mathbf{u}_L, \tag{1.47}$$

$$\dot{\mathbf{x}}_D = \mathbf{A}_D\mathbf{x}_D + \mathbf{B}_D\mathbf{u}_D, \tag{1.48}$$

with:

$$\mathbf{x}_L = [\widetilde{V}, \widetilde{\gamma}, \widetilde{\alpha}, \widetilde{q}]^\intercal,$$

$$\mathbf{u}_L = [\widetilde{\delta}_e, \widetilde{\delta}_{x,1}, \ldots, \widetilde{\delta}_{x,12}]^\intercal,$$

$$\mathbf{x}_D = [\widetilde{\beta}, \widetilde{p}, \widetilde{r}, \widetilde{\phi}]^\intercal,$$

$$\mathbf{u}_D = [\widetilde{\delta}_a, \widetilde{\delta}_{x,1}, \ldots, \widetilde{\delta}_{x,12}]^\intercal.$$

1.7 Conclusion

This chapter aimed at introducing the mathematical model and formulations that will be used throughout the study. Most of the tools introduced are well known to aircraft flight dynamics and few modifications were brought to adapt them to the study of DEP aircraft. In particular, the geometrical arrangement and electric thrust model for the propulsion was introduced in section 1.3. The choice was made to neglect the gyroscopic moments of propellers because propellers are assumed to be contra-rotating. The trim algorithm uses a gradient based optimization method to handle the added degrees of freedom brought by the number of engines viewed as actuators (see section 1.5). Finally, numerical linearisation of the problem is formulated for stability evaluation and control design (see section 1.6).

Chapter 2

Aerodynamic database

Contents

The objective of this chapter is to obtain an aerodynamic module capable of evaluating the aerodynamic forces $\mathbf{F}^a$ and moments $\mathbf{M}^b$. Particularly, force and moment derivatives with respect to the state variables $\mathbf{x}$: $\frac{\partial \mathbf{F^a}}{\partial \mathbf{x}}$, $\frac{\partial \mathbf{M}}{\partial \mathbf{x}}$ and derivatives with respect to the inputs: $\frac{\partial \mathbf{F^a}}{\partial \mathbf{u}}$ and $\frac{\partial \mathbf{M}}{\partial \mathbf{u}}$ will be used to evaluate the aircraft stability and design the control laws. Other aerodynamic characteristics relevant to flight performances such as lift to drag ratio or minimum drag, are of less importance. The aerodynamic module should be in accordance with the gradient based optimization used in the trim algorithm. The aerodynamic efforts being evaluated at each gradient evaluation, a fast execution time for the aerodynamic module should be favoured.

Two problems arise when considering the aerodynamics:

1. The first one is to evaluate the lateral static stability and lateral coefficients of the aircraft with varying vertical tail surface area.

2. The second is the aero-propulsive interactions that may arise between a propeller slipstream and the portion of the wing immersed in it.

The first problem could be treated as a simple linear relationship between the change in stability derivatives and the vertical tail surface area as depicted by the

formulation of directional moment coefficient [Torenbeek 1982]:

$$C_{n_\beta} = C_{n_{\beta,A-h}} + C_{Y_{v_\beta}} \frac{S_v l_v}{Sb} \left(1 - \frac{\partial \sigma_v}{\partial \beta}\right) \left(\frac{V_v}{V_a}\right)^2, \tag{2.1}$$

where $C_{n_{\beta,A-h}}$ describes the contribution of wing and fuselage assembly, $C_{Y_{v_\beta}}$ is the vertical tail side force derivative with respect to side slip. The geometric parameters S_v and l_v are respectively the vertical tail surface area and level arm. V_v represents the airspeed at the location of the VT and σ_v is the side wash. σ_v and $\frac{V_v}{V_a}$ describe the change in vertical tail efficiency due to interferences with other aircraft components. $C_{Y_{v_\beta}}$ can be determined in the same way as the lift slope of an isolated symmetric wing. It is dependent on aspect ratio, sweep angle and Mach number.

There are two ways of varying the vertical tail size, either by maintaining the aspect ratio constant and varying the span, or inversely. In the first case, S_v only varies and a linear variation of C_{n_β} can be assumed provided that the interference terms remain constant.

In the second case, $C_{Y_{v_\beta}}$ varies together with S_v. The change in C_{n_β} is likely to be non-linear and the same uncertainty remains on interference terms. In summary, there is a need to evaluate both the VT side force gradient and the interference terms with varying VT surface area and aspect ratio.

Determining the contribution of the VT to the natural static stability and lateral coefficients is one part of the problem. The other part is that for traditional tube and wing configurations, the combination of fuselage and wing presents an important negative static stability, $C_{n_{\beta,A-h}} < 0$. In addition to determining vertical tail aerodynamic contribution to directional stability, fuselage and wing contributions must be known as well.

Problem 2 concerns the forces that may arise from aero-propulsive interactions between propellers placed at the leading edge and the wing. When a wing is locally immersed in a jet of higher velocity, induced rolling moment due to asymmetric lift distribution can be generated. This can be the case when using differential thrust.

The fact that these forces are induced from differential thrust gives the intuition that they are of secondary importance with respect to vertical tail contribution to directional and lateral stability. For this reason, it was decided to create a baseline aerodynamic module that ignores aero-propulsive interactions and focus on determining aircraft coefficient with varying VT. The aero-propulsive interactions will be treated in detail in a distinctive chapter (see Chapter 3).

This chapter introduces the reference aircraft and the DEP version of it in section 2.1. Following, the tools and methodologies for calculating the aerodynamic coefficients are reviewed and compared to our needs. A composite module is built using a combination of existing numerical methods and semi-empirical model. Some characteristics are shown to illustrate the impact of varying VT surface area on the aerodynamic derivatives in section 2.2.

2.1 Reference Aircraft

The selection of an aircraft class, restrains the type of aerodynamics to consider. In the case of electric propulsion, subsonic commuter aircraft are often cited as the next big step in developing electric airplanes since most of their mission are within the limits of electric propulsion in terms of endurance [Moore 2014], [Stückl 2015]. These aircraft are usually equipped with turboprop engines. A good representative of this class of aircraft is the ATR72 shown in Fig 2.1.

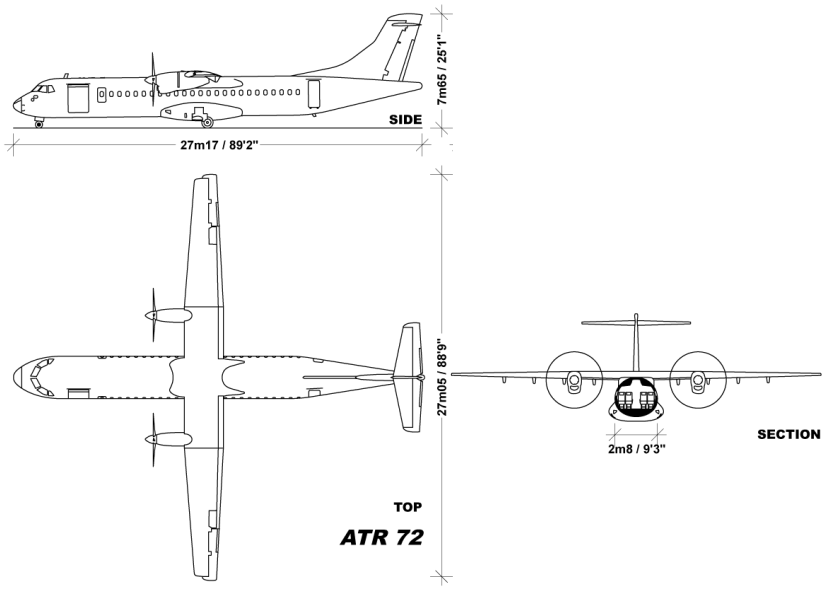

Figure 2.1 – ATR72 blue prints drawings (©Julien.scavini)

The aircraft dimensions, weights and typical velocities are retrieved from the literature, blueprints and aircraft flight manual. They are summarized in Table 2.1. The next step is to lay down the assumptions for an equivalent DEP aircraft.

2.1.1 Conversion to electric

A detailed conversion to electric propulsion is outside the scope of the study. Here the interest is mostly about one end of the propulsion chain which is the electric motors and their location on the aircraft.

The methodology is built such that any even number of motors can be considered on the aircraft. For comparison with the reference aircraft, an arbitrary number of twelve motors of equal power have been selected. This number is set for exploration and is subject to change as the study progresses. The idea followed for

Geometric parameters	
Wingspan	27 m
Wing surface area	61 m^2
VT surface area	12.5 m^2
Engine level arm	4.1 m
Weight and inertia characteristics	
MTOW	21500 kg
MEW	13500 kg
I_x	289873 kg.m^2
I_y	298442 kg.m^2
I_z	573579 kg.m^2
Propulsion	
Engines	Two PW127b
Total continuous power	4 100 kW
Propeller diameter	3.96m
Propeller efficiency	$\mu_p = 0.8$
Velocities (ISA conditions)	
Stall speed, landing V_{sr}	46.3 m/s
Stall speed, take off V_{sr}	50.9 m/s
Maximum manoeuvre speed, V_m	90 m/s
Typical cruise speed V_c	125 m/s
Maximum demonstrated cross wind limit	18 m/s
Altitudes (ISA conditions)	
Maximum ceiling	7500 m
Maximum take off	2590 m

Table 2.1 – ATR 72 general details [Federal Aviation Administration 2015], [Jackson 2014], [aircraft 2000] [Lan 2005]

positioning the motors is that the propellers cover the entire wing leading edge from the fuselage to the wingtips, as depicted in Fig 2.2, with a spacing of 10% of the propeller diameter in between each propeller disc. In addition, the propeller discs are contained within the limit of the wingspan and don't spread further than the wingtips. The characteristic of the DEP ATR72 are summarized in Table 2.2.

In order to compare the original turboprop aircraft with its electric counter part, most parameters are maintained constant. The external geometry remains untouched with the exception of the vertical tail. Thanks to a power to mass ratio

Propulsion	
motors	12
Mechanical power per engine (continuous)	333.3 kW
Propeller diameter (D_p)	1.88m
Propeller spacing	$0.1D_p$
Propeller efficiency	$\mu_p = 0.8$

Table 2.2 – Characteristics of DEP ATR 72, same as Table 2.1, except if explicitly mentioned

of electric motors similar or better than that of turboshaft engine [Hepperle 2012], it is assumed that there is no change in aircraft mass for the same continuous mechanical power. By doing so, it is postulated that lateral control can be realized with differential thrust and the same amount of power as that needed for the normal operation of the twin-engine reference aircraft.

Although electric motors can withstand repeated short power overloads, this may not be as true for the electrical system and the power generation system. The present study aims at being generic so as to be used with any power architecture. To include arbitrary types of power generation systems, it is assumed no power overload of the electric motors. This applies both in steady states and in transient manoeuvres.

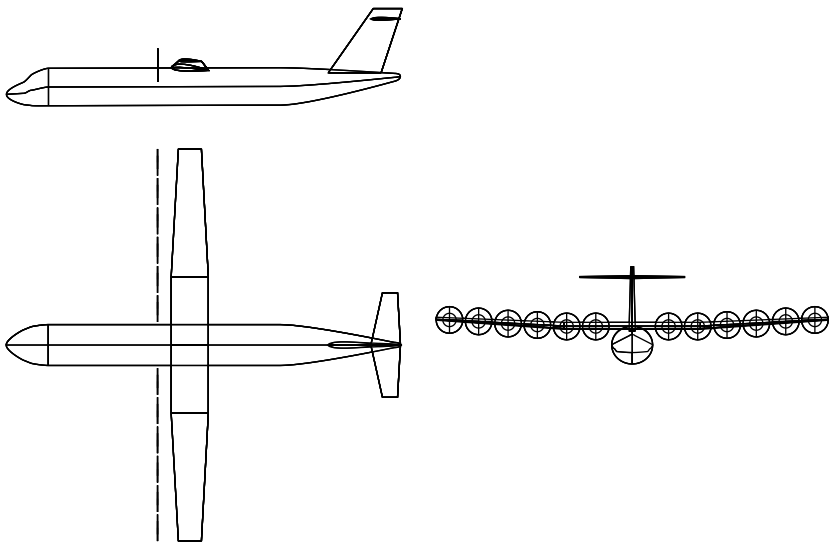

Figure 2.2 – ATR72 in a DEP configuration with twelve identical motors.

The mass and inertia terms can be subject to discussion when considering dis-

tributed propulsion. As motors are moved further from the fuselage, the inertia terms, mainly I_z and I_x are likely to change. To be precise two contributions are opposing: distributed motors with their nacelles and equipment further from the centre of gravity and the structural mass savings due to the relief of wing bending moment. The final mass can be discussed since for an full electric or a hybrid electric aircraft the mass is likely to increase to maintain the same level of performance [Hepperle 2012]. All of them falling in the detailed design step and no previous experience could be found at the moment of writing.

It is therefore assumed that the mass and inertia terms are reasonably preserved and the original values are used throughout the study.

The only feature allowed to change is the vertical tail which will be reduced so as to obtain relaxed lateral stability or a lightly unstable aircraft. Consequently, a weakly unconventional aircraft configuration will be analysed.

2.2 Building the Aerodynamic Database

For unconventional configurations, it is necessary to carefully select the method with which one can establish the aerodynamic database. As Chudoba explains in [Chudoba 2001] and [Chudoba 2003], the means of calculating aerodynamic characteristics can be organized in three categories summarized in Table 2.3.

Table 2.3 – Methods for aerodynamic analysis.

Category	Example of methods
Analytical	Lifting Line, Swept Wing Theory, ...
Empirical, semi-empirical	DATCOM, ESDU, ...
Numerical	VLM, Panel Method, CFD, ...

Both analytical and empirical/semi-empirical methods are built on experience accumulated over time in analyzing conventional configurations. Therefore they can hardly be considered as generic methodologies. Numerical methods offer different level of fidelity allowing to capture the specificity of unconventional design. For preliminary designs, Vortex Lattice Method (VLM) or Panel Method, both based on potential flow theory, are often preferred over Computation Fluid Dynamics (CFD) for their favourable precision relative to computational cost. Semi-empirical, analytical and low fidelity numerical methods are favored for their rapid execution time.

Although the configuration is only weakly unconventional, analytical or empirical / semi-empirical methods can not capture the effect of geometrical changes in VT because of the important influence of other aircraft components on the flow impacting the VT. This has been demonstrated by Nicolosi in [Nicolosi 2013], where his research team investigated the differences obtained between DATCOM, ESDU estimation techniques and CFD methods complemented with wind tunnel experiments.

The main contributors to flow perturbation impacting the VT are the fuselage and the horizontal tail which are acting as end plates, reducing the downwash at the root and tip of the vertical tail.

Using numerous CFD simulations complemented with wind tunnel tests on a generic commuter aircraft model, Nicolosi and his research team could establish a new semi-empirical method called Vertical tail Design, Stability and Control (VeDSC). This methodology is well adapted to this work because it allows the rapid calculation of the VT aerodynamics contribution for various size and configurations.

2.2.1 Determination of the aerodynamic derivatives of a variable vertical tail.

The VeDSC method focuses on predicting the VT efficiency as a function of the VT and aircraft components geometry. The main assumption is the fact that contribution of each component of the aircraft on lateral coefficients: $\{C_Y, C_l, C_n\} \equiv C_{\text{lat}}$, can be decoupled in the following way:

$$C_{\text{lat}_\beta} = C_{\text{lat},F_\beta} + C_{\text{lat},W_\beta} + C_{\text{lat},v_\beta} \tag{2.2}$$

Where subscripts F, W, v refer respectively to fuselage, wing and vertical tail and the subscript β designates a side slip derivative: $C_{._\beta} = \frac{\partial C_.}{\partial \beta}$. It is also assumed that the contribution of the VT, C_{lat,v_β} is influenced by the fuselage, wing and horizontal tail but does not influence the other coefficients C_{lat,F_β} and C_{lat,W_β}. The VeDSC method furnishes a way to estimate the coefficient C_{lat,v_β} through a reformulation of the vertical tail side force gradient coefficient a_v:

$$a_v = K_F K_W K_H C_{Y_{v_\beta}}, \tag{2.3}$$

with $C_{Y_{v_\beta}}$ the side force derivative of a swept wing determined using Diederich formula for swept wing [Diederich 1951]. K_F, K_W and K_H are corrective coefficients taking into account respectively the fuselage, wing and horizontal tail interference. The reader is referred to [Nicolosi 2017] and [Ciliberti 2017] for the complete formulation of these parameters. K_F and K_H depend on vertical tail geometry parameters, principally its span b_v. Their value vary with varying vertical tail shape and surface area. K_W on the other hand is independent of vertical tail geometry and remains constant.

The advantage of this method is that the interference terms $\frac{V_v}{V_a}$ and σ_v in equation (2.1) are directly included in the factors K_F, K_W and K_H. It allows the direct evaluation of vertical tail efficiency with surface area variation with either constant aspect ratio or span and the evaluation of interference on a modified vertical tail.

The VT contribution to lateral coefficients are calculated using formulas given by Etkin [Etkin 2012]:

$$C_{Y,v_\beta} = C_{Y_{v_\beta}} \frac{S_v}{S} \left(1 - \frac{\partial\sigma}{\partial\beta}\right) \frac{V_v}{V_a}, \tag{2.4}$$

$$C_{Y,v_p} = -C_{Y_{v_\beta}} \frac{S_v}{S} \left(2\frac{z_v}{b} - \frac{\partial\sigma}{\partial p}\right) \frac{V_v}{V_a}, \tag{2.5}$$

$$C_{Y,v_r} = C_{Y_{v_\beta}} \frac{S_v}{S} \left(2\frac{l_v}{b} + \frac{\partial\sigma}{\partial r}\right) \frac{V_v}{V_a}, \tag{2.6}$$

$$C_{l,v_\beta} = -C_{Y_{v_\beta}} \frac{S_v z_v}{Sb} \left(1 - \frac{\partial\sigma}{\partial\beta}\right) \frac{V_v}{V_a}, \tag{2.7}$$

$$C_{l,v_r} = C_{Y_{v_\beta}} \frac{S_v z_v}{Sb} \left(2\frac{l_v}{b} + \frac{\partial\sigma}{\partial r}\right) \frac{V_v}{V_a}, \tag{2.8}$$

$$C_{n,v_\beta} = C_{Y_{v_\beta}} V_V \left(1 - \frac{\partial\sigma}{\partial\beta}\right) \frac{V_v}{V_a}, \tag{2.9}$$

$$C_{n,v_p} = C_{Y_{v_\beta}} V_V \left(2\frac{z_v}{b} - \frac{\partial\sigma}{\partial p}\right) \frac{V_v}{V_a}, \tag{2.10}$$

$$C_{n,v_r} = -C_{Y_{v_\beta}} V_V \left(2\frac{l_v}{b} - \frac{\partial\sigma}{\partial r}\right) \frac{V_v}{V_a}. \tag{2.11}$$

Here, z_v is the height of the vertical tail quarter chord with respect to centre of gravity, l_v is distance between wing quarter chord to VT quarter chord and $V_V = \frac{S_v l_v}{Sb}$ is the vertical tail volume ratio. Provided that the interference terms are now taken into account by VEDSC, equations (2.4) to (2.11) can be re-written with a_v

as defined in equation 2.3, as:

$$C_{Y,v_\beta} = a_v \frac{S_v}{S} \tag{2.12}$$

$$C_{Y,v_p} = -a_v \frac{S_v}{S} \frac{2z_v}{b} \tag{2.13}$$

$$C_{Y,v_r} = a_v \frac{S_v}{S} \frac{2l_v}{b} \tag{2.14}$$

$$C_{l,v_\beta} = -a_v \frac{S_v z_v}{Sb} \tag{2.15}$$

$$C_{l,v_r} = a_v \frac{S_v z_v}{Sb} \frac{2l_v}{b} \tag{2.16}$$

$$C_{n,v_\beta} = a_v V_V \tag{2.17}$$

$$C_{n,v_p} = a_v V_V \frac{2z_v}{b} \tag{2.18}$$

$$C_{n,v_r} = -a_v V_V \frac{2l_v}{b} \tag{2.19}$$

Variation and validity intervals of some parameters of interest are shown in Table 2.4. The method could be extrapolated to VT of aspect ratio from 0.5 to 4 since the Diederich formula is valid for this interval.

Table 2.4 – A few parameters on which VEDSC has been constructed and their interval of variation (from [Ciliberti 2013])

Description	Range
VT aspect ratio	$[1, 2]$
Wing aspect ratio	$[6, 16]$
Wing vertical position	Low wing to high wing
Horizontal Tail Vertical Position	Conventional to T-tail

Dorsal fin.

The dorsal fin is defined by [Obert 2009] as the "*forward extension of the fin root area*". This part is purposely ignored in the model of the DEP ATR72 (Fig 2.2) but it is present on the original ATR72 in Fig 2.1. The main usage of this part is to increase the vertical tail efficiency at high angle of side slip and to avoid sudden stall. It does not change the aerodynamic characteristics of the vertical tail at low angles of side slip. Another purpose of the dorsal fin is to improve spin recovery characteristics [Torenbeek 1982]. In both cases, it is not accounted in the

calculation of lateral static stability. Here, it does not intervene in the aerodynamic calculations but it is assumed present and ensuring constant properties of the VT and no stall up to a side slip of $\beta_a = 15°$. Reaching higher side slip angle during normal flight operation is not desired and side slip angle higher than $\beta_a = 15°$ will not be studied in this work. Doing so would require higher fidelity aerodynamic models to determine the non linearities induced by detached, viscous flow. Such models are computationally expensive and usually avoided in preliminary design.

Rudder

VEDSC also provides a correction for the rudder efficiency in the same form as for the vertical tail. The side force derivative due to a rudder deflection is modified as follows:

$$a_{\delta_R} = \tau_r K_R C_{Y_\beta}, \tag{2.20}$$

where K_R is the corrective term for interference and τ_r is the effectiveness factor of the rudder on an isolated VT. Similarly as the VT contribution to lateral derivatives, the contribution a rudder deflection to coefficients derivatives are:

$$C_{Y_{\delta_R}} = a_{\delta_R} \frac{S_v}{S}, \tag{2.21}$$

$$C_{l_{\delta_R}} = a_{\delta_R} \frac{S_v z_v}{Sb}, \tag{2.22}$$

$$C_{n_{\delta_R}} = a_{\delta_R} \frac{S_v l_v}{Sb}. \tag{2.23}$$

With K_R being dependent on K_F and vertical tail aspect ratio, it is also subject to change with varying vertical tail.

2.2.2 Determination of overall aircraft coefficient derivatives.

Fuselage and wing contributions to lateral and longitudinal derivatives still have to be determined. The contribution of the wing and the horizontal tail can be quickly obtained using potential flow solvers such as VLM with sufficient accuracy for flight stability and control studies. This solution was selected for both the wing and horizontal tail. The software used for that purpose is OpenVSP [Gloudemans 1996], a parametric geometry software that offers aerodynamic analytical tools, used in many preliminary studies [Ope 2020].

The fuselage contribution is more problematic to compute with a VLM solver because its large cross section is approximated by two perpendicular surfaces. By

comparing the output of the OpenVSP software with analytical or semi-empirical methods ([Torenbeek 1982] and [Nicolosi 2016]), it was found that a good estimation of the fuselage pitching and yawing moment derivatives was obtained with the software. The contribution of the fuselage alone to the side force is considered small with respect to the contribution of the tail and will be ignored.

The derivatives due to the wing, fuselage and horizontal tail are hence determined entirely through VLM simulations using the geometry of the ATR72 without its vertical tail. The VeDSC method is used on top of the VLM simulation results to adjust the aerodynamic characteristics to the variable VT.

Drag model

Only first order derivatives are considered except for the drag coefficient which is modelled with a second order polynomial in α_a:

$$C_d = C_{d_0} + C_{d_1}\alpha_a + C_{d_2}\alpha_a^2 \tag{2.24}$$

The coefficients C_{d_1}, C_{d_2} are obtained with the VLM analysis of OpenVSP and C_{d_0} is obtained through a drag breakdown mostly accounting for the total wetted surface area. A flap deflection is taken into account a fixed increment of drag and lift.

It is possible now to explore the total aircraft derivatives with the variation of VT surface area. Two ways of modifying the vertical tail are available. The first is to change the surface area while maintaining the aspect ratio constant. This gives nearly linearly varying coefficients as can be seen in Fig 2.3, despite the fact that vertical tail efficiency is increased at small S_v due to stronger interference. It is essentially the lateral force derivatives C_{Y_β}, C_{Y_r}, the dihedral effect C_{l_β}, the directional stability C_{n_β} and associated damping term C_{n_r} that are impacted by the reduction of vertical tail. The major consequence being on the directional static stability coefficient C_{n_β} becoming negative for $S_v < 0.7S_{v,0}$, announcing an unstable aircraft.

The second way of reducing the vertical tail is by changing the aspect ratio up to reasonable values to limit extrapolation as shown in Fig 2.4. Although not well adapted to a T-tail configuration, this variation induces non linear variation of the coefficient and may be found useful as the derivatives do not vary as much. For example the directional static stability becomes negative only for $S_v < 0.5S_{v,0}$.

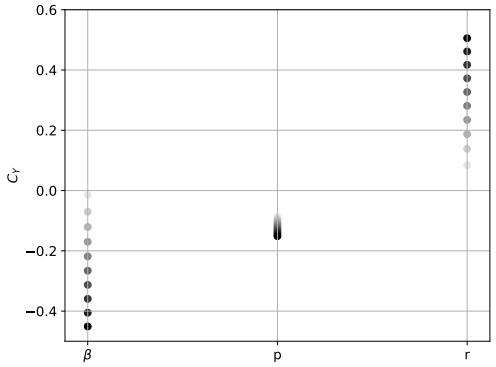

(a) All derivatives are per radians.

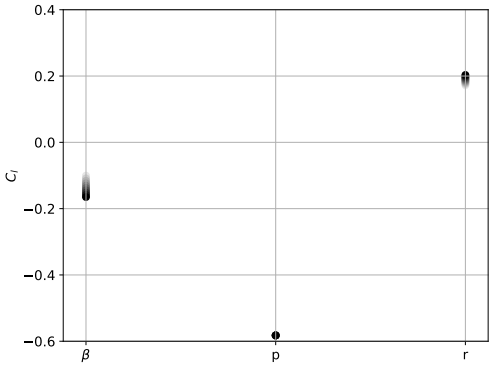

(b) All derivatives are per radians.

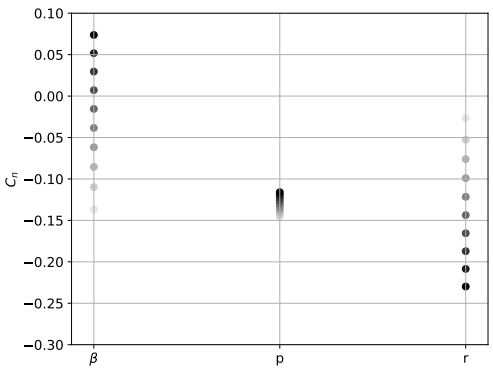

(c) All derivatives are per radians.

Figure 2.3 – Evolution of the aircraft lateral coefficients with variation of VT area for constant AR. Whitest marker represents $S_v = 0.1S_{v,0}$, darkest represents $S_v = S_{v,0}$, per step of $0.1S_{v,0}$.

2.3 Chapter conclusion

The goal of this chapter was to create an aerodynamic module capable to provide aerodynamic forces $\mathbf{F}^a$ and moments $\mathbf{M}^b$. The aerodynamic being specific to the aircraft class, a typical commuter aircraft, the ATR72 was selected as baseline. Its baseline DEP counterpart and accompanying assumptions were defined in section 2.1.

The choice has been made to separate the baseline aerodynamics and the aero-propulsive interaction arising from the interaction between propeller slipstreams and a wing. The baseline aerodynamics without blowing effect that focus on the variation of VT surface area is treated in this chapter and the aero-propulsive interactions are discussed in the dedicated chapter 3.

The aerodynamic module had to be suitable for use with optimisation routines.

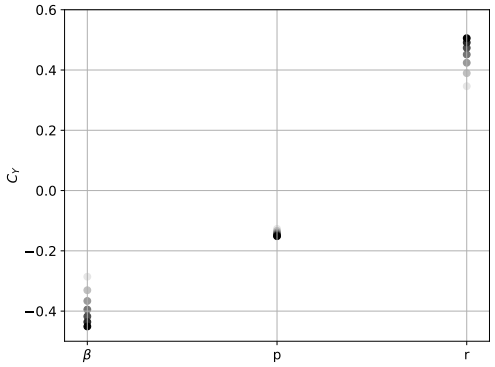

(a) All derivatives are per radian.

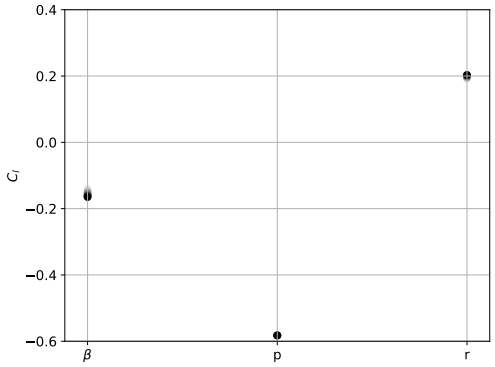

(b) All derivatives are per radians.

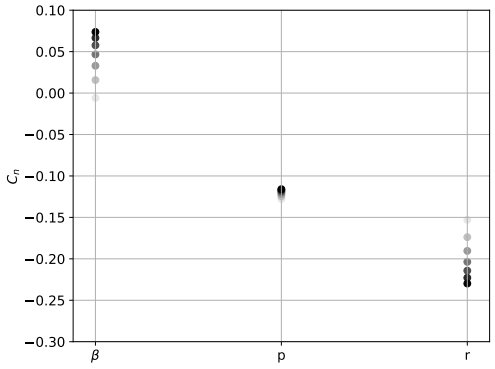

(c) All derivatives are per radians.

Figure 2.4 – Evolution of the aircraft lateral coefficients derivatives with variation of VT area for constant span. Whitest marker represents $S_v = 0.4S_{v,0}$, darkest represents $S_v = S_{v,0}$, per step of $0.1S_{v,0}$ The interval of AR swept is [1.56, 3.9]

Challenges encountered were to include changes in vertical tail geometry while taking into account interference from other aircraft components and the determination of the fuselage directional derivatives.

The solution consisted in creating a composite module where a low fidelity software is used to obtain the aerodynamic derivatives of the constant geometry while a new semi-empirical method VEDSC is used to determine vertical tail contribution. First order derivatives with respect to the aircraft states $\mathbf{x}$ and surface deflections are considered with the exception of the drag coefficient, quadratic in α_a.

An exploration of the total aircraft derivatives showed that the aircraft exhibits a negative static directional stability at vertical tail surface area lower than 70% of the original. Changing the vertical tail size by keeping the aspect ratio constant translates into mostly linear changes in lateral derivatives while a reduction at constant span translates into non-linear changes and lower total variation in lateral

coefficients.

Chapter 3

Aeropropulsive interaction

Contents

The term "aero-propulsive interactions" designates here any interactions between a propulsive system and a surface generating aerodynamic lift.

One of the purposes of a DEP configuration is to generate aero-propulsive interactions to bring substantial benefits to the aircraft performance. This idea supposes that such interactions generate significant forces and moments on the aircraft. The purpose of this chapter is to investigate what kind of forces and moments, in which conditions and whether it should be accounted for in the stability analysis, control laws design and VT sizing.

(a) NASA X57 research aircraft [Borer 2016]

(b) Onera Dragon concept plane [Schmollgruber 2019]

As such, aero-propulsive interactions open a diverse domain which becomes rapidly specific to technology and configuration choices. Taking as example two existing and opposite concept aircraft:

— The concept plane Dragon [Schmollgruber 2019],

— The all electric X-57 [Borer 2016].

The first aircraft has fans located at the trailing edge and on the lower wing. The X-57 has small propellers located at the leading edge and larger propulsion engines located at the wingtips. In the first case, engines located in the lower wing, benefit from the compression zone of the super-critical airfoil. The airflow is slowed down before the intake which is an advantage for transonic flight. In the second case, wing blowing is used as hyper-lift system instead of flaps. The type of interaction are of different nature and their choice is mainly dependent on the mission of the aircraft.

In this optic, the context of our study is recalled to limit the interest to the relevant interaction effects. The study concerns regional transport and subsonic aircraft in the class of 70 pax such as the ATR72. The favored propulsion for these aircraft are turbo-propeller engines. For these types of aircraft, it was thought relevant to limit the study to propeller wing interactions. Furthermore, the type of interaction taken into account was limited to propellers located at the leading edge of the wing, as this configuration is most commonly encountered for regional transport aircraft.

This chapter is organized as follows, first an overview of the physical phenomena at play in propeller wing interactions and their magnitude are studied in section 3.1. Following this study, it was decided to include a model for propeller wing interaction. A second section 3.2, presents a review of the relevant methods that exist to model these interactions. The construction of the model used for this study is detailed in section 3.3 and finally, it is evaluated in section 3.4.

3.1 Physics of propeller wing interaction

The goal of this section is to enumerate and to explain the physical phenomena contributing to propeller wing interactions. According to Hoerner [Hoerner 1985], interactions can be decomposed in two major phenomena:

1. Propeller forces generated when the propeller axial axis is not aligned with the airflow.
2. Effect of the propeller slipstream on the wing.

When a propeller is placed in front of the wing leading edge, it may be within the up-wash region created by the wing, such that the propeller axial axis is not parallel to the airflow and normal forces are created. These propeller forces are discussed in section 3.1.1. Subsequently, the impact of a propeller slipstream on a wing is analysed in section 3.1.2. On a configuration with propellers located at the wing leading edge, this leads to two ways interactions where the wing influences the airflow impacting the propeller disc and the propeller modifies the airflow impacting the wing.

3.1.1 Forces of a propeller at an angle of attack

It is known that propellers at an angle of attack produce a normal force parallel to the radial plan of the propeller [Hoerner 1985], [Ribner 1945]. This comes from the fact that for a positive angle of attack, the airspeed seen by the down going blade is larger in comparison to the airspeed seen by the up going blade. This asymmetric load resolves in both a normal force and a yawing moment.

The effect is the same for a propeller at yaw, where the system resolves in a lateral force and a pitching moment.

An important remark is that if the direction of the normal force depends only one the angle between the propeller disk and the incoming airflow, it is not the case for the moment which depends on the direction of rotation of the propeller. Counter-rotating propellers, provided that they are identical and functioning at the same regime, can be used to cancel the global moment produced on the aircraft [Ribner 1945].

The estimation of propeller forces can be made with a good accuracy with propeller Blade Element Theory [Ribner 1945]. This method however requires to define the propeller geometry in terms of chord, airfoils and twist angle distribution. De Young in [De Young 1965], rendered the formula obtained by Ribner more general

using statistical propeller data to reduce the number of variables at play. The propeller side force coefficient $C_{Y,p}$ is estimated by the thrust coefficient C_{T_p}, propeller solidity σ_p and propeller twist angle at three quarter of the radius β_p:

$$C_{Y,p} = C_{Y,p_\beta} \sin\beta \tag{3.1}$$

$$C_{Y,p_\beta} = -\left(1 + \frac{3C_{T_p}}{8(1+\frac{2}{3}C_{T_p})^{0.5}}\right)\frac{4.25\sigma_p}{1+2\sigma_p}\sin(\beta_p+8)\,, \tag{3.2}$$

$$C_{Tp} = \frac{T}{\frac{1}{2}\rho V_a^2 S_p}\,, \tag{3.3}$$

$$\sigma_p = \frac{4N_p\bar{c}_b}{3\pi D_p}\,, \tag{3.4}$$

$$\bar{c}_b = 0.16\left(\frac{5}{4}c_{b_{0.25}} + 2c_{b_{0.5}} + 2c_{b_{0.75}} + c_{b_{0.95}}\right)\,, \tag{3.5}$$

where N_p is the number of blades, D_p is the propeller diameter, $\bar{c}_b$ is the mean blade chord and c_b is the blade chord expressed at different radius position. V_a is the air velocity outside the slipstream and S_p being the propeller disc area. Note that the coefficient $C_{Y,p}$ is rendered non-dimensional using as reference surface area the propeller disc surface area S_p. The propeller solidity σ_p is a measure of how much of the propeller disc is solid (blade) and how much it is void. Large blade chords and high number of blades increase the solidity ratio.

This formula remains dependent of the geometrical parameters of the propeller such as chord and twist angle. It can be argued that these parameters are part of a detailed design phase which is outside the scope of this study.

Furthermore, distributing propulsion for a better propulsion efficiency assumes to lower the thrust loading $\frac{T}{S_p}$ or the power loading $\frac{P}{S_p}$ of a propeller. In turns, the solidity and thrust coefficient of the propeller will decrease as thrust and power are distributed across a larger propeller area. In the limit $\sigma_p \to 0$, equation (3.2) tends toward 0 and the propeller normal forces may be neglected.

As for the moment created by these normal forces, propellers located at the wing leading edge generally have a level arm too small to impact the aircraft flight dynamics. For propellers located further from the centre of gravity, for example at the nose, moments created by normal forces can be significant enough to disturb the aircraft flight dynamic [Hoerner 1985], [Etkin 2012].

3.1.2 Propeller Slipstream effect on the wing

A propeller slipstream impacts the wing in two major ways, in the order of importance:

1. The increase of dynamic pressure and the change in total angle of attack seen by the portion of the wing immersed in the slipstream [Hoerner 1985], [McCormick 1999], [Patterson 2015].
2. The swirl induced by the propeller locally increasing or decreasing the angle of attack on the portion of the wing immersed in the slipstream [Obert 2009], [Veldhuis 2005].

The increase of dynamic pressure in the slipstream is illustrated by experimental measurements in Fig 3.2. Dynamic pressure on a survey plane parallel to the propeller plane is plotted for varying thrust coefficients.

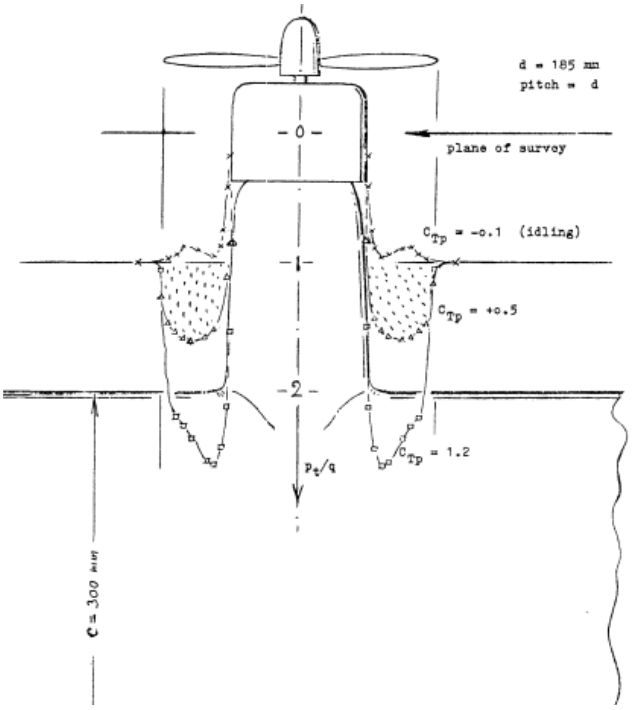

Figure 3.2 – Dynamic pressure in propeller slipstream, in the figure C_{T_P} is defined in equation 3.3. Abring ZWB FD 1908 (1942) reproduced from [Hoerner 1985]

The velocity distribution is not uniform across the slipstream but it shows an axial symmetry. Only the portion of the wing inside the slipstream is impacted by the change of dynamic pressure. In this 2D representation, there is no information about a local change of angle of attack for the portion of the wing immersed in the

slipstream. If the angle of attack is assumed constant, then the lift coefficient of the wing is unchanged and it is the increase of dynamic pressure that increases the overall lift force. However, the change in lift is conveniently modelled through an increase of lift coefficient and is most of the time presented in this way.

The effect of increased slipstream velocity on the lift coefficient is visible in Fig 3.3.

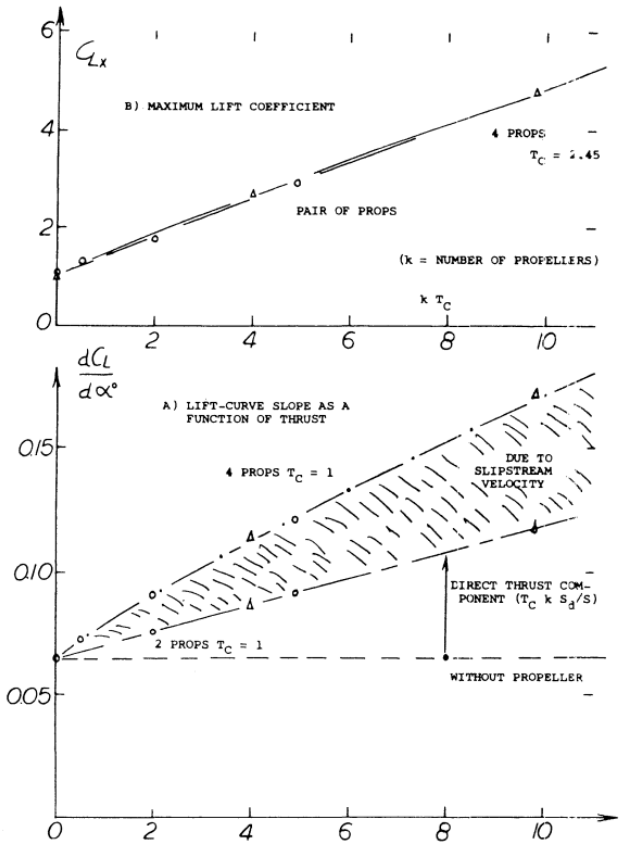

Figure 3.3 – Effect of propeller slipstream on the maximum lift and the lift slope coefficient C_{L_α} reproduced from [Hoerner 1985]

When the aerodynamic coefficient is computed relative to the free-stream velocity, the maximum lift coefficient increases linearly with the factor kT_c which represents in this figure the number of propellers multiplied by the thrust coefficient defined in equation (3.3). The same can be said for the lift slope coefficient. It seems possible to double even triple these two coefficients depending on the number of operating propellers and thrust coefficient. This particularity was put forward to motivate the use of wing blowing as a complement, or a replacement, for high lift devices. Although useful as illustrative example, this source has since been put in

doubt by a more recent study that suggest a non linear evolution of the lift slope coefficient with respect to the thrust coefficient [Dilinger 2018].

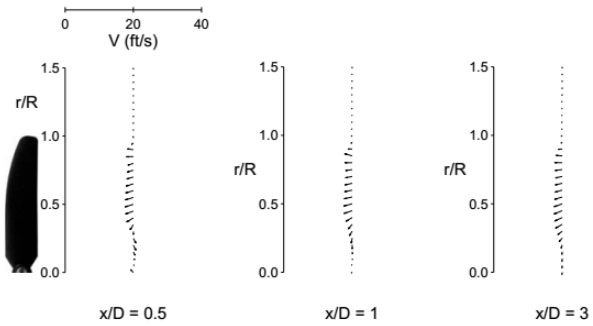

Figure 3.4 – Swirl velocity at different location after the propeller disc, reproduced from [Deters 2015]

The effect of the swirl is a tangential velocity impulsed by the propeller and it can be visualized by Particle Image Velocimetry (PIV) flow measurements in wind tunnel in Fig 3.4. The tangential velocity distribution through the propeller disc plan and slipstream is not symmetric such that the portion of the wing located behind the down going blade will see a decrease in angle of attack while the portion of the wing behind the up going blade will see an increase of angle of attack.

When combined together, these effects modify the lift distribution as shown in Fig 3.5 where both flight test measurements and Euler simulations on a Fokker 50 are shown. Flight tests are performed at low velocity with high thrust coefficient and at high velocity with low thrust coefficient. The lift increase in the slipstream is asymmetric due to the tangential velocity and higher in the region of the wing covered by the up-going blade where the tangential velocity and dynamic pressure increase combine. At the down going blade, the dynamic pressure and tangential velocity oppose each other.

The intensity of interactions depends largely on the thrust coefficient and are observed to be most important at low speed. From this observation, one can deduce that there is a chance that their contribution will be significant for dimensioning the vertical tail at low speed.

An additional observation one can make is that, despite the fact that the induced velocity is well contained within the slipstream, lift variation propagates outside of it. Veldhuis in [Veldhuis 2005] explains this phenomenon as the impact of the interaction between the slipstream and the portion of the wing immersed in it on the general inflow condition.

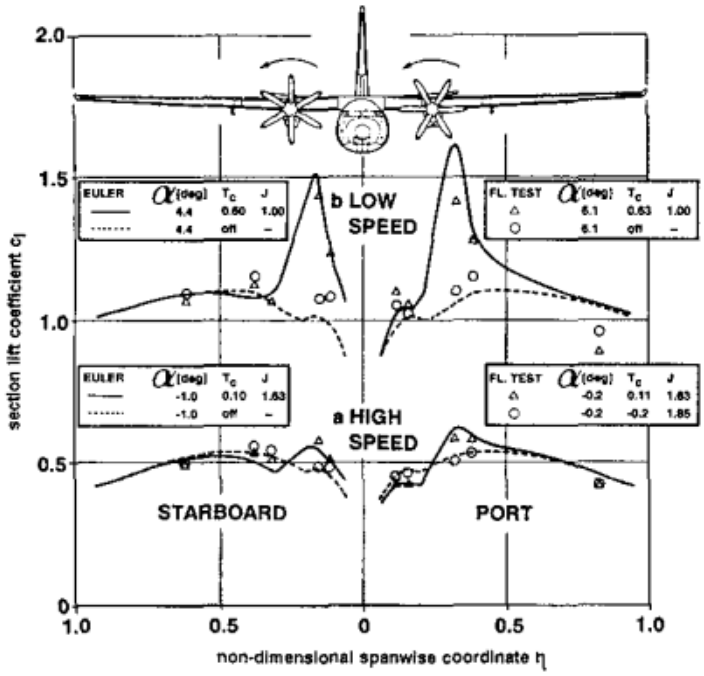

Figure 3.5 – Total effect of slipstream on wing, computed and measured in flight tests. Reproduced from [den Borne 1990].

More recently, Veldhuis [Veldhuis 2004] has reviewed experimentally with wind tunnel tests, the impact of the following parameters:

— propeller rotation direction,

— propeller streamwise, spanwise and vertical position,

— propeller angle of attack with respect to wing,

on the aircraft lift and drag coefficients.

The streamwise and vertical position of the propeller have negligible effects compared to the spanwise position where the results show an increase of lift to drag ratio when the propeller is moved toward the wingtip. The extreme position leading to an increase of the order of 40%. This gain depends on the propeller rotation direction. The swirl is mostly at play in this effect, interacting with the wingtip vortex. When the swirl rotates in the opposite direction from the wingtip vortex, the intensity of the last one is lowered [Miranda 1986].

The consequence of the angle of attack of the propeller, for a 10° tilted down propeller, leads to an increase in 9% in propulsion efficiency and 14% in lift to drag ratio. These improvements are explained by the up-wash created by the propeller on the wing. It increases the lift and at the same time, tilts the lift forward, generating

a positive thrust force.

When discussing the aerodynamic characteristics of a wing in a slipstream, one can wonder how the boundary layer is developing in this particular air flow condition. The development of the boundary layer being responsible for the friction drag, it can be of importance when an important part of the wing is immersed in the slipstream. Catalano in [Catalano 2004] and Miley in [Miley 1988] studied experimentally the effect of propeller slipstream on the boundary layer. It was found that the boundary layer in the slipstream transitions to turbulent when the wake of a blade passes over the wing. Shortly after the blade wake, the boundary layer transitions back to laminar if the conditions are met. In turn, the boundary layer can be cyclic going back and forth from laminar to turbulent each time a wake passes over the wing.

3.1.3 Effect of propeller wing interaction on other aircraft parts

Obert in [Obert 2009] warns about the impact of propeller wing interaction propagating rearwards and affecting the tail. The slipstream being deflected downward by the wing, the impact on the downwash angle is usually negative.

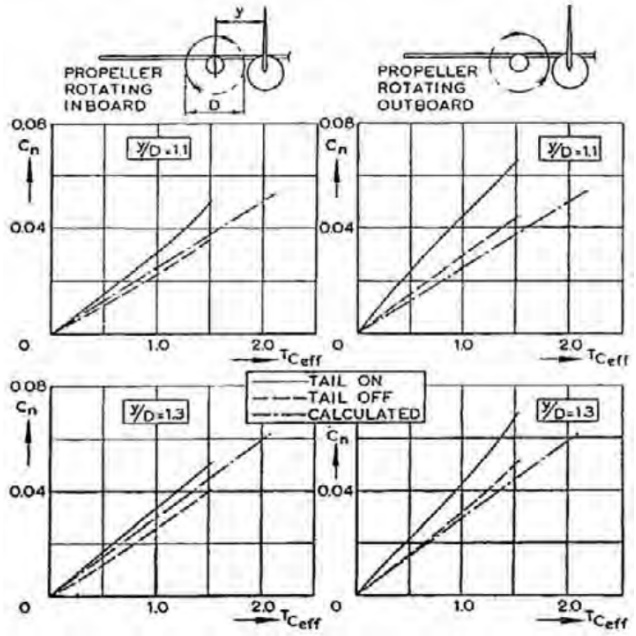

Figure 3.6 – Yawing moment coefficient as a function of engine spanwise position. $T_{C_{\text{eff}}}$ in the figure is the thrust coefficient using the forward force instead of propeller thrust. Reproduced from [Obert 2009]

.

The vertical tailplane can be impacted by the abrupt lift variation in the spanwise

direction. Similarly to flap deflection, a trailing vortex can be created downstream of the portion of the wing immersed in the slipstream. When approaching the vertical tail, this vortex induces a lateral flow on the vertical tail, creating a lateral force. This effect is illustrated through experimental tests in Fig 3.6 and Fig 3.7by Mannée [Mannée 1962] and reproduced from Obert [Obert 2009].

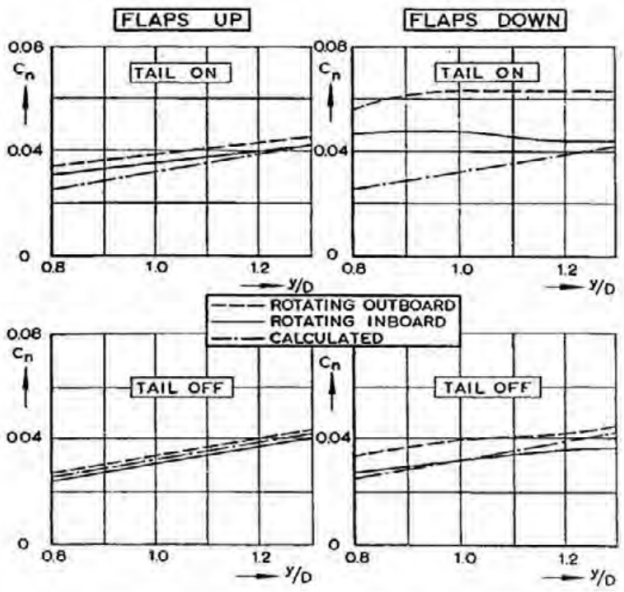

Figure 3.7 – Yawing moment coefficient as a function of engine spanwise position, effects of flap. Reproduced from [Obert 2009]

.

In this test, a yawing moment is generated by one engine placed on the wing. The yawing moment of the aircraft with and without tail are compared. One of the consequence of this interaction is that in the proximity of the fuselage: "*placing the engines further outboard does not lead to a larger yawing moment*" [Obert 2009]. Deflecting flaps results in a more abrupt lift variation, it amplifies the effect as shown in Fig 3.7.

3.1.4 Consequences of aeropropulsive interactions on the lateral flight dynamics

The impact of propeller wing interactions on the lateral flight dynamics could be observed in flight test by Van Rooyen in [van Rooyen 1981], where the effects of both propeller forces and propeller-wing interaction on the lateral-directional stability were investigated. The aircraft considered for this study was an HP 137

twin-turboprop with three bladed Hamilton Standard 23LF propellers of 2.59m of diameter.

In this study, it was found that the dihedral effect or the rolling moment induced by side slip C_{l_β} and the yawing moment due to yaw rate C_{n_r} were the two coefficients that were the most impacted by thrust coefficient variation. They in turn were the most impacting for the lateral modes. Particularly, the spiral mode was found to become unstable at low velocity, with flaps deployed and high thrust coefficients.

It was deduced that the variation in C_{l_β} was mostly due to the propeller slipstreams deflected by the side slip and producing an asymmetric lift distribution on the wing. The roll moment produced by the lateral force of the propellers was found small because of the small vertical level arm between propellers and the centre of gravity of the aircraft.

The variation of C_{n_r} is explained by the propeller negative thrust gradient with respect to velocity. Due to the yaw rate creating local increase or decrease in the airspeed seen by the propellers, a differential thrust is created that helps dampen the yawing motion. In a lesser extent, it is supposed that the reduced airspeed at one propeller increases the thrust coefficient and the wing drag due to stronger interactions. This effect is destabilizing but of lower intensity. The lack of additional data and study makes it difficult to state definitely the importance of this effect.

Propeller forces, although significant, were not found to be sufficiently varying with power to be further investigated. No mention of aero-propulsive interaction propagating rear-ward and impacting the tail surfaces was made in this study.

3.1.5 Conclusion on aero-propulsive interaction review

A number of phenomena thought to be relevant for this thesis have been explained. The existing literature gives some examples of the magnitude with which propeller wing interactions can impact the aerodynamic efforts.

It was reported that with a rather small portion of the wing immersed in a slipstream, the consequences are already noticeable on the aircraft motion. The consequence of propeller-wing interactions on aircraft flight mechanics when a large portion, or possibly the whole wing is immersed in a collection of slipstreams, has not received much attention at the time of writing. In addition, there remain evidences that strong interactions can exist at low velocity, close to the dimensioning point of the vertical tail.

Upon these uncertainties it was decided to include aero-propulsive interactions

in the study, with the objective to determine how interactions impact the stability analysis and control laws design. The questions of interest for these future analyses are, how is the natural stability of the aircraft impacted by interactions and can they be considered as external disturbances to simplify the control laws design?

The propeller normal forces are assumed negligible and will be omitted because of the expected low solidity of propellers on a distributed propulsion and because it was shown to be negligible for aircraft lateral motion.

The next section tries to establish a list of possible techniques to estimate aero-propulsive interactions and define the criteria to select an adapted method.

3.2 Modeling propeller wing interaction

Now that a review of aero-propulsive interactions and their magnitude have been given, the interest is about modelling and predicting these interactions. In this scope, different methods have been studied and the idea here is to propose a classification.

It is possible to classify the methods both chronologically and by complexity. The first methods that have been developed are the direct methods derived by solving potential flow equations. They don't require iterative computation and allow a rapid estimation of the lift increment. The low fidelity numerical methods that are based on Lifting Line (LL) theory or VLM method have a low computation time and allow the representation of more complex interactions. Finally the high fidelity numerical methods using finite volume analysis allow to investigate the unsteady behaviour of the interactions.

3.2.1 Direct methods

Köning [Köning 1934] is often cited as having laid down the basics of propeller wing interactions using potential flow formulation. His work is however complex and solutions more easily usable by the designer have been formulated in further developments.

One of the reference works is presented by Smelt & Davis in [Smelt 1937] where the authors present a linearised theory between two opposite cases. In one case, the propeller diameter is much larger than the chord and in the other, the chord is much larger than the propeller diameter. A lift factor is interpolated between these two cases based on empirical work.

Other authors assembled theoretical work with experimental results, offering semi-empirical methods like Kuhn and Draper [Kuhn 1959]. A reference work for prediction of lift and drag increment for a fully immersed wing is the method developed by Jameson in [Jameson 1968] and [Jameson 1970]. This method can be extended to partially immersed wings, wings with flaps and is specifically made for estimating performances of V/STOL aircraft. It remains a reference work and is used in preliminary design to estimate take off performances of an efficient commuter aircraft in [Stoll 2016].

Recently, Patterson motivated the need for a new and simpler method to predict lift increase and proposed a new method for the design of the high lift system of the NASA X57 [Patterson 2015]. When compared to the previously mentioned reference work, this method was found similar to Jameson in term of accuracy except at high disk loading were Patterson's method performed better.

3.2.2 Low fidelity numerical methods

Low fidelity numerical methods discretize the aircraft in small elements and find a potential flow solution by solving the equations iteratively. The total aerodynamic forces are then computed by integrating over all the segments. The most widely used methods are the LL [W.F. 2000], the VLM [Miranda 1977] or the panel method [Hess 1972].

To represent a wing immersed in a slipstream with these computer programs, the usual methodology is to input the flow induced by a propeller and let the program find a solution with the new inflow conditions [Hunsaker 2006], [Bohari 2018], [Fisher 2017]. The flow induced by the propeller can be calculated by disc actuator theory or blade element theory. This methodology usually models one way interaction.

It is possible to model two ways interaction by including a potential flow representation of the slipstream [Miranda 1986] or model the propeller as a lifting surface as well [Witkowski 1989]. This methodology is better suited for studying propeller at wing tip where the interaction with propeller swirl and wingtip vortex is strong.

If the interaction between slipstream and wing is propagated rearward, the effect on the tail can be modelled [Schroijen 2010]. This works well for configurations without flap but viscous effects appearing for example with flap deflection quickly degrades the accuracy of the prediction.

These methods are of a good accuracy with a reasonable computation time of

the order of a few seconds to a few minutes. A comparison with higher fidelity methods in [Fisher 2017] and experiment in [Veldhuis 2004] showed an error in drag prediction and a lack of precision in capturing the ability of the wing to reduce the tangential velocity in the slipstream. This phenomenon called swirl recovery, can be approximated by an additional efficiency factor. For more precise modelling, higher fidelity methods are necessary.

3.2.3 High fidelity methods

By high fidelity methods, it is referred to numerical methods employing finite volumes. These methods can easily solve two way interactions. In such case, they are called homogeneous methods. However, hybrid methods aiming at reducing computational cost also exist. For hybrid methods, the propeller flow is solved using a different, simpler solver, either actuator disc (in two dimensions) or blade element theory, and the resulting slipstream is then coupled to a CFD solver, typically Reynolds-Averaged Navier-Stokes (RANS). This has been done at ONERA by Fischer in [Fisher 2017] but also by Patterson in [Patterson 2016]. This methodology avoids the lengthy unsteady simulations at the price of a small precision loss. Results remain of interest as they allow the description of propeller slipstream and swirl as well as local wing lift and drag increments.

Stuermer in [Arne W 2006] has investigated a case representative of regional turbo-propeller aircraft using unsteady CFD simulations and compared it with experimental data from [Samuelsson 1987]. The unsteady nature of the simulation allows the full development of propeller wake, computation of unsteady forces on propeller blades and unsteady interaction with the wing. The simulation allows the detailed description of propeller forces and interaction effects in terms of lift and drag increment. Additionally, the interaction with the nacelle which leads to higher pressure drag, is captured. Simulations agree well with the experimentation and give a good drag breakdown of the portion of the wing within the slipstream.

3.2.4 Intermediate conclusion

The previous section gave an overview of the existing methods to analyse and to predict propeller-wing interaction. The focus now lies in the definition of criteria to select an appropriate method.

Recalling the context around this chapter, propeller wing interactions should be used to compute flight envelopes where the trim state is found through optimisation

Table 3.1 – Evaluation of the number of calls to the aero-propulsive function.

Number of states	$n_x = 8$
Typical engine number and input number	$N_m = 1.10^1$, $n_u = N_m + 3$
Optimisation steps for trim (typical) and linearisation	$n_{op} = 6$
Function calls for evaluation of a Jacobian	$n_{\text{it}} = n_{op}\left[n_x \cdot n_x + n_u \cdot n_x\right] \approx 1 \times 10^3$
Flight points for flight envelope	$n_{fp} = 800$
Function calls for a flight envelope	$n_{fp} n_{\text{it}} \approx 8.10^5$

and each engine is an actuator. After trimming, the system is linearised to apply control theory. The method should be suited for regional subsonic transport aircraft with distributed propeller of arbitrary number, power and position. A specific difficulty to take into account is that interactions should be evaluated both locally and globally on the wing to evaluate the interactions due to differential thrust.

The following criteria were chosen to select a relevant technique:

1. **Flexible to engine number and position:** flexible here in the sense that any change in engine number or position should be quickly taken into account without having to recompute a database.
2. **Low computation time:** the trim algorithm through optimization makes an important number of function calls to evaluate aerodyamic efforts. The order of magnitude of the function calls is evaluated in Table 3.1. It shows that if one wants to keep computation time within a reasonable limit, the function execution time should be of the order of 1×10^{-1} s.
3. **Engine effects evaluated independently:** each engine being controlled independently, the interactions should be computed locally behind each propeller so as to be able to estimate a roll induced moment and yaw induced moment locally.
4. **Interfacing with other preliminary aerodynamics evaluation tools:** the methodology developed in this study does not aim at designing a whole aircraft but is a local optimization. Therefore it should be able to use inputs from tools used at different design steps and particularly the global aerodynamic analysis.

The requirement for low computation and flexibility ruled out the high fidelity methods as the computation time is of the order of hours for one point. Creating a

database constituted of look-up tables would be enough to study one configuration but it would not be convenient if the engine number and/or position were changed.

Direct methods and low fidelity numerical methods would satisfy most of the requirements. There remained a doubt about the execution time of numerical methods. A benchmark between a direct method from [Patterson 2015] and a non-linear VLM from [Bohari 2018] favoured the direct method over the VLM for the significant lower computation time, less convergence issues and similar accuracy (this comparison is presented later in Fig 3.11).

This direct method focuses on lift increase and suffers the lack of prediction for drag increase and the lack of aileron or flap deflection. Despite these drawbacks, it was decided to experiment an enhancement of the available direct method as it fulfils all other criteria otherwise.

An additional drawback of this method that it does not model the rearward propagation of the interactions. The impact on the tail surfaces cannot be estimated. Only a low fidelity numerical method can give this estimate in a sufficiently short time and this field remains an open subject as explained in [Schroijen 2010].

3.3 Construction of the propeller wing interaction model

This section explains the construction of the propeller wing interaction model for stability and control analysis. The starting point is the lift increase model of propellers in front of a wing developed by Patterson [Patterson 2015] and described in 3.3.1. The ideas and modifications brought to this method are described in 3.3.2.

3.3.1 Patterson lift increase model

The method is described in detail in [Patterson 2016] and is summarized here to prepare the field for the modifications [1]. This model offers a rapid estimation of the lift increase due to a propeller located at the leading edge of a wing. The hypothesis considered for this model are:

- The method is developed in 2d and generalized to 3d using a pre-existing lift distribution and assuming linear propagation.
- The overall effect of the swirl is negligible, this technique makes use of momentum theory to predict the airspeed in the slipstream which does not take

1. Readers interested in detailed construction and validation of this method are referred to [Patterson 2016]

into account swirl.

- The air velocity in the slipstream is uniform.
- The propeller is assumed far ahead of the wing such that one way interaction only takes place.
- Wingtips are not embedded in a slipstream. The method assuming no swirl, interaction between swirl and wingtip vortex can not be predicted.

A key feature of this model is that it models both the increase of dynamic pressure and the modification of the angle of attack seen by the wing.

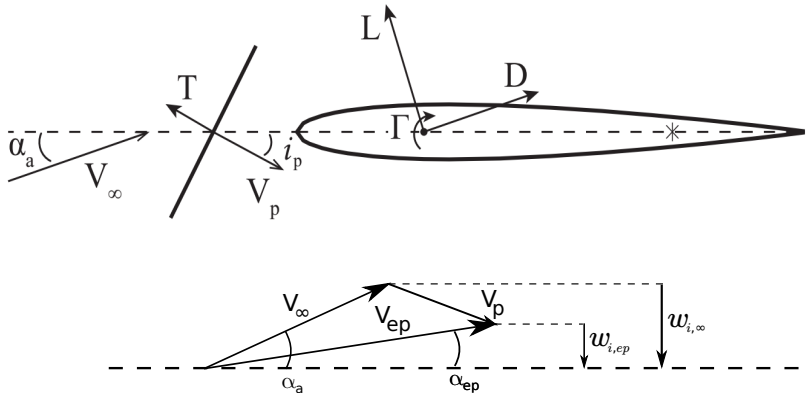

Figure 3.8 – Patterson circulation formulation (reproduced from [Patterson 2016]).

The basic idea, represented in Fig 3.8, is to start from the lift of a 2d airfoil given by Kutta-Jukowski:

$$L = \rho V \Gamma \,, \tag{3.6}$$

where the circulation Γ is determined from the airfoil induced velocity, w_i:

$$\Gamma = \pi c w_i, \tag{3.7}$$

with c being the airfoil's chord. The relative change between the lift of a blown L_{ep} and unblown airfoil L_∞, can be written as:

$$\frac{\Delta L}{L_\infty} = \frac{L_{ep} - L_\infty}{L_\infty} \,, \tag{3.8}$$

$$\frac{\Delta L}{L_\infty} = \frac{\rho V_{ep} \pi c w_{i,ep} - \rho V_\infty \pi c w_{i,\infty}}{\rho V_\infty \pi c w_{i,\infty}} \,, \tag{3.9}$$

$$\frac{\Delta L}{L_\infty} = \frac{V_{ep}}{V_\infty} \frac{w_{i,ep}}{w_{i,\infty}} - 1 \,, \tag{3.10}$$

where the term $\frac{V_{ep}}{V_\infty}$ represents the change in airspeed and the term $\frac{w_{i,ep}}{w_{i,\infty}}$ represents the change in induced flow. Based on Fig 3.8, one can express $w_{i,\infty}$ and $w_{i,ep}$ as:

$$w_{i,\infty} = V_\infty \sin \alpha_a \,, \tag{3.11}$$

$$w_{i,ep} = V_{ep} \sin \alpha_{ep} \,. \tag{3.12}$$

The slipstream velocity V_{ep} and the new angle of attack α_{ep} can be determined by analysis of fig 3.8 as well:

$$V_{ep} = \sqrt{V_\infty^2 + 2V_\infty V_p \cos(\alpha_a + i_p) + (V_p)^2} \,, \tag{3.13}$$

$$\tan \alpha_{ep} = \frac{V_\infty \sin \alpha_a - V_p \sin i_p}{V_\infty \cos \alpha_a + V_p \cos i_p} \,, \tag{3.14}$$

$$\alpha_{ep} \approx \frac{\alpha_a - V_p/V_\infty i_p}{1 + V_p/V_\infty} \,. \tag{3.15}$$

In this formulation, the propeller induced velocity V_p is found by momentum theory, allowing to estimate the total lift increase on a two dimensional airfoil totally immersed in an uniform flow. To account for the slipstream height, a correction factor ν is associated with the propeller induced velocity. A surrogate model, built from 2d finite element CFD is given to compute this correction factor in [Patterson 2016].

When introducing equations (3.11), (3.12), (3.13) in equation (3.10), one obtains the general equation for lift increase:

$$L_m = \left(1 - \frac{\nu V_p \sin i_p}{V_\infty \sin \alpha_a}\right) \frac{\left(V_\infty^2 + 2V_\infty V_p \nu \cos(\alpha_a + i_p) + (\nu V_p)^2\right)^{0.5}}{V_\infty} - 1 \,, \tag{3.16}$$

where $L_m = \frac{\Delta L}{L_\infty}$, is the lift multiplier to apply to the lift coefficient of the wing sections covered by the propeller. Extension to 3d cases is made by computing the lift multipliers behind each propeller and summing the modified local lift coefficients:

$$C_L = \sum_{j=1}^{N_s} c_{L_j} (L_{m_i} + 1) \frac{S_j}{S} \,, \tag{3.17}$$

where N_s is the total number of sections of the wing, c_{L_j} and S_j are the unblown section lift coefficient and section surface area. L_{m_i} is the lift multiplier corresponding to the i^{th} propeller.

To use the model, it is necessary to know the local unblown lift distribution over

the wing in term of the section's lift coefficient c_{L_j}. This input can be easily and reliably found by a VLM and or LL method. In this case, it is calculated with VLM simulations using the software OpenVSP [Gloudemans 1996]. The section's lift slope a_j is evaluated through VLM simulations and the section's lift coefficient is retrieved using a linear relationship:

$$c_{L_j} = a_j \alpha_a \ . \tag{3.18}$$

In this case, the effect of the downwash on the overall airflow, is included in the local lift slope a_j.

The induced propeller velocity V_p can be obtained from various propeller models. As for the original method, a model derived from momentum theory is used in this work. Specifically the model described by [McCormick 1999], for a propeller at an angle of attack:

$$T = 2\rho S_p V_{ep} V_p \ , \tag{3.19}$$

using equation (3.13), one can obtain a quadratic expression in V_p:

$$V_p^4 + V_p^3 2V_\infty \cos(\alpha + i_\mathrm{p}) + V_p^2 V_\infty = \left(\frac{T}{2\rho S_p}\right)^2 \ . \tag{3.20}$$

This equation is rendered non-dimensional with V_∞ since only forward flight is considered such that $\frac{V_p}{V_\infty}$ never diverges towards infinite values:

$$\left(\frac{V_p}{V_\infty}\right)^4 + \left(\frac{V_p}{V_\infty}\right)^3 2\cos(\alpha + i_\mathrm{p}) + \left(\frac{V_p}{V_\infty}\right)^2 = \left(\frac{T}{2\rho S_p V_\infty^2}\right)^2 \ . \tag{3.21}$$

This equation is solved numerically to obtain $\frac{V_p}{V_\infty}$ using as input the factor defined as the non dimensional thrust coefficient for this model:

$$T_c = \frac{T}{2\rho S_p V_\infty^2} \ . \tag{3.22}$$

This coefficient is the starting point to determine L_m. It also allows a quick and simple measure of the magnitude of the propeller wing interaction.

To illustrate how the method works, it has been implemented on a simple test case used by Fisher in [Fisher 2017]. The test case consists of a single rectangular wing of aspect ratio 15, fitted with 16 leading edge propellers. The lift distribution with uniform blowing is shown in Fig 3.9a and differential thrust in Fig 3.9b.

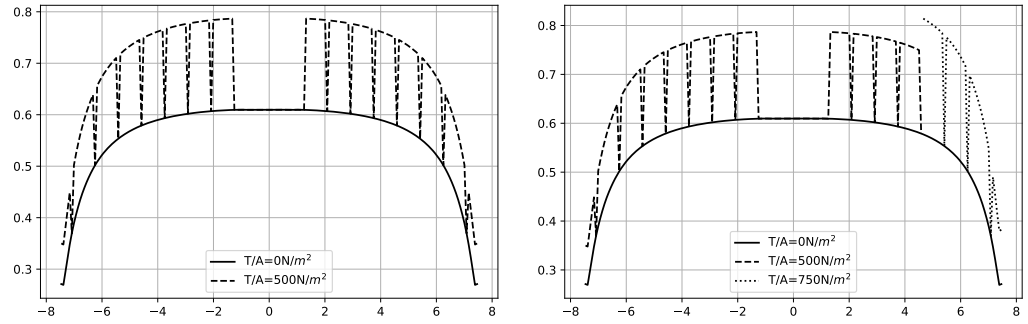

(a) Lift increase due to blowing with a disc loading $\frac{T}{A} = 500\text{N/m}^2$.

(b) Differential thrust, the four outer right engines are set to $\frac{T}{A} = 750\text{N/m}^2$.

Figure 3.9 – Illustration of the Patterson method for the treatment of differential thrust.

This test case is not used for validation but serves as a simple illustrative example of the effect of lift increase and differential thrust on the lift distribution. The parameter used to quantify the level of interaction in the original study of Fischer is the thrust loading $\frac{T}{S_p}$. The asymmetric lift distribution resulting from differential thrust shown in fig 3.9b is similar to what an aileron deflection could produce. This could justify the idea of using the propulsion more actively in the lateral control of the aircraft and ultimately reducing the aileron surface area.

This represents the baseline to compute lift increase due to leading edge propellers. The modification to come will concern the inclusion of aileron and flap in the model and the estimation of the drag from the output of this initial model.

3.3.2 Augmentation of the model

Two kinds of features are added to the model, in the first place, the method is modified to into consideration of flap and aileron. In a second part, a methodology is added to estimate the drag from the newly obtained lift distribution.

3.3.2.1 Flap and ailerons

The idea to take into account flaps or ailerons comes from the treatment of Jameson [Jameson 1970]. In his guidelines, Jameson reminds that a flap or aileron deflection has the effect, in the linear regime, of modifying the zero lift line of the airfoil. As long as the flap deflection remains in the linear interval, this statement is correct and in addition, the change in the zero lift line is proportional to the

deflection of the flap or the aileron.

The initial development of Patterson relies on the situation illustrated in Fig 3.8 where all angles are defined relative to the zero lift line of the airfoil. A flap or aileron deflection, in thin airfoil theory, is seen as a change of camber which assuming no flow separation, influences directly the circulation in the same manner as the angle of attack as illustrated by:

$$\Gamma = 4\pi a V \sin(\alpha_a + f) \tag{3.23}$$

Where α_a and f are respectively the angle of attack and a measure of the camber [Pope 2009].

In case of a plain flap or aileron deflection, it appears logical to introduce a modification on the zero lift line and let the modification propagate in the existing model. Hence the situation for a 2d airfoil with flap is modified as in Fig 3.10. One simply has to shift the zero lift line by an angle δ_{α_0}.

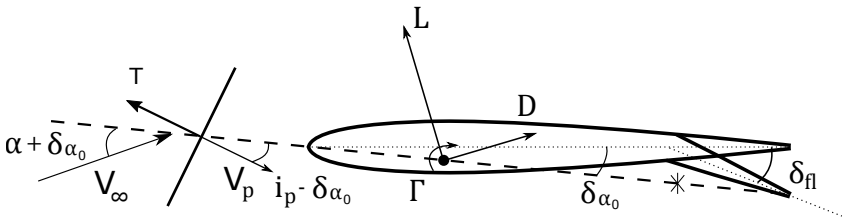

Figure 3.10 – Illustration of the modifications caused by a flap deflection.

According to Fig 3.10, the total angle of attack is expressed as:

$$\alpha_t = \alpha_a + \delta_{\alpha_0} \tag{3.24}$$

$$\alpha_t = \alpha_a + \frac{\partial \alpha_0}{\partial \delta_{fl}} \cdot \delta_{fl} \tag{3.25}$$

According to Fig 3.10 equation (3.16) will be modified as follows:

$$L_m = \left(1 - \frac{\nu V_p \sin(i_p - \delta_{\alpha_0})}{V_\infty \sin(\alpha_t)}\right) \frac{\left(V_\infty^2 + 2V_\infty V_p \nu \cos(\alpha + i_p) + (\nu V_p)^2\right)^{0.5}}{V_\infty} - 1 \tag{3.26}$$

The results of this modification is compared with a non linear VLM [Bohari 2018] using again the test case described by Fischer in [Fisher 2017]. A full span flap with a chord of $c_{fl} = 0.30 \cdot c$ is deployed. A positive angle is downward deflection such that the lift increases. The comparison between the modified Patterson and the non

linear VLM is shown in Fig 3.11.

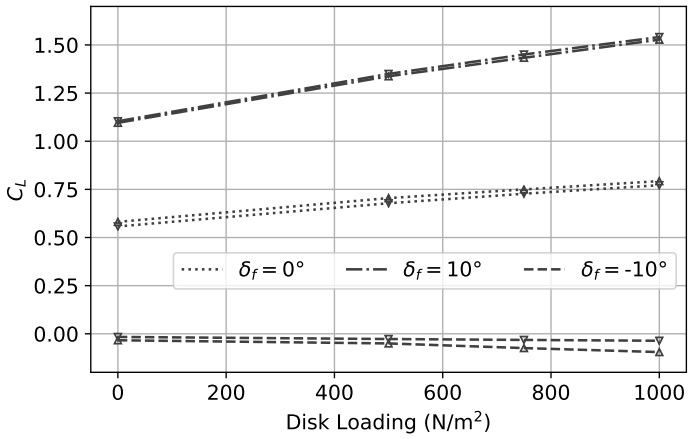

Figure 3.11 – Lift increase for different flap deflection. Up triangles : VLM. Down triangles : Patterson

Both positive and negative deflections are illustrated to account for the use of aileron. The results are encouraging, especially the rate of change of the lift versus the propeller disk loading agrees well. For the use of differential propulsion and in case of a blown aileron, it is of primary importance. The modified model shows less agreement at negative deflection. This is due to the proximity of zero lift.

The magnitude of lift change with flap deflection and blowing is similar with both models which validates the modification brought to the Patterson model.

Despite the fact that the VLM code has been validated against experimental data, it uses the same underlying formulation (velocity triangle) as the Patterson model. This could be the reason why their predictions agree so well. Though the Non Linear VLM showed good performance in predicting lift and drag increase of blown wing with flaps (see [Bohari 2018]). A validation against a higher fidelity method or experimental data would be necessary to confirm the validity of the method.

3.3.2.2 Drag increment of propeller wing interactions

The starting point to drag estimation is a traditional drag break-down to decompose the different drag effects involved:

Friction drag : The friction drag on a wing is mainly due to the development of the boundary layer. The location of the transition between laminar and

turbulent flow and the subsequent increase in skin friction coefficient impacts the friction drag C_{D_0}. So called laminar airfoils are designed to delay the transition point (for example NACA 63-64 series), others are called turbulent airfoil when the transition point is around 30% of the chord. When adding a propeller in front of the airfoil, the turbulent wake of the propeller tend to force the transition as observed earlier in the work of Catalano [Catalano 2004] and Miley [Miley 1988]. To simplify the problem and because the ATR72 is unlikely to have a large laminar boundary layer [2], the transition from laminar to turbulent is forced at 10% of the chord [Hoerner 1958].

Induced Drag : The induced drag is the drag penalty that one has to pay when generating lift. In lifting line theory, it is due to and is calculated based on the lift distribution of a wing [Pope 2009]. Following this idea, since the Patterson model allows to predict the lift distribution of a blown wing, one can recompute the induced drag created by the new lift distribution. In order to do so, it is possible to proceed in two steps:

1. After the blowing effect has been calculated, the new lift distribution is used to evaluate the new induced velocity around the wing. At this point one should recompute the lift distribution taking into account the new induced velocity and do so until convergence. This step is not performed for two reasons:
   (a) The original lift distribution (unblown) comes from a converged VLM simulation, so it is not necessary to iterate at this step.
   (b) As for the Patterson method, it is assumed that the propellers are far from the wingtip where the effect on the induced velocity is the strongest.
2. Since the propeller also creates an up/downwash, the resulting lift and drag will be tilted by the value of the up/downwash due to the propeller. This means that the lift can contribute to thrust (upwash from propeller) or drag (downwash from propeller). This is illustrated in Fig 3.12. When computing the new local lift coefficient, the resulting apparent angle of attack is used to project the local lift onto the V_∞ direction.

Pressure drag : due to pressure difference in front and behind the wing. This type of drag is mostly observed after stall when the flow is completely detached.

2. Due to the presence of pneumatic de-icing devices.

For subsonic aircraft its importance is low with respect to the two previously mentioned sources of drag. The increase of dynamic pressure will be the most impacting parameter for this source of drag. One should note however that its value can be largely impacted by propeller positioned at the wing trailing edge [Catalano 2004].

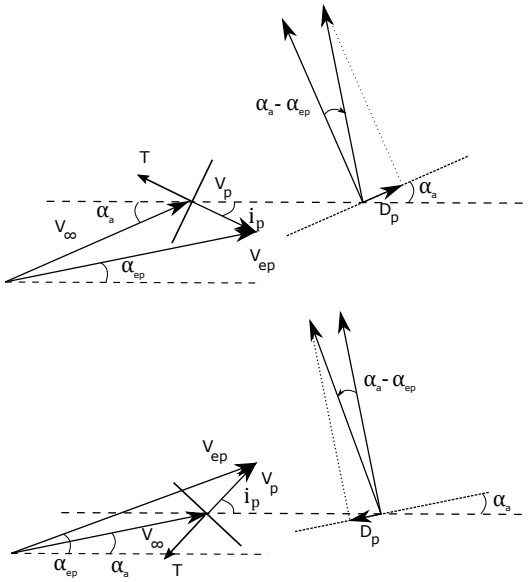

Figure 3.12 – Illustration of propeller up/downwash and the contribution of the lift force to thrust or drag.

In practice, this is implemented as follows, let c_{L_1} be the section lift coefficient obtained after applying the lift increase model. c_{L_1} is used to compute the induced drag following the lifting line theory. First, the induced velocity function $w(y_1)$ describing the induced velocity at a spanwise position y_1 is computed using [Pope 2009]:

$$w(y_1) = \frac{1}{4\pi} \int_{-\frac{b}{2}}^{\frac{b}{2}} \frac{\frac{\partial \Gamma(y)}{\partial y}}{y_1 - y} \mathrm{d}y \,. \tag{3.27}$$

The circulation function $\Gamma(y)$ in two dimensions is found through equation **??**Eq:LiftCirculation), the local lift and airfoil chord:

$$L(y) = \rho V \Gamma(y) \,,$$

$$\frac{1}{2} \rho c(y) V^2 c_{L_1}(y) = \rho V \Gamma(y) \,,$$

$$\Gamma(y) = \frac{1}{2} c(y) V c_{L_1}(y) \,. \tag{3.28}$$

The induced velocity function is used to compute the induced drag through:

$$D_i = \frac{1}{S} \int_{-\frac{b}{2}}^{\frac{b}{2}} L(y) \frac{w(y)}{V} \, \mathrm{d}y \,. \tag{3.29}$$

Introducing equations (3.28) in (3.27), it is possible to obtain the following:

$$w(y_1) = \frac{V}{8\pi} \int_{-\frac{b}{2}}^{\frac{b}{2}} \frac{\frac{\partial c(y) c_{L_1}(y)}{\partial y}}{y_1 - y} \, \mathrm{d}y \,, \tag{3.30}$$

$$C_{D_i} = \frac{1}{S} \int_{-\frac{b}{2}}^{\frac{b}{2}} c(y) c_{L_1}(y) \frac{w(y)}{V} \, \mathrm{d}y \,, \tag{3.31}$$

$$C_{D_i} = \frac{1}{8\pi S} \int_{-\frac{b}{2}}^{\frac{b}{2}} c(y) c_{L_1}(y) \, \mathrm{d}y \cdot \int_{-\frac{b}{2}}^{\frac{b}{2}} \frac{\frac{\partial c(y) c_{L_1}(y)}{\partial y}}{y_1 - y} \, \mathrm{d}y \,. \tag{3.32}$$

These expressions are integrated numerically to obtain the new induced drag coefficient C_{D_i}.

The propeller up/downwash contribution to the drag is calculated separately. From Fig 3.12, one can deduce that the lift is tilted by an angle : $\alpha - \alpha_{ep}$. This angle is computed at each wing section behind each propeller and the local lift is projected using this angle:

$$c_{D_i,w} = c_{L_1} \sin(\alpha - \alpha_{ep}) \,. \tag{3.33}$$

Finally the total induced drag with blowing effect is :

$$C_{D_i,b} = \frac{1}{S} \int_{-\frac{b}{2}}^{\frac{b}{2}} c(y) c_{L_1}(y) \frac{w(y)}{V} + c(y) c_{L_1}(y) \sin(\alpha_{ep} - \alpha) \, \mathrm{d}y \,, \tag{3.34}$$

$$C_{D_i,b} = C_{D_i} + C_{D_i,w} \,. \tag{3.35}$$

To this result, it is still necessary to add the friction drag, determined from airfoil analysis with forced transition $C_{D_0,tur}$. Its contribution is additionally weighted by $\frac{V_{ep}^2}{V_\infty^2}$, representing the increase in dynamic pressure. The total drag can be expressed

as :

$$C_D = C_{D_0,tur}\frac{V_{ep}^2}{V_\infty^2} + C_{D_i} + C_{D_{i,w}}\,. \tag{3.36}$$

Since lift and drag are computed at each wing panel, it is possible to integrate both the lift and drag over the wingspan to obtain induced roll and yawing moment expressed as:

$$L_{P,i} = \sum_{j=1}^{N_s} -C_{L_j}(L_{m_i}+1)\frac{y_j}{b}\frac{S_j}{S}\,, \tag{3.37}$$

$$N_{P,i} = \sum_{j=1}^{N_s} -C_{D_j}\frac{y_j}{b}\frac{S_j}{S}\,. \tag{3.38}$$

With this calculation, it is possible to take into account the induced aero-propulsive efforts due to differential thrust.

3.3.2.3 Stall model

One of the key factors of wing blowing is the ability to change the apparent stall angle. The stall is modeled using a general lift model based on the work of Jameson [Jameson 1970]. The stall limit remains fixed by hand, based either on 2D numerical simulation or wind tunnel experiments and α_{ep} instead of α_a is used to determine if a wing section is stalled:

$$c_{L_j} = a_j\alpha_t,\ \text{if } \alpha_{\text{ep}} \leq \alpha_{\text{s}}$$
$$c_{L_j} = C_{L_{\alpha_a}}\sin\alpha_s\frac{\cos\alpha_t}{\cos\alpha_s},\ \text{if}\alpha_{\text{ep}} \geq \alpha_{\text{s}}$$

The goal of this model being not to give an accurate estimation of the lift beyond stall but to model the delay in stall caused by wing blowing.

The airfoil pressure drag after stall is determined using 2D numerical simulation (Xfoil) and is added directly to the local friction drag component. Again, the goal is not to give an accurate prediction, rather to have consistent models in order to avoid post-stall equilibrium with the trim algorithm.

3.4 Extended model evaluation

The lift increase model formulated by Patterson was able to capture the lift increase and modification of lift slope. The goal of this section is to evaluate the modification brought to the original method. For this evaluation, the problem of lack of relevant and reliable data was faced. Two mains reasons can explain this:

— The unconventional nature of the design. Few experimental studies exist on distributed propulsion aircraft.

— The lack of recent studies. Most relevant studies were conducted between the 1930's and 1960's.

Additionally when data are available, the test cases can be reported with insufficient details to reproduce the test in a simulation environment.

Two experimental studies were available and already used in previous study to validate models, these are NASA technical reports TND-4448 [V Robert 1968] and TND-1586 [Marvin 1964]. However, some inputs are missing or irregularities were found in the data reported, such that to evaluate further the model it was decided to investigate a way to use flight data obtained in during the experimental work of the thesis.

The comparison of the model performances versus the data from the literature is discussed in section 3.4.1 and the comparison versus flight data is available in section 3.4.2.

3.4.1 Evaluation against data available in the literature

In TND-4448, a large scale powered STOL aircraft, similar to the Breguet 940, was tested in wind-tunnel. Three aspect ratios were tested in this study. The medium aspect ratio wing was selected for comparison because it satisfies the model's hypothesis and sufficient data were available. The study also includes data with flap deflection that will not be used here because the deflection considered (more than 40°) is outside the limit of linearity assumed for the use of flaps in the model.

Here, the lift slope variation and the drag increase as a function of the thrust coefficient are compared. It is worth to note that the local lift slope coefficients are manually tuned to fit the zero thrust case. This has been done since an anomaly was reported in [Jameson 1970] with the lift slope coefficient being lower than the predicted one. Interaction with the fuselage is believed to be the source of this disturbance. None the less, once the unblown lift slope is adjusted, it is possible to

study the effect of the thrust coefficient. In addition, the stall model described in section 3.3.2.3 is not included in these evaluations.

The comparison between experimental data and the model for the lift slope versus angle of attack is available in Fig 3.13a.

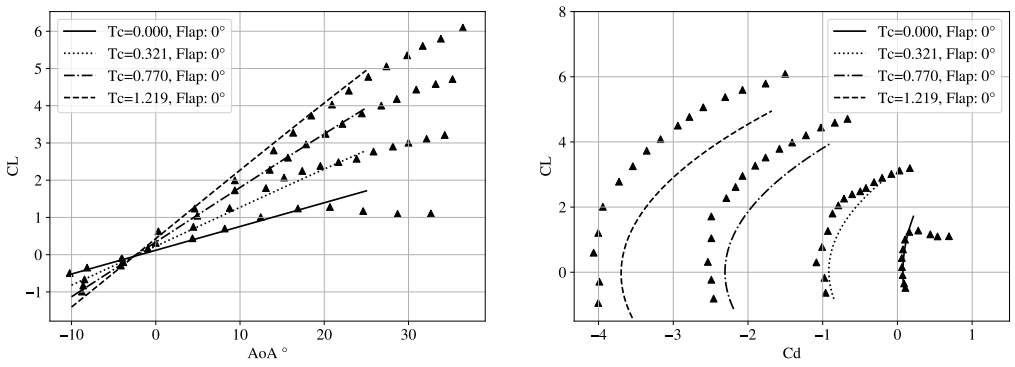

(a) Lift versus angle of attack.

(b) Lift versus drag.

Figure 3.13 – Comparison of the extended Patterson method against the TND4448 experimental data. Coefficients include thrust and are rendered non-dimensional with respect to free stream velocity. Markers: wind tunnel data, lines: extended Patterson model.

The lift slope increase due to thrust coefficient shows a good agreement with the data point except at angles of attack close to stall angle. This figure confirms the capability of the original model of Patterson to capture the lift increase and lift slope increase as a function of the thrust ratio up to $T_c \approx 1.2$.

The comparison of the drag increase due to wing blowing is available in Fig 3.13b. A problem with the data of study TND4448, which was already put in light by Jameson in [Jameson 1970] is faced here. The original study presents a drag coefficient that does not match with the thrust coefficient a zero lift. This is the reason for an offset at $C_L = 0$. Therefore in this comparison only the trends can be evaluated and further evaluations will be made with the data from report TND1586. Despite this drawback, Fig 3.13b shows a rather correct evolution of the drag with lift with more uncertainty at the highest thrust coefficient.

Although not enough to conclude on the validity of the drag model, this study is the only one that focuses on an aircraft with four engines and allows to study the effect of propeller spacing. In TND-4448 the propellers are spaced by a distance of: $0.035D_p$, with D_p the propeller diameter. This is small in the sense that it is possible to assume that the propeller slipstreams merge in a large rectangular-

like slipstream. In the case where propellers are further apart, the slipstreams are assumed to remain independent. It is possible to reproduce independent slipstream if the mesh used for the VLM analysis of the wing allows to place at least one panel in between the propellers. This panel's local lift coefficient will be unchanged by a slipstream.

To illustrate this, the lift distribution of the same aircraft as TND4448, is shown with two different propeller spacings in Fig 3.14.

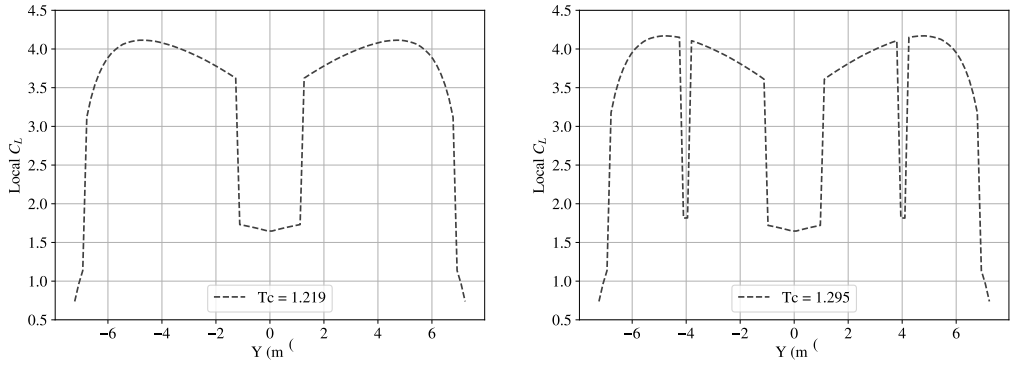

(a) Lift distribution with propeller spacing $0.035D_p$.

(b) Lift distribution with propeller spacing $0.1D_p$.

Figure 3.14 – Effect of propeller spacing on the lift distribution for $\alpha = 25°$

In Fig 3.14a the space between propellers is the original $0.035D_p$ and in Fig 3.14b the space is $0.1D_p$, sufficient to have one wing panel in between each propeller slipstream.

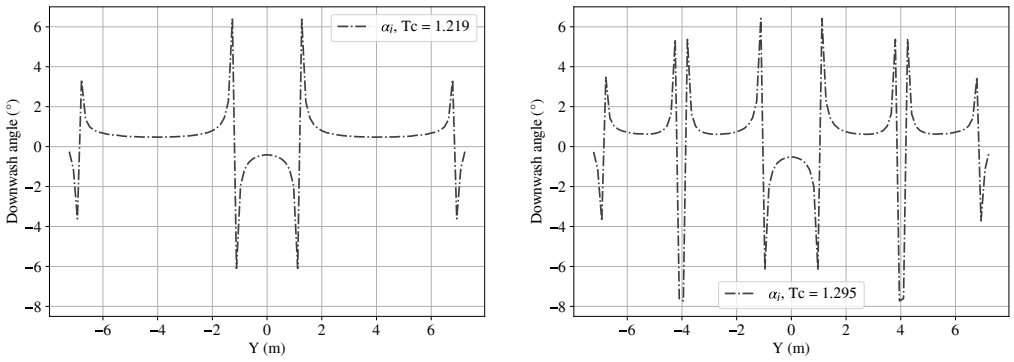

(a) Downwash angle distribution with propeller spacing $0.035D_p$.

(b) Downwash angle distribution with propeller spacing $0.1D_p$.

Figure 3.15 – Effect of propeller spacing on the downwash angle $\alpha_i = w_i/V$ distribution for $\alpha = 25°$

As one can expect, the sharp lift variation in the spanwise direction results in large spikes in downwash angle. These are visible in Fig 3.15, where the downwash angle distribution is illustrated.

The corresponding lift versus drag curves are plotted in Fig 3.16. The higher propeller spacing shows a shift in the drag polar towards the right at high lift and increasing with T_c.

Based on the comparison with TND4448 data, it appears that the slipstream are merging in this example therefore the wing panels are adjusted such that all panels are within a propeller slipstream.

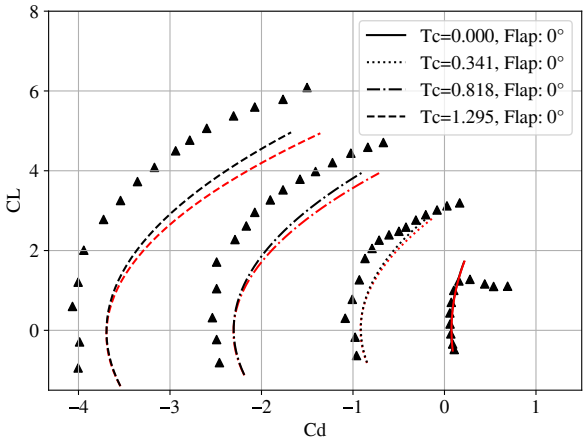

Figure 3.16 – Lift versus drag in black with propeller spacing $0.035D_p$ and in red with propeller spacing $0.1D_p$.

This feature is however entirely dependent on the understanding of the user as it is should be manually set and at the time of writing, no advice can be given to judge when slipstreams can be considered merging and when not.

In the report TND-1586, a half wing with one engine and propeller placed at the centre of the half wing is studied. A full span flap is present and deflected by 20°. This flap deflection being more reasonable, it is taken into consideration for validation of the extended Patteron model. No manipulation of the clean wing lift slope has been found necessary in this case to have a good agreement in unblown conditions. The comparison between experimental data and the model is available in Fig 3.17.

For the configuration with flap at 0°, in fig 3.17a the lift increase and lift slope increase is again correctly captured up to the stall limit. The highest thrust coefficient showing the largest deviation. In fig 3.17b, the lift versus drag polar shows

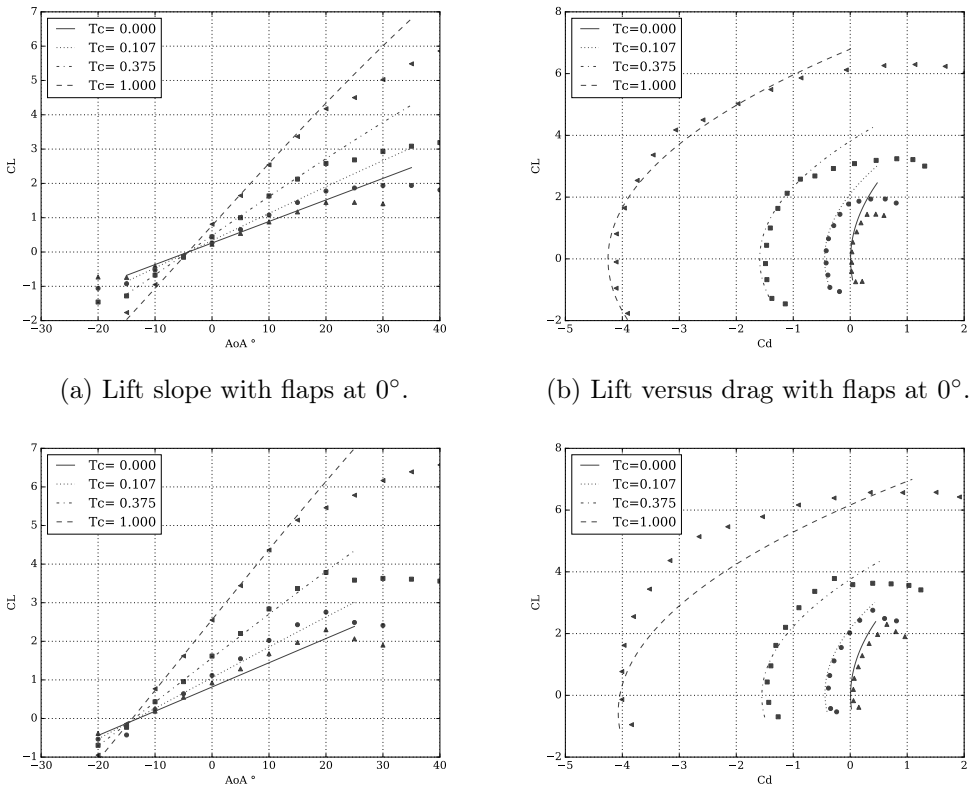

(a) Lift slope with flaps at 0°.

(b) Lift versus drag with flaps at 0°.

(c) Lift slope with flap at 20°.

(d) Lift versus drag with flap at 20°.

Figure 3.17 – Comparison of the extended Patterson model against TND-1586 experimental data. Markers: wind tunnel data, lines: extended Patterson model.

a good agreement, without the constant offset observable with the data from TND-4448. In this configuration, the drag estimation can be considered reliable for control purposes up to $T_c = 1.0$.

Fig 3.17c and Fig 3.17d, show the same results with flap deflected at 20°. Although more approximative, the lift increase and lift slope increase remain well approximated for all thrust coefficients. As for the drag estimate, there is a degradation in the accuracy especially at $T_c = 1.0$ although at $T_c = 0.375$ the drag polar already starts to deviate from the data points.

One reason for this deviation, could be an interaction with a stronger wingtip vortex due to the deflection of the flap. The propeller tip stops exactly at the wingtip in TND-1586. At high thrust coefficient, therefore high disk loading, an important interaction between the slipstream swirl and the wingtip vortex can take place. With the propeller model used in this methods, the swirl is neglected and

cannot estimate this effect.

Based on the comparison of the prediction of the extended model and the experimental data, one can conclude that:

— The Patterson method extended to the use of flap and aileron in the linear regime can give correct lift and drag estimation for thrust coefficient at least up to $T_c = 0.375$ and flap or aileron deflection at least up to 20°.

— These conclusions are valid in the case where a significant part of the wing is immersed in slipstream.

3.4.2 Evaluation against flight data

The Part IV of this thesis details the experimental work realized with a small scale DEP aircraft equipped with eight engines. As flight data became available, an additional way to verify the aero-propulsive model with flight data was studied. This is reported in this section as it is a complement to the extended model validation. The reader is referred to Chapter 9 for a detailed description of the small scale demonstrator DEmonstrateur COntrol Latéral, (Lateral Control Demonstrator) (DECOL). An idea was suggested by Kimberlin in [Kimberlin 2003]. The lift and drag coefficients of a powered lift aircraft are function of the thrust coefficient. The performances are estimated through an airspeed-flight path angle diagram (V_a - γ_a) with the underlying assumption that for a given thrust setting, the flight path angle is function of airspeed only.

The idea is to compare the measured and predicted flight path angle in a series of steady climb manoeuvres. The results of the extended Patterson model will be compared with the baseline VLM aerodynamic database and the original lift increase method of Patterson. This test allows to estimate the relevancy of each model to represent the aerodynamic forces without calculating the drag from flight data, a task that is difficult to accurately complete with a small scale demonstrator.

This can be formalized mathematically using the equation for excess thrust T_{ex} and the equation for lift in a steady climb [Kimberlin 2003]:

$$T_{\text{ex}} = T_x^a - D = mg \sin \gamma_a \,, \tag{3.39}$$

$$L = W \cos \gamma_a \,. \tag{3.40}$$

It is possible to isolate γ_a as:

$$\tan\gamma_a = \frac{T_x^a}{\frac{1}{2}\rho S V_a^2 C_L} - \frac{C_D}{C_L}\,, \tag{3.41}$$

and use the second equation to express the lift coefficient as:

$$\frac{C_L}{\cos\gamma_a} = \frac{mg}{\frac{1}{2}\rho S V_a^2}\,. \tag{3.42}$$

In equation (3.41), the climb angle depends on the thrust, the airspeed and the aircraft polar. Airspeed is measured directly on board the aircraft through the dynamic pressure probe. The thrust can be determined from the measurement of engine rotation rates, the airspeed and the propeller model.

Remains only the polar, $C_L(\alpha)$ and $C_D(\alpha)$ that can be computed by the three models with the thrust coefficient deduced from the airspeed and the thrust. Knowing this, it is possible to find a set of $\gamma_a(\alpha)$ function of the angle of attack using the interaction model and equation (3.41). The value corresponding to steady climb is then found by finding the pair of C_L and γ_a satisfying equation (3.42).

The climb angle is computed from flight data using the assumptions that the wind is uniform and an additional assumption was made that the vertical component of the wind in the NED frame, w_w^o, is zero. The climb angle is hence determined from flight data using equations (1.8) and (1.9):

$$\sin\gamma_a = \frac{w_a^o}{V_a}\,, \tag{3.43}$$

$$\begin{pmatrix} u_a^o \\ v_a^o \\ w_a^o \end{pmatrix} = \begin{pmatrix} V_N \\ V_E \\ -V_Z \end{pmatrix} - \begin{pmatrix} u_w^o \\ v_w^o \\ w_w^o \end{pmatrix}\,. \tag{3.44}$$

$$\tag{3.45}$$

Assuming $w_w^o = 0$:

$$\gamma_a = \arcsin\frac{-V_Z}{V_a}\,, \tag{3.46}$$

where V_Z is given by the IMU from inertial and GNSS measurements and V_a is deduced from the dynamic pressure measured at the fuselage tip. The thrust is

determined directly from the propeller model.

The procedure is summarised in the following steps:

1. Flight test are realized with steady climb manoeuvres at different power level and velocity.
2. Flight data are filtered to extract quasi-static flight period in steady-climb.
3. From these periods, aerodynamic climb angle, airspeed and engine rotation rates are extracted.
4. The lift versus drag polar is calculated for the thrust coefficient defined by the airspeed and the thrust.
5. For each point of the polar, the corresponding flight path angle is computed using equation (3.41).
6. Equation (3.42) is solved with the tabulated value of $C_L(\alpha_a)$ and $\gamma_a(\alpha_a)$.

To assess the gain in accuracy allowed by the extended Patterson method with respect to the other methods, the climb angle is computed using the following three models:

— Polar obtained from VLM, fig 3.18a and 3.19a

— Lift increase only, fig 3.18b and fig3.19b

— Lift and drag increase, fig 3.18c and 3.19c

The predicted γ_a is plotted as a function of the measured γ_a, hence the closer the marker is from the $y = x$ dashed line, the better the model agrees with flight data.

The extended Patterson model gives a better agreement between the predicted climb angle and measured one especially at high climb angle, where the thrust coefficient and interactions are the most important. At climb angles lower than $\gamma_a = 5°$, the difference is not significant and for negative climb angles, the method is extrapolated to negative thrust (propeller windmilling).

Data points used to compare the climb angle are flight points where the accelerations are sufficiently low to be considered steady climbing flight. Each marker in Fig 3.18 and Fig 3.19 represents a series of flight data points. The analysis of the model performance can therefore be enhanced by statistical analysis. Negative flight path angles being inaccurately predicted (due to extrapolation to negative thrust), the statistical analysis was limited to positive flight path angles. After extracting points with positive climb angles a total of 80 and 95 points respectively are available for each flight.

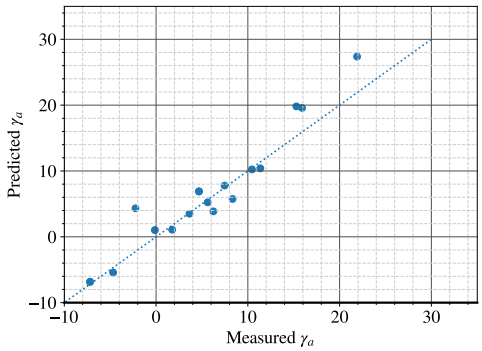

(a) Flight 1: no interaction, original polar.

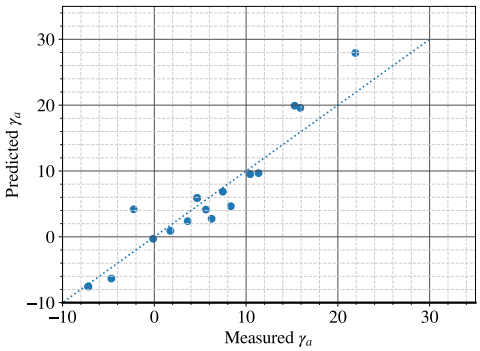

(b) Flight 1: lift increase applied only.

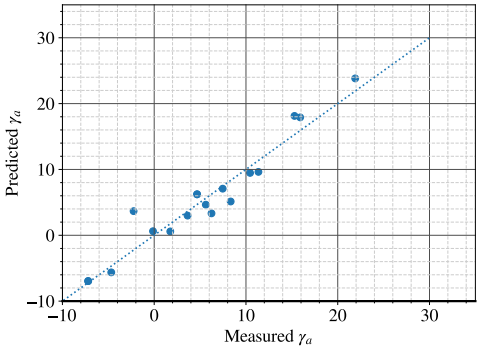

(c) Flight 1: lift and drag increase.

Figure 3.18 – Comparison of predicted flight path angles with different models and compared with flight data point collected with DECOL. The dashed line is $y = x$. Flight 1.

The root mean square of the error between the predicted γ_a and the measured one for the three models are compared. Additionally, a linear least square fit is calculated between measured and predicted values. These quantities are shown in Table 3.2.

The mean error is shown to be lower when using the full interaction. The highest error being obtained when using the lift increase only. It seems reasonable as the increase of lift without taking into account the drag penalty results in overestimated the lift to drag ratio and consequently overall aircraft performances. The least square fit should be closer to 1 or y=x, to be more accurate. It is shown that the full interaction model performs better for both flights with similar R^2 value indicating a good estimation between the fit and the data for all models.

On the point of view of control effort, one can assume that the interaction efforts will be low or of second order of importance during a rather long part of the

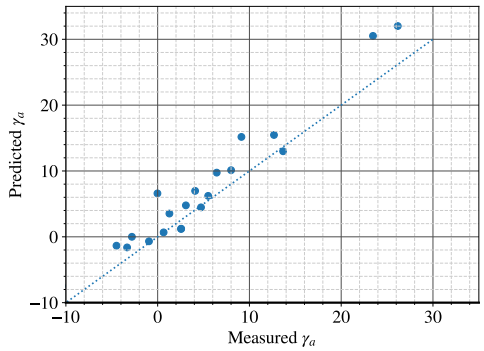

(a) Flight 2: no interaction, original polar.

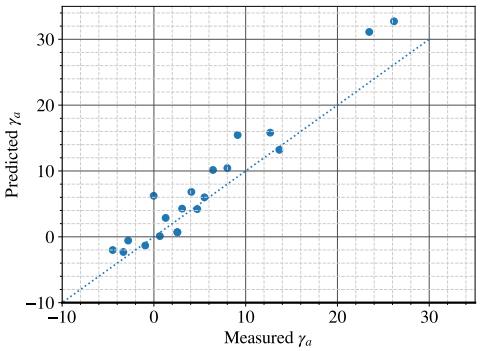

(b) Flight 2: lift increase only.

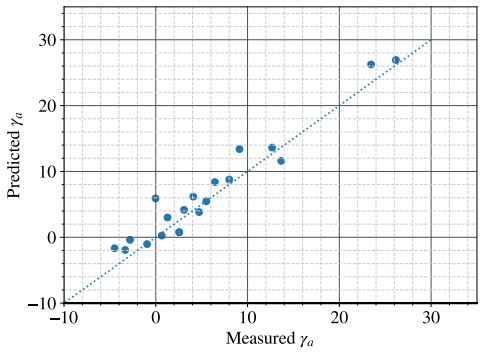

(c) Flight 2: lift and drag increase.

Figure 3.19 – Comparison of predicted flight path angles with different models and compared with flight data point collected with DECOL. The dashed line is $y = x$. Flight 2.

flight. At high velocity and low thrust coefficients, interactions could be neglected in the computation of the control laws and may be taken as external disturbances. At high thrust coefficient, rather low velocity, the results show that interactions increase rapidly with the thrust coefficients. This justifies the effort to include these efforts for studying flight conditions at low velocity.

3.5 Conclusion on Aero-propulsive Interactions

In this chapter, the aero-propulsive interactions arising when a propeller is placed at the leading edge of a wing were studied. The physical phenomena at play in this particular aero-propulsive interaction were explained and it was shown that propeller-wing interaction are composed of propeller forces and slipstream effects on the wing. It was found from the literature that propeller forces can be neglected

Table 3.2 – Statistical analysis between the predicted and the flight measured γ_a, for data point where $\gamma_a > 0°$.

	No interaction	Lift increase only	Lift and drag increase
Flight 1 mean error	$3.10° \pm 0.11°$	$3.89° \pm 0.14°$	$2.32° \pm 0.07°$
Flight 1 slope fit	1.142	1.173	0.994
Flight 1 r-squared fit value	0.997	0.996	0.992
Flight 2 mean error	$2.84° \pm 0.08°$	$3.00° \pm 0.10°$	$1.94° \pm 0.06°$
Flight 2 slope fit	1.322	1.36	1.163
Flight 2 r-squared fit value	0.934	0.931	0.942

in the case of distributed propulsion because of the low solidity and disc loading obtained when distributing power across a larger propeller area. On the contrary, it was found that the effect of slipstream on the wing is non negligible and it was decided to model this effect (see section 3.1).

Three types of model, in the order of complexity were reviewed. A low fidelity model was selected and enhanced with an estimation of the additional drag arising from the lift increase and the addition of flap and aileron. This choice was justified by the fact that a fast method to estimate interaction effect on various aircraft geometry and propulsion distribution was needed (see section 1.3 and 3.3).

This enhanced model was evaluated against experimental data available in the literature and flight data produced by the flight demonstrator DECOL. It gave satisfactory estimates for the usage that is considered in this thesis.

A knowledge of propeller-wing interaction and a tool to estimate the global effect of propeller-wing interactions on the aircraft flight dynamics were built. This tool will be the standard tool to evaluate the effect of propeller wing interaction for the rest of the study.

Chapter 4

Flight envelope study

Contents

The tools developed prior to this chapter are now used to compute the flight envelopes of the DEP ATR72 aircraft and compare it to the traditional twin engine ATR72 which is studied as a reference. The goal is to determine the flight conditions for sizing the VT of a DEP aircraft.

In addition to this first goal, it is desired to assess the influence of aero-propulsive interactions on the flight envelope of DEP aircraft at low speed. The question

to answer is: can aero-propulsive interaction be neglected in the determination of aircraft static stability?

Both questions are answered throughout the chapter: the means of demonstration of directional static stability and control requirements as well as the major consequences of aero-propulsive interactions are then gathered in the chapter's conclusion.

The framework detailed in Chapter 1 is used to generate the results presented in this section. First, introductory remarks such as the format used to present the results, are announced in section 4.1. The reference twin-engine ATR72 is studied in presence of OEI at take-off in section 4.2. The impact of aero-propulsive interactions on flight performances later largely influence the organization of this chapter.

A detailed investigation of the flight performances of the original twin-engine ATR72 using aero-propulsive interaction is given in section 4.3. The knowledge gained is then used in a bottom-up approach to configure the DEP aircraft and determine the flight conditions for evaluating the DEP ATR72 directional characteristics in section 4.4. Finally, the effect of reduced vertical tail on the directional flight envelope of a DEP aircraft can be established in section 4.5.

4.1 Introductory remarks

In this section, the performance indicators that will be followed throughout the analysis of the twin-engine and DEP ATR72 are defined.

The analysis is placed in the context of vertical tail sizing for directional static stability and control requirements. More specifically, the conditions specified in the EASA certification specifications paragraph CS25.121, CS25.147 and CS25.149 are used to define the requirements on flight path angle, directional control and minimum control speed V_{mc}, in case of one or multiple engine failures. The requirements are split between longitudinal flight performance and directional control.

4.1.1 Longitudinal performance requirement

For longitudinal flight performances, the most critical flight path angle to maintain during the take-off path (CS 25.121) is 3% for aircraft with four engines or more. Although it is lower for twin-engines, the same 3% requirement is used for the original ATR72 and the DEP version.

4.1.2 Directional requirements

The typical lateral and directional requirements that size the vertical tail are:

— a static stability requirement fixed by the minimum control velocity V_{mc},

— directional controllability requirement for cross wind flight.

The regulation fixes minimum values for each of these requirements:

1. CS25.149 establishes a V_{mc} not less than $1.13V_{sr}$, where V_{sr} is the 1g reference stall speed with engines idling and an angle of roll no more than 5°.
2. CS25.147 specifies that: "*It must be possible with the wings level, to yaw into the operative engine and to safely make a reasonable sudden change in heading of up to* 15°", in level flight at $1.3V_{sr}$ with one to two critical engines inoperative,
3. CS25.237 sets the maximum cross wind to withstand to 25kt or 12.8 m/s without mention of powerplant failure.

Although CS25.147 specifies a minimum heading change, this condition is rarely used as a design criterion [Obert 2009], [Torenbeek 1982], [Nicolosi 2017]. It is assumed to follow from the V_{mc} sizing criterion [Klunk 2018a], probably relying on the fact that aerodynamic forces arising from the vertical tail increase quadratically

with airspeed, while the thrust decreases linearly with airspeed. The cross wind flight criterion is evaluated independently without consideration of engine failure. This methodology applied for DEP aircraft with differential thrust can be questioned since the directional control power is expected to be inversely proportional to airspeed.

With a reference stall of $V_{sr} = 50.9$ m/s at MTOW, CS25.237 translates as a constant side slip of 11.1° at $1.3V_{sr}$, below the control requirement stated by CS25.147. The latter one being more constraining, CS25.237 is assumed to follow from CS25.147.

The region of interest in the flight envelope relative to the two selected requirements are:

— The minimum trimmable velocity that may be limited by V_{sr} or V_{mc}, referred herein as directional static stability requirement,

— $1.3V_{sr}$ where a minimum of ±15° of side slip should be available, referred herein as controllability requirement,

all of which are considered in presence of one or many motor failures. It should be emphasized that the failure of a motor does not imply the failure of a device producing power on-board the aircraft. With an architecture physically decoupling engines (producing the power) and motors (converting electrical power to mechanical power), it could be possible to reallocate entirely the power on the remaining motors. In this study, since the motors are not allowed to be overloaded, this option is not considered. To be more specific, it will be refer to the loss of motors instead of engines for the DEP version of the ATR72.

4.1.3 Indications for reading flight envelope maps

Flight envelope maps are presented under the form of a grid where each box represents a flight point (this form is inspired by the work of Goman in [Goman 2008]). The presence of a green marker in a box signifies that an equilibrium was found. If this point is on the edge of the equilibrium map, a line shows the limiting parameter. It can be the 5° limitation in roll, stall or rudder saturation.

Additionally, for flight envelope maps with varying flight path angle γ_a, a fixed dashed line represents the minimum 3% climb angle required by certification regulation in case of motor failures.

For distributed propulsion, motor saturation is indicated with different markers. A rectangular marker signifies that one motor is saturated, up-triangle two motors,

down triangle three motors, left triangle four motors and finally right triangle five motors and more. An motor is assumed saturated when it reaches 97.5% of its continuous rated power. Additionally, the complete zone after $\|\beta\| \geq 15°$ is faded, signifying that any equilibrium is valid under the condition that the VT did not yet experience stall.

4.2 Twin-engine ATR72 flight envelope maps at take-off

In this section, the aerodyamic database and interaction model developed in Chapter 2 and Chapter 3 respectively, are used to generate the flight envelope maps of the reference twin-engine aircraft in side slip and airspeed, designated as $\beta_a - V_a$ flight envelopes. The goal is to assess the results that are possible to obtain with the framework and the tools developed in the previous chapters. The flight envelopes obtained with the two aerodynamic models are compared here:

1. **A/C with simple aerodynamics**, determined with VLM simulations in Chapter 2, without aero-propulsive interaction.
2. **A/C with aero-propulsive interactions**, calculated with the model developed in Chapter 3.

The flight conditions corresponding to a OEI at take-off are described in Table 4.1.

The aircraft with aero-propulsive interactions is analysed at a 0% flight path angle because it could not be trimmed with a 3% climb gradient. The situation is discussed in detail in section 4.2.2.

The flap deflection and reference airspeed are taken from the ATR flight crew manual ([aircraft 2000]). They are adapted to the indicated mass in normal non-icing conditions. Additionally, in the event of OEI, the aircraft crew manual indicates that airspeed should be maintained within: $1.13V_{\text{sr}} \leq V_a \leq 1.13V_{\text{sr}} + 10\text{kts}$. The aircraft should therefore be trimmable from $1.13V_{\text{sr}}$ while climbing.

For the two aerodynamic models, the stall angle is set such that the aircraft stall velocity matches the ATR72's V_{sr} without accounting for the additional lift coming from wing blowing.

An observation should be made about the rudder efficiency used in this comparison: the ATR72 is a stretch of the ATR42 and the two aircraft share a certain amount of parts. The vertical tail is one of the common parts ([Jackson 2014], [Nita 2008]), which gives the ATR72 an excellent flight envelope at low speed. To

Table 4.1 – Aircraft Configurations, reference velocities are taken from the ATR's crew manual [aircraft 2000].

Description	Twin-engine ATR72, simple aerodynamic	Twin-engine ATR72, aero-propulsive interactions
Design parameters		
Continuous power	4.1MW	
Engines	2	
VT area	S_{v_0}	
Rudder efficiency	$\tau_r = 0.3$	
Propeller	Feathered, no drag assumed if inoperative.	
Flight conditions		
Inoperative engine	1	
Climb gradient	3%	0%
Turn rate, Ω (rad/s)	0	
Mass	21.5 T	
Flap deflection	15°	
V_{sr}	50.9 m/s	
$1.13V_{\text{sr}}$	57.5 m/s	
$1.3V_{\text{sr}}$	66.2 m/s	

illustrate the problematic of vertical tail sizing, the efficiency of the rudder τ_r is artificially lowered by 50% [1]. The $\beta_a - V_a$ flight envelope maps of the twin-engine ATR72 presented in this section are not representative of the real performances of the aircraft and are here for comparison only.

4.2.1 Original twin-engine ATR72 with simple aerodynamics

The baseline ATR72 is presented in Fig 4.1a and the trim inputs at $1.3V_{\text{sr}}$ in Fig 4.1b.

The climb gradient is slightly unfavorable for this configuration, nevertheless even with a rudder efficiency reduced by 50%, it is the stall that limits the lower part of the flight envelope. This means that V_{mc} is well contained below V_{sr}. At $1.13V_{\text{sr}}$ and $1.3V_{\text{sr}}$, the flight envelope is comfortable with at least $\beta = \pm 10°$. The 15° side slip at $1.3V_{\text{sr}}$ is just reached. It seems that a sufficient controllability is available at $1.3V_{\text{sr}}$ if V_{mc} is below V_{sr}.

1. It should be noted that resizing the VT for the same volume ratio than the ATR42 is another solution to illustrate the problem.

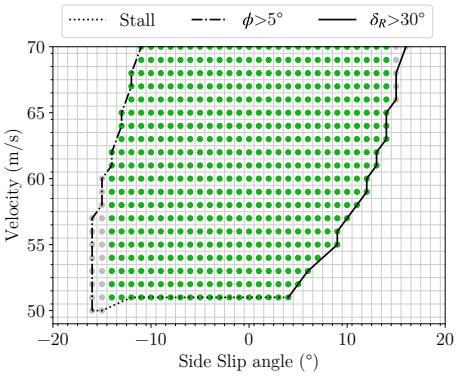

(a) Original ATR72, flight envelope.

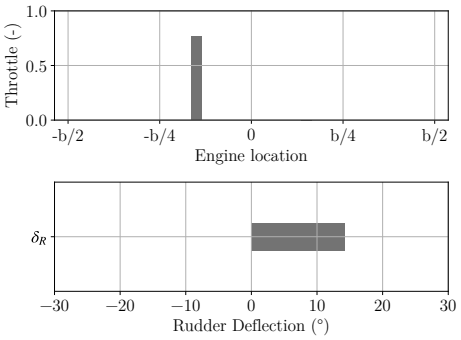

(b) Throttle level and rudder deflection at $1.3V_{\text{sr}}$ and $\beta = 0°$.

Figure 4.1 – Flight envelope of the original twin-engine ATR72 with simple aerodynamics.

The limiting parameters for the flight envelope are the bank angle limitation for negative side slip and rudder deflection for positive side slip.

4.2.2 Original twin-engine ATR72 with aero-propulsive interaction

Fig 4.2 shows the flight envelope of the twin-engine ATR72 with aero-propulsive interaction.

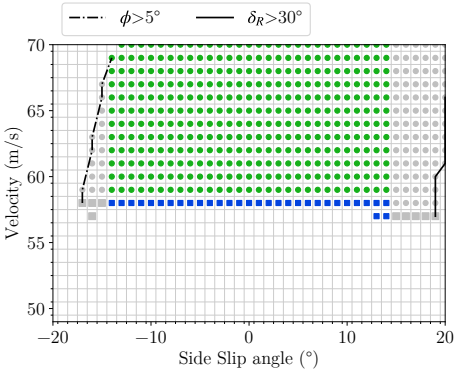

(a) Flight envelope.

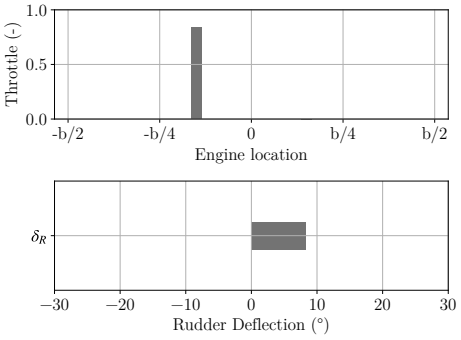

(b) Throttle level and Rudder deflection at $1.3V_{\text{sr}}$ and $\beta = 0°$.

Figure 4.2 – Original twin-engine ATR72 with interaction, climb gradient reduced to 0%.

Aero-propulsive interactions change the aircraft polar by increasing both lift and drag. When used with a twin-engine configuration, it was found that the aircraft could not be trimmed to reach a 3% climb angle. It was decided to investigate the

$\beta_a - V_a$ flight envelope at a zero flight path angle.

When comparing with Fig 4.1a, the flight envelope is wider and the rudder deflection is less for the same flight settings. Additionally, it is not the stall velocity that sets the lower trimmable speed limit but the engine saturation.

This first comparison brings questions about the aero-propulsive model, as it was not possible to trim the aircraft for a positive climb angle in an OEI event while the original aircraft is certified according to the EASA regulation. It seems that the aero-propulsive model under-estimates the longitudinal performance of the aircraft. This result was expected because the aero-propulsive model was not developed to this aim. The importance of the change comes however as a surprise and calls for more analysis before studying the DEP aircraft. It is the objective of the next section.

4.3 Investigation on the reduction of flight envelope induced by aero-propulsive interactions

This section aims at explaining the rather unexpected reduction of longitudinal flight performance caused by aero-propulsive interactions.

There are two main questions to be answered:

1. Is the aero-propulsive model sufficiently accurate for the study?
2. Has the problem been addressed from the correct point of view?

Question **1** is raised by the limited longitudinal performance of the twin-engine aircraft using the aero-propulsive interaction while the model has been validated against experimental data. The validation process showed a limited accuracy in the estimation of drag when flaps are deployed but no deviation that can explain the difference in performance. Part of the problem can be that the accuracy of the aero-propulsive model for twin-engine aircraft, where the wing is not fully embedded in the propeller slipstreams was not assessed during the validation of the model. In this condition, it is not possible to take the results presented in section 4.2.2 as representative. For DEP aircraft the interaction model was validated but the longitudinal performance should be compared to the twin-engine with simple aerodynamics. If an important deviation persists, particularly the impossibility to maintain a 3% flight path angle with motor failures, the aero-propulsive model may be rejected for the rest of the study.

Question **2** discusses the decision made in section 4.2 to assess the directional static stability and control capability at constant and predetermined longitudinal flight conditions. This resembles the traditional vertical tail design practices, where it is assumed that the maximum remaining thrust in OEI ensures a sufficient flight path angle. With the aero-propulsive interactions affecting primarily the longitudinal trim conditions, shouldn't the longitudinal performances with aero-propulsive interactions be assessed first, in order to deduce the flight condition in which the directional static stability and control requirements have to be analyzed?

To answer these questions, the longitudinal flight performances will be investigated and estimated through $V_a - \gamma_a$ flight envelope maps. The same reading advice as described in section 4.1.3 hold. In addition, the linearisation technique described in Chapter 1, section 1.6, is employed to extract the motor efficiencies.

The focus remains the twin-engine ATR72 aircraft with simple aerodynamic and interaction for the moment. The flight conditions for the generation of $V_a - \gamma_a$ flight envelope are summarised in Table 4.2. For the two versions, all motors operative and OEI scenario are considered.

4.3.1 Twin-engine ATR72 $\gamma_a - V_a$ flight envelope maps.

The $V_a - \gamma_a$ flight envelopes of the ATR72 with simple aerodynamics are shown with all engines operative in Fig 4.3a and with OEI in Fig 4.3b. The maximum climb angle at $1.13V_{\text{sr}}$ goes from 11° for all engines operative to 3° in OEI. The aircraft is capable of maintaining a 3% flight path and the rudder saturation is visible with OEI at flight path angle larger than 3%.

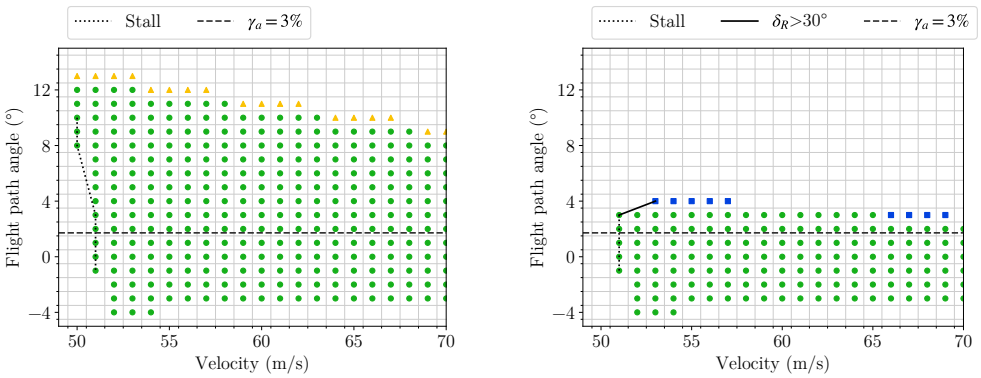

(a) All engines operative.

(b) Right engine inoperative.

Figure 4.3 – Twin engine ATR72 $V_a - \gamma_a$ flight envelope map, without interaction.

Table 4.2 – Flight condition and configuration for the $V_a - \gamma_a$ flight envelopes of the twin-engine ATR72.

Description	Twin-engine, simple aerodynamic	Twin-engine, simple aerodynamic	Twin-engine, aero-propulsive interaction	Twin-engine, aero-propulsive interaction
Design parameters				
Continuous power	4.1MW			
Engines	2			
VT area	S_{v_0}			
Rudder efficiency	$\tau_r = 0.3$			
Propeller	Feathered, no drag assumed if inoperative.			
Flight conditions				
Inoperative engine	0	1	0	1
Side slip	0°			
Turn rate, Ω (rad/s)	0			
Mass	21.5 T			
Flap deflection	15°			
V_{sr}	50.9 m/s			
$1.13V_{\text{sr}}$	57.5 m/s			
$1.3V_{\text{sr}}$	66.2 m/s			

Fig 4.4a shows the $V_a - \gamma_a$ flight envelopeof the ATR72 with aero-propulsive interactions and all engines operative. The complementary OEI case is shown in Fig 4.4b. For both maps, powered lift is visible as the aircraft is trimmable at velocities lower than V_{sr}. The maximum flight path angle at $1.13V_{\text{sr}}$ and all engines operative is reduced to $\gamma_a = 6°$.

Fig 4.4a and Fig 4.4b both show a flight envelope that shrinks with decreasing airspeed. This suggests that the induced drag deduced from interaction rises faster than the engine thrust with decreasing velocity. This tendency and the predicted low speed climbing performance can be discussed for the twin-engine ATR72 as suggested at the end of section 4.2.

For the OEI scenario with aero-propulsive interaction, the flight envelope shows a climbing capability lower than 1°, not satisfying the 3% flight path requirement. The step size of 1° does not allow to visualize the engine saturation but this is the limiting parameter. The maximum climb performance is reduced from 6° with both engines operational to 0° in OEI.

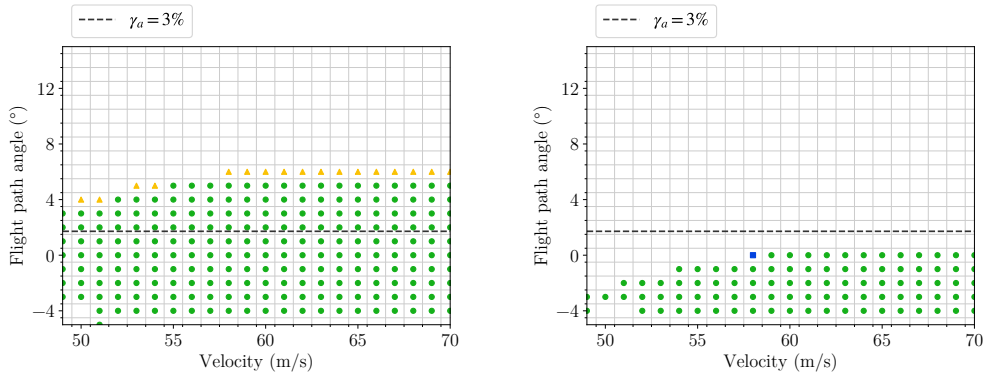

(a) All engines operative. (b) Right engine inoperative.

Figure 4.4 – Twin engine ATR72 $V_a - \gamma_a$ flight envelope map, with interaction.

From these observations one may suppose that the aero-propulsive interactions have a non-linear evolution with velocity or thrust level. To verify this information, it is possible to observe the evolution of the engine efficiency with the airspeed. The thrust model being known and linear, it would be simple to evaluate a deviation from linearity.

4.3.2 Engine efficiencies in presence of aero-propulsive interaction.

The engine efficiencies calculated using the simple aerodynamic model and the interaction model for the twin-engine configuration are compared in this section. Engine efficiencies are extracted by linearization after trimming the system. The thrust efficiency is measured by the term $\frac{\partial \dot{V}}{\partial \delta_{x,i}}$. The efficiency at yawing with differential thrust is measured by the term $\frac{\partial \dot{r}}{\partial \delta_{x,i}}$. The aircraft is trimmed for level, symmetric flight conditions and airspeed varying from V_{sr} to 90 m/s.

The evolution of the thrust efficiency is presented in Fig 4.5a and the yawing efficiency is presented in Fig 4.5b.

Fig 4.5a and Fig 4.5b, both show a large reduction in engine efficiencies, observed with the aero-propulsive model and explaining the reduction in flight envelope. In both figures, two regions can be identified, separated by the discontinuity in the interaction curve. This discontinuity is due to the flaps, which are deployed up to 71 m/s according to the ATR72 crew manual. At airspeed higher than 71 m/s, the two curves show a converging trend. The thrust efficiency $\frac{\partial \dot{V}}{\partial \delta_{x,i}}$ obeys an inverse decrease, depicting the inverse relationship between propeller thrust and airspeed. At airspeed slower than 71 m/s, the interaction curves have a highly non-linear

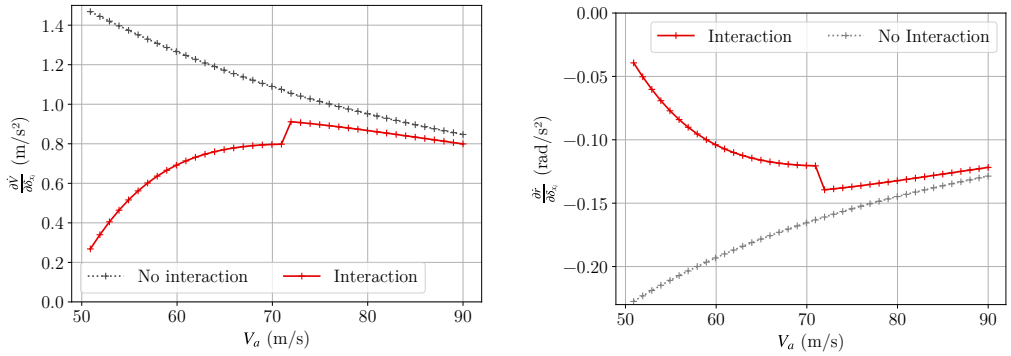

(a) $\frac{\partial \dot{V}}{\partial \delta_{x,i}}$. (b) $\frac{\partial \dot{r}}{\partial \delta_{x,i}}$.

Figure 4.5 – Engine efficiencies on the twin-engine ATR72.

evolution, depicting the predominance of aero-propulsive interactions in this region.

The additional observation that can be made with Fig 4.5a and Fig 4.5b is the important contribution of the flap deployment in the reduction of performance. This reduction may be the reason of the limited performance compared to the simple aerodynamic model. The accuracy of the prediction at velocities lower than 71 m/s is likely to be low. The effect of interactions being probably over-predicted.

Although, the reduction in thrust efficiency may be explained by the fact that a flap deflection would bend the propeller slipstream and transform a large part of the thrust into a lift, the principal source of error is believed to be the the drag estimation of the combination of an isolated and highly loaded propeller and a flap deflection.

Nevertheless, a good knowledge of the impact of interactions on longitudinal flight performances is gained through this top-bottom analysis. It is now possible to reverse the procedure and use a bottom-up approach, starting with engine efficiencies, to define a flight condition at which a DEP aircraft should be analyzed. The next section starts with the determination of engine efficiencies of the DEP aircraft with different flap settings in order to determine the most appropriate.

4.4 Establishing the reference configuration and flight condition for DEP aircraft

The principal idea followed in this section is to reverse the approach used in the previous section to answer two objectives. First, to investigate the validity of the

results obtained using the aero-propulsive interaction model with a DEP aircraft. The second is to define a flight configuration specific to this aircraft, for evaluation of directional static stability and control requirements. The starting point of this bottom-up approach is hence, the motor efficiencies.

Table 4.3 – Flight configuration and conditions for the DEP ATR72 motor efficiency study.

Description	DEP 1	DEP 2	DEP 3
Design parameters			
Continuous power		4.1MW	
Engines		12	
VT area		S_{v_0}	
Rudder efficiency		$\tau_r = 0.3$	
Flight conditions			
Inoperative motors		0	
Side slip		0°	
Flight path angle		0°	
Turn rate, Ω (rad/s)		0	
Mass		21.5 T	
Flap deflection	15°	7.5°	0°

4.4.1 DEP, motors efficiencies

Fig 4.5a and Fig 4.5b have shown that the deployment of flaps, a high lift device, worsen motor efficiencies. For DEP aircraft, wing blowing is already a high lift system. With the results observed previously, the deployment of flaps seem not recommended to maintain motor efficiencies at low speed. An investigation is made in this section in order to determine the correct flap deflection if any, for DEP aircraft.

Engine efficiencies are computed for the DEP aircraft in the conditions described by Table 4.3 with flap settings of 15°, 7.5° and 0°. The idea is not to determine the optimal flap setting but to determine if a reduced deflection or no deflection at all should be considered.

Engines efficiency are plotted in the 3D Figures 4.6 to 4.8, each figure gathers motor number 7 to 12, corresponding to the motors located on the right wing. For comparing the thrust capability, the thrust efficiency of one equivalent motor without interactions is shown. For yawing moment capability, each motor efficiency is compared with its equivalent without interaction.

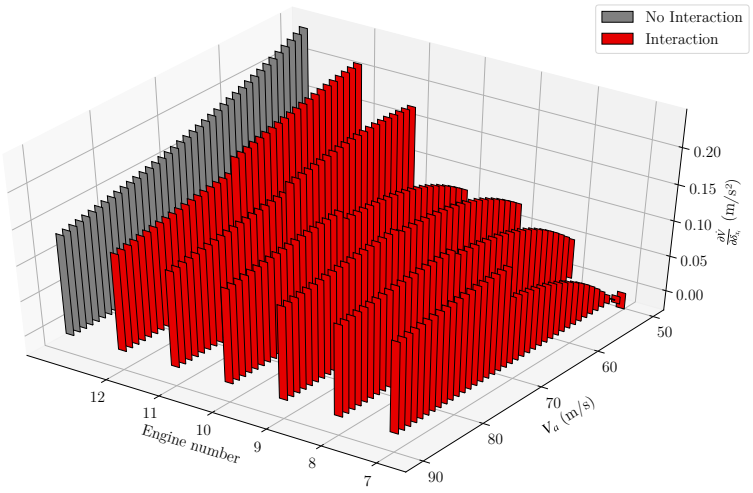

(a) $\frac{\partial \dot{V}}{\partial \delta_{x,i}}$ at 15° flap deflection.

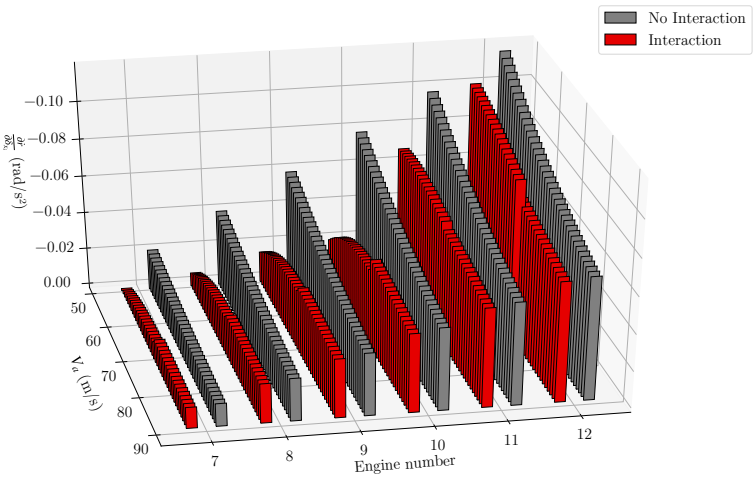

(b) $\frac{\partial \dot{r}}{\partial \delta_{x,i}}$ at 15° flap deflection.

Figure 4.6 – Engine efficiencies on the DEP ATR72 at 15° flap deflection.

Engines thrust efficiency are represented in Fig 4.6a, Fig 4.7a and Fig 4.8a. The flap deflection is visible in Fig 4.6a and Fig 4.7a through the the discontinuity at 71 m/s. In these two figures, at V_{sr}, motors 11 and 12 are at least 50% more efficient than the other motors and have an overall efficiency reduced by no more than 25% compare to the simple aerodynamic case.

At zero flap deflection, Fig 4.8a shows a more regular decrease in motor thrust efficiency even though the global efficiency of motor 11 and 12 are reduced to two third of their efficiency without interaction. With increasing velocity, motors recover their efficiencies up to the point where it is almost similar to ones with simple

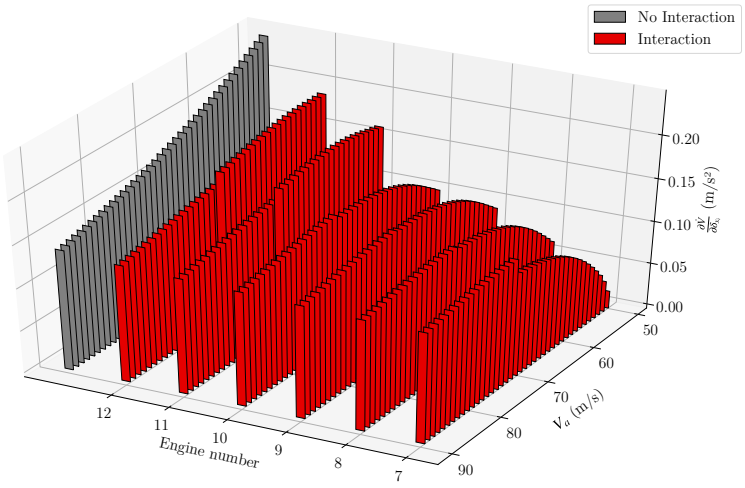

(a) $\frac{\partial \dot{V}}{\partial \delta_{x,i}}$ at 7.5° flap deflection.

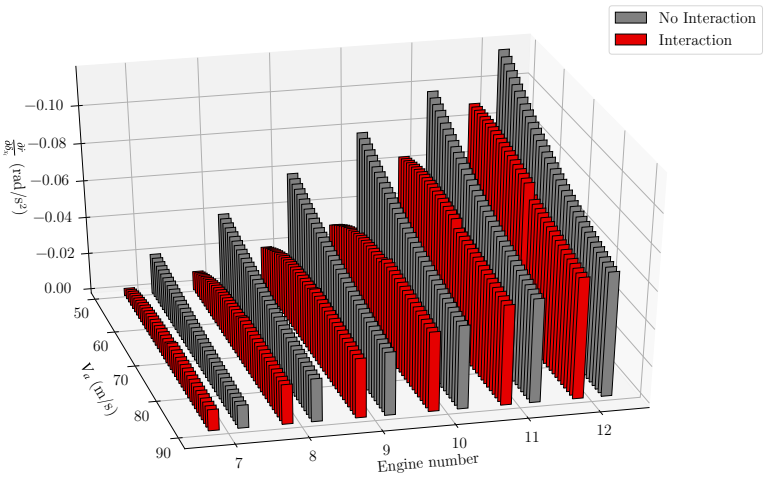

(b) $\frac{\partial \dot{r}}{\partial \delta_{x,i}}$ at 7.5° flap deflection.

Figure 4.7 – Engine efficiencies on the DEP ATR72 at 7.5° flap deflection.

aerodynamics.

A non-linear behaviour in efficiencies is mostly observed on the inner motors 7 to 10, positioned in front of the flap. A reduction of flap deflection to 0° lowers the velocity at which interactions become predominant and preserves the efficiency of motors 7 to 10 at lower airspeed.

The same tendency is observed for the yawing moment capability in Fig 4.6b, Fig 4.7b and Fig 4.8b. Motor 11 and 12 having the highest level arm, they become the key actuators for yawing, if one uses a flap as high-lift device.

In the consideration of motor loss, the outer motors are the most critical for

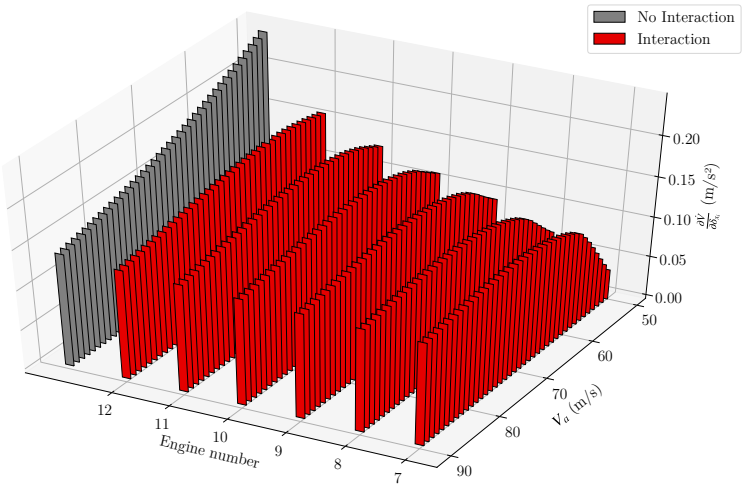

(a) $\frac{\partial \dot{V}}{\partial \delta_{x,i}}$ at 0° flap deflection.

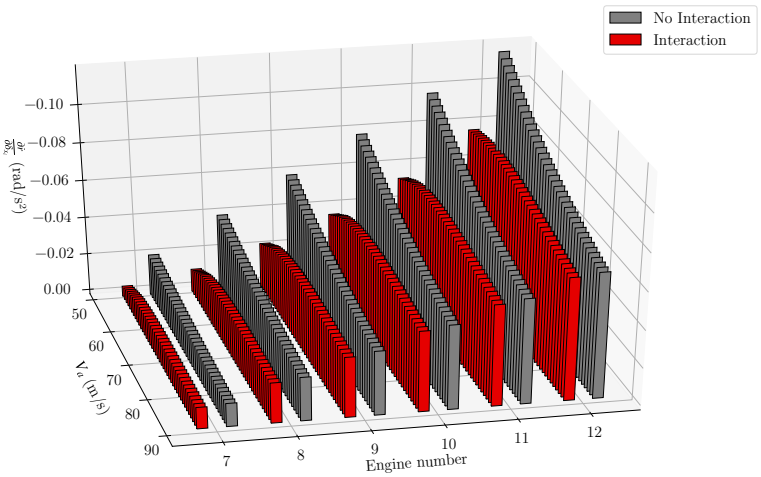

(b) $\frac{\partial \dot{r}}{\partial \delta_{x,i}}$ at 0° flap deflection.

Figure 4.8 – Engine efficiencies on the DEP ATR72 at different flap deflection.

directional control with differential thrust. Efficiencies show that the outer motors are also critical for forward thrust and therefore longitudinal performances. The loss of one or both outer motors translates as a double loss in thrust and directional control. Consequently reducing the advantage of redundancy envisioned with DEP. This observation holds for all aircraft configurations but is exacerbated with flap deflection.

This characteristic motivates the decision to consider no flap deflection at all for the DEP aircraft to maintain a high natural redundancy at low velocity. By doing so, the aircraft low speed characteristics will rely entirely on the high lift effect

obtained by wing blowing.

This decision can adversely affect the reference airspeeds, since the reference stall velocity is determined in 1g level flight, with motors idling. However, this definition can hardly be kept if the aircraft is designed to use powered lift as high lift device. In these conditions, the minimum flight velocity should be defined according to motor failures and can be now assessed by computing $V_a - \gamma_a$ flight envelope maps of DEP aircraft with various motor failures.

4.4.2 $\gamma_a - V_a$ flight envelope maps with aero-propulsive interactions in presence of motor failures.

In the previous section, it was decided to suppress the flap as high lift device to maintain motor efficiencies at low airspeed. The aircraft has to rely on the wing-blowing high lift effect to reach low airspeed. Motor failures now adversely affect the low speed aircraft characteristics and the goal here, is to define a new reference stall velocity, if necessary, in the presence of motor failures, before moving to the directional static stability and control analysis. This procedure ensures that the longitudinal flight performance requirement can be satisfied.

The analysis is made by computing $V_a - \gamma_a$ flight envelope maps with increasing number of motor failure. Starting with the outer right motor (engine number 12), up the loss of motor number 8 to 12, representing the loss of five motors out of twelve. The flight conditions for this analysis are summarised in Table 4.4. Flight envelope maps are presented in Fig 4.9a to Fig 4.9f.

Question **1** asked in section 4.3, can be answered by comparing the climbing performance of the twin-engine aircraft with simple aerodynamics and the DEP aircraft with interactions, or comparing Fig 4.3a and Fig 4.9a. The difference between the maximum climbing performance with all motors operative is now 4° and the climbing performance at 70 m/s differs by 1°. Comparing also the climbing performances between the twin-engine in OEI scenario and the DEP with five inoperative motors, or Fig 4.3b and Fig 4.9f: the maximum climb performances are identical. The longitudinal performances between the twin-engine with simple aerodynamic model and the DEP with interaction are more in agreement.

The major difference is observed in the maximum climb angle at low airspeed with all motor operational which is not the major interest in this study. The low speed performances with up to five motor failures being identical to the twin-engine in OEI, it was judged adequate to conserve the aero-propulsive model for the study

Table 4.4 – Flight configurations and conditions for the calculation of $V_a - \gamma_a$ flight envelope maps for the DEP aircraft with motor failures and aero-propulsive interactions.

Description	DEP 0	DEP 1	DEP 2	DEP 3	DEP 4	DEP 5
Design parameters						
Continuous Power	4.1MW					
Engines	12					
VT area	S_{v_0}					
Rudder efficiency	$\tau_r = 0.3$					
Propeller	Feathered, no drag assumed if inoperative.					
Differential thrust	Deactivated					
Flight conditions						
Engine inoperative	None	12	11 to 12	10 to 12	9 to 12	8 to 12
Side slip	0°					
Turn rate, Ω (rad/s)	0					
Mass	21.5 T					
Flap deflection	0°					

of DEP aircraft. Its use with twin-engine aircraft is however discouraged before further validation can be realized.

Following the answer to question **1**, one can observe that the longitudinal performances are satisfying up to the loss of five motors on the same wing. The rudder saturation is becoming the limiting parameter at low airspeed in Fig 4.9e and Fig 4.9f. Additionally, with a maximum of five inoperative motors, the minimum trimmable airspeed is 51m/s. This airspeed can be interpreted as the minimum reference velocity V_{sr}. The rudder saturation line crosses the 3% climb gradient limit at 55m/s, which can be interpreted as the minimum control velocity at take-off V_{mc}. Note that in Fig 4.9f, $V_{\text{mc}} \leq 1.13 V_{\text{sr}}$: these performances comply with the EASA regulation paragraph CS25.149, defining the limit for V_{mc}.

The descent performance of DEP aircraft using powered lift, in presence of motor failure, should be commented as well. The maximum descent flight path is limited to 3° and rarely 4°, around 57 m/s, with up to five motor failures. More importantly, the rudder deflection is not the limiting parameter indicating that longitudinal performances are more limiting than directional control. Take-off with positive flight path angle seem to remain the most demanding flight point for directional control and will be given priority.

It is fortunate that the minimum airspeed found in Fig 4.9f corresponds to the original twin-engine ATR72 but it confirms that removing the flaps was adequate. It

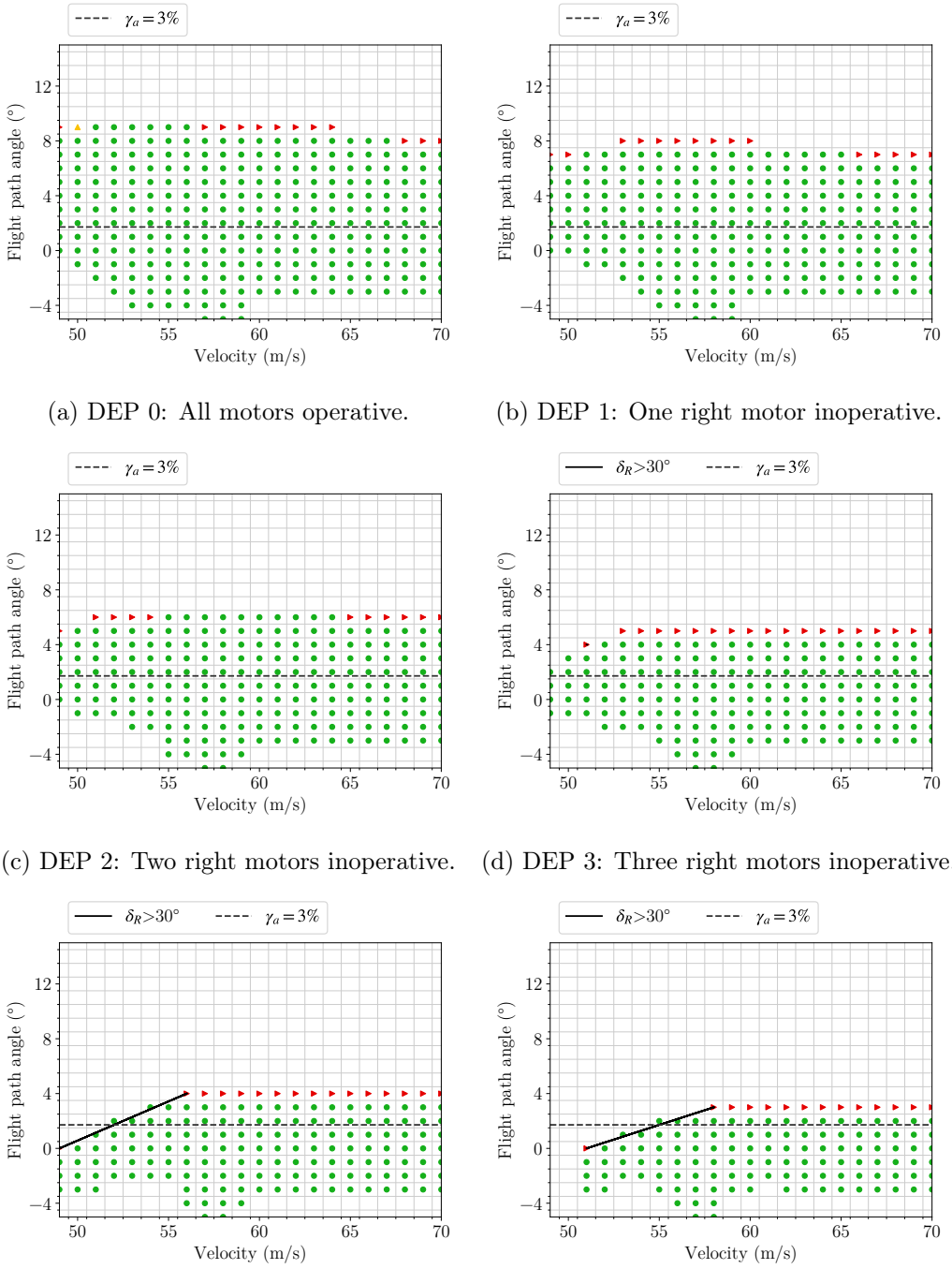

(a) DEP 0: All motors operative.

(b) DEP 1: One right motor inoperative.

(c) DEP 2: Two right motors inoperative.

(d) DEP 3: Three right motors inoperative.

(e) DEP 4: Four right motors inoperative.

(f) DEP 5: Five right motors inoperative.

Figure 4.9 – DEP ATR72 $V_a - \gamma_a$ flight envelope maps with increasing number of motor failures.

seems possible to achieve the same low airspeed performances even with an impor-

tant proportion of inoperative motors ($\frac{5}{12} \approx 40\%$) and asymmetric thrust. The high redundancy aspect of DEP is maintained, at least for longitudinal performances, without need of redefining the minimum reference velocity. The only modification being that, the minimum reference velocity does not refer to the 1g stall velocity with motors idling, but to the minimum airspeed at which, the aircraft is trimmable in levelled flight condition. With this new criterion, there is no need to increase take-off or landing airspeed. The aircraft configuration, reference airspeeds and longitudinal performances being known for the DEP aircraft, it is now possible to study the directional static stability and control capabilities offered by differential thrust.

4.4.3 Effectiveness of differential thrust for directional control.

The effectiveness of differential thrust for directional control is assessed by computing $\beta_a - V_a$ flight envelope maps, in presence of one, or many, motor failures and without the rudder control surface.

Deduced from the previous section, the flight condition investigated in priority is the positive 3% flight path angle at take-off after one, or many motor failures. The flight conditions and aircraft configuration are described in table 4.5.

It is known from previous section, that the DEP aircraft can handle up to five motor failures with its original rudder and the minimum control speed requirement: $V_{\text{mc}} \leq 1.13 V_{\text{sr}}$. Knowing that motor efficiencies decrease with decreasing airspeed, a minimum control velocity should be appearing and the interest is to characterize its evolution with motor failures.

Fig 4.10a to Fig 4.10d, show the $\beta_a - V_a$ flight envelope maps with increasing number of motor failures, from none to 3 outer right motor failures. The flight envelopes were extended to the minimum achievable flight velocity with all motors operational to picture the contraction due to motor failures. With all motors operational, in Fig 4.10a, the minimum achievable velocity is 37 m/s and a side-slip of $\beta_a = \pm 10°$ is achievable. With increasing airspeed the maximum achievable side-slip is increased up to a maximum of $\beta_a = \pm 17°$ around 52 m/s. The limiting parameter being the 5° bank angle. At airspeed higher than 56 m/s the flight envelope shrinks slowly. The $\pm 15°$ of side slip at $1.3 V_{\text{sr}}$ requirement is not reached due to bank angle limitation. The absence of motor saturation on the sides of the map means that the controllability requirement could well be achieved without the 5° bank limitation.

Engine failures are represented in Fig 4.10b to Fig 4.10d. The flight envelope is

Table 4.5 – Flight configuration and conditions for the calculation of $\beta_a - V_a$ flight envelope maps for the DEP aircraft with interactions.

Description	DEP 0	DEP 1	DEP 2	DEP 3
Design parameters				
Continuous Power	4.1MW			
Engines	12			
VT area	S_{v_0}			
Rudder efficiency	Rudder not allowed			
Propeller	Feathered, no drag assumed if inoperative.			
Differential thrust	Activated			
Flight conditions				
Engine inoperative	None	12	11 to 12	10 to 12
Climb angle	3%			
Turn rate, Ω (rad/s)	0			
Mass	21.5 T			
Flap deflection	0°			
V_{sr}	51 m/s			
$1.13V_{\text{sr}}$	57.6 m/s			
$1.3V_{\text{sr}}$	66.3 m/s			

reduced first at low speed, below 46 m/s for one motor failure in Fig 4.10b. From two motor failures, in Fig 4.10c, the maximum achievable side-slip is limited by motor saturation and moves toward higher velocity, around 56 m/s.

The large contraction between Fig 4.10b and Fig 4.10c is the consequence of losing the two most efficient motors. The combined effect of motor failure is to reduce the low speed trim capability, corresponding to V_{mc}, and reduce the maximum side-slip achievable at higher velocity, corresponding to the controllability requirement. From three motor failures, in Fig 4.10d, it is just possible to trim the aircraft at $\beta_a = 0$ at $1.13V_{\text{sr}}$. The tendency indicates that, an additional motor failure would move the lower flight envelope limit up, toward higher velocities and the low stability margin at $1.13V_{\text{sr}}$ would be insufficient. Nevertheless, all scenarios comply with the certification regulation, as it is possible to trim the aircraft at airspeed lower than $1.13V_{\text{sr}}$.

On the other hand, the controllability requirement cannot be achieved before motor saturation. This is due to the natural directional static stability of the aircraft. A reduction of the vertical tail size should translate into an increase in the

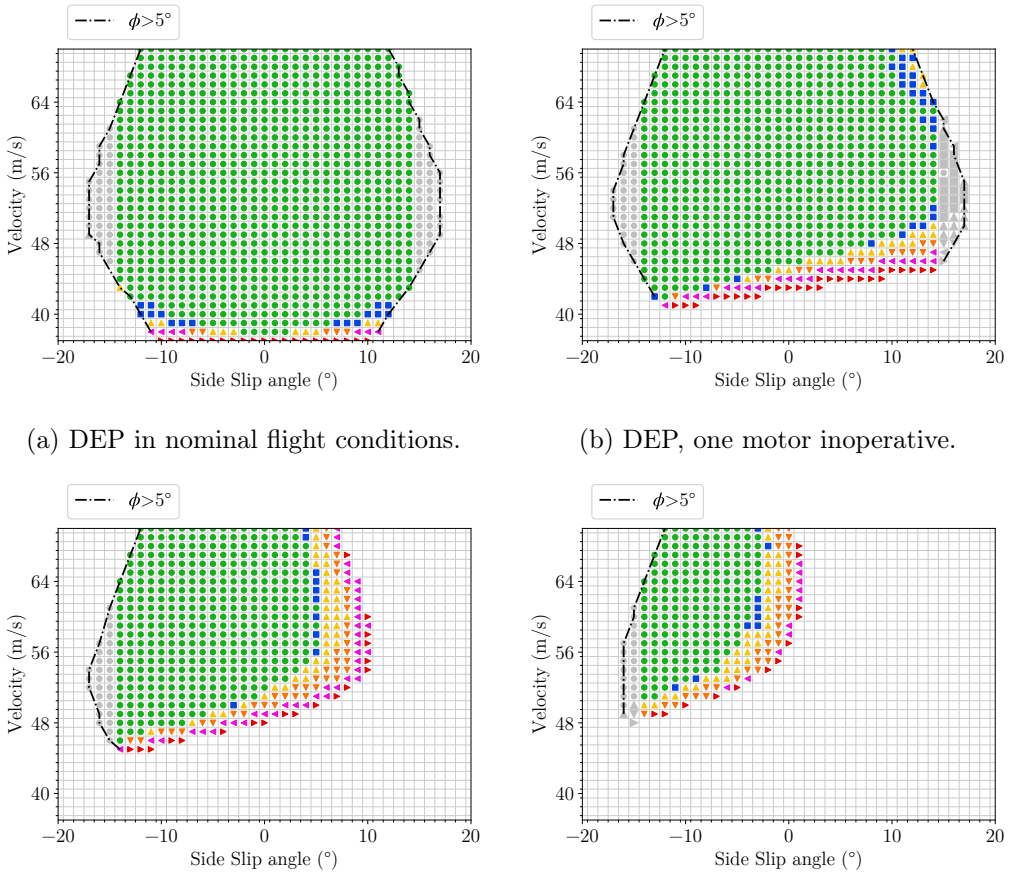

(a) DEP in nominal flight conditions.

(b) DEP, one motor inoperative.

(c) DEP, two motors inoperative.

(d) DEP, three motors inoperative.

Figure 4.10 – Evolution of flight envelope maps with increasing number of motor failure at 3% climb gradient.

controllability. This increase should be obtained at the cost of reduced dynamic stability and may also adversely affect the minimum control speed. The scenarios with two and three motor failures are selected to apply a vertical tail surface area reduction.

4.5 Effect of a small tail on directional static stability in presence of motor failures

Finally, the effect of reduced vertical tail can be assessed, with the aircraft configuration and flight conditions defined throughout this chapter. Two flight conditions were judged interesting to study: the cases with two and three outer motor failures (summarised in Table 4.6).

Table 4.6 – Aircraft configuration and flight condition for the calculation of $\beta_a - V_a$ flight envelope for the DEP aircraft with small tail.

Description	DEP 0	DEP 1
Design parameters		
Continuous Power	4.1MW	
Engines	12	
VT area	$0.8S_{v_0}$	
Rudder efficiency	Rudder not allowed	
Propeller	Feathered, no drag assumed if inoperative.	
Differential thrust	Activated	
Flight conditions		
Engine inoperative	11 to 12	10 to 12
Climb angle	3%	
Turn rate, Ω (rad/s)	0	
Mass	21.5 T	
Flap deflection	0°	
V_{sr}	51 m/s	
$1.13V_{\text{sr}}$	57.6 m/s	
$1.3V_{\text{sr}}$	66.3 m/s	

Since the vertical tail is a passive stability surface and the aircraft naturally stable, a restoring yawing moment is opposing differential thrust at non-zero side slip. As a result, the $\beta_a - V_a$ flight envelope maps with reduced vertical tail are expected to expend.

It was decided to apply an arbitrary 20% reduction in vertical tail surface area at constant aspect ratio, a quantity for which the aircraft remains naturally stable. The objective being to determine the motor failure scenario for which the vertical tail has to be sized.

The $\beta_a - V_a$ flight envelope maps with small tail are presented in Fig 4.11a with two motor failures and in Fig 4.11b with three motor failures. These two figures have to be compared with Fig 4.10c and Fig 4.10d. With two motor failures, the reduction of vertical tail increases the flight envelope up to $\beta_a = 19°$ compared to $\beta_a = 10°$ for the original tail size. More importantly, the limiting parameter is not anymore motor saturation but the 5° bank angle. The $\pm 15°$ requirement at $1.3V_{\text{sr}}$ is fulfilled and the flight envelope at V_{sr} and $1.13V_{\text{sr}}$ is increased.

The three motor failures case does not show the same improvement, with a

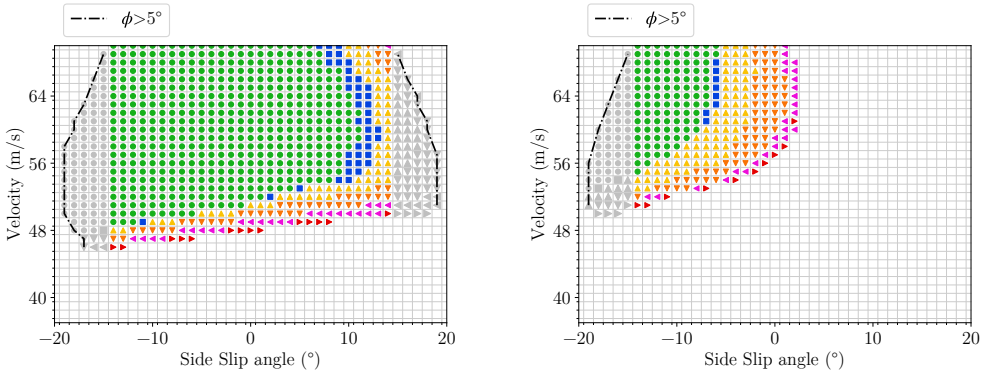

(a) DEP, motor 11 and 12 inoperative.

(b) DEP, motor 10 to 12 inoperative.

Figure 4.11 – $\beta_a - V_a$ flight envelope of DEP with small tail $S_v = 0.8S_{v,0}$

maximum $\beta_a = 3°$ compared to a maximum $\beta_a = 2°$ for the original vertical tail size. There is a higher number of saturated motors in the negative side of the flight envelope due to less restoring moment coming from the smaller vertical tail. An extension in the negative plane has to be mentioned with a bank angle limit moved to $-19°$ compared to $-16°$ with the original vertical tail size. At V_{sr}, the flight envelope is reduced compared to Fig 4.10d however, it is maintained at $1.13V_{\text{sr}}$. Since it was possible to trim the aircraft at $\beta_a = 0°$ with three motor failures, it was possible to reallocate the thrust to avoid thrust asymmetry. Therefore, the vertical tail size does not influence this equilibrium. The interpretation one can make from this observation is that, V_{mc} does not depend on vertical tail size but on the ability to reallocate thrust to avoid asymmetry.

Based on this last study, the failure of three outer motors definitely represents the most severe failure scenario for the aircraft considered in this study, if one limits directional control to differential thrust only. The addition of a rudder control surface would allow an increased number of motor failures and higher redundancy since the longitudinal performance can be maintained up to five motor failures.

The flight envelope obtained with two motor failures and small tail are suggesting that up to two motor failures can be handled while complying with the static stability and controllability requirements and employing only differential thrust. This opens the way to the suppression of the rudder control surface, although this can hardly be considered safe at the present time, in regard of full power loss or in the case of a naturally unstable aircraft.

The idea may be found useful for unconventional aircraft configurations, where

neutral natural directional static stability is sought. It was decided to challenge this idea with the ATR72 aircraft that exhibits a large and unstable fuselage. In this optic, the vertical tail has to be designed for the event of two outer motor failures since directional static stability and control requirements cannot be satisfied with three motor failures.

Table 4.7 – Reference DEP aircraft configuration and flight condition for vertical tail sizing.

Description	Reference DEP aircraft configuration
Design parameters	
Continuous power	4.1MW
Engines	12
Rudder efficiency	Rudder not allowed.
Propeller efficiency	0.8
Propeller	Feathered, no drag assumed if inoperative.
Differential thrust	Activated.
Flight conditions	
Engine inoperative	11 and 12
Climb angle	3%
Turn rate, Ω (rad/s)	0
Mass	21.5 T
Flap deflection	0°
V_{sr}	51 m/s
$1.13V_{sr}$	57.6 m/s
$1.3V_{sr}$	66.3 m/s

Since no aerodynamic control surface for directional control will be considered for the rest of the study, a few observations should be made to mark the change of paradigm brought by this decision.

The reduction of vertical tail with three motor failures, shows that compliance of V_{mc} with certification regulation, does not necessarily drive the controllability requirement of $\pm 15°$ of side-slip angle at $1.3V_{sr}$ when using differential thrust. In fact, this last requirement becomes the sizing point for the vertical tail. The results with two motor failures suggest a reduction of vertical tail to satisfy this criterion. A trade-off may be necessary between controllability offered at $1.3V_{sr}$ and static stability at $1.13V_{sr}$, with motor efficiencies reducing at airspeed close to $1.13V_{sr}$. For these reasons, both flight points are selected for the design of the vertical tail at the

moment.

The reference aircraft configuration and flight condition can finally be defined for the sizing of vertical tail with a DEP aircraft and are summarised in Table 4.7.

4.6 Conclusion

This chapter contributes both to methodological and technical aspects. In regard to DEP aircraft subjected to aero-propulsive interaction, a bottom-up methodology is employed to determine the aircraft configuration, reference flight velocity and failure scenario, in which the aircraft directional stability and control characteristics have to be analysed.

When the strategy is to make an intensive use of the propulsion system for aircraft stability and control, the idea exploited in this chapter is to start by analysing motor thrust and yawing efficiencies with regards to aero-propulsive and aircraft configuration. The goal is to configure the aircraft to keep a high motor efficiency and redundancy, in the sense that no single motor loss should result in an catastrophic degradation of flight performance or stability and control.

With a new configuration, the reference airspeeds should be updated according to the performance of a DEP aircraft, especially the reference minimum velocity that cannot hold the definition of CS25.103, for an aircraft employing powered lift as high-lift device.

This methodology leads to different aircraft configuration and flight conditions, than the original twin-engine ATR72 for determination of aircraft directional stability and control characteristics. In this sense, the methodology answers question **2** formulated at the beginning of section 4.3. Prior to the evaluation of directional stability and control characteristics, the longitudinal performances of a DEP aircraft employing aero-propulsive interaction, have to be fully characterized.

Technical limitations appearing with the aero-propulsive model, led to the development of the mentioned methodology. The non-linear evolution of aero-propulsive interaction reduces significantly motor thrust efficiency and consequently yawing efficiency, if differential thrust is employed. The first results obtained for the twin-engine configuration conducted to question the accuracy of the aero-propulsive interaction model. Effectively tested for distributed propulsion, the model was not validated with an isolated engine on a wing. A comparison of the DEP aircraft performances with regard to the twin-engine using simple aerodynamics proved that

the model is more accurate with DEP architectures. Nonetheless, it's accuracy at predicting longitudinal performances remains limited because it was not developed for this purpose (see section 4.3).

Once longitudinal performances with sufficient accuracy are available, it is possible to identify the critical flight position where directional characteristics limit the flight envelope. It was found that a positive flight path at take-off remains the most demanding flight position. The impact of successive motor failures on $\beta_a - V_a$ flight envelope maps showed that a minimum control speed appears but remains below $1.13V_{\text{sr}}$, as long as it is possible to reallocate the thrust to avoid asymmetry, while keeping the required positive flight path angle. More importantly, the vertical tail size seems to have no effect on this characteristic.

Finally, the reduction of vertical tail allows the compliance with both directional stability and controllability requirements in the event of two outer motor failures, while utilizing only differential thrust. This flight condition was chosen for the rest of the study and more particularly for the dynamic stability and control analysis, as it represents an original application case for unconventional aircraft configuration (see section 4.4).

Chapter 5

A continuous propulsion model for co-design of distributed propulsion and vertical tail

Contents

In the previous chapter, the interest was to determine the control capability offered by differential thrust and the corresponding sizing conditions for the vertical tail.

The study was rendered tedious by the number of failure cases that have to be considered. The critical failure case for directional control was determined by analysing the successive possibilities of motor failure until the directional stability and control requirement could not any more be satisfied. This iterative process was made manually and cannot be included in a global optimization process in its actual form.

The discrete nature of the propulsion system combined with a gradient based optimization solver is believed to be the major drawback in this approach. If the number of motor grows, a discrete optimization method may be facilitating this step. Another way to see the problem is to make abstraction of the motor number and

approximate the propulsion as a continuous function. If one can define a continuous propulsion system and a continuous variable representing the severity of failure; the distribution of propulsion along the wing could be calculated considering a predetermined level of failure, longitudinal performances and directional static stability and controllability requirements.

The idea is to guess a function that describes the power distribution on the wing subjected a given level of failure to ease the analysis of distributed propulsion and failure scenario through optimization.

This chapter proposes the formulation of such a function and explores the possibilities of designing the propulsion to answer both longitudinal performances and directional stability and control requirements with the consideration of failure severity. Using this approach can allow the designer to set the safety requirements for the propulsion systems or take into account the propulsion system limitations in terms of reliability when positioning the propulsion.

The chapter is organized as follows, the power distribution function with the failure severity are formulated in section 5.1 along with the transformation to obtain thrust and yawing moment. Section 5.2 introduces a mass and drag model for the inclusion of vertical tail into the design, formulates the new optimization problem and the flight conditions used for the design. Section 5.3 presents the results of power distribution calculated to satisfy flight performance and flight control constraints with varying severity of failure.

5.1 Definition of power distribution function

This section describes the idea and the methodology used to estimate a power density function along the aircraft wingspan. To simplify the model and because the interest is to be less specific and more general about distributed propulsion architecture, aero-propulsive interactions are not part of the study.

A power distribution or power density function $P(y)$ is searched, where y is the spanwise coordinate: $y \in \left[-\frac{b}{2}; \frac{b}{2}\right]$. $P(y)$ should be integrable to compute the total power $P_T = \int_{-\frac{b}{2}}^{\frac{b}{2}} P(y)\mathrm{d}y$ and positive or null, $p(y) \geq 0$, since braking is not considered.

The problem is common to the field of estimation theory with a major difference being that it is not an interpolation problem. Nevertheless, one can use the same tools to identify this function since the goal is the same i.e., shaping a function.

Suppose there exists an optimal power distribution function $\hat{P}(y)$ that for one flight condition minimizes the power. This power distribution $\hat{P}(y)$ can be estimated by a linear combination of basis functions $h_i(y)$:

$$P(y) = \frac{P_0}{N_g} \sum_{i=1}^{N_g} w_i h_i(y), \tag{5.1}$$

with P_0 a reference power density (W/m), N_g the total number of basis functions on the interval $[-\frac{b}{2}; \frac{b}{2}]$ and $w_i \in \mathbb{R}$ is the constant weight associated with the i$^{\text{th}}$ basis function. This formulation is a single layer of radial basis function network, selected because of its ability of universal approximation [Park 1991]. The selection of a basis function $h_i(y)$, allows different properties for $P(y)$. Our goal is to be efficient in the trim algorithm, especially for the integration of $P(y)$ to obtain the total power, thrust and yawing moment. Therefore a common radial basis function which integral form is finite is selected, the Gaussian distribution:

$$h_i(y) = e^{-N_g\left(\frac{2(y-c_i)}{b}\right)^2}, \tag{5.2}$$

where $c_i \in [-\frac{b}{2}; \frac{b}{2}]$ is the spanwise center of the i$^{\text{th}}$ basis function. The factor $N_g(\frac{2}{b})^2$ is a constant width factor to scale the basis functions on the interval $\left[-\frac{b}{2}; \frac{b}{2}\right]$. This factor is defined as constant, rendering the radial basis network linear. The integral form of the Gaussian distribution, the error function, is finite and allows the explicit computation of total power, thrust and torque without numerical integration:

$$\frac{\mathrm{d}}{\mathrm{d}x}\mathrm{erf}(x) = \frac{2}{\sqrt{\pi}} e^{-x^2}. \tag{5.3}$$

Starting from equation (5.1), the total power is obtained by integrating $P(y)$:

$$P_T = \frac{P_0}{N_g} \sum_{i=1}^{N_g} w_i \int_{-\frac{b}{2}}^{\frac{b}{2}} h_i(y)\mathrm{d}y\,. \tag{5.4}$$

A degraded flight condition can be simulated by bringing the power distribution function to zero within a specific portion of the wing, prior to integration for thrust and moment computation. A window function, $s(y)$, can be used to this aim:

$$s(y) = \begin{cases} 0 & \text{if } y_0 \leq y \leq y_1, \\ 1 & \text{otherwise,} \end{cases} \tag{5.5}$$

with, y_0 and y_1 the spanwise positions that delimits the power loss. The total power in case of simulated power failure writes:

$$P_T = \frac{P_0}{N_g} \sum_{i=1}^{N_g} w_i \int_{-\frac{b}{2}}^{\frac{b}{2}} h_i(y) s(y) \mathrm{d}y \ , \tag{5.6}$$

and by linearity of the integral:

$$P_T = \frac{P_0}{N_g} \sum_{i=1}^{N_g} w_i \left[\int_{-\frac{b}{2}}^{y_0} h_i(y) \mathrm{d}y + \int_{y_1}^{\frac{b}{2}} h_i(y) \mathrm{d}y \right] \ . \tag{5.7}$$

A particular case was chosen to specifically study directional static stability and control with $y_0 = Y_c$, with $Y_c \in \left[0; \frac{b}{2}\right]$ and $y_1 = \frac{b}{2}$. This allows the study of power loss from full power loss on the right wing to all power available. The total power in degraded flight conditions simplifies to:

$$P_T = \frac{P_0}{N_g} \sum_{i=1}^{N_g} w_i \int_{-\frac{b}{2}}^{Y_c} h_i(y) \mathrm{d}y \ . \tag{5.8}$$

The thrust is obtained with the thrust model of equation (1.30) and the total power or power distribution:

$$T(y) = \frac{P_0}{N_g} \frac{\eta_m \eta_p}{V} \sum_{i=1}^{N_g} w_i h_i(y), \tag{5.9}$$

$$T = \frac{P_0}{N_g} \frac{\eta_m \eta_p}{V} \sum_{i=1}^{N_g} w_i \int_{-\frac{b}{2}}^{Y_c} h_i(y) \mathrm{d}y. \tag{5.10}$$

Note:
Propeller and motor efficiencies are supposed constant in this example. In reality, it is known from the propeller disc theory that a propeller efficiency depends on the thrust loading [McCormick 1999]. The propeller efficiency could therefore be linked to the power distribution for a more global optimization.

The yawing moment in the body reference frame N^b is obtained from the integration of the thrust distribution pre-multiplied by the spanwise coordinate y:

$$N^b = -\frac{b}{2} \int_{-\frac{b}{2}}^{Y_c} y T(y) \mathrm{d}y \tag{5.11}$$

$$N^b = \frac{P_0}{N_g}\frac{\eta_m\eta_p}{V}\sum_{i=1}^{N_g} w_i \int_{-\frac{b}{2}}^{Y_c} -yh_i(y)\mathrm{d}y \tag{5.12}$$

At this point it is recommended to render the interval of definition of the basis function non-dimensional. This is done by the change of variables: $y = \frac{b}{2}\bar{y}$ where $\bar{y}$ is the non-dimensional spanwise coordinate, $c_i = \frac{b}{2}\bar{c}_i$ and $Y_c = \frac{b}{2}\bar{Y}_c$, with $\bar{y}, \bar{c}_i \in [-1; 1]$ and $\bar{Y}_i \in [0, 1]$. Equation (5.1) and (5.8) are re-arranged as:

$$P(\bar{y}) = \frac{P_0}{N_g}\sum_{i=1}^{N_g} w_i e^{-N_g(\bar{y}-\bar{c}_i)^2}, \tag{5.13}$$

$$P_T = \frac{P_0}{N_g}\frac{b}{2}\sum_{i=1}^{N_g} w_i \int_{-1}^{\bar{Y}_c} e^{-N_g(\bar{y}-\bar{c}_i)^2}\mathrm{d}\bar{y}. \tag{5.14}$$

Similarly for the thrust and the yawing moment:

$$T = \frac{P_0}{N_g}\frac{\eta_m\eta_p}{V}\frac{b}{2}\sum_{i=1}^{N_g} w_i \int_{-1}^{\bar{Y}_c} e^{-N_g(\bar{y}-\bar{c}_i)^2}\mathrm{d}\bar{y}, \tag{5.15}$$

$$N^b = \frac{P_0}{N_g}\frac{\eta_m\eta_p}{V}\frac{b^2}{4}\sum_{i=1}^{N_g} w_i \int_{-1}^{\bar{Y}_c} -\bar{y}e^{-N_g(\bar{y}-\bar{c}_i)^2}\mathrm{d}\bar{y}. \tag{5.16}$$

Using equation (5.3), it is now possible to write explicit equations for total power, thrust and yawing moment:

$$P_T = \frac{P_a}{N_g}\frac{b}{2}\sum_{i=1}^{N_g} w_i \frac{\sqrt{\pi}}{2\sqrt{N_g}}\left[\mathrm{erf}\left(\sqrt{N_g}(\bar{y}-\bar{c}_i)\right)\right]_{-1}^{\bar{Y}_c}, \tag{5.17}$$

$$T = \frac{P_a}{N_g}\frac{\eta_m\eta_p}{V}\frac{b}{2}\sum_{i=1}^{N_g} w_i \frac{\sqrt{\pi}}{2\sqrt{N_g}}\left[\mathrm{erf}\left(\sqrt{N_g}(\bar{y}-\bar{c}_i)\right)\right]_{-1}^{\bar{Y}_c}, \tag{5.18}$$

$$N^b = \frac{P_a}{N_g}\frac{\eta_m\eta_p}{V}\frac{b^2}{4}\sum_{i=1}^{N_g} w_i c_i \frac{\sqrt{\pi}}{2\sqrt{N_g}}\left[\mathrm{erf}\left(\sqrt{N_g}(\bar{y}-\bar{c}_i)\right) - \frac{1}{2N_g}e^{-N_g(\bar{y}-\bar{c}_i)^2}\right]_{-1}^{\bar{Y}_c}. \tag{5.19}$$

The power distribution defined by radial basis network can approximate any distribution provided that there is a sufficient number of basis functions N_g [Chen 1991], [Cybenko 1989] and [Park 1991]. For interpolation problems, N_g can be set based on the size of the data set. In this study, there is no prior information about $P(\bar{y})$,

no training data to determine the number and position of basis centres.

This is the reason why the basis centres are uniformly distributed on the interval $[-1; 1]$. A graphical representation of this distribution is given in Fig 5.1.

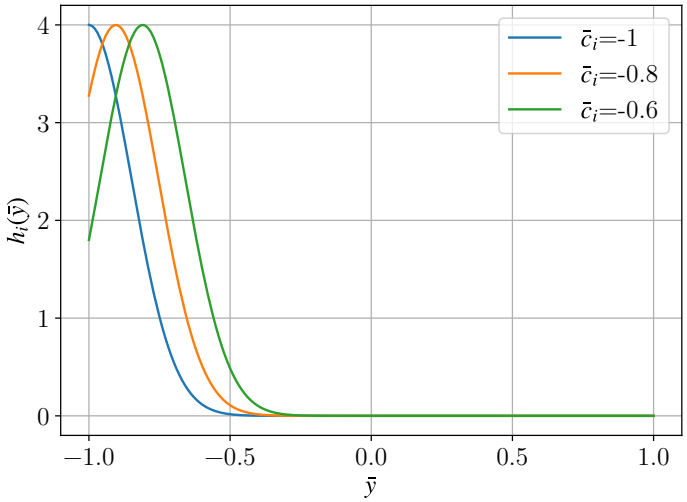

Figure 5.1 – Gaussian basis functions for $N_g = 10$ and $w_i = 4$

For the number of basis function, a convergence test was performed using as metrics, the maximum total power later defined in 5.2.3 by equation (5.26), to determine a minimum value for N_g. The study is available in Annexe A and showed that no less than 80 centres should be used. $N_g = 100$ was considered for the rest of the study. Only the weights w_i are remaining to shape the power function, these are found in optimisation through the trim algorithm. $\bar{Y}_c$ can be set freely to simulate a degraded flight condition.

5.2 Design of power distribution and vertical tail size.

With the new power function, the idea is now to find an optimal trade-off between on-board power and vertical tail size, for different flight conditions or severity of failure. The optimal trade-off is defined as the one that minimizes the on-board power, with an optimal allocation of directional control between rudder and differential thrust. The corresponding objective function for optimization is hence P_T.

To minimize the VT in parallel, it is possible to define as objective function a linear combination of power and VT surface area. This solution has been avoided as the vertical tail cannot be put at the same level of importance as the power in a

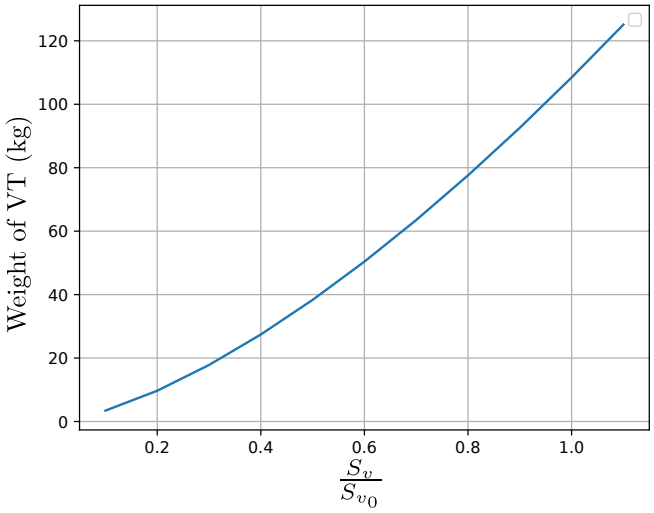

Figure 5.2 – Vertical tail mass as a function of its relative surface area

global aircraft optimization. On the point of view of the designer, it is difficult to justify the installing of additional power on an aircraft to only reduce the vertical tail surface area.

Rather, the interest is to represent the impact of vertical variation on the total power. As presented up to now, a variation in S_v only modifies the lateral aerodynamic coefficients. To find a trade-off the impact on total mass and skin friction drag have to be modelled.

5.2.1 Vertical tail reduction: modelling the impacts on the power

The vertical tail impacts the power needed in flight mainly through mass and skin friction drag. The energy needed for the rudder actuator is neglected.

Vertical tail mass model

A statistical structural model for light aircraft, which airspeed is limited to 250 kts, is used to estimate the vertical tail mass W_v, as a function of its surface area [Torenbeek 1982]:

$$W_v = 0.64 \left(n_u + S_v^2\right)^{0.75}, \tag{5.20}$$

With n_u the ultimate load factor, taken as $n_u = 6$. The evolution of the ATR72 vertical tail mass, as a function of its relative surface area is shown in Fig 5.2. The impact on the fuselage mass is neglected with this model.

Skin friction drag

The skin friction associated with the vertical tail is determined from the drag decomposition obtained from VSPaero. The contribution of the ATR72 vertical tail to the parasitic drag amounts to 8%. Its reduction is modeled with a linear transformation:

$$C'_{D_0} = C_{D_0}(0.92 + 0.08\frac{S_v}{S_{v_0}}) \tag{5.21}$$

With these contributions to weight and parasitic drag the total on-board power is directly sensitive to vertical tail ratio $\frac{S_v}{S_{v_0}}$ and minimizing the power will result in minimizing the vertical tail size in symmetric flight conditions.

5.2.2 Optimization problem formulation

The power distribution and vertical tail are found by minimizing P_T while satisfying trim constraints similarly as in Chapter 1, section 1.5. The optimization problem is reformulated as:

$$\frac{\widehat{S}_v}{S_{v_0}},\, \widehat{w}_i = \arg\min_{\mathbf{x}} P_T \tag{5.22}$$

$$\text{With: } \mathbf{x} = [\alpha,\, p,\, q,\, r,\, \phi,\, \theta,\, \delta_a,\, \delta_e,\, \delta_R,\, \frac{S_v}{S_{v_0}},\, w_1,\, \ldots,\, w_{N_g}] \tag{5.23}$$

Subject to:

$$\begin{pmatrix} 0 \\ -mV_a(p\sin\alpha_a - r\cos\alpha_a) \\ mV_a\left[\sin\beta_a(p\cos\alpha_a + r\sin\alpha_a) - q\cos\beta_a\right] \end{pmatrix} = mg \begin{pmatrix} -\sin\gamma_a \\ \cos\gamma_a\sin\mu_a \\ \cos\gamma_a\cos\mu_a \end{pmatrix} + \mathbf{F}^a + \mathbf{T}^a$$

$$0 = \mathbf{M} + \mathbf{M}_T - \begin{pmatrix} p \\ q \\ r \end{pmatrix} \times \mathbf{I} \begin{pmatrix} p \\ q \\ r \end{pmatrix}$$

$$0 = p + q\sin\phi\tan\theta + r\cos\phi\tan\theta$$

$$0 = q\cos\phi - r\sin\phi$$

$$\Omega = (q \sin\phi + r \cos\phi) \sec\theta$$

$$\sin\gamma_a = \cos\alpha_a \cos\beta_a \sin\theta - \sin\beta_a \sin\phi \cos\theta - \sin\alpha_a \cos\beta_a \cos\phi \cos\theta$$

$$0 \leq w_i$$

$$0.1 \leq \frac{S_v}{S_{v_0}} \leq 1$$

where $\mathbf{T}^a$ is calculated with equation (5.18) and $\mathbf{M}_T$ is calculated with equation (5.19) The same bounds as defined in Table 1.1 remain valid and w_i are bounded to ensure $P(\bar{y}) > 0$.

5.2.3 Flight conditions

An optimal power distribution $\hat{P}(\bar{y})$ and associated surface ratio $\frac{\hat{S}_v}{S_{v_0}}$ can be found by solving problem (5.22) for any pre-defined flight condition but it will result in a design susceptible to be trimmable only at the given flight point. To cope with this, many flight conditions are analysed and the weights associated with the j^{th} flight condition $\tilde{w}_{i,j}$ are saved during the process. The final power distribution to install on the aircrat P_{in} is obtained by selecting the maximum weights over the number of flight conditions analysed:

$$P_{\text{in}}(\bar{y}) = \frac{P_0}{N_g} \sum_{i=1}^{N_g} \mathrm{w}_i e^{-N_g(\bar{y}-\bar{c}_i)^2} \tag{5.24}$$

$$\mathrm{w}_i = \max(\hat{w}_{i,j}) \tag{5.25}$$

$$P_{T_{\text{in}}} = \frac{P_a}{N_g} \frac{b}{2} \sum_{i=1}^{N_g} \mathrm{w}_i \frac{\sqrt{\pi}}{2\sqrt{N_g}} \left[\operatorname{erf}\left(\sqrt{N_g}(y - c_i) \right) \right]_{-1}^{1}, \tag{5.26}$$

with $\mathrm{w}_i = \max(\hat{w}_{i,j})$ being the maximum $\hat{w}_i$ over every considered flight condition. A similar procedure is followed for the vertical tail, selecting the maximum trade off obtained for all flight conditions.

The next step consists in defining the flight conditions to design the power distribution and vertical tail. The selected flight conditions are described in Table 5.1, based on the conclusion of Chapter 4.

In addition to the directional static stability and controllability, two flight conditions, particularly important for the power sizing are added: the best climb (FP 6 in Table 5.1) and the cruise (FP 7 in Table 5.1). For these two additional con-

Table 5.1 – Flight Point (FP) description for the design of power distribution function. With H the flight altitude and R the radius of turn.

Parameters	FP 1	FP 2-3	FP 4-5	FP 6	FP 7
V(m/s)	$1.13V_{sr}$	$1.3V_{sr}$	$1.3V_{sr}$	90	130
β_a	$0°$	$\pm 15°$	$\pm 15°$	$0°$	$0°$
γ_a	$1.37° = 3\%$	$1.37° = 3\%$	$-3°$	$4.5°$	$0°$
R (m)	0	0	0	3000	0
H (m)	0	0	0	0	7500
$\bar{Y_c}$	< 1	< 1	< 1	1	1
Weight (T)	21.5	21.5	15.5	21.5	21.5

ditions, a coordinated turn, corresponding to a 15° bank angle (a low bank turn for the ATR72) is imposed. In all flight conditions, except the last two points described, the aircraft is assumed to be affected by a power failure, meaning that $\bar{Y_c} < 1$. These eight flight conditions regroup a set of symmetric and asymmetric power/thrust conditions.

It is re-called here that even if the flight conditions are based on the conclusion of Chapter 4, aero-propulsive interactions are not used in this study.

For the present study, the consequences of $\bar{Y_c}$, or the severity of the failure, on the power distribution and the vertical tail surface area are explored. This is one of the goal of the present power formulation.

5.3 Distributed power and vertical tail design for varying failure severity

The framework defined previously allows to explore the consequences of an imposed level of failure severity on the power distribution and vertical tail surface area.

The interest is to vary $\bar{Y_c}$ in the interval $[0.2; 1]$, where $\bar{Y_c} = 1$ means that the whole power is available. It represents a nominal flight where best climb performances and cruise velocity should be obtained. In the case where only differential thrust is considered for directional control, it is not possible to reach $\bar{Y_c} = 0$. This value is identical to the OEI for twin engines. For differential thrust, the failure severity was limited to $\bar{Y_c} = 0.2$.

A power distribution and vertical tail surface area, satisfying all flight conditions

of Table 5.1 are computed for each value of $\bar{Y}_c$. The evolution of power distribution $P(\bar{y})$ is shown in Fig 5.3. The total installed power $P_{T_{in}}$, the optimal vertical tail $\frac{\tilde{S}_v}{S_{v_0}}$ and the remaining power ratio after failure $\frac{P}{P_{T_{in}}}$, in Fig 5.4.

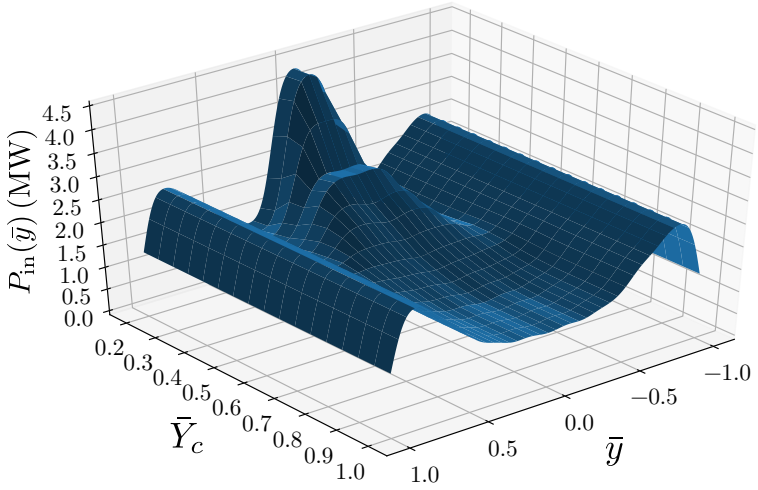

Figure 5.3 – Power distribution along the wingspan $P_{\text{in}}(\bar{y})$ as a function of the level of failure $\bar{Y}_c$.

Before analysing these results, it should be stressed that this methodology does not show the optimal power distribution and vertical tail ratio but a trade-off obtained from optimal power distributions calculated at each flight condition.

The results of Figures 5.3 and 5.4 should be analysed in parallel for interpretation. The power distribution for varying failure severity in Fig 5.3, shows a concentration of the power at the centre of the wing for an initial value of $\bar{Y}_c = 0.2$ and additional power peaks at the wingtips. As $\bar{Y}_c$ increases (decreasing level of failure severity), power is rapidly removed from the centre part of the wing. Eventually, the power distribution at the center part of the wing flattens for $\bar{Y}_c \geq 0.8$. Only the minor peaks at wingtip remain for the whole range of $\bar{Y}_c$. Indeed, Fig 5.4 shows a decrease in installed power between $\bar{Y}_c = 0.4$ and $\bar{Y}_c = 0.8$. The remaining power ratio after failure shows a steeper increase in the interval $0.6 < \bar{Y}_c < 1.0$.

The vertical tail surface ratio remains constant over the whole range of Y_c at $\frac{S'_v}{S_{v_0}} = 0.64$. This point corresponds to a neutral static stability. This can interpreted by the fact that, the imposed flight conditions require more control power than natural stability. In this case and in the absence of control surface, the vertical tail

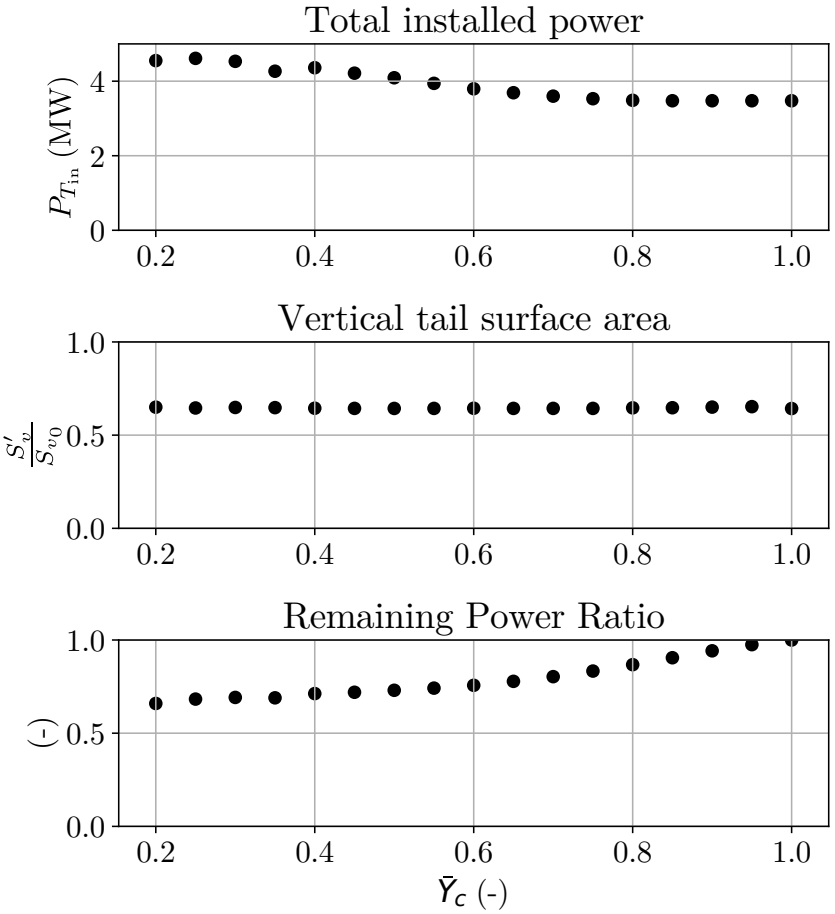

Figure 5.4 – From top to bottom: Total installed power $P_{T_{in}}$, vertical tail ratio $\frac{\tilde{S}_v}{S_{v_0}}$, power ratio remaining after failure $\frac{P}{P_{T_{in}}}$.

could be sized for neutral directional stability.

The power peaks at wingtips are due to the flight position FP 6, the climbing flight and coordinated, low bank turn. In such case, differential thrust is used to maintain zero side-slip. At high velocity and power, it is advantageous to have more power at wingtips to increase the efficiency of differential thrust. For low failure severity ($\bar{Y}_c \geq 0.75$), this distribution is not a disadvantage for directional requirements. Starting from $\bar{Y}_c \leq 0.75$ however, more power is required at the center part of the wing to maintain longitudinal performance and symmetric thrust, as shown by the steady total power increase in Fig 5.4.

The flight conditions dimensioning the power distribution and total on board power are:

— FP 2 and 3 for $0.2 < \bar{Y}_c < 0.7$, representing an asymmetric thrust condition,

— FP 6 for $\bar{Y}_c > 0.7$, representing a nominal flight condition.

For the vertical tail ratio, the dimensioning flight conditions are:

— FP 2 to 5, ($\beta > 0$), representative of directional controllability requirements at take-off and landing in an asymmetric thrust condition.

These results show that if differential thrust is the only means of directional control, the optimal power distribution depends on the failure severity considered during the preliminary design. There seem to be a critical $\bar{Y}_c$ value at which additional power is required at the wing centre to avoid thrust asymmetry. For $\bar{Y}_a \geq 0.75$, power distribution favouring an important directional control, seem to satisfy all flight conditions.

As means of comparison, in Chapter 4, two motors failure correspond to $\bar{y}_c = 0.73$ and three motors failure corresponds to $\bar{y}_c = 0.59$. Despite the fact that the interaction are not taken into account in this chapter, it is possible to draw a parallel between the critical value of $\bar{y}_c = 0.75$ and the two motor failure chosen as critical failure in Chapter 4.

The same study including the rudder control surface for $0.0 \leq \bar{Y}_c \leq 1.0$ and leading to similar general conclusions but with a smaller vertical tail surface area, is available in Annex A.2.

5.3.1 Limitation

The results should be mitigated by the fact that propeller wing interactions are not taken into account in this exploration. As seen in Chapter 4, they influence largely the efficiency of motors for thrust and yaw control. They should therefore be added to the analysis to be able to make more specific conclusions. The results presented here should be taken as general information about power distribution for distributed propulsion, prior to the consideration of aero-propulsive interactions.

Additionally, as stressed at the beginning of the section, the power distribution does not represent an optimal and may be overestimated especially for low values of $\bar{Y}_c$ due to the fact that the maximum weights w_i for all flight are selected. An optimal solution could be found if all flight conditions were solved in parallel with the same set of w_i rather than sequentially.

Similarly, there remains a lot of room for improvements in the determination of the number of basis functions, the weights and width of basis functions. The

only degree of freedom in the optimization was the weights but it is possible to use learning algorithms to make N_g, and the width of basis functions evolve during the optimization process. This is however outside the scope of the present study.

5.4 Conclusion

This chapter began with the motivation to remove the discrete nature of motor distribution and motor failure in the study of distributed propulsion aircraft. The idea was that by doing so, the analysis of the severity of failure would be rendered more versatile and flexible.

The formulation proposed is a power distribution function $P(\bar{y})$ where $\bar{y}$ is the non-dimensional spanwise coordinate (see section 5.1). It takes the form of a single layer of radial basis function network, where the weights w_i are calculated when trimming the aircraft at particular sizing flight conditions. Simplistic mass and skin friction drag models of the vertical tail have been added to the aircraft properties. This allowed the determination of a trade-off between vertical tail size and power distribution that minimizes the power required for flight (see section 5.2).

The study does not consider interaction and brings less specific but more general information about distributed propulsion, particularly about power distribution. A general interpretation could be that the optimal power distribution considering a specific failure severity avoids thrust asymmetry after failure. This may be obtained with a power distribution sized for nominal flight operation if the failure severity is below a certain critical value, here: $\bar{Y}_c = 0.75$ and $\frac{P}{P'_T} = 0.83$. For lower values of $\bar{Y}_c$, the power distribution should be dimensioned specifically taking into account power failure. This may adversely affect the total on-board power. At the opposite, the optimal size of the vertical tail, without its rudder control surface and for the selected flight points, seems to be the neutral point where the highest controllability is obtained (see section 5.3). More importantly, the dimensioning flight condition for the VT is always $1.3V_{\text{sr}}$ and the $\pm 15°$ side slip requirement. The size of the VT does not depend on the severity of failure.

Despite the parallel drawn with the results of Chapter 4, these quantities may hardly be generalized to all configurations. They confirm however that the advantage of distributed propulsion lies in the possibility of avoiding asymmetry in the thrust distribution at all time.

Part II Conclusion

The main focus of this first Part was the determination of trim states and directional flight envelops for the study of static flight conditions. The outcomes of Chapter 4 were rather unexpected and this opens a door for discussing the approach that was employed. Traditionally flight dynamic and control is studied apart from flight performance. The two domains use different levels of fidelity in the determination of aerodynamic coefficients. The flight dynamic and control at a preliminary design stage is most of the time performed using direct or empirical methods and low fidelity numerical methods. This level of fidelity is sufficient because the control design is always performed with gain and phase margins to cope with model simplifications. The aircraft modes can be approximated with reduced order models and low fidelity aerodynamics data, simplifying in turn the control law design and robustness analysis.

When getting interested in the distributed electric propulsion, it is tempting to proceed in the same way: simplify the complexity due to the added degrees of freedom with the idea of covering model uncertainties with margins during the control design. The actual aircraft concepts with distributed propulsion favour close coupled propulsion and aerodynamics, and the exploitation of aero-propulsive interactions. It is rather un-common in the field of aircraft stability and control to deal with a platform designed to favour aero-propulsive interaction. Therefore, it was decided to include a model of these interactions in the study. The major concern, before realizing the study, was the additional coupling between directional and lateral control due to eventual large local lift increase when differential thrust is used.

While most actual methodologies focus on the increase of lift, it was anticipated that both lift and drag polar would be necessary to evaluate the impact of aero-propulsive interaction. The development of the method focused on versatility and computation cost, to be used efficiently by a trim algorithm. In this study, it was used for establishing flight envelop maps of up to a thousands points, allowing to easily identify the sizing flight conditions and criteria for the VT on a DEP aircraft. The low computational cost of the method helped exploring a diversity of aircraft configurations and flight conditions.

On the point of view of stability and control design, the aero-propulsive interac-

tion model gave satisfactory results on validation cases (see section 3.4). However, it was realized through the study of flight envelops with motor failure conditions that longitudinal performances and directional control become closely coupled because the total directional control depends on both motor saturation and trim power. Flight performances and directional control being coupled, it is actually necessary to have accurate aerodynamics data, especially the drag at low speed, to determine accurately the longitudinal trim and the directional control power. The aero-propulsive model was not developed with this information in mind and gave questionable results when applied to the ATR72 in its original twin-engine configuration. The highlight should therefore be put on the methodology used for exploration of DEP aircraft flight envelops and the determination of the sizing point for the VT with aero-propulsive interaction rather than the results themselves before the aero-propulsive interaction model can be further validated.

With the limitation underlined previously, the interest will now be to explore the flight dynamics and handling qualities of a DEP aircraft. Without the rudder control surface, Chapter 5 showed that the VT best size seem to be the neutral point, this at low airspeed and independently of the number of motor failures. With the simplistic uniform propulsion distribution considered on the ATR72, it was determined that two outer motor failure at take-off represents the critical failure. Compliance with the trim and controllability requirements for an unconventional aircraft without rudder may be not sufficient to determine the optimal vertical tail surface area. Therefore, the investigation of flight dynamics and handling qualities now becomes necessary and will be the subject of Part III.

Part III

Control and Co-Design

Introduction

The first part of the thesis concluded that a reduction of the VT surface area was necessary to increase the directional flight envelop when utilizing only differential thrust for directional control. Trim and flight envelop requirements would size the VT at the neutral point for maximum controllability. However, it is known that a small VT penalizes the yaw damping of the aircraft [Abzug 2005], [Feuersänger 2008], [Morris 2013], necessitating a stability augmentation system. Without considering a rudder control surface, this functionality has to be undertaken by the propulsion system. Part III deals with the question of how much the VT shall be reduced taking into account the desired flight envelop, flight handling quality requirements, and engine limitations, for a given distributed propulsion.

The problem of sizing a stability surface with consideration of a stability augmentation system is a co-design problem where both control law gains and aircraft geometrical parameters are tunable variables. With the recent advances in non-smooth optimization, it is possible to realize a co-design with inclusion of flight envelop and handling qualities. The methodology presented by Denieul [Denieul 2017], can be used for this work, with the difference that the VT and the control law have to be sized for normal and asymmetric thrust conditions. The present work follows the path of [Denieul 2016] and seeks the integration of engine failures alongside the normal flight conditions.

More specifically, if one relies solely on differential thrust for flight control, Part III tries to answer the question: which flight handling qualities, at what cost for the control system and aircraft design can be expected?

The general goal to answer this question is to be able to compute a trade off between VT surface area and actuator solicitation, given a particular set of flight envelop/handling qualities. Additionally, this has to be done in order to accommodate symmetric and asymmetric thrust conditions.

The starting point is the preparation of the co-design framework and the definition of the fundamental theory behind the tools that will be used in Chapter 6. The second step, presented in Chapter 7 is to gain further knowledge on the system sensitivity to design variables since this configuration is quite unconventional. The third and last point, Chapter 8 focuses on the inclusion of the critical engine failure condition determined in Chapter 4 in the co-design framework, in order to determine

a design trade-off suitable for both nominal and degraded flight conditions.

Chapter 6

Co-Design architecture

Contents

The objectives of this chapter is to prepare the co-design environment and lay down the fundamental background for multi-objective optimization. The fundamentals of H_∞ norm and associated H_∞ based solvers used for co-design with multi-objectives, are introduced with a simple example in section 6.1. Following this, a preliminary analysis and treatment of the aircraft open-loop dynamics with varying VT for inclusion in the co-design is presented in section 6.2. The control structure and system architecture are explained in section 6.3. Finally, the first exploration step under the form of a sequential co-design is presented in section 6.4.

6.1 Structured H_∞ based co-design

This section introduces the H_∞ norm for Single Input Single Output (SISO) and Multiple Input Multiple Output (MIMO) systems and its used for the codesign

of a plant's controller and design parameters.

6.1.1 H_∞ norm definition

The H_∞ norm of a SISO transfer function $\mathrm{T}_{\mathrm{w}\to\mathrm{z}}(s)$ from a signal w to an output z is defined as [Zhou 1998], [Francis 1987]:

$$\|\mathrm{T}_{\mathrm{w}\to\mathrm{z}}(s)\|_\infty = \sup_\omega \left(|\mathrm{T}_{\mathrm{w}\to\mathrm{z}}(j\omega)|\right), \tag{6.1}$$

The H_∞ norm gives a maximum bound of the transfer function gain across all frequencies ω. It can be interpreted graphically by the largest peak in the Bode diagram representation.

It is a generalisation of the $\mathcal{L}_2$ norm which is explained here to give a more physical meaning. The $\mathcal{L}_2$ norm is defined for a temporal signal $\mathrm{z}(t)$ as:

$$\|\mathrm{z}(t)\|_2 = \left(\int_0^\infty \mathrm{z}(t)^2 dt\right)^{\frac{1}{2}}. \tag{6.2}$$

With $\mathrm{z}(t)$ representing the system impulse response, the $\mathcal{L}_2$ norm represents the energy of the output signal. Parseval's equality gives the equivalence of equation (6.2) in the frequency-domain:

$$\|\mathrm{z}(s)\|_2 = \left(\frac{1}{2\pi}\int_{-\infty}^\infty \mathrm{z}(-j\omega)\cdot\mathrm{z}(j\omega)\ d\omega\right)^{\frac{1}{2}}. \tag{6.3}$$

Furthermore, a signal $\mathrm{z}(s)$ is said to be part of the $\mathcal{H}_2$ space if:

$$\|\mathrm{z}(s)\|_2 < +\infty. \tag{6.4}$$

Supposing an input signal $\mathrm{w}(s)$ such that $\mathrm{w}(s) \in \mathcal{H}_2$, one can write the H_∞ norm of the transfer between $\mathrm{w}(s)$ and $\mathrm{z}(s)$ as:

$$\|T_{\mathrm{w}\to\mathrm{z}}(s)\|_\infty = \max_\omega \frac{\|\mathrm{z}\|_2}{\|\mathrm{w}\|_2}. \tag{6.5}$$

It is a measure of the maximum gain on the output signal z when a system is excited by any signal $\mathrm{w}(s)$ of finite energy.

By extension, for MIMO systems, the $\mathcal{H}_2$ norm of a transfer $\mathbf{T}_{\mathbf{w}\to\mathbf{z}}(s)$ is the $\mathcal{L}_2$

norm of its impulse responses.

$$\|\mathbf{T}_{\mathbf{w}\to\mathbf{z}}(s)\|_2 = \left[\frac{1}{2\pi}\int_{-\infty}^{\infty} \mathrm{Tr}\left(\mathbf{T}^T_{\mathbf{w}\to\mathbf{z}}(-j\omega)\mathbf{T}_{\mathbf{w}\to\mathbf{z}}(j\omega)\right) d\omega\right]^{\frac{1}{2}}, \tag{6.6}$$

and the H_∞ norm applied to MIMO systems is:

$$\|\mathbf{T}_{\mathbf{w}\to\mathbf{z}}(s)\|_\infty = \sup_\omega \bar{\sigma}\left(\mathbf{T}_{\mathbf{w}\to\mathbf{z}}(j\omega)\right), \tag{6.7}$$

where $\bar{\sigma}(\cdot)$ denotes the maximum singular value of the matrix $\mathbf{T}_{\mathbf{w}\to\mathbf{z}}(s)$ [1].

6.1.2 H_∞ control design and co-design

Before applying a co-design, it is necessary to determine a stabilizing control law with H_∞ criterion.

6.1.2.1 Control design with the H_∞ norm

The control laws are designed using the loop-shaping technique. This technique is described here with a simple example. Assuming the SISO plant presented in Fig 6.1, a reference signal y_r has to be followed by the output y of the plant P(s). An output feedback and a controller K on the tracking error are used to this end. The plant is constituted of a first order actuator dynamic of bandwidth ω_{act} and a transfer function G(s).

The tracking error e is weighted by a block W and monitored through the signal z. This tracking error should be low at low frequencies. This requirement can be expressed by an H_∞ norm and tuned with the weighting block W.

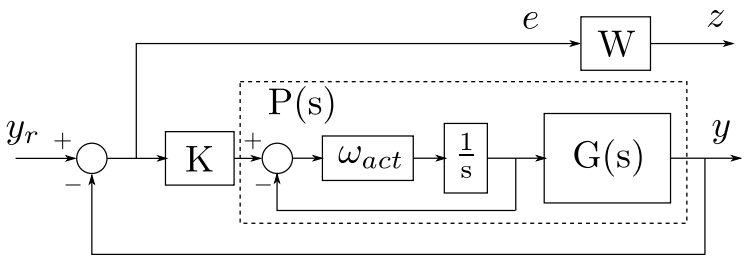

Figure 6.1 – Illustration of H_∞ control and co-design.

1. The singular values of the complex matrix $\mathbf{T}_{\mathbf{w}\to\mathbf{z}}(s)$ are the square root of the eigen-values of the Hermitian matrix: $\mathbf{T}^*_{\mathbf{w}\to\mathrm{z}}(s)\mathbf{T}_{\mathbf{w}\to\mathrm{z}}(s)$ where * denotes the complex conjugate transpose.

The transfer between the reference input y_r and the signal z, $\mathrm{T}_{y_r \to z}$ is expressed as:

$$\begin{aligned}
\mathrm{T}_{y_r \to z} &= \mathrm{W}\mathrm{T}_{y_r \to e}, \\
\mathrm{T}_{y_r \to z} &= \mathrm{W}\left(1 - \mathrm{T}_{y_r \to y}\right), \\
\mathrm{T}_{y_r \to z} &= \mathrm{W}\left(1 - \frac{P(s)\mathrm{K}}{1 + \mathrm{P}(s)\mathrm{K}}\right), \\
\mathrm{T}_{y_r \to z} &= \mathrm{W}\left(1 + \mathrm{P}(s)\mathrm{K}\right)^{-1}, \qquad (6.8)
\end{aligned}$$

with $(1 + P(s)\mathrm{K})^{-1}$ the definition of the sensitivity function $S(s)$. Then:

$$\mathrm{T}_{y_r \to z} = \mathrm{W}S(s). \qquad (6.9)$$

The weighting block is set by the user to assign the desired closed loop dynamics by $\mathrm{W} = \frac{1}{S_{\mathrm{des}}}$. For example, let the desired response of the system to a solicitation be a first order dynamic with bandwidth ω_{des}. S_{des} takes the form of a high pass filter to reject tracking errors at frequencies lower than ω_{des}:

$$\mathrm{W} = \frac{1}{S_{\mathrm{des}}} = \left[\frac{s}{s + \omega_{\mathrm{des}}}\right]^{-1}. \qquad (6.10)$$

Therefore, if the H_∞ norm of $\mathrm{W}S(s)$ is lower or equal to one, the transfer $\mathrm{T}_{y_r \to e}$ will be, at most equal to W^{-1}, and for any sinusoidal reference signal of finite energy $y_r \in \mathcal{L}_2$, the error signal e will be at most equal to $\|S_{\mathrm{des}} y_r\|_\infty$. The control design problem can hence be written using the H_∞ norm. Given a real positive γ:

$$\text{Find K,} \qquad (6.11)$$

$$\text{such that :}$$

$$\|\mathrm{T}_{y_r \to z}\|_\infty = \left\| \frac{(1 + \mathrm{P}(s)\mathrm{K})^{-1}}{S_{\mathrm{des}}} \right\|_\infty \leq \gamma,$$

$$\text{with :}$$

$$S_{\mathrm{des}} = \frac{s}{s + \omega_{\mathrm{des}}}$$

A controller $\widehat{\mathrm{K}}$ solution of (6.11) with $\gamma \leq +\infty$ guarantees stability of the system with a modulus margin at least equal to $\frac{1}{\gamma}$. For any harmonic reference input signal

y_r an upper bound on the servo-loop error is guaranteed:

$$\|T_{y_r \to e}(s)\|_\infty \leq \gamma \|S_{\text{des}}\|_\infty \, . \tag{6.12}$$

The control design problem is solved with optimization algorithms based on LMIs, Riccati equations or non-smooth optimization techniques depending on the order of the controller. The order refers to the number of states of the plant $P(s)$ to control. In the special case where the order of the controller is equal to the order of the plant, hence the term "full-order", the problem becomes convex and efficient numerical methods can be used [Gahinet 2011]. The use and implementation of full order controllers is discussed in [Gahinet 2011] and [Zhou 1998].

Controllers of lower orders can be used in combination with non-convex optimization to solve problem (6.11) (see for example the calculation of longitudinal aircraft control laws in [Gabarrou 2013]). These optimization tools allow the inclusion of additional constraints on the structure of the controller. Hence, the parameters of a fixed-structure controller satisfying problem (6.11) can be calculated.

6.1.2.2 Co-design with H_∞ objectives

Since non-smooth optimization works with a set of decision variables, the gains of the fixed order controller, the idea for the co-design is to include some of the plant's parameters in the set of decision variables. An objective function is created to manage the trade off between the performance of the controller and the plant's parameters or to minimize a metric. It can be for example to minimize the actuator bandwidth so as to reduce the plant's costs.
In this case, given a real positive γ, the codesign problem is:

$$\widehat{K}, \, \widehat{\omega}_{act} = \arg \min_{K, \omega_{act}} \omega_{act}, \tag{6.13}$$

such that:

$$\left\| \frac{(1 + P(s)K)^{-1}}{S_{\text{des}}} \right\|_\infty \leq \gamma.$$

The advantages of the co-design can now be fully appreciated with the possibility to optimize the design of the plant and guarantee a control performance in parallel. An example of such actuator/controller co-design in illustrated in [Alazard 2013].

Non-smooth optimization tools implemented in the Matlab® function `systune`

are used in this work. The main drawback of these tools is that convergence to local optimum is provided. Because of the nature of the H_∞ norm, by definition non-smooth (max of a function) and the non-smooth optimization, there is no guarantee to find a global optimum. Multiple evaluations with varying initial solutions are necessary to overcome this difficulty. For more details on this solver the reader is referred to [Apkarian 2006], [Gahinet 2011], [Apkarian 2012].

Practical example of a co-design

A remarkable introduction to co-design with a pendulum is given in [Denieul 2016] and to illustrate how co-design is used in this work, an example is given here based on the block diagram in Fig 6.2.

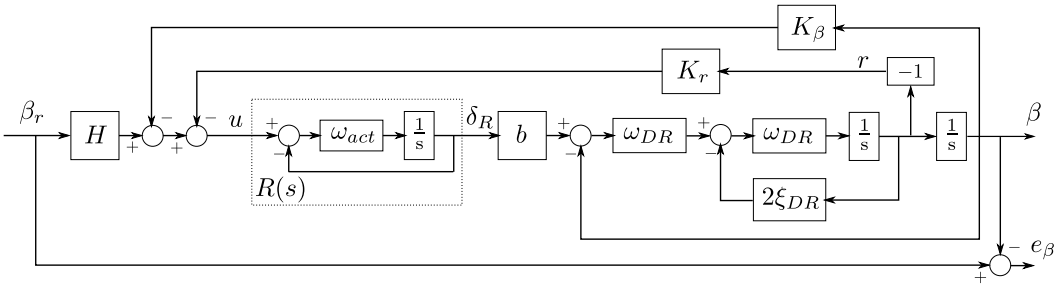

Figure 6.2 – Illustration of H_∞ control and co-design on a second order model imitating the Dutch-Roll.

An oscillator that mimics the Dutch Roll of the reference ATR72 aircraft is used as a representative example. First the control laws will be calculated to answer a prescribed dynamic. Then the actuator bandwidth will be minimized with a co-design. The frequency $\omega_{DR} = 1.0\,\text{rad/s}$ and the damping $\xi_{DR} = 0.15$ of the Dutch Roll calculated in section 6.2 are used to construct the oscillatory system. To be more illustrative the two states are designated as the side slip β and the yawing rate r, where one uses the simplification $\dot{\beta}_a = -r$. The input is assumed to be a rudder deflection generating a yawing moment only, with efficiency $b = 0.6$ and the actuator dynamic, denominated $R(s)$, remains first order. β and r are both measured and used as feedback signals.

The tracking of the reference side slip β_r is performed with two state feedback gains K_r, K_β and a feed-forward gain H. From the block diagram of Fig 6.2, the side slip output $\beta(s)$ can be expressed as a function of the rudder deflection signal $\delta_R(s)$:

$$\beta(s) = \frac{\delta_R(s) b \omega_{DR}^2}{s^2 + 2\xi_{DR}\omega_{DR}s + \omega_{DR}^2}\,. \tag{6.14}$$

In turn, the rudder deflection can be expressed as a function of the states, the controller gains, the reference side slip and the actuator dynamic:

$$\delta_R(s) = \left[H\beta_r(s) - K_\beta\beta(s) + K_r r(s)\right] R(s)\,. \tag{6.15}$$

Then using $r(s) = -s\beta(s)$, the transfer function between $\beta_r(s)$ and $\beta(s)$, $T_{\beta_r\to\beta}(s) = \frac{\beta}{\beta_r}(s)$ can be written:

$$\begin{aligned}\beta(s) &= \frac{\left[H\beta_r(s) - \left(K_\beta + sK_r\right)\beta(s)\right] R(s) b\omega_{DR}^2}{s^2 + 2\xi_{DR}\omega_{DR} + \omega_{DR}^2}\,,\\ \frac{\beta}{\beta_r}(s) &= \frac{R(s)Hb\omega_{DR}^2}{s^2 + \left(2\xi_{DR}\omega_{DR} + R(s)K_r b\omega_{DR}^2\right)s + \left(R(s)K_\beta b + 1\right)\omega_{DR}^2}\,.\end{aligned} \tag{6.16}$$

Finally the error signal $e_\beta(s)$ and the transfer between the reference side slip to the error $T_{\beta_r\to e_\beta}(s) = \frac{e_\beta}{\beta_r}(s)$ can be expressed:

$$\begin{aligned}e_\beta(s) &= \beta_r(s) - \beta(s)\,,\\ \frac{e_\beta}{\beta_r}(s) &= \left(1 - \frac{\beta}{\beta_r}(s)\right)\,,\\ \frac{e_\beta}{\beta_r}(s) &= \frac{s^2 + \left(2\xi_{DR}\omega_{DR} + R(s)K_r b\omega_{DR}^2\right)s + \left((K_\beta - H)R(s)b + 1\right)\omega_{DR}^2}{s^2 + \left(2\xi_{DR}\omega_{DR} + R(s)K_r b\omega_{DR}\right)s + \left(R(s)K_\beta b + 1\right)\omega_{DR}^2}\,.\end{aligned} \tag{6.17}$$

The first goal is compute the controller gains K_β, K_r and H such that the system has a closed loop frequency of $\omega_{\text{des}} = 0.5\,\text{rad/s}$ and the steady state error is zero. This can be done analytically with the transfer function $T_{\beta_r\to e_\beta}$. For example the closed loop frequency can be imposed by setting:

$$\left(R(s)K_\beta b + 1\right)\omega_{DR}^2 = \omega_{\text{des}}^2\,,$$

which can be used to determine the gain K_β, especially if the actuator dynamic $R(s)$ can be neglected with ω_{act} sufficiently high with respect to the oscillator dynamic (it is the case for the initial value of $\omega_{act} = 10\,\text{rad/s}$). Then the feed-forward gain H can be computed analytically to ensure a null DC-gain on the transfer function (6.17) since $R(0) = 1\ \forall\ \omega_{act}$:

$$H = K_\beta + \frac{1}{b}\,.$$

The control design using H_∞ norm allows to compute all gains at once by im-

posing the constraint:

$$\left\| \frac{e_\beta}{\beta_r}(s) \right\|_\infty \leq \|1.2 S_{\text{des}}(s)\|_\infty \ ,$$

where the factor 1.2 is present to account for the waterbed effect [Stein 2003] and the frequency template S_{des} takes the form of a first order high pass filter, fixing the dynamic of the system and ensuring reference tracking at low frequencies:

$$\left\| \frac{s^2 + \left(2\xi_{DR}\omega_{DR} + R(s)K_r b\omega_{DR}^2\right) s + \left((K_\beta - H)R(s)b + 1\right)\omega_{DR}^2}{s^2 + \left(2\xi_{DR}\omega_{DR} + R(s)K_r b\omega_{DR}\right) s + \left(R(s)K_\beta b + 1\right)\omega_{DR}^2} \right\|_\infty \leq \left\| \frac{1.2s}{s + 0.5} \right\|_\infty . \tag{6.18}$$

Since the actuator is a first order dynamics, there are three poles with associated damping $\xi_{i=1,\,2,\,3.}$. A constraint is added to ensure a sufficient damping of the poles and avoid too large gains. The problem for the control design can be written:

$$\text{Find: } \widehat{K_\beta}, \widehat{K_r}, \widehat{H} \ , \tag{6.19}$$

Such that:

$$\left\| \frac{e_\beta/\beta_r(s)}{S_{\text{des}}(s)} \right\|_\infty \leq 1 \, ,$$

$$\xi_i \geq 0.6 \, .$$

For the co-design, the actuator bandwidth is minimized. Inevitably, it will no longer be possible to ignore its dynamic in the calculation of the gains. This can render the analytical solution more difficult to obtain while it is already taken into account in the co-design problem by the constraints previously defined.
The co-design problem is written:

$$\widehat{\mathbf{K}}, \ \widehat{\omega}_{act} = \arg \min_{\mathbf{K}, \omega_{act}} \omega_{act}, \tag{6.20}$$

with: $\mathbf{K} = [K_\beta, K_r, H]$ and such that:

$$\left\| \frac{e_\beta/\beta_r(s)}{S_{\text{des}}(s)} \right\|_\infty \leq 1 \, ,$$

$$\xi_{i=1,\,2,\,3.} \geq 0.6 \, .$$

The resulting gains, the actuator bandwidth and the poles after the two design steps are presented in Table 6.1. The initial step 0, gives the characteristics of the system in open loop with the two complex conjugate poles of the oscillator and the real pole of the actuator.

Parameters	Step 0	Step 1	Step 2
$\widehat{\omega}_{act}$ (rad/s)	10	10	4.1
$\widehat{K}_\beta$	0	0.77	0.47
$\widehat{K}_r$	0	4.70	4.19
H	0	2.42	2.12
$\omega_{\lambda_{1,2}}$ (rad/s)	1.0	5.2	3.25
$\xi_{\lambda_{1,2}}$	0.15	0.94	0.6
ω_{λ_3} (rad/s)	10	0.54	0.49
ξ_{λ_3}	1.0	1.0	1.0

Table 6.1 – H_∞ control and codesign applied to a second order model of the Dutch-Roll.

After step 1, the gains are tuned and the constraints are easily satisfied since the two complex conjugate poles have a damping largely exceeding 0.6. The third real pole becomes the dominant one at a frequency of $\omega_{\lambda_3} = 0.54\,\text{rad/s}$. Fig 6.3a shows the transfer function $T_{\beta_r \to e_\beta}$ and the frequency template S_{des}, it illustrates the fact the constraints are easily satisfied as the transfer function does not saturate the frequency template in low-frequency. Thus the solution from step 1 reveals a performance margin in low frequency.

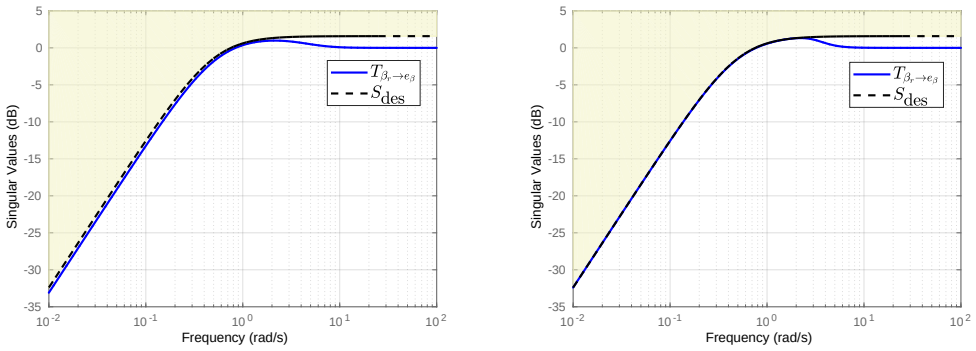

(a) Step 1. (b) Step 2.

Figure 6.3 – Bode plots of the transfer function $T_{\beta_r \to e_\beta}$.

After step 2, the actuator bandwidth is reduced to 4.1 rad/s. This represents

the best trade off with respect to the damping of the complex conjugate poles which now reach the minimum bound of 0.6. Fig 6.3b confirms this observation since the transfer function now almost overlays the frequency template.

6.2 Dynamic aircraft model with varying VT surface area

In this section, the impact of the vertical tail surface area on the aircraft open loop dynamics is reviewed before explaining how the variability of the VT is implemented in the co-design.

6.2.1 Variation of the Vertical Tail Surface Area

The aerodynamic variations accompanying geometrical changes in the VT are captured with the semi-empirical model VEDSC (see section 2.2). Coupled with the trim algorithm detailed in section 1.5, it allows the computation of a collection of linearised systems $[\mathbf{A}_{D,j}, \mathbf{B}_{D,j}]$, recalling section 1.6:

$$\begin{pmatrix} \dot{\tilde{\beta}} \\ \dot{\tilde{p}} \\ \dot{\tilde{r}} \\ \dot{\tilde{\phi}} \end{pmatrix} = \mathbf{A}_{D_j} \begin{pmatrix} \tilde{\beta} \\ \tilde{p} \\ \tilde{r} \\ \tilde{\phi} \end{pmatrix} + \mathbf{B}_{D_j} \begin{pmatrix} \tilde{\delta}_a \\ \tilde{\delta}_R \\ \tilde{\delta}_{x,1} \\ \vdots \\ \tilde{\delta}_{x,12} \end{pmatrix} . \tag{6.21}$$

Each system is representative of a particular VT surface area indicated by the subscript $j = 10\frac{S_v}{S_{v_0}}$. With this collection, the evolution of the lateral mode of the aircraft with varying VT surface area can be plotted in Fig 6.4. This result is obtained for the flight condition $[V_a, \beta_a, \gamma_a, \Omega] = [1.3V_{\text{sr}}, 0°, 3\%, 0°/s]$, which was selected at the end of Chapter 4. Aircraft with the two considered aerodynamic models, referred to as "simple aerodynamics" and "interactions" are represented in Fig 6.4 (see point 1 and respectively point 2 of section 4.2 for the differences between these models).

As the vertical tail reduces, the side slip oscillation gradually becomes unstable and changes to an aperiodic divergent behaviour for values $S_{\text{v}}/S_{\text{v}_0} \leq 0.2$ with two unstable real poles.

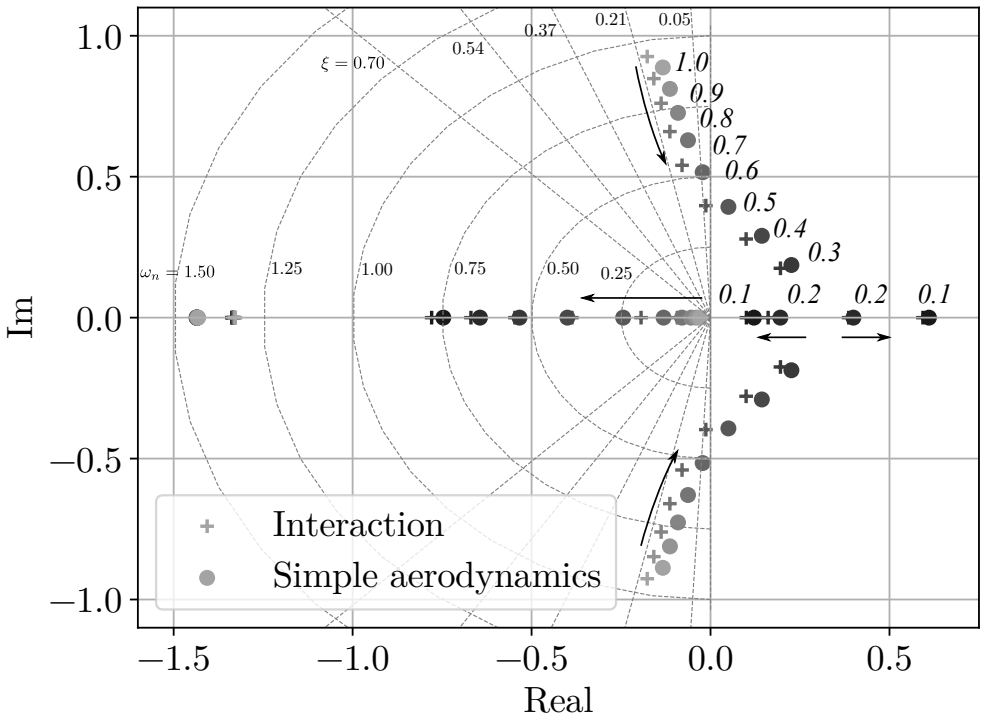

Figure 6.4 – Evolution of lateral modes of the reference aircraft with the reduction of the VT surface area, from $S_v/S_{v_0} = 1$ to $S_v/S_{v_0} = 0.1$. The number in italic next to an eigenvalue indicates the corresponding S_v/S_{v_0}. Regular numbers next to radial and circumferential dashed line refer to damping and natural frequency respectively.

In parallel, the spiral mode is pushed further into the negative plane while no significant changes can be observed in the roll subsidence mode.

There is little difference in the evolution of the modes between simple aerodynamics and interaction model. The aircraft with interactions has poles slightly shifted to the left hand side, except for the Roll Subsidence mode which is slightly shifted to the right hand side. This shows a slightly better damped Dutch Roll and slightly slower Roll mode in the presence of interactions. This shift has no impact on the system behaviour except for $S_v/S_{v_0} = 0.5$ where the interactions are sufficient to bring the Dutch roll back in the negative real plane.

Based on this comparison, it would be sufficient to determine the aircraft flight dynamics with the simple aerodynamic model for the control design, as it represents a conservative case. The same figure at airspeed $1.13V_{sr}$ is available in Annex B.1 and leads to the same conclusion. There remains an important difference between

simple aerodynamic and interaction models: the difference in motor, or actuator, thrust efficiency. This difference had a significant impact on the directional flight envelop as demonstrated in Part II, mainly in Chapter 4. Based on this knowledge, the comparison between the two aerodynamic models will be continued later in Chapter 7 to quantify the impact of aerodynamic interactions on the co-design.

6.2.2 Linear Fractional Representation

The collection of lateral linear systems $[\mathbf{A}_{D,j}, \mathbf{B}_{D,j}]$ is conveniently used during co-design under a Linear Fractional Representation (LFR). In this representation the fixed dynamics of the model is gathered into one block $\mathbf{M}$ composed of linear time invariant matrices, while the varying parameter is stored in a block diagonal matrix $\mathbf{\Delta}$ as illustrated in Fig 6.5.

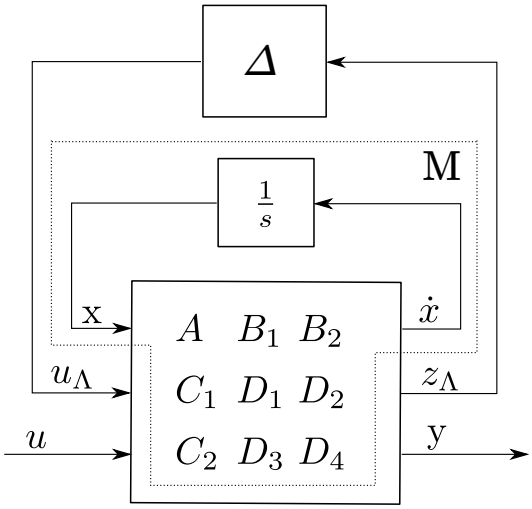

Figure 6.5 – Linear Fractional Representation (LFR) further simplified to $M - \Delta$ form.

The $\mathbf{M} - \mathbf{\Delta}$ form is commonly used to represent a model uncertainty and tools are available to compute the matrices A to D_4 in Fig 6.5 from tabulated data. The set of linear systems is computed for VT surface area ranging from $0.1S_{\mathrm{v},0}$ to $1.2S_{\mathrm{v},0}$, with steps of $0.1S_{\mathrm{v},0}$. The Matlab® toolbox APRICOT [Roos 2014] is used to compute the LFR from these data. A linear approximation (Matlab® function `lsapprox`) with polynomial of degree 3 is selected to keep the maximum root-mean-square error lower than 1% which is quite sufficient at this preliminary design phase.

Then $\mathbf{\Delta} = \delta_v \, \mathbf{1}_{n_\Delta}$ where $\delta_v = S_\mathrm{v}/S_{\mathrm{v}_0}$ is the tail surface ratio, varying between

0.1 to 1.2 and $\mathbf{1}_{n_\Delta}$ is the $n_\Delta \times n_\Delta$ identity matrix of the size of the resulting LFR.

6.3 Control Architecture and System Block Diagram

The strategy for the control design is to keep a simple architecture, specifically integral controllers are not employed to avoid dealing with anti-wind up in preliminary design. It is a conservative approach to cope with the design uncertainties associated with the preliminary design phase.

6.3.1 Control Architecture

The longitudinal/lateral flight control law is depicted in Fig 6.6 and involves:

— static feed-forward gains $\mathbf{H}_L$ (2×2) and $\mathbf{H}_D$ (2×2), respectively for the longitudinal and the lateral motion, to scale the DC-gain between the reference signals $\mathbf{w} = [V_r,\, V_{z_r},\, \beta_r,\, \phi_r]^T$ and outputs $\mathbf{z} = [V,\, V_z,\, \beta,\, \phi]^T$,

— static feedback gains $\mathbf{K}_L$ (2×2) linked to the airspeed V_a and the flight path angle γ_a, $\mathbf{K}_D$ (2×4), linked to the side slip β_a, the roll and yaw rates p, r and the bank angle ϕ, for the longitudinal, and lateral motion, for flight control,

— a longitudinal inner loop to control the short period mode through the gains K_α and K_q,

— the symmetrical thrust and differential thrust allocation matrices $\mathbf{L}_L$ (6×1) and $\mathbf{L}_D$ (6×1), where $\mathbf{L}_L = [L_{L_1},\, 0,\, 0,\, 0,\, 0]$ means that motor 1 and 12 are actuated at level L_1 and similarly for $\mathbf{L}_D$ (see Fig 1.4 and Fig 2.2 for the motor placement and numbering on the aircraft).

This set of gains (in green boxes in Figure 6.6) are the control decision variables $\mathcal{K}$ to be tuned by the optimization process for the control design:

$$\mathcal{K} = \{\mathbf{H}_L, \mathbf{H}_D, \mathbf{K}_L, \mathbf{K}_D, K_\alpha, K_q, \mathbf{L}_L, \mathbf{L}_D\}\ .$$

The whole allocation matrix, for the 12 throttle commands, reads:

$$\mathbf{A}_{12\times 2} = \begin{bmatrix} \mathbf{1}_6 & \mathbf{1}_6 \\ \mathbf{P}_6 & -\mathbf{P}_6 \end{bmatrix} \begin{bmatrix} \mathbf{L}_L & \mathbf{0}_{6\times 1} \\ \mathbf{0}_{6\times 1} & \mathbf{L}_D \end{bmatrix} = \begin{pmatrix} \mathbf{L}_L & \mathbf{L}_D \\ \mathbf{P}_6\mathbf{L}_L & -\mathbf{P}_6\mathbf{L}_D \end{pmatrix} = [\mathbf{A}_l \mathbf{A}_d]\,,$$

where the permutation matrix $\mathbf{P}_n$ is defined by:

$$\mathbf{P}_n(i,j) = \begin{cases} 1 \text{ if: } i+j = n+1, \\ 0 \text{ otherwise.} \end{cases}$$

Note that, with this matrix, a symmetric, respectively anti-symmetric allocation is forced for longitudinal, respectively lateral control input. In addition, $\mathbf{S} = \text{diag}([1, \frac{1}{V}, \frac{\pi}{180}, \frac{\pi}{180}])$ is an input shaping gain to take into account the reference input on vertical velocity $V_z \approx V\gamma$ since requirements specify decoupling between V and V_z (see for example [Döll 1997]), the side slip and bank angle reference inputs $\widetilde{\beta}_r$ and $\widetilde{\phi}_r$ are expressed in degrees. Thus, a unitary step on each of the 4 components of the reference input $\mathbf{w}$ is expected to create roughly the same thrust magnitude.

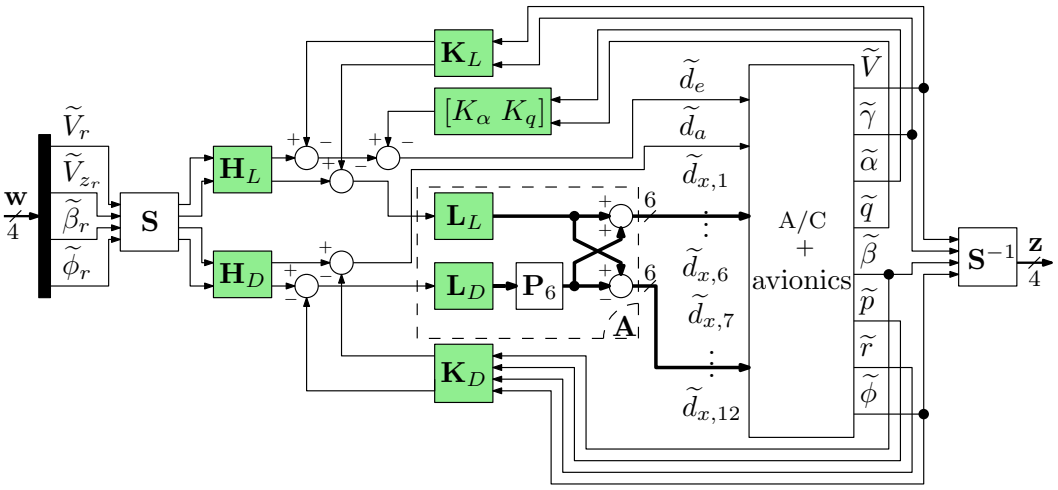

Figure 6.6 – The longitudinal/lateral closed-loop control block-diagram.

The aircraft (A/C) and avionics block of Figure 6.6 is detailed in Figure 6.7. It consists of the fixed longitudinal dynamics and the lateral dynamics (in LFR form) completed by the avionics model between the required control signals $\widetilde{d}_e$, $\widetilde{d}_a$, and $\widetilde{d}_{x,i}$ $(i = 1, \cdots 12)$ computed by the control law and the really applied actuations $\widetilde{\delta}_e$, $\widetilde{\delta}_a$ and $\widetilde{\delta}_{x,i}$. This avionics block considers a second order model on each of the 14 actuators with a damping ratio of 0.7 and a cut-off frequency of ω_e, ω_a and ω_p on the elevator, the ailerons and the 12 propeller motors, respectively. In this block, 2 additional decision variables (in green) are added for the optimization process: the vertical tail surface ratio δ_v (n_Δ occurrences) and the propeller motor bandwidth ω_p (24 occurrences), referred to as design variables to distinguish from the control variables $\mathcal{K}$.

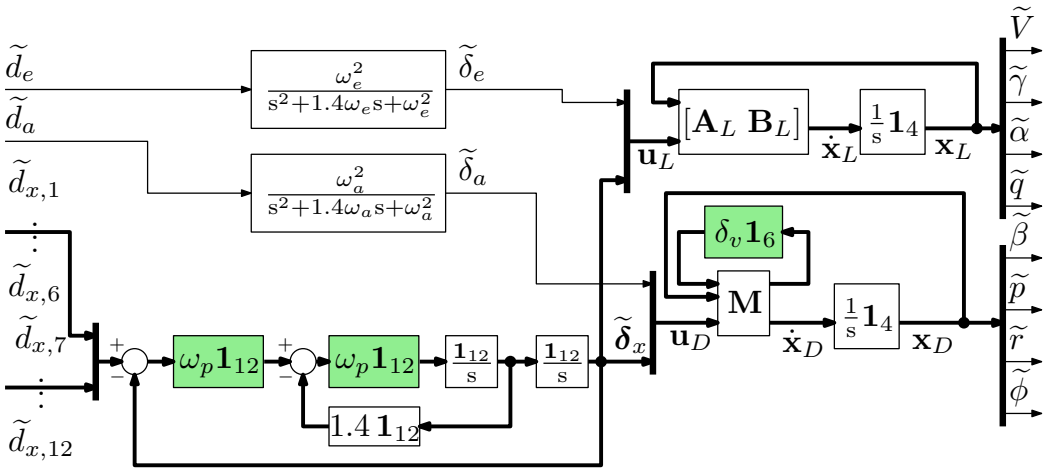

Figure 6.7 – The A/C + avionics block-diagram.

6.3.2 Initialization of Control laws

The control law gains and the allocation matrix are decision variables $\mathcal{K}$ to be computed during the co-design at the same time as the design variables, δ_v and ω_p as introduced in section 6.1. The structured H_∞ solver provides convergence to a local optimum depending on the initially provided solution. To obtain reasonable and reproducible results, the idea is to initialize the control gains by eigenstructure assignment. The assignment is done with the original VT surface area, thus δ_v is initialized to 1.

Using as example the static lateral state space system $[\mathbf{A}_{D,10}, \mathbf{B}_{10}]$ corresponding to $\delta_v = 1$:

$$\dot{\mathbf{x}}_D = \mathbf{A}_{D,10}\mathbf{x}_D + \mathbf{B}_{D,10}\mathbf{u}_D \ ,$$

$$\mathbf{y}_D = \mathbf{C}_{D,10}\mathbf{x}_D + \mathbf{D}_{D,10}\mathbf{u}_D \ ,$$

which in this case is simplified by assuming all states are observable, hence $\mathbf{C}_{D,10} = \mathbf{I}_4$, and $\mathbf{D}_{D,10} = 0$:

$$\dot{\mathbf{x}}_D = \mathbf{A}_{D,10}\mathbf{x}_D + \mathbf{B}_{D,10}\mathbf{u}_D \ , \tag{6.22}$$

$$\mathbf{y} = \mathbf{x}_D \ .$$

The control law depicted in Fig 6.6, with the feedback and feedforward matrices

$\mathbf{K}_D$, respectively $\mathbf{H}_D$, and the lateral allocation matrix $\mathbf{A}_d$ writes:

$$\mathbf{u}_D = \mathbf{A}_d \left[-\mathbf{K}_D \mathbf{x}_D + \mathbf{H}_D \mathbf{u}_{D_r} \right] , \tag{6.23}$$

with the lateral reference input $\mathbf{u}_{D_r} = (\tilde{\beta}_r, \tilde{\phi}_r)^T$. In this initialisation phase, only motor number 1 and 12 are used for lateral control by setting $\mathbf{L}_D = [1; 0; 0; 0; 0; 0]$. After introducing (6.23) into (6.22), the closed loop system writes:

$$\begin{aligned} \dot{\mathbf{x}}_D &= \mathbf{A}_{D,10}\mathbf{x}_D - \mathbf{B}_{D,10}\mathbf{A}_d\mathbf{K}_D\mathbf{x}_D + \mathbf{B}_{D,10}\mathbf{A}_d\mathbf{H}_D\mathbf{u}_{D_r} , \\ \mathbf{y} &= \mathbf{x}_D . \end{aligned}$$

For the sake of brevity, the following notation is introduced: $\mathbf{B}'_{D,10} = \mathbf{B}_{D,10}\mathbf{A}_d$ and the system reduces to:

$$\begin{aligned} \dot{\mathbf{x}}_D &= \left(\mathbf{A}_D - \mathbf{B}'_{D,10}\mathbf{K}_D \right) \mathbf{x}_D + \mathbf{B}'_{D,10}\mathbf{H}_D\mathbf{u}_{D_r} , \\ \mathbf{y} &= \mathbf{x}_D . \end{aligned} \tag{6.24}$$

The eigenstructure assignment aims at finding the controller $\mathbf{K}_D$ to place the eigen values λ_i of $\left(\mathbf{A}_D - \mathbf{I}_4\lambda_i - \mathbf{B}'_{D,10}\mathbf{K}_D \right)$. This is guaranteed if the controller satisfies [Döll 2001]:

$$\begin{bmatrix} \mathbf{A}_D - \mathbf{I}_4\lambda_i & \mathbf{B}'_{D,10} \end{bmatrix} \begin{pmatrix} v_i \\ w_i \end{pmatrix} = 0, \tag{6.25}$$

$$-\mathbf{K}_D v_i = w_i , \tag{6.26}$$

with v_i the right eigen vector associated with λ_i. The matrix input vector $\mathbf{u}_D$ being of dimension $n_{u_D} = 2$, it is possible to decouple the eigen vectors by imposing at most $n_{u_D} - 1$ additional constraints: $P_i v_i + Q_i w_i = 0$ with $P_i \in \mathbb{R}^{(n_{u_D}-1)\times 4}$ and $Q_i \in \mathbb{R}^{(n_{u_D}-1)\times 2}$. With this additional constraint, equation (6.25) becomes:

$$\begin{bmatrix} \mathbf{A}_D - \mathbf{I}_4\lambda_i & \mathbf{B}'_{D,10} \\ P_i & Q_i \end{bmatrix} \begin{pmatrix} v_i \\ w_i \end{pmatrix} = 0 , \tag{6.27}$$

and the gain $\mathbf{K}_D$ remains given by (6.26). As an example the interest for the initial solution is to have the eigen values of the Dutch Roll mode at $-1 \pm j$ and decoupled

from the bank angle ϕ. In this case, with the state vector being $\mathbf{x}_D = [\beta_a,\, p,\, r,\, \phi]^T$ and the vector of reference signals $\mathbf{u}_D = [\beta_r, \phi_r]$ the corresponding v_i and w_i are found by setting $P_i = [0, 0, 0, 1]$, $Q_i = [0, 0]$ and solving (6.27). Once all λ_i are set and all v_i, w_i are obtained, $\mathbf{K}_D$ is calculated by inverting (6.26).

Additionally, the feedfoward block $\mathbf{H}_D$ is computed to have an identity DC-gain from reference to output:

$$\lim_{s\to 0} \frac{\mathbf{x}_D}{\mathbf{u}_D}(s) = 1\ . \tag{6.28}$$

Using the Laplace transform of equation (6.24):

$$\left[s\mathbf{I}_4 - \mathbf{A}_{D,10} + \mathbf{B}'_{D,10}\mathbf{K}_D\right]\mathbf{x}_D(s) = \mathbf{B}'_{D,10}\mathbf{H}_D\mathbf{u}_{D_r}(s),$$

$$\frac{\mathbf{x}_D}{\mathbf{u}_D}(s) = \frac{\mathbf{B}'_{D,10}\mathbf{H}_D}{s\mathbf{I}_4 - \mathbf{A}_{D,10} + \mathbf{B}'_{D,10}\mathbf{K}_D}\ . \tag{6.29}$$

Applying equation (6.28):

$$\frac{\mathbf{B}'_{D,10}\mathbf{H}_D}{-\mathbf{A}_{D,10} + \mathbf{B}'_{D,10}\mathbf{K}_D} = 1,$$

$$\mathbf{H}_D = \left[\left(-\mathbf{A}_{D,10} + \mathbf{B}'_{D,10}\mathbf{K}_D\right)^{-1}\mathbf{B}'_{D,10}\right]^{-1}, \tag{6.30}$$

where $\mathbf{K}_D$ is previously calculated to assign the eigenstructure. The same procedure is followed for the initialization of the longitudinal control law.
Finally, the complete initialisation routine can be summarized:

1. The initial A/C configuration is defined by $\delta_v = 1.0$. The avionics are assumed without delay and saturation.
2. The allocation matrix $\mathbf{A}$ is initialized with: $\mathbf{L}_L = [0, 0, 0, 0, 0, 1]^T$, $\mathbf{L}_D = [1, 0, 0, 0, 0, 0]^T$ in such a way that symmetrical thrust uses only inner motors 6 and 7 and differential thrust uses only outer motors 1 and 12,
3. Then, using the reduced $(\alpha - q)$ model, K_α and K_q are designed to assign the short-period mode with a natural frequency $\omega_{SP} = 1.2\,\mathrm{rad/s}$ and a damping of $\xi_{SP} = 0.7$, the roots of $\mathrm{s}^2 + 2\xi_{SP}\omega_{SP}\mathrm{s} + \omega_{SP}^2$.
4. $\mathbf{K}_L$ is designed to assign the eigenstructure of the longitudinal long-term model (also called $(V - \gamma)$ model) with two real eigenvalues, *i.e.* place the eigenvalue corresponding to V to -0.2 while decoupling the associated eigenvector from

γ and place the eigenvalue corresponding to γ to -0.3 while decoupling the associated eigenvectors from V. See more details in [Döll 1997]. $\mathbf{H}_L$ is then computed to have an identity DC-gain between $[\widetilde{V}_r,\ \widetilde{\gamma}_r]^T$ and $[\widetilde{V},\ \widetilde{\gamma}]^T$ on this $(V-\gamma)$ model,

5. $\mathbf{K}_D$ is designed to assign the 4 eigenvalues of the lateral model to $-1 \pm j$ for the Dutch-Roll, -1 for the Spiral, -5 for the Roll subsidence mode, and the associated eigenvectors decoupled from ϕ for the Dutch-roll and from β for the Spiral and the Roll subsidence mode. $\mathbf{H}_D$ is then computed to have an identity DC-gain between $[\widetilde{\beta}_r,\ \widetilde{\phi}_r]^T$ and $[\widetilde{\beta},\ \widetilde{\phi}]^T$,

6.4 Sequential Co-Design for design exploration

The sequential co-design is a first, non-optimal approach for co-design. It is used to gain a better knowledge of the system to optimize before applying a more integrated optimization procedure.

6.4.1 Requirements and objectives

The handling qualities are expressed through frequency-domain templates $\mathbf{S}_{o,des}(i,j)$ $(i,j=1,2,3,4)$ on each element of the 4×4 output sensitivity function $\mathbf{S}_o(\mathrm{s}) = \mathbf{1}_4 - \mathbf{T}_{\mathbf{w}\to\mathbf{z}}(\mathrm{s})$ where $\mathbf{T}_{\mathbf{w}\to\mathbf{z}}(\mathrm{s})$ is the closed-loop transfer between $\mathbf{w}$ and $\mathbf{z}$ as depicted in Figure 6.6:

$$\gamma_1 = \max_{i,j=1,2,3,4} \left\| \frac{\mathbf{S}_o(i,j)}{\mathbf{S}_{o,des}(i,j)}(\mathrm{s}) \right\|_\infty \leq 1, \tag{6.31}$$

with:

$$\mathbf{S}_{o,des}(i,j) = \begin{cases} \frac{1.4\,\mathrm{s}}{\mathrm{s}+\omega_i}, \text{ if: } i=j, \\ 0.14, \text{ otherwise.} \end{cases} \quad \text{and :}$$

$$\omega_1 = 0.2,\ \omega_2 = 0.3,\ \omega_3 = \omega_4 = 1\,(rd/s)\ .$$

As introduced in section 6.1, such a multivariate template allows to prescribe low-frequency disturbance rejection and reference input tracking inside the bandwidth ω_1, ω_2 on the servo-loop for V, V_z respectively and ω_3, ω_4 for β and ϕ respectively, while ensuring cross couplings to be lower than 14%. The side slip cut off frequency will be the main focus in the next chapter and is set for now with regard to open-loop behaviour.

To avoid too high gains in the feed-forward path of the control law and so to

reduce as much as possible the thrust magnitude in response to reference inputs, the decision variables must be tuned in order to minimize the maximum of the 12 closed-loop propeller transfer functions $\mathbf{T}_{\mathbf{w}\to\widetilde{d}_{x,i}}$ [2]:

$$J_1 = \max_{i=1,\cdots 12} \left\| \mathbf{T}_{\mathbf{w}\to\widetilde{d}_{x,i}}(\mathrm{s}) \right\|_\infty \ . \tag{6.32}$$

Minimizing the objective function J_1 defined in (6.32) under the constraint defined in (6.31) is performed with the help of Matlab® function `systune` that implements non-smooth optimization tools (discussed in section 6.1.2.2). The challenge here is to minimize also the design parameters δ_v and ω_p using 2 additional objective functions:

$$J_2 = \delta_v \quad \text{and} \quad J_3 = \omega_p \ . \tag{6.33}$$

6.4.2 Multi-step optimization process

The multi-step process described below splits the initial multi-objective optimization problem into several consecutive single objective optimization problems where the previously reached objectives are constrained to stay inside a given sub-optimal solution set for the next optimization step. That allows to better understand the optimization process and to manage the trade-off between the various objective functions which is particularly useful during the preliminary design phase. Furthermore, such an approach is also justified since the different objectives J_1, J_2 and J_3 have not yet normalized units at this step.

6.4.2.1 Step 0: Initialization.

The control gains are initialized as described in section 6.3. The design variables are initialized with $\delta_v = 1$, $\omega_p = 20\,\mathrm{rad/s}$. The elevator and aileron actuator bandwidths are initialized at $\omega_a = \omega_e = 20\,\mathrm{rad/s}$.

2. An important remark is that $\mathbf{T}_{\mathbf{w}\to\widetilde{d}_{x,i}}$ is a multiple input single output transfer matrix and not a vector of SISO transfers. This detail is the main driver in the determination of the allocation matrix during optimisation.

6.4.2.2 Step 1: Optimization on the initial A/C configuration.

This optimization aims at meeting the constraint (6.31) while minimizing J_1 using the control decision variables $\mathcal{K}$:

$$\widehat{\mathcal{K}} = \arg\min_{\mathcal{K}} J_1, \text{ s.t. (6.31) holds.}$$

Let us denote $\widehat{J}_{i,j}$ the optimal value of J_i obtained at step j. Thus $\widehat{J}_{1,1} = \min_{\mathcal{K}} J_1$.

6.4.2.3 Step 2: Vertical tail minimization.

This step aims at minimizing the vertical tail surface J_2 while meeting the constraint (6.31) and keep the objective function J_1 lower than a sub-optimal value $\bar{J}_1 > \widehat{J}_{1,1}$:

$$\{\widehat{\mathcal{K}}, \widehat{\delta}_v\} = \arg\min_{\mathcal{K},\delta_v} J_2, \text{ s.t. (6.31) holds and } J_1 \leq \bar{J}_1.$$

6.4.2.4 Step 3: Motor bandwidth minimization.

This step aims at minimizing the motor bandwidth J_3 while meeting the constraints of step 2 and keep the objective function J_2 lower than a sub-optimal value $\bar{J}_2 > \widehat{J}_{2,2}$:

$$\{\widehat{\mathcal{K}}, \widehat{\delta}_v, \widehat{\omega}_p\} = \arg\min_{\mathcal{K},\delta_v,\omega_p} J_3, \text{ s.t. (6.31) holds and}$$

$$J_1 \leq \bar{J}_1, \quad J_2 \leq \bar{J}_2 \, .$$

$\bar{J}_1$ and $\bar{J}_2$, respectively chosen after step 1 and step 2, can be seen as sub-optimality tolerances required to relax the optimality obtained at the previous step in order to add a new objective at the current step.

6.4.3 Results

In this section, the results of a sequential co-design applied to the aircraft with simple aerodynamic (see Point 1 of Chapter 4) at the flight conditions presented in section 6.2 are presented. The hard constraint γ_1 and the three objective functions J_1, J_2 and J_3 after each step of the optimization process are resumed in Table 6.2.

The big gap between $\widehat{J}_{1,0} = 0.729$ and $\widehat{J}_{1,1} = 0.081$ motivates the choice of sub-optimal values $\bar{J}_1 = 0.15$ for step 2 and 3, while the gap between $\widehat{J}_{2,1} = 1.0$ and $\widehat{J}_{2,2} = 0.1$ the sub-optimal value $\bar{J}_2 = 0.4$. As expected, in step 3, a trade-off between J_2 and J_3 has to be managed. The obtained solution allows the vertical

Table 6.2 – Constraint γ_1 and objective function values during optimization process.

step	γ_1	J_1	$J_2 = \delta_v$	$J_3 = \omega_p\,(rd/s)$
0	1.107	0.729	1.0	20
1	0.999	0.081	1.0	20
2	0.979	0.147	0.1	20
3	0.999	0.149	0.4	5.45

tail surface to be reduced in a significant way ($\widehat{\delta}_v = 0.4$) while using a low propeller motor bandwidth $\widehat{\omega}_p = 5.45\,\text{rad/s}$.

Additionally, it is worth to mention that the initialization does not meet the hard constraint when the full model and avionics are taken into account.

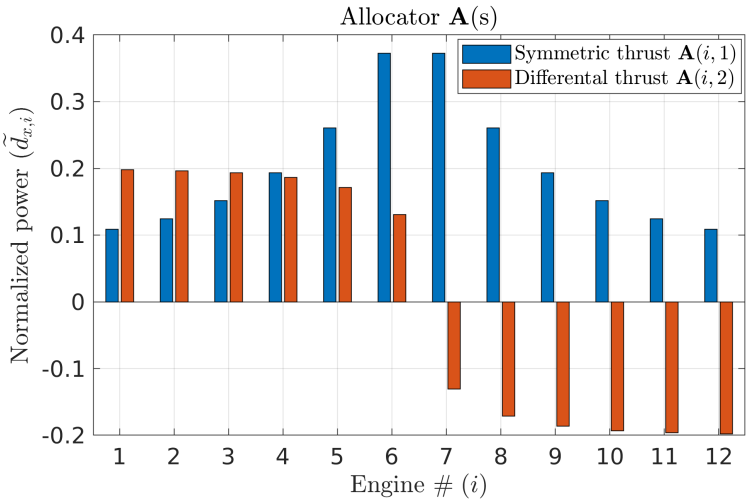

Figure 6.8 – Bar-diagram of the allocation matrix $\mathbf{A}$.

The obtained optimal allocation matrix $\mathbf{A}$ is represented on the bar-diagram of Figure 6.8. As expected, symmetrical thrust uses mainly inner motors while differential thrust takes benefit of the lever-arm effect and uses mainly outer ones. In addition, Figure 6.9 displays the bar-diagram of the direct feed-through from the 4 reference inputs (vector $\mathbf{w}$) to the 12 throttle commands $\widetilde{d}_{x,i}$: $\mathbf{A}\begin{bmatrix} \mathbf{H}_L(2,:) & \mathbf{0}_{1\times 2} \\ \mathbf{0}_{1\times 2} & \mathbf{H}_D(2,:) \end{bmatrix}\mathbf{S}$. Obviously, the most demanding manoeuvres from the total thrust magnitude point of view are the forward velocity $\widetilde{V}_r$ and the side-slip angle $\widetilde{\beta}_r$ command.

The closed loop poles and zeros of the aircraft after step 1 and step 3 are represented in Fig 6.10. The poles after step 3 are all in the negative real plane showing that the aircraft is stable in closed loop despite the natural directional instability.

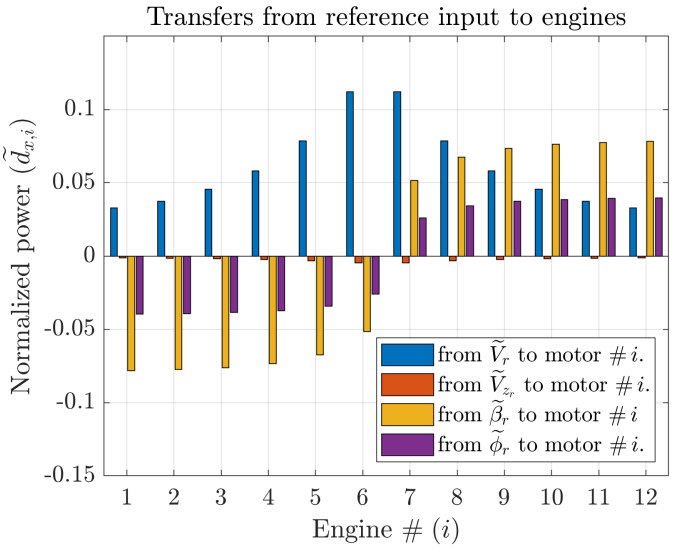

Figure 6.9 – Bar-diagram of the direct feed-through from reference input to throttle commands.

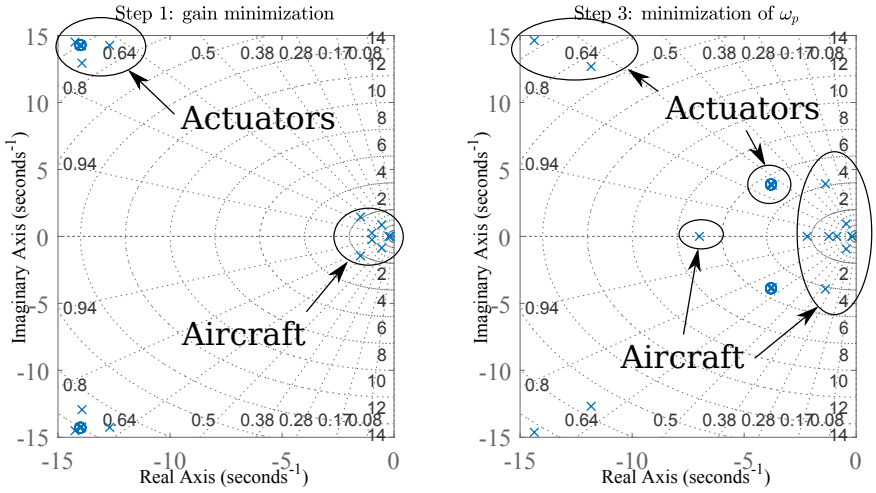

Figure 6.10 – Aircraft poles after step 1 and step 3.

One can observe that all poles are well damped after the gain minimization of step 1 with the exception of a pair of complex conjugate poles located at $-0.56 \pm 0.87i$ (associated damping $\xi = 0.54$ and frequency $\omega = 1.03\,\text{rad/s}$). These poles are associated with the dynamics of the ailerons and the roll subsidence mode (this is illustrated later in section 8.3.2, Fig 8.10). After gain relaxation and minimization of actuator bandwidth, four complex conjugate poles are shifted toward the top right, respectively bottom right of the complex plane, worsening their associated

damping (minimum damping of 0.33 in the case of Fig 6.10). This can be avoided by adding a constraint to the H_∞ synthesis which makes sure that all poles have a damping greater or equal to 0.7. However, as will be seen in Chapter 7, gain limitations translating flight envelop constraints and actuator saturation limits can be sufficient to keep a good damping.

6.5 Conclusion

This chapter introduced the co-design framework to compute the longitudinal and lateral control law of the aircraft without rudder and manual trade off between VT surface area and actuator bandwidth. The codesign methodology similar to [Denieul 2016] was introduced in section 6.1. It is based on non-smooth, multi-objective H_∞ optimization tools. The difference of aircraft open loop dynamics between the simple aerodynamic and interaction models was presented in section 6.2 along with the LFR form used to represent the variation of VT surface area in the codesign. A simple control law, in agreement with a preliminary design phase, is presented in section 6.3. Finally, a sequential co-design was presented in section 6.4 as a first approach to co-design.

The co-design allowed the determination of thrust allocation for both longitudinal and lateral manoeuvres while the trade off between control law gains, VT surface area and actuator bandwidth had to be managed by hand. The results are encouraging with a VT reduction of 60% and small motor bandwidth of $\omega_p = 5.45$ rad/s while satisfying the imposed flight handling qualities, at least in the linear domain. The following limitations remain and should be overcome in the following chapter:

— inclusion of flight envelop requirements,

— no guarantee that the initialization procedure leads to an optimal design,

— use of the simple aerodynamic model is optimistic in regard of motor thrust efficiency.

Chapter 7

Direct Co-Design with flight envelop constraints

Contents

The previous chapter served as setting up the co-design environment and realizing a first design exploration through a sequential co-design. Encouraging results are obtained: large reduction of the vertical tail and motor bandwidth seem possible. The main drawback being that the trade-off between control law gains, VT size and motor bandwidth is manual with the sequential optimization. Using this type of approach can easily result in missing the optimal trade-off. In addition, flight envelop requirements and actuator limitations in regard to longitudinal trim are not yet taken into account. The solution found in the previous chapter is stable and satisfies the required handling qualities, up to actuator saturation and without guarantee on the achievable flight envelop.

The objective of this chapter is to adapt the methodology to obtain a direct co-design and trade-off determined through optimisation. This can be achieved essentially through the addition of constraints translating actuator saturations and flight envelop requirements. Section 7.1 introduces the problem faced with the definition of additional constraints that must translate design requirements and be feasible at the same time. For this, additional knowledge about the design is sought through a sensitivity analysis presented in section 7.2. Finally, with this additional knowledge, the new constraints are formulated and the results of a direct co-design are obtained and discussed in section 7.3.

7.1 Towards a direct co-design: transcription of actuator saturation into frequency constraints

Additional constraints are formulated based on flight envelop and actuator saturation. For the aircraft to achieve a certain flight envelop in side slip using differential thrust, motor power level must remain within the continuous power range. This translates as an upper bound on the steady state gain between reference input and actuator entries. Additionally, to avoid disturbing the longitudinal dynamics, differential thrust must be anti-symmetric, such that the saturation limit for differential thrust depends on the power level at the trim condition.

The motor saturation limits depending on the trim level $d_{x_i,trim}$ are first introduced:

$$\bar{d}_{x,i} = \min\left[1 - \max(d_{x_i,\,\mathrm{trim}}),\ \min(d_{x_i,\,\mathrm{trim}})\right] \ , \tag{7.1}$$

$$\underline{d}_{x,i} = \max(1 - d_{x_i,\,\mathrm{trim}}, d_{x_i,\,\mathrm{trim}}) \, . \tag{7.2}$$

The first saturation to be hit is $\bar{d}_{x,i}$. It is possible to increase the yawing moment beyond the first limit without respecting an anti-symmetric differential thrust, resulting in disturbances on the longitudinal axis. The second saturation limit $\underline{d}_{x,i}$ represents the maximum yawing moment that can be generated by differential thrust.

Referring to Fig 6.9, it is recalled that the level of thrust during a manoeuvre is given by $\tilde{d}_{x,i}(s) = \mathrm{T}_{\tilde{\beta}_r \to \tilde{d}_{x,i}}(s)\beta_r(s)$. A constraint can therefore be expressed as a maximum gain on the transfer function $\mathrm{T}_{\tilde{\beta}_r \to \tilde{d}_{x,i}}$ as a function of the trim power level:

$$\bar{d}_{x,i} \geq \left|\tilde{d}_{x,i}(s)\right| = \left|\mathrm{T}_{\tilde{\beta}_r \to \tilde{d}_{x,i}}(s)\beta_r(s)\right| \, . \tag{7.3}$$

Equation (7.3) must be turned into a constraint during steady states to ensure a certain achievable directional flight envelop. In this case using the final value theorem, equation (7.3) becomes:

$$\bar{d}_{x,i} \geq \lim_{s\to 0}\left|\tilde{d}_{x,i}(s)\right| = \lim_{s\to 0}\left|s\mathrm{T}_{\tilde{\beta}_r \to \tilde{d}_{x,i}}(s)\beta_r(s)\right| \, ,$$

if $\beta_r(s)$ is a step of amplitude β_{req}, then:

$$\bar{d}_{x,i} \geq \lim_{s\to 0}\left|\tilde{d}_{x,i}(s)\right| = \lim_{s\to 0}\left|s\mathrm{T}_{\tilde{\beta}_r \to \tilde{d}_{x,i}}(s)\frac{\beta_{\mathrm{req}}}{s}\right| \, ,$$

which can be reduced to:

$$\left|\lim_{s\to 0} \mathrm{T}_{\tilde{\beta}_r \to \tilde{d}_{x,i}}(s)\right| \leq \frac{\bar{d}_{x,i}}{\beta_{\mathrm{req}}} \,. \tag{7.4}$$

Constraint (7.4) requires that the absolute value of the steady state gain of the transfer function $\mathrm{T}_{\tilde{\beta}_r \to \tilde{d}_{x,i}}(s)$ should be lower than the first saturation limit $\bar{d}_{x,i}$ weighted by the required flight envelop side slip angle β_{req}.

During transient manoeuvres, it is possible that the imposed handling qualities require a large gain that can temporarily saturate the engines. In this case, saturation is tolerable if it leads to slightly degraded handling qualities. However, it is desirable to avoid this scenario and the constraint (7.4) could be generalized to the full frequency range by rearranging equation (7.3):

$$1 \geq \left|\mathrm{T}_{\tilde{\beta}_r \to \tilde{d}_{x,i}}(s)\beta_r(s)\right| \frac{1}{\bar{d}_{x,i}} \,,$$

and taking the maximum norm when $\beta_r(s)$ is a Dirac impulse of amplitude β_{req}:

$$\left\| \mathrm{T}_{\tilde{\beta}_r \to \tilde{d}_{x,i}}(s) \frac{\beta_{\mathrm{req}}}{\bar{d}_{x,i}} \right\|_\infty \leq 1 \,. \tag{7.5}$$

With the exploration made so far, it is not clear which design variable influence most the thrust level required to achieve prescribed flight envelop and handling qualities. Uncertainties remain on lateral closed loop transfer functions and more particularly on $\mathrm{T}_{\tilde{\beta}_r \to \tilde{d}_{x,i}}(s)$. Additionally, it is not certain that equation (7.5) and equation (6.31) can be both satisfied, which would lead to a dead end during optimisation. To answer these questions and refine the constraints definition, a sensitivity analysis is conducted using the framework already available.

7.2 Sensitivity analysis

The sensitivity analysis will be conducted on the ATR72 with simple aerodynamics and with aeropropulsive interactions (respectively point 1 and point 2 of Chapter 4) in parallel. Only symmetric thrust cases are studied, asymmetric thrust conditions will be discussed in Chapter 8.

7.2.1 Methodology

The idea for the sensitivity analysis is to minimize criterion J_1 (minimum gain, see equation (6.32)) under handling qualities constraints (6.31) and track the transfer functions $\widehat{\mathrm{T}}_{\tilde{\beta}_r \to \tilde{d}_{x,i}}(s)$. After optimizing for J_1, $\widehat{\mathrm{T}}_{\tilde{\beta}_r \to \tilde{d}_{x,i}}(s)$ represents the minimum transfer function needed to achieve handling qualities with the imposed set of vertical tail and motor bandwidth. Key quantities are then calculated from $\widehat{\mathrm{T}}_{\tilde{\beta}_r \to \tilde{d}_{x,i}}(s)$: the maximum steady state gain (7.6) to measure the achievable flight envelop, the maximum H_∞ norm (7.7) and corresponding frequency (7.8) for transient manoeuvres.

$$C_1 = \frac{\lim\limits_{s\to 0} \widehat{\mathrm{T}}_{\tilde{\beta}_r \to \tilde{d}_{x,i}}(s)}{\left|\lim\limits_{s\to 0} \widehat{\mathrm{T}}_{\tilde{\beta}_r \to \tilde{d}_{x,i}}(s)\right|} \max_{i=1,\cdots 12} \left|\lim_{s\to 0} \widehat{\mathrm{T}}_{\tilde{\beta}_r \to \tilde{d}_{x,i}}(s)\right| , \tag{7.6}$$

$$C_2 = \max_{i=1,\cdots 12} \left\| \widehat{\mathrm{T}}_{\tilde{\beta}_r \to \tilde{d}_{x,i}}(s) \right\|_\infty , \tag{7.7}$$

$$C_3 = \omega_{H_\infty} , \tag{7.8}$$

such that:

$$\max_{i=1,\cdots 12} \left| \widehat{\mathrm{T}}_{\tilde{\beta}_r \to \tilde{d}_{x,i}}(j\omega_{H_\infty}) \right| = C_2 .$$

The set of parameters that are varied in the analysis is defined as follows:

$$\delta_{\mathbf{p}} = [\delta_v, \omega_p, \omega_3, \bar{q}], \tag{7.9}$$

respectively, the VT surface area, motor cut-off frequency, handling quality template cut-off frequency for the side slip and the dynamic pressure. This last parameter is varied by changing the flight condition.

The standard configuration and starting point for this sensitivity analysis is detailed in Table 7.1. To ensure that the transfer functions $\widehat{\mathrm{T}}_{\tilde{\beta}_r \to \tilde{d}_{x,i}}(s)$ are close to a global optimum during design exploration, the solution of the standard configuration is computed with pole placement initialization as presented in section 6.3 and with multiple random start. The best result is then used as initial solution for the sensitivity analysis.

Table 7.1 – Standard configuration for sensitivity analysis.

Optimization settings	
Constraints	$\gamma_1 \leq 1$
Objective function	J_1
Design Parameters	
δ_v	1
ω_p	20 (rad/s)
ω_3	1 (rad/s)
$\bar{q}$	$0.5\rho_0(1.3V_{\text{sr}})^2$
Reference flight conditions	
Airspeed	$1.3V_{\text{sr}}$
Flight path angle	3%
Altitude	Sea level
Turning rate	0 °/s

7.2.2 Initial solution

The comparison between initialisation with eigenstructure assignment and multiple random start is given in Table 7.2. The solution with random initialisation is marginally better for the aircraft with simple aerodynamics. It shows that the eigenstructure assignment provides an appropriate initial solution.

Table 7.2 – Difference of optimality between initialisation with eigenstructure assignment and multiple random start.

Initialization Method	Simple aerodynamics		Aeropropulsive interaction	
	$\widehat{J}_1$	γ_1	$\widehat{J}_1$	γ_1
Eigenstructure assignment	0.081	0.9998	0.147	0.9994
Multiple random initialisation	0.080	0.9997	0.085	0.9993

For the aircraft with interactions, multiple random start allowed to find a significantly better initial solution than with eigenstructure assignment. The reasons for this difference are :

— For the aircraft with simple aerodynamics model, the two initialization methods giving similar results, it seems that the solution found is close to a global optimum. It may be stated that the co-design problem was almost convex. This is probably due to the fact that the simple aerodynamics model intro-

duces a linear variation of the motor efficiencies with their lateral position on the wing (see section 4.4).

— For the aircraft with aeropropulsive interactions, the two initialization methods lead to different results. It seems that the solutions are sub-optimal solutions for the allocation. This is probably due to the aero-propulsive interaction model introducing non-linearities in the variation of the motor efficiencies (explored in section 4.4).

The key parameter driving these observation has been found to be the final allocation ($\widetilde{d}_{x,i}$: $\mathbf{A}\begin{bmatrix}\mathbf{H}_L(2,:) & \mathbf{0}_{1\times 2}\\ \mathbf{0}_{1\times 2} & \mathbf{H}_D(2,:)\end{bmatrix}\mathbf{S}$), available for the two aircraft in Fig 7.1. One can notice that the allocations are similar for the two aircraft. The main difference with the allocation found for the ATR72 with simple aerodynamics is the input in $\tilde{\phi}_r$ that uses the induced rolling moment offered by DT. Additionally, an input in $\tilde{\beta}_r$ is more distributed with a higher solicitation of the inner motors.

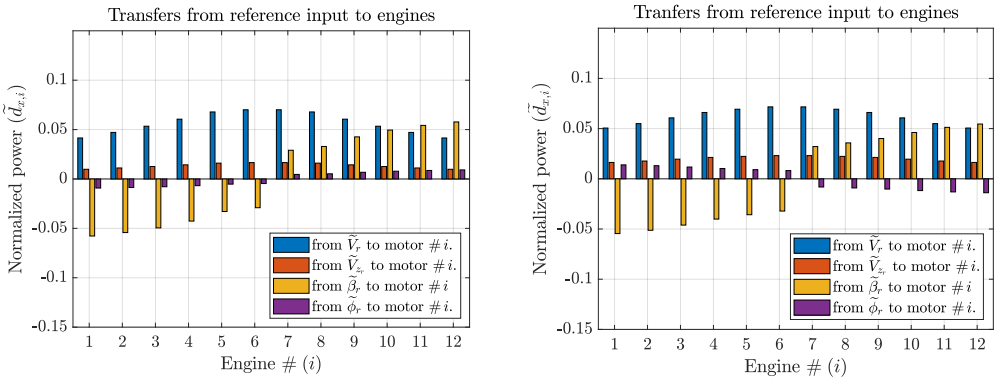

(a) Simple aerodynamics model.

(b) Aeropropulsive interaction model.

Figure 7.1 – Initial solutions allocation.

7.2.3 Variation of Vertical tail surface area and motor bandwidth

The influence of δ_v and ω_p on C_1, C_2 and C_3 is represented in surface plots in Figure 7.2, Figure 7.3 and Figure 7.4.

The analysis of Figure 7.2 reveals that the VT size has a major influence on the steady state gain, whilst the motor bandwidth has negligible impact. This is a reasonable result, as a large vertical tail brings a natural stability to the aircraft, or inversely, an important aircraft instability requires a larger control effort to maintain a certain side slip. It is worth to mention that the evolution of the steady state gain

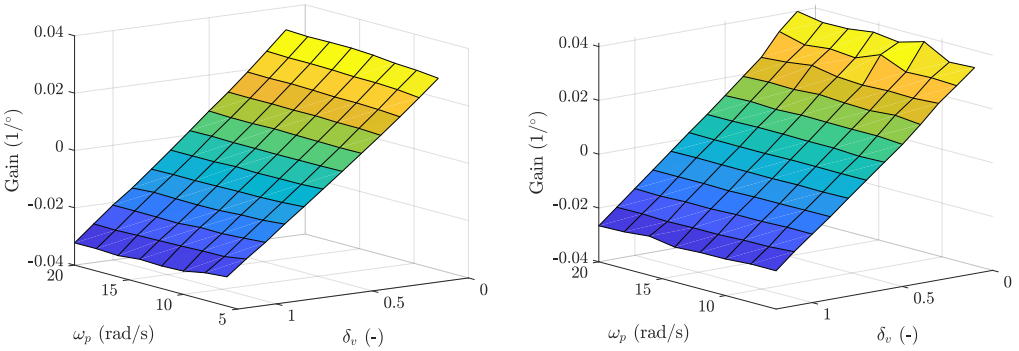

(a) Simple aerodynamics.

(b) Aeropropulsive interactions.

Figure 7.2 – Evolution of the steady state gain C_1, with motor bandwidth, ω_p and VT size δ_v.

as a function of δ_v is almost linear. This effect was anticipated in chapter 2 where it was shown that a variation of surface area at constant aspect ratio translates as a linear variation of lateral coefficients.

From Fig 7.2b, the same observation holds in presence of interactions, motor bandwidth does not impact C_1. The surface appears shifted towards higher gains when compared to Fig 7.2a.

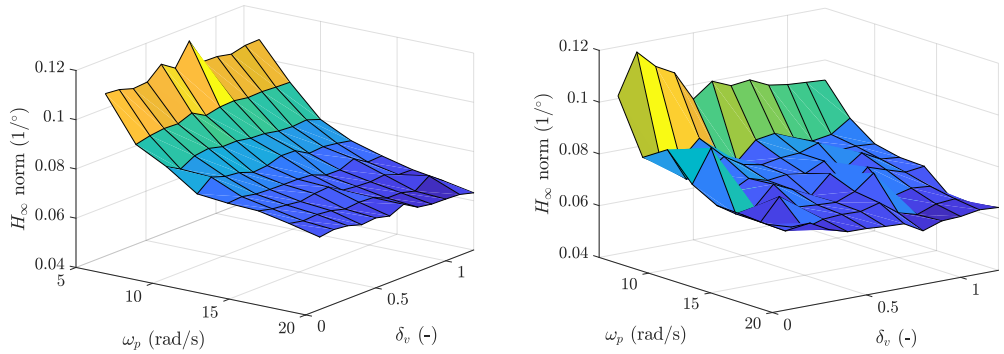

(a) Simple aerodynamics.

(b) Aeropropulsive interaction models

Figure 7.3 – Evolution of the H_∞ norm C_2 with motor bandwidth ω_p and VT size δ_v.

From Figure 7.3, the motor bandwidth has a great influence on the maximum gain which shows an important increase for motor bandwidth lower than 10 rad/s in Fig 7.3a. The vertical tail size has a small influence. The control effort is reduced for larger surface area but its contribution is much smaller than the motor bandwidth.

In Fig 7.3b, the same threshold effect but located at $\omega_p = 8\,\text{rad/s}$ can be observed. The surface is less smooth with higher gains in the region of low δ_v and ω_p. This tendency to higher gains is not generalized, at low ω_p and large δ_v for example, the gain is lower than for simple aerodynamics. The VT surface area has more impact on C_2 with a clear disadvantage for value $\delta_v \leq 0.5$.

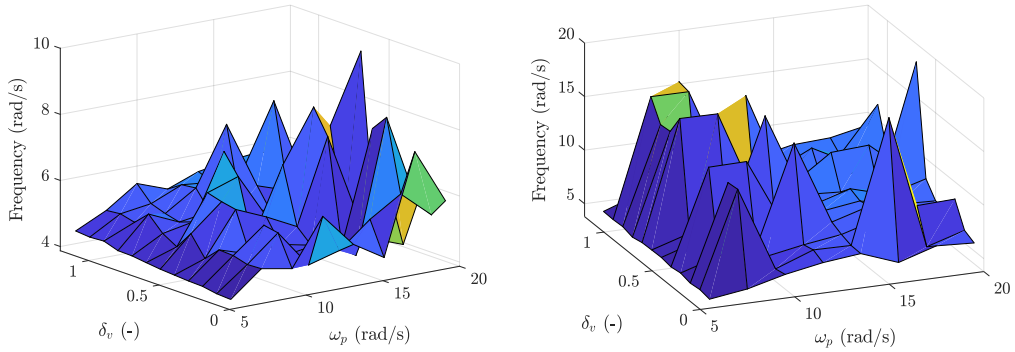

(a) Simple aerodynamics.

(b) Aeropropulsive interaction model.

Figure 7.4 – Evolution of the H_∞ frequency C_3 with motor bandwidth ω_p and VT size δ_v.

Figure 7.4a confirms that the maximum control effort is necessary for transient manoeuvres as C_3 does not go below 4 rad/s and increases with increasing motor bandwidth. Figure 7.4b shows a more chaotic behaviour such that it is more complicated to statute. If one smooths the spikes, it seems that the same observation as for Fig 7.4a can be made.

The low surface smoothness of Fig 7.3b may be explained by local optima. It was already seen for the initial reference solution that a minimum solution and corresponding allocation is not as straight forward in presence of non-linearities in motor efficiency.

Sub-optimal local minima may be easily reached when the allocation matrix is part of the decision variables especially without proper initialization. This variability and the previous observations argue in favour of a fixed allocation matrix for the co-design. In other words, the allocation matrix should be determined during the initialisation and then should be removed from the set of decision variables for the co-design.

To give strength to this idea, the evolution of C_1 and C_2 in function of δ_v and ω_p were generated by freezing the allocation matrix found during the initialization

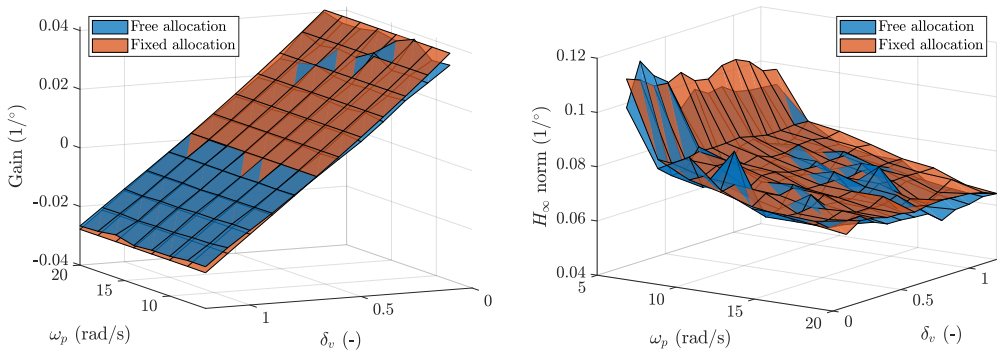

(a) Evolution of the steady state gain C_1, with motor bandwidth, ω_p and VT size δ_v. Aircraft with aero-propulsive interactions.

(b) Evolution of the DC gain C_3, with motor bandwidth, ω_p and VT size, δ_v. Aircraft with aero-propulsive interactions.

Figure 7.5 – Comparison of a free and fixed allocation in variation of motor bandwidth and VT surface area.

step. The resulting surfaces are compared to the previous results in Fig 7.5a and Fig 7.5b.

Both surfaces are quite similar and if the free allocation allows in general a slightly lower control effort, the fixed allocation gives a smoother surface. This guarantees a better stability and a more robust convergence during optimization with a low impact on the performance. The allocation matrix will hence be frozen after the initialization step for the co-design.

7.2.4 Variation of Handling qualities template cut-off frequency

C_1 is shown to be loosely dependent on ω_3 (see Figure 7.6). When comparing the value of C_1 and C_2 of Figures 7.6a and 7.7a, one can observe that in the standard configuration C_2 is at least three times more important than C_1. A reduction of the handling quality template cut-off frequency to 0.6 rad/s brings C_2 to the same level than C_1. Consequently, at $\omega_3 < 0.6$ rad/s, maintaining steady state requires more control effort while for $\omega_3 > 0.6$ rad/s, the transient dynamics requires more effort. Increasing the side slip handling quality template cut-off frequency translates as a faster aircraft response when an input is issued by the pilot. Consequently and as shown by Figure 7.7, C_2 increases with increasing ω_3. Doubling the flight handling requirement from $\omega_3 = 0.6\,\text{rad/s}$ to $\omega_3 = 1.2\,\text{rad/s}$, necessitates to quadruple C_2, showing the sensitivity of this parameter. Comparing the two aerodynamic models of Fig 7.7a and Fig 7.7b shows an identical evolution of the parameter C_2 with ω_3.

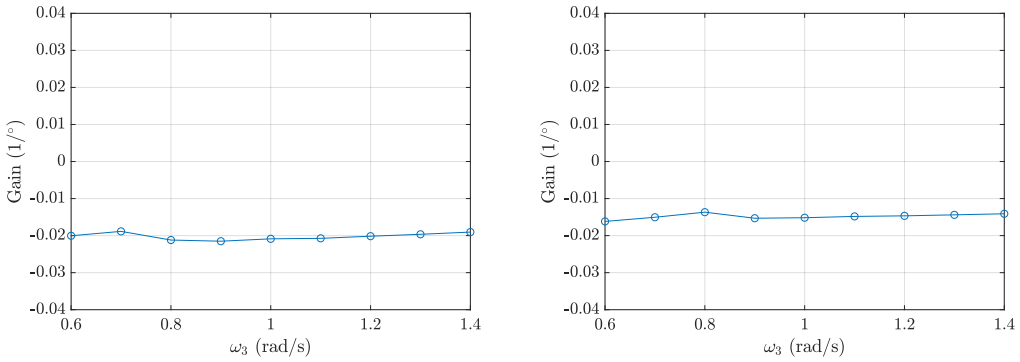

(a) Simple aerodynamics. (b) Aeropropulsive interaction model.

Figure 7.6 – Evolution of steady state gain C_1 with variation of the side slip cut-off frequency ω_3.

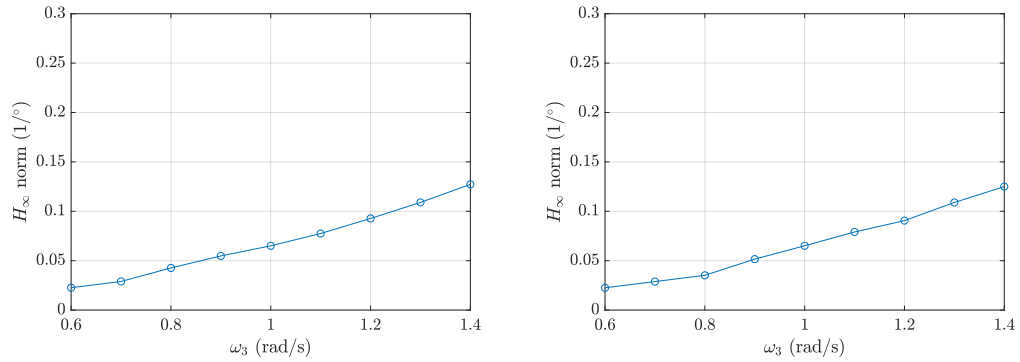

(a) Simple aerodynamics. (b) Aeropropulsive interaction model.

Figure 7.7 – H_∞ gain C_2 evolution with variation of the side slip cut-off frequency ω_3.

The parameter C_3 remains chaotic in both Fig 7.8a and Fig 7.8b. The main information to retain from these figures is the level of frequencies where the peak gain is reached. At least $C_3 \geq 4\,\text{rad/s}$ for the aircraft with simple aerodynamic model and $C_3 \geq 6\,\text{rad/s}$ for the aircraft with aero-propulsive interactions.

7.2.5 Flight point variation

Four flight conditions are studied, they represent the conditions selected at the end of Chapter 4 at different altitudes:

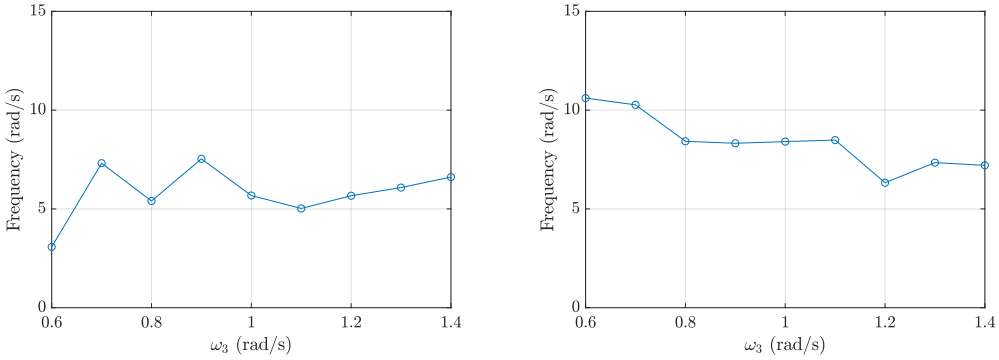

(a) Simple aerodynamics.

(b) Aeropropulsive interaction model.

Figure 7.8 – H_∞ frequency C_3 evolution with variation of the side slip cut-off frequency ω_3.

— 1.3 V_{sr} FL0, steady flight at air velocity 1.3 times higher than the stall speed [1] V_{sr} (see Table 2.1) and flight level 0 (sea level).

— 1.3 V_{sr} FL100, same as the previous but at the flight level FL100, altitude of $10,000$ft or 3048m.

— 1.13 V_{sr} FL0, a velocity corresponding to V_{mc} of the minimum control velocity at the flight level 0 (sea level).

— 1.13 V_{sr} FL100, same as previous at the flight level FL100, altitude of $10,000$ft or 3048m.

In Fig 7.9a, C_1 shows an important sensitivity to velocity, as expected from the thrust model equation (1.30). Remaining on the same figure, it is interesting to note that for a given velocity, the absolute value of C_1 decreases with altitude. The limiting flight condition for maintaining a large flight envelop seemed to be a low altitude.

The flight point variation reveals the added complexity brought by aero-propulsive interactions. In Fig 7.9b, the tendency is the same as in Fig 7.9a with lower absolute values (as previously observed) except for the flight condition $1.3V_{\text{sr}}$ and FL100. This flight condition shows particular results in all three figures 7.9b, 7.10b and 7.11b. This is due to a particular allocation that makes use of inner motors for lateral control while the outer motors are used primarily for longitudinal control, resulting in an overly high gain. Although the results of all flight conditions have

1. All indicated airspeeds are true airspeed.

been obtained with multiple random initial start, they should be considered with care as they may not represent an optimal solution.

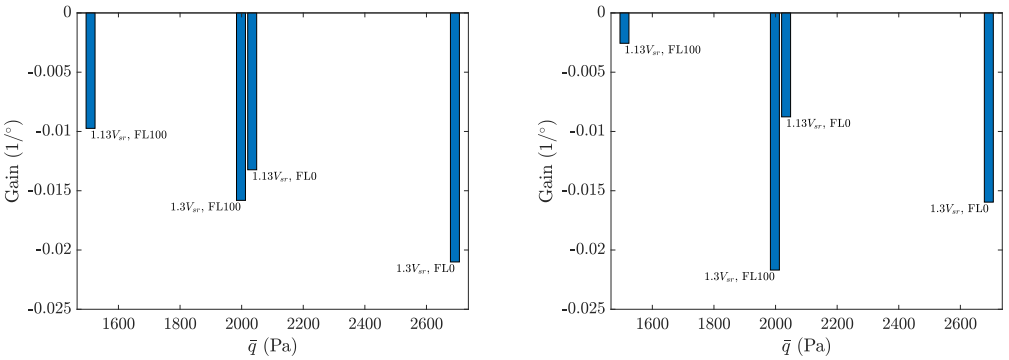

(a) Simple aerodynamics. (b) Aeropropulsive interaction model.

Figure 7.9 – Steady state gain C_1 evolution with variation of airspeed and altitude.

Analysis of Figure 7.10a shows that for a given airspeed, the altitude does not influence C_2. Fig 7.10b contrary to Fig 7.10a shows that a higher peak gain is necessary at higher altitude, translating the motor efficiency loss. The same observation holds for C_3 when comparing the figure 7.11a and 7.11b. Although the flight condition $1.3V_{\text{sr}}$ FL100 gives questionable results so the interpretation is limited.

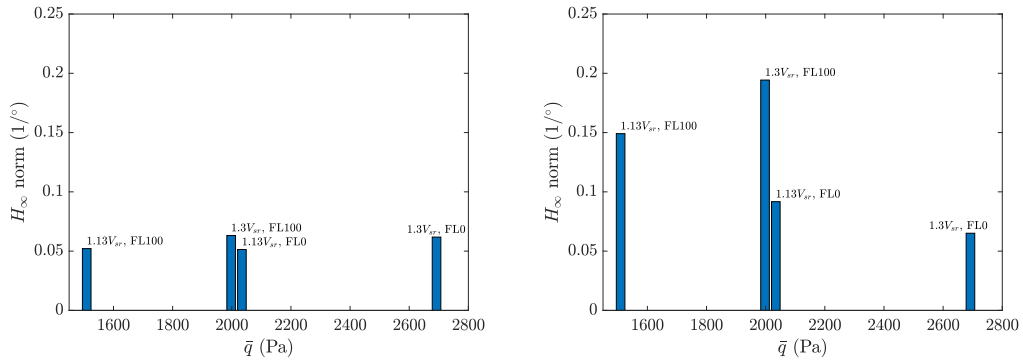

(a) Simple aerodynamics. (b) Aeropropulsive interaction model.

Figure 7.10 – H_∞ gain C_2 evolution with variation of airspeed and altitude.

An important limitation should be underlined in this section for the results of the aircraft with the aero-propulsive interaction model. At low velocity and high altitude, the aircraft requires more important high lift effect obtained by wing blowing as the DEP aircraft does not use flaps (see section 4.4). The intensity of

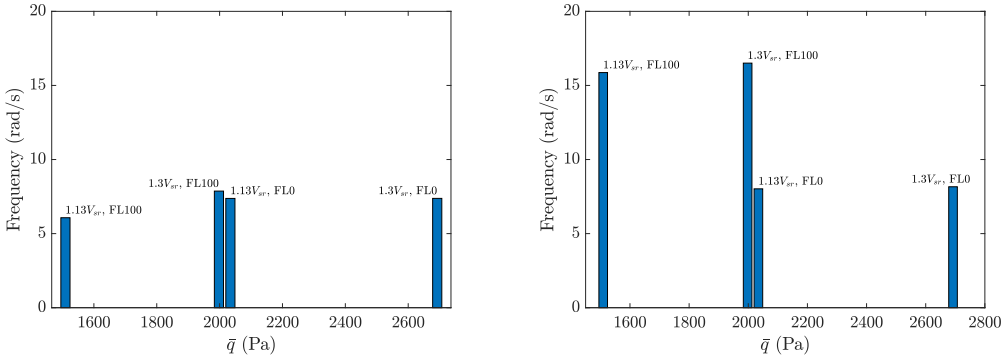

(a) Simple aerodynamics.

(b) Aeropropulsive interaction model.

Figure 7.11 – H_∞ frequency C_3 evolution with variation of airspeed and altitude.

aero-propulsive interaction is higher in these conditions, giving birth to strong non-linearities in motor thrust efficiency. Such non-linearities were found to be the source of sub-optimal solutions during H_∞ synthesis. The results for the flight condition $1.13V_{\text{sr}}$ FL100 is an example of such behaviour and may not be considered as a physical result.

7.2.6 Interpretation

The most surprising result is the fact that vertical tail surface area has a low influence on the H_∞ norm C_2 with respect to motor bandwidth, such that the primary focus for limiting the transient gain should be put on motor bandwidth rather than natural stability. This observation may be linked to the fact that a yaw damper is almost always necessary on a transport aircraft despite the natural directional stability.

The large difference between C_1 and C_2 can explain this result. During steady state, the motors only have to counter the aircraft natural stability mainly given by the vertical tail. When the difference between C_1 and C_2 is large, the vertical tail surface area represents only a small added effort in transient manoeuvres with respect to inertia. The sensitivity of C_2 with respect to δ_v can increase as C_2 approaches C_1 values. At this moment, efforts due to inertia and those due to aerodynamics will be of similar magnitude.

When decreasing motor bandwidth, the fact that C_2 increases rapidly (see Fig 7.3) while C_3 remains higher than 4 rad/s (see Fig 7.4) suggests that this is a particularly important frequency for the actuator to cover.

7.2.6.1 Impact of interaction on control effort

The principal differences upon introduction of interaction are:

1. More difficulties to converge toward a global optimum in the determination of the allocation,
2. General higher DC gains and no significant difference in the peak gain,
3. The airspeed and altitude have a more important impact on the control gains.

Item 1 can be solved by removing the allocation matrices from the set of decision variables after the initialisation step as was shown in section 7.2.3. More generally, the allocation problem may have to answer different and additional needs than just minimizing the control gains. It is possible to integrate more constraints thanks to the degrees of freedom brought by the twelve motors. This would be even beneficial for the global optimization as it could reduce the number of local optima in the solution space.

The similar peak gain should result in similar requirements for dynamic manoeuvres, however the higher DC gain should results in a more limited reduction in vertical tail size for the same flight envelop.

Most of the differences observed can be explained by the non-linear motor efficiency variation with aero-propulsive interaction. Using the observation of section 4.4, these differences become important at low airspeed and or altitude when the intensity of aero-propulsive interaction increases. This result is in line with the observation made in section 4.4 where the non linearities in motor efficiency are characterised.

On the point of view of control and co-design, the main problem concerns the allocation which is harder to find through optimization for the aircraft with aero-propulsive interaction. Although the result of a H_∞ control synthesis for the aircraft using simple aero-dynamics have not been tested with the aircraft using aero-propulsive interactions, it could be valid if the intensity of interactions remains low. Specifically, it was demonstrated through the sensitivity analysis that at $1.3V$sr and sea level, with a symmetric thrust, the aero-propulsive interaction may be neglected for preliminary aircraft design.

With these final remarks, it has been decided to end the comparison between the two versions of the ATR72 and continue toward the direct co-design with the ATR72 and aero-propulsive interactions model. This model was chosen to account for the study of motor losses where higher and asymmetric aero-propulsive interactions are

expected. This will impact the constraints for co-design and the final results but the methodology can be used indifferently.

7.3 Consequences for direct co-design

The previous section highlighted the necessary information to define constraints related to directional flight envelop and actuator saturation. It is also possible to draw a workflow for the co-design answering the objectives of this chapter. This section first defines the additional constraints before explaining the co-design workflow deduced from the sensitivity analysis.

7.3.1 Definition of additional contraints

Recalling the possible constraints (7.4) and (7.5) of section 7.1:

$$\left|\lim_{s\to 0} \mathrm{T}_{\tilde{\beta}_r \to \tilde{d}_{x,i}}(s)\right| \leq \frac{\bar{d}_{x,i}}{\beta_{\text{req}}} \,.$$

$$\left\| \mathrm{T}_{\tilde{\beta}_r \to \tilde{d}_{x,i}}(s) \frac{\beta_{\text{req}}}{\bar{d}_{x,i}} \right\|_\infty \leq 1 \,.$$

it is now possible to evaluate if these constraints are realizable. Limiting the steady state gain to reach a desired flight envelop of $\beta_{\text{req}} = 15°$ seems easily feasible by adjusting the vertical tail size. This constraint allows an interval of VT where the aircraft may be unstable. Actuator saturation for an unstable aircraft is potentially catastrophic and must be avoided. Equation (7.4) is sufficient to avoid motor saturation in steady-states.

For transient manoeuvres, it is necessary to evaluate the factor $\frac{\bar{d}_{x,i}}{\beta_{\text{req}}}$ with the trim power levels $d_{x,i}$ and compare it with Fig 7.3b and Fig 7.7b. At the flight condition corresponding to $1.3V_{\text{sr}}$ FL0, the trim power level is $d_{x,i} = 0.436$, then $\frac{\bar{d}_{x,i}}{\beta_{\text{req}}} = 0.029/°$. To satisfy constraint (7.5), one must observe: $\left\|\mathrm{T}_{\tilde{\beta}_r \to \tilde{d}_{x,i}}(s)\right\|_\infty \leq \frac{\bar{d}_{x,i}}{\beta_{\text{req}}}$ and based on Fig 7.3b and Fig 7.7b, it is not possible. Equation (7.5) in combination with equation (6.31) can only be satisfied if a smaller directional flight envelop or lower handling quality template cut-off frequency ($\omega_3 = 0.6\,\text{rad/s}$) are imposed.

Using the second saturation limit $\underline{d}_{x,i}$ for constraint (7.5) allows more margin with the corresponding factor $\frac{\underline{d}_{x,i}}{\beta_{\text{req}}} = 0.038$, which would allow the handling quality template cut-off frequency to be set at $\omega_3 = 0.7\,\text{rad/s}$. Since the longitudinal $V - \gamma$ mode is much slower than the directional mode, the perturbation associated with the

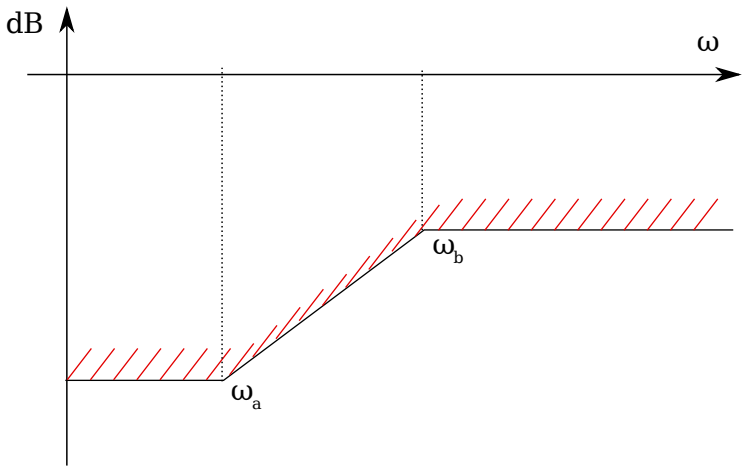

Figure 7.12 – Template definition for $\mathrm{T}_{\tilde{\beta}_r \to \tilde{d}_{x,i}}(j\omega)$

utilization of the second saturation limit will have a low impact on the longitudinal axis and may be considered for dynamic manoeuvres.

Constraints on saturation are hence defined with two levels of severity. The most severe is used for static equilibrium, the less severe is used for dynamic manoeuvres. If this relaxation is not sufficient, the remaining degree of freedom is the handling quality template cut-off frequency [2].

7.3.1.1 Actuator frequency template

Both directional flight envelop and motor saturation requirements can be obtained by imposing a frequency-domain template from the lateral reference input to the motor input commands $\mathrm{T}(s, \bar{d}_{x,i}, \underline{d}_{x,i})$ defined by a transfer function of the form:

$$\mathrm{T}(s, \bar{d}_{x,i}, \underline{d}_{x,i}) = \frac{(s+\omega_a)^2}{(as+\omega_b)^2}, \tag{7.10}$$

with:

$$\lim_{s\to\infty} \mathrm{T}(s, \bar{d}_{x,i}, \underline{d}_{x,i}) = \frac{1}{a^2} = \frac{\bar{d}_{x,i}}{\beta_{\mathrm{req}}}\,, \tag{7.11}$$

$$\lim_{s\to 0} \mathrm{T}(s, \bar{d}_{x,i}, \underline{d}_{x,i}) = \frac{\omega_a^2}{\omega_b^2} = \frac{\underline{d}_{x_i}}{\beta_{\mathrm{req}}}\,,. \tag{7.12}$$

This template is illustrated in Figure 7.12 For this template, the required side slip

2. In regard of perturbation rejection, it may not be less than 0.5 rad/s for this type of aircraft [Cook 2013]

is set by the certification regulation CS25.147 (see section 4.1). ω_b is chosen based on the sensitivity analysis. A value small enough has to be chosen to include the peak gain according to the evolution of C_3 (see Fig 7.4b and Fig 7.8b). A value of $\omega_b = 2$ rad/s can be reasonably chosen. This template is imposed on the transfer matrix gathering both lateral inputs:

$$\left\| \frac{\mathbf{T}_{\tilde{\beta}_r,\, \tilde{\phi}_r \to \tilde{d}_{x,i}}(s)}{\mathrm{T}(s, \bar{d}_{x,i}, \underline{d}_{x,i})} \right\|_\infty \leq 1 \,. \tag{7.13}$$

It remains to bound the longitudinal gains as well since the constraints are now split between longitudinal and lateral [3]. From section 6.4, it was found that longitudinal closed loop transfer could be constrained by a simple gain $\varepsilon_{V,\gamma}$ without loss of performances due to the slow prescribed dynamics. This translates as constraints defined as:

$$\left\| \frac{1}{\varepsilon_{V,\gamma}} \mathbf{T}_{\widetilde{V}_r,\, \widetilde{V}_{z_r} \to \tilde{d}_{x,i}}(s) \right\|_\infty \leq 1 \,. \tag{7.14}$$

7.3.2 Direct co-design workflow

There will remain two steps in the co-design but the principal limitation, the manual trade-off, can be overcome. The first step is an initialization to determine the allocation matrices $\mathbf{L}_D$ and $\mathbf{L}_L$ that minimize motor solicitation. This step is performed with multiple random starts. The allocation matrices are then removed from the set of decision variables while VT size δ_v and motor bandwidth ω_p are added.

The objective function can be defined in terms of design variables only since the control gains are well constrained. The objective function for the co-design is a combination of normalized design variables:

$$J_{\mathrm{co}} = \delta_v + \frac{\omega_p}{\omega_{p_0}} \,, \tag{7.15}$$

with ω_{p_0} the initial value of 20 rad/s. The flight handling quality constraints are defined by equation (6.31), flight envelop constraints and motor saturation limits by the motor frequency template (7.13). The co-design steps, objectives and constraints are resumed in Table 7.3.

3. This is reasonable since the allocation is held fixed.

Table 7.3 – Direct Co-design workflow

1. Initialisation			
Variables	$\mathcal{K}_1 = [\mathbf{H}_L, \mathbf{H}_D, \mathbf{K}_L, \mathbf{K}_D, K_\alpha, K_q, \mathbf{L}_L, \mathbf{L}_D]$	Solve	$\arg\min_{\mathcal{K}_1} J_1$
Objective	$J_1 = T_{\mathrm{w}\to\tilde{d}_{x,i}}$		Such that:
Constraints	Flight handling qualities		$\left\|\frac{\mathbf{S}_0(i,j)}{\mathbf{S}_{0,des}(i,j)}\right\|_\infty \leq 1$
2. Co-design			
Variables	$\mathcal{K}_2 = [\mathbf{H}_L, \mathbf{H}_D, \mathbf{K}_L, \mathbf{K}_D, K_\alpha, K_q, \delta_v, \omega_p]$	Solve	$\arg\min_{\mathcal{K}_2} J_{\mathrm{co}}$
Objective	$J_{\mathrm{co}} = \delta_v + \frac{\omega_p}{\omega_{p_0}}$		Such that:
Constraints	Flight handling qualities		$\left\|\frac{\mathbf{S}_0(i,j)}{\mathbf{S}_{0,des}(i,j)}\right\|_\infty \leq 1$
	Directional flight envelop		$\left\|\frac{\mathbf{T}_{\tilde{\beta}_r,\,\tilde{\phi}_r\to\tilde{d}_{x,i}}(s)}{\mathrm{T}(s,\tilde{d}_{x,i},\underline{d}_{x,i})}\right\|_\infty \leq 1$
	Motor saturation		
	Longitudinal gain relaxation		$\left\|\frac{1}{\varepsilon_{V,\gamma}}\mathbf{T}_{\widetilde{V}_r,\,\widetilde{V}_{z_r}\to\tilde{d}_{x,i}}(s)\right\|_\infty \leq 1$

7.4 Application of the Direct Co-design

The case study for the direct codesign is the ATR72 with aero-propulsive interactions in the flight condition retained in Table 4.7 and more particularly at airspeed $1.3V_{\mathrm{sr}}$. The flight condition and the corresponding numerical values of the parameters of Table 7.3 are summarized in Table 7.4. In more details, the trim power level in this symmetric case is $d_{x_i,\mathrm{trim}} = 0.436$, leaving as maximum peak gain $\frac{d_{x,i}}{\beta_{\mathrm{req}}} = 0.038$. The handling quality template cut-off frequency, $\omega_3 = 0.7\,\mathrm{rad/s}$ is chosen in consequence with the help of Fig 7.7b. Such value should allow a possible solution with sufficient margin to widen the solution space. As for the longitudinal axis, the limiting gain $\varepsilon_{V,\gamma} = 0.15$ used in Chapter 6 remains adequate as the performance of the initial solutions (minimization of control gain) are comparable (see $\widehat{J_1}$ in Table 7.2).

The initial solution found by multiple random starts is the same as presented in section 7.2.2 since the flight conditions are identical.

The results of the co-design are available in Table 7.5. A trade off has been found between vertical tail surface area and motor bandwidth. The motor bandwidth has been reduced to 7.66 rad/s, corresponding to a rather high C_2 value. A VT surface area $\delta_v = 0.28$ is found, corresponding to an unstable aircraft in open loop.

With γ being lower than 1, the solution satisfies all constraints with unsaturated actuators (see Fig 7.13).

Table 7.4 – Case study for the direct co-design application

Aircraft configuration	
Engines	All operative
Flight condition	
Airspeed	$1.3V_{\text{sr}}$
Flight path angle	3%
Altitude	Sea level
Parameter	Value
β_{req} (°)	15
$d_{x_i,\,\text{trim}}$ (-)	0.436
$\frac{\bar{d}_{x,i}}{\beta_{\text{req}}}$ (/°)	0.029
$\frac{d_{x_i}}{\beta_{\text{req}}}$ (/°)	0.038
ω_3 (rad/s)	0.7
$\varepsilon_{V,\gamma}$	0.15

Additionally, the poles of the aircraft for the initial solution and the result of the co-design are given in Fig 7.14. Compared to the result obtained in section 6.4.3, the poles are all well damped thanks to the more severe gain limitations for the lateral dynamics. One may notice that the poles associated with the aileron dynamics and roll subsidence, already present after step 1 in section 6.4.3, is pushed toward higher frequencies in the initial solution obtained with multiple random starts. The co-design does not seem to be affected by this result.

To estimate the performance degradation due to motor saturation, a time simulation of a $\beta_r = 15°$ step followed by a return to symmetric flight is simulated. The comparison between saturated and unsaturated actuators is given in Fig 7.15 with the response of motors one and twelve alongside. Motor twelve arrives exactly at saturation in steady state as expected for the required $\tilde{\beta}_r = 15°$. The aircraft being unstable, the most control effort is required to maintain the aircraft in steady side-slip and inversely, returning to $\beta_a = 0°$ is the most difficult manoeuvre due to the proximity of the saturation points

Table 7.5 – Co-design results

Step	γ	δ_v	ω_p (rad/s)
Initial	0.9993	1	20
Final	0.9999	0.28	7.66

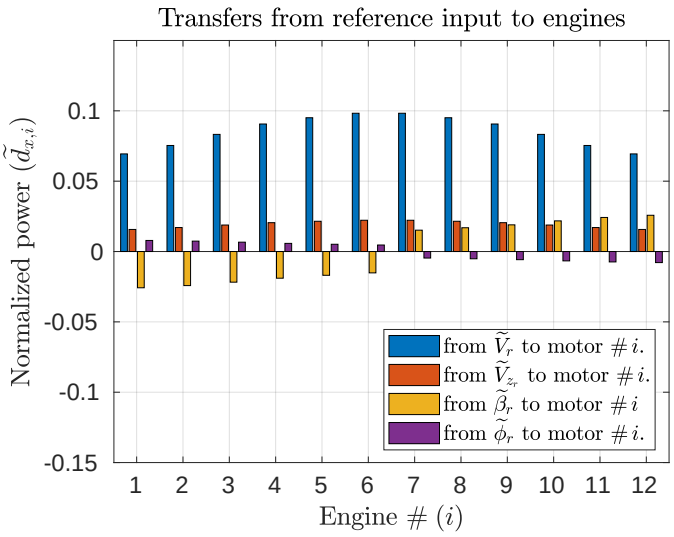

Figure 7.13 – Solution for the allocation after constrained co-design.

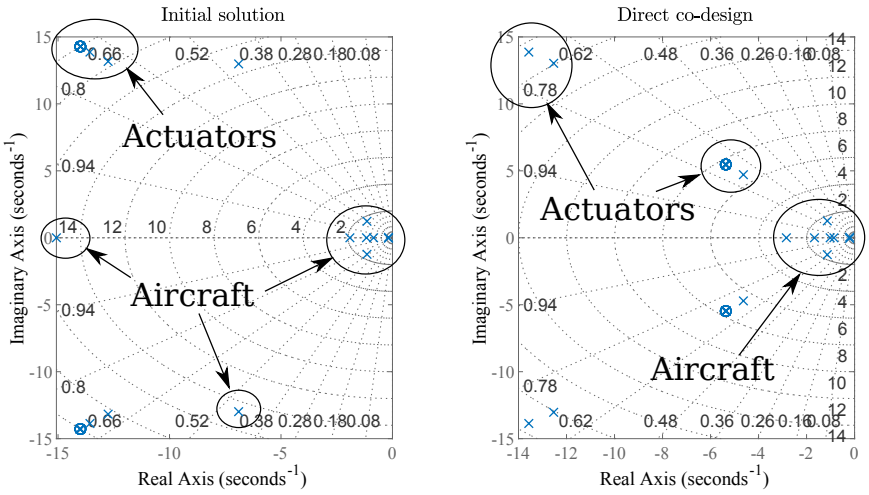

Figure 7.14 – Aircraft poles.

It can be seen however that despite the saturation of outer motors, the performance degradation is small and this is due to the fact that not all motor are saturated during the manoeuvre, as shown in Fig 7.16 where the time responses of all lateral states, all motors and the aileron deflection due to a $\beta_r = 15°$ doublet input are plotted.

The corresponding time responses of the longitudinal states and the elevator deflection are given in Fig 7.17. Perturbations on the longitudinal axis appear when motors are saturated at 15 s and remain lower than 0.05 m/s for V and V_z, which

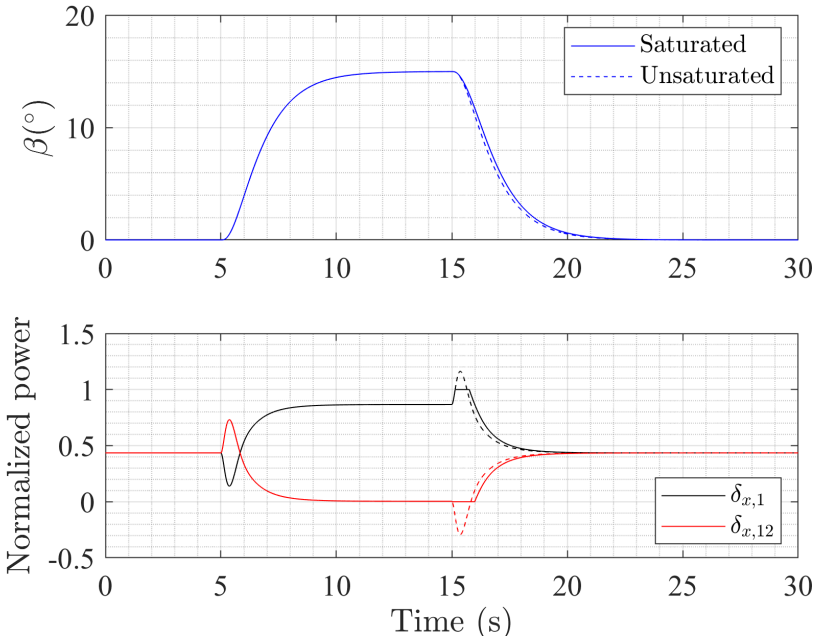

Figure 7.15 – Response to a $\beta_r = 15°$ doublet input. Dashed line, unsaturated actuators, continuous line, saturated actuator.

is largely acceptable.

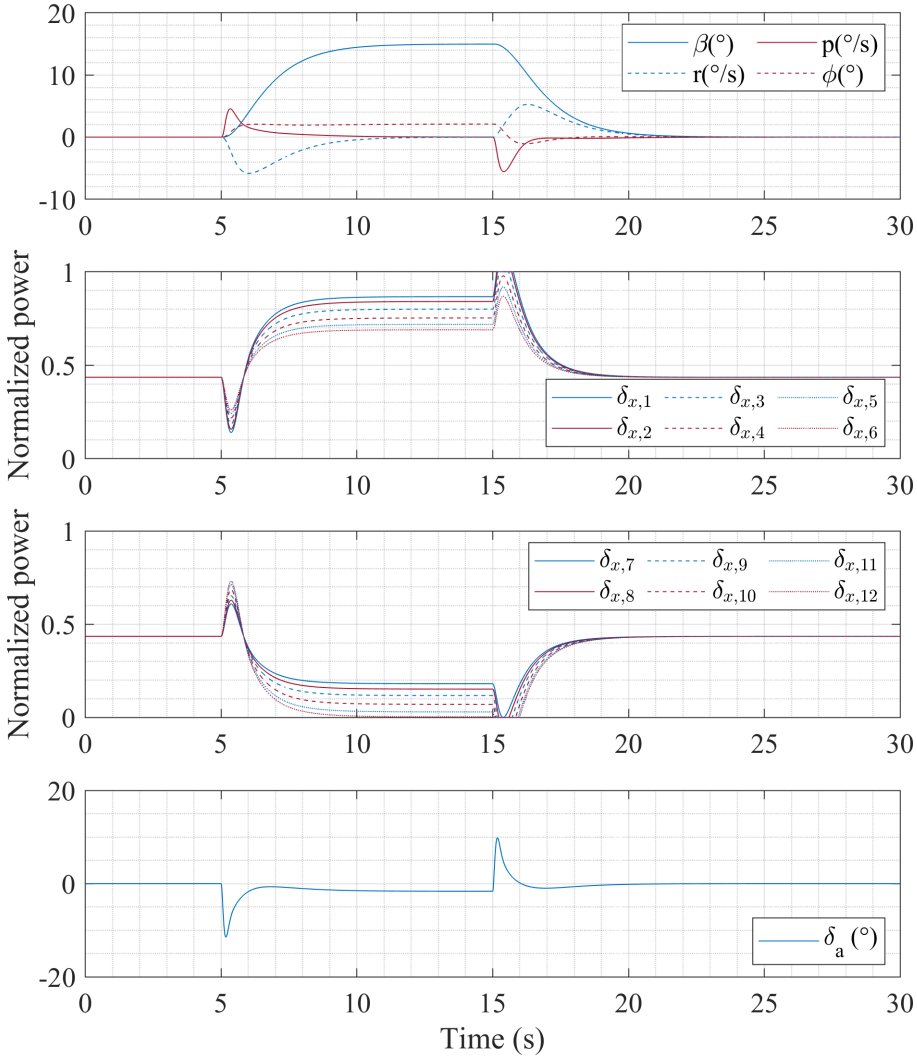

Figure 7.16 – Lateral state responses to a $\beta_r = 15°$ doublet.

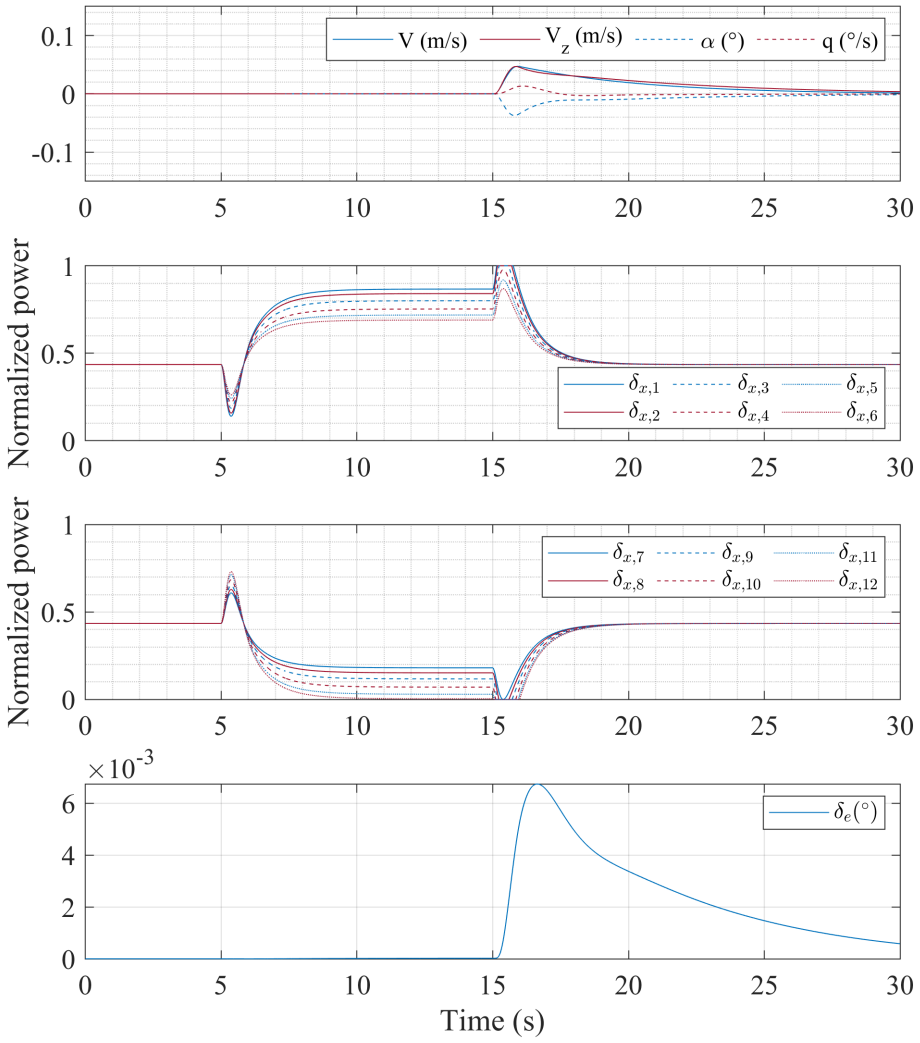

Figure 7.17 – Longitudinal state responses to a $\beta_r = 15°$ doublet.

7.5 Conclusion

Where Chapter 6 introduced the co-design framework, this chapter brought a knowledge of the system necessary to define adequate design constraints and obtain a trade-off through optimization.

This was performed essentially by a sensitivity analysis where the influence of a mix of control and design variables was tracked. It was found that motor bandwidth has the most impact on the control effort necessary to satisfy handling quality requirements, such that the focus should be put on sufficient motor bandwidth rather than aircraft natural stability.

Engine saturation cannot be avoided with the handling qualities cut-off frequency $\omega_3 = 1\,\text{rad/s}$ as imposed in Chapter 6. In Chapter 7, the parameter ω_3 was reduced to $\omega_3 = 0.7\,\text{rad/s}$, translating in a time constant of $1.43\,\text{s}$ in response to a side slip order. As a consequence, the entire replacement of the rudder by differential thrust on an aircraft such as the ATR72 is not recommended. However, the entire replacement of VT by active differential thrust can remain advantageous for aircraft having a lower inertia.

The reference aircraft modelled with simple aerodynamics and with aero-propulsive interactions were compared in the sensitivity analysis (section 7.2). The non-linear variation of motor efficiencies due to interactions explains the differences between the two versions of the aircraft. More difficulties to obtain an optimal allocation were found with aero-propulsive interactions. The sensitivity to airspeed and altitude was more important but the maximum control effort in dynamic manoeuvres is similar.

This knowledge about the design was then employed to define optimisation constraints in order to satisfy the directional flight envelop and avoid motor saturation. To improve convergence, it has been decided to use a constant allocation matrix during the co-design. This matrix is found in an initialization step by multiple random starts to avoid local optima. The co-design stills counts two steps but the trade-off between control law gains, VT size and motor bandwidth is found through optimization (see section 7.3).

The final trade-off with direct co-design gives a VT reduction of 72%, a motor bandwidth of 7.66 rad/s which remains an interesting compromise with respect to the results obtained at step 2 ($\delta_v = 0.1$ with $\omega_p = 20\,\text{rad/s}$) and step 3 ($\delta_v = 0.4$ with $\omega_p = 5.45\,\text{rad/s}$) with the sequential co-design approach of Chapter 6, see section 6.4.3. The aircraft being unstable, particular attention has to be taken with

regards to motor saturations. It was shown in non-linear time simulations that motor saturation are avoided for manoeuvres up to the required 15° side slip angle. However limitations exist in these simulations starting with the absence of time delay, rate saturation and atmospheric perturbations.

Another limitation should be highlighted: the sensitivity analysis and co-design was realized for a fixed centre of gravity. With the small VT surface area obtained in the co-design, the variation of position of the center of gravity would significantly influence the directional static stability and damping of the aircraft. To validate the co-design, time simulations with various centre of gravity could give a first thought and to improve the knowledge about the system, a sensitivity analysis with respect to the centre of gravity can be realised.

Chapter 8

Co-Design for motor failures

Contents

Previously we formulated the flight envelop requirements and actuator limitations as optimization constraints, allowing to find a trade-off between control law gains, VT surface area and motor bandwidth, while guaranteeing flight handling quality and flight envelop constraints.

The framework and methodology obtained in the previous Chapter can be generalized to the whole aircraft operational airspeeds and nominal flight conditions to obtain a general trade off. The situation with motor failures on the contrary cannot be treated with this previous architecture because of the forced symmetric and anti-symmetric allocation module (see section 6.3).

Inclusion of motor failures in the co-design is the missing step to arrive at a valid VT design. This is the objective of this chapter without consideration of failure detection and isolation. The underlying goal is to show that the same design as for symmetric thrust can also satisfy prescribed flight handling quality and flight envelop constraints in asymmetric thrust condition. The only degree of freedom

is the reconfiguration of the flight control laws, leaving the VT size and motor bandwidth with minimum changes for the detailed design step.

The failure detection, isolation and dynamic reconfiguration is outside the scope of this study. The techniques developed to handle multiple motor failures on multicopters may provide a good starting point to solve this problem [Saied 2015].

The control strategy for reallocation and co-design is first described in section 8.1. Following this in section 8.2, a sensitivity analysis as in Chapter 7, section 7.2 is employed to gain knowledge of the aircraft in presence of motor failures. Finally, the problem is formulated and results of a co-design with motor failure are presented in section 8.3.

8.1 Strategy for motor failure

The degraded flight condition for which the co-design will be realised is recalled from section 4.5, Table 4.7. The critical motor failure was determined to be two simultaneous outer motor failures on the same wing. The two outer right motors are supposed inoperative in this chapter.

8.1.1 Linear systems for asymmetric thrust

A drawback of the ATR72 with simple aero-dynamics model is that the failure of one or many motors does not modify the thrust efficiency of the remaining motors and therefore not the aircraft dynamics. The same linearized system could be used for co-design by adjusting of the motor trim levels of the remaining motors.

On the contrary, aero-propulsive interactions render motor efficiencies rapidly evolving with the local thrust coefficient. Hence, linearized systems are deduced for asymmetric thrust conditions before the analysis. [1]

8.1.2 Co-design architecture for parallel symmetric and asymmetric thrust

Sizing the VT surface area and motor bandwidth for both symmetric and asymmetric thrust suggests to solve the codesign problem with these two flight conditions in parallel. An associated block diagram with parallel linearized aircraft models is created and illustrated in Fig 8.1.

1. This supposes that the distributed propulsion alone allows to trim the aircraft in the critical motor failure condition, as demonstrated in Chapter 5, section 5.3.

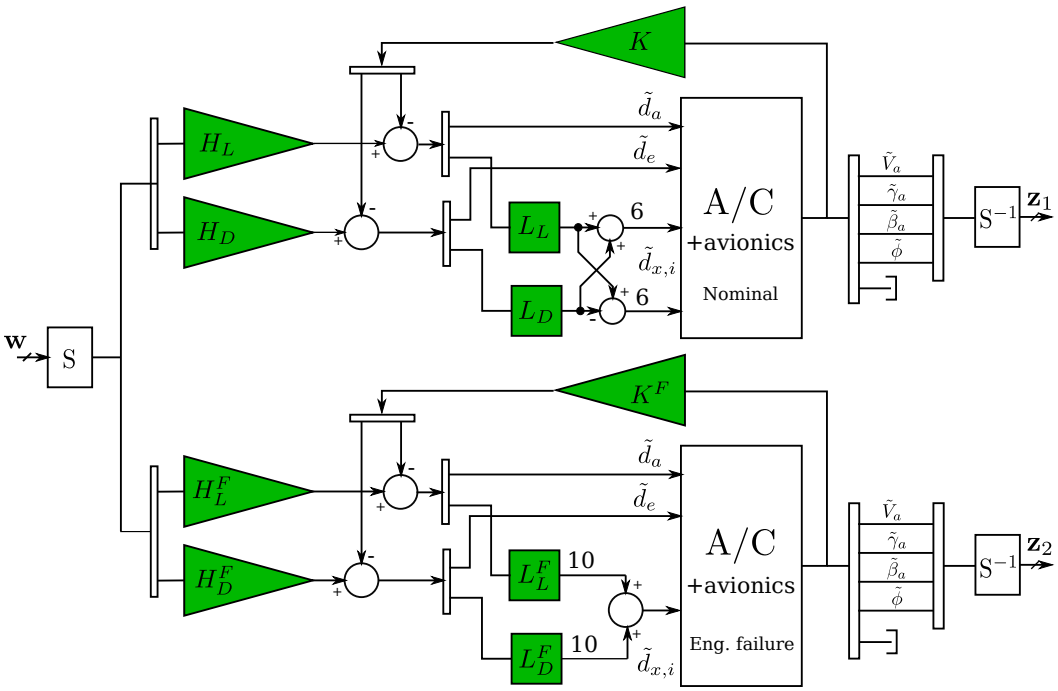

Figure 8.1 – Block diagram for co-design with motor failure. Feedback gains $\mathbf{K}_L, \mathbf{K}_D, K_\alpha, K_q$ are gathered under the block $\mathbf{K}$.

The nominal and degraded aircraft share the same design variables, the VT surface area δ_v and motor bandwidth ω_p. The same control law architecture is used with the exception of the allocation matrix. The symmetric and anti-symmetric thrust allocation is removed for the aircraft with motor failure and replaced by two allocation matrices L_L^F and L_D^F for longitudinal, lateral allocation respectively. The A/C blocks are identical to those described in section 6.3 except that ten motor inputs instead of twelve are considered for the aircraft with motor failures.

This leaves three possibilities for codesign with reconfigurable flight control:

1. It is possible to hold the allocation matrices $\mathbf{L}_L, \mathbf{L}_D, \mathbf{L}_L^F, \mathbf{L}_D^F$ fixed (determined during initialization) and vary the control law gains $\mathbf{H}_L^F, \mathbf{H}_D^F, \mathbf{K}^F$ between the two flight conditions,
2. Inversely, the control law gains are shared, like the design variables, and the allocation matrices are varied between the two flight conditions,
3. All control variables (gains and allocation matrices) are varied between the two flight conditions.

Option 3 can cause convergence issues as was discussed in section 7.2.3 due to the high degrees of freedom. Option 1 would allow the definition of relaxed handling

qualities, tolerable in the situation of motor failures, which is apparently not possible with option 2. The choice may be difficult without prior knowledge on the system. To cope with this, a sensitivity analysis similar the one presented in section 7.2 is conducted on the aircraft with asymmetric thrust.

8.2 Sensitivity analysis with asymmetric thrust

The conditions detailed in Table 7.1 are used again for this analysis. The varying parameters are restrained to δ_v, ω_p and ω_3.

8.2.1 Initial solution

The initial solution with eigenstructure assignment and multiple random initialisation is presented in Table 8.1. As for the aircraft with aero-propulsive interactions, local optima are more easily found and multiple random initialization allows to find a better solution in term of J_1 than eigenstructure assignment.

Initialization Method	$\widehat{J_1}$	γ_1
Eigenstructure assignment	0.254	0.99556
Multiple random initialisation	0.128	0.9985

Table 8.1 – Difference of optimality between initialisation with eigenstructure assignment and multiple random start.

A noticeable point is that $\hat{J}_1$ with multiple random initialisation is 50% larger than in the symmetric case, yet only 17% of the thrust is missing with two motor failures.

The allocation corresponding to the minimum $\widehat{J_1}$ is presented in Fig 8.2. The resulting allocation shows a higher contribution of motors five to ten for longitudinal inputs while motors one to four are privileged for lateral inputs. One can observe the prominent use of the outer motors one to three for lateral control compared to motors seven to ten. A coupling between lateral and longitudinal axis is observed with this allocation. A $\beta_r = 1°$ induces a $\tilde{V}_a = 0.05\,m/s$ or 5% steady state error in airspeed and about the same in vertical speed. It is more than what is observed in symmetric thrust conditions but is still less than the authorized cross-over of 14% (see section 6.4).

As a rule of thumb, motors seven to ten should be more solicited than motors one and two during a lateral input to avoid disturbances on the longitudinal axis.

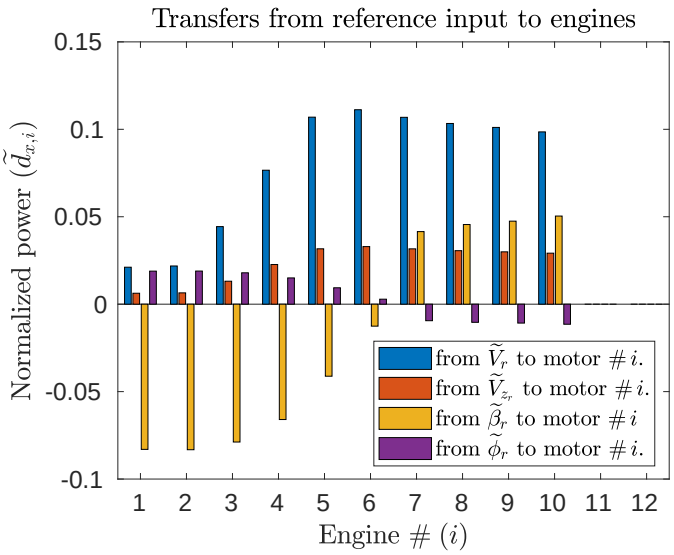

Figure 8.2 – Initial transfers and allocation found after multiple random starts.

However, the criteria for optimality here is $J_1 = \max_{i=1,\dots,12} \left\| \mathrm{T}_{\mathbf{w}\to\tilde{d}_{x,i}} \right\|_\infty$. Motors seven to ten being already highly solicited for longitudinal orders, the lateral control is attributed to motors one to three that are less used for longitudinal orders. The allocation of Fig 8.2 is optimal in the sense of J_1, but this criterion may not be suitable to define an optimal solution in asymmetric thrust conditions. For example, one may want to minimize separately the gains due to longitudinal and lateral input, which will be done during co-design.

8.2.2 Variation of Vertical tail surface area and motor bandwidth

The impact δ_v and ω_p variation on the DC gain and on the peak gain are presented in Fig 8.3a and Fig 8.3b respectively. One can notice the generally higher gains consecutive to the loss of the two outer motors. The tendency and conclusions obtained by the sensitivity analysis of the aircraft with simple aerodynamics and aero-propulsive interaction still hold. The DC gain is only impacted by the VT size and it may be rendered small by adjusting δ_v.

The VT has little impact on the peak gain as shown in Fig 8.3b. The motor bandwidth remains the most important parameter with the same threshold at $\omega_p = 8\,\mathrm{rad/s}$. The surface shows large spikes due to local optima as it was obtained with free allocation matrices.

An analysis for fixed allocation was also conducted in the same idea as presented

in section 7.2 but was found to give several unsatisfying solutions (violating the flight handling quality constraints). The results are available in Annex B.2.1. The interpretation to give to these unsatisfying results can be that allocation brings additional degrees of freedom, necessary in this context where longitudinal and lateral control are closely coupled.

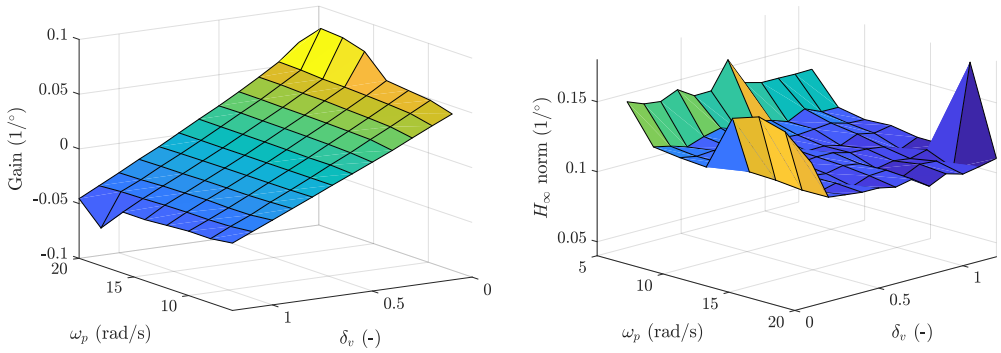

(a) Evolution of the steady state gain C_1.

(b) Evolution of the H_∞ norm C_2.

Figure 8.3 – Evolution of the steady state gain C_1 and H_∞ norm C_2, with motor bandwidth, ω_p and VT size, δ_v. Aircraft with motor failures.

8.2.3 Variation of Handling quality template cut-off frequency

With an allocation far from a linear thrust distribution, tracking the maximum of the transfers $\mathrm{T}_{\widetilde{\beta}_r \to \widetilde{d}_{x_i}}$ results in loss of information. To be more general, the sum of all peak gains is tracked during the variation of ω_3:

$$C_4 = \sum_{i=1}^{10} \|\mathrm{T}_{\tilde{\beta}_r \to \tilde{d}_{x_i}}\|_\infty \,. \tag{8.1}$$

This quantity will then be compared to the maximum control power remaining from the trim power level when defining the motor frequency template. Similarly, the sum of DC gain is tracked:

$$C_5 = \sum_{i=1}^{10} \lim_{s \to 0} \mathrm{T}_{\tilde{\beta}_r \to \tilde{d}_{x_i}} \,. \tag{8.2}$$

These two quantities may be compared to Fig 7.6b and Fig 7.7b after dividing by the number of operational motors (hence averaging), however no hard conclusions should be taken since they are not the same quantities.

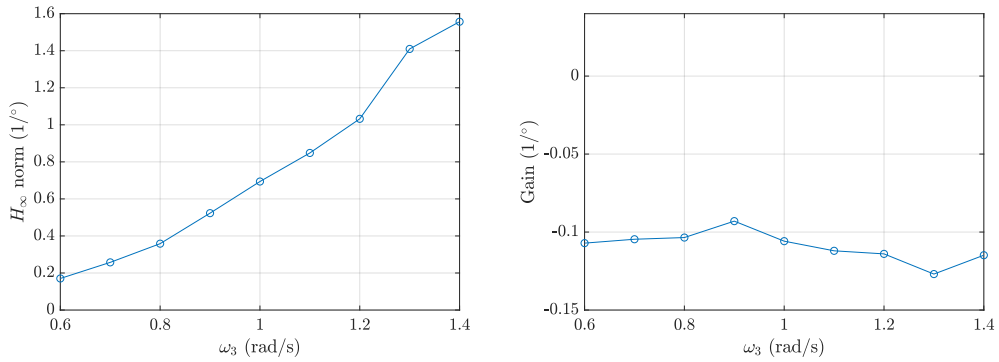

(a) Evolution of H_∞ norm C_4 with ω_3 (b) Evolution of DC gain C_5 with ω_3

Figure 8.4 – Variation of the side slip cut-off frequency ω_3. Aircraft with motor failure.

The variation of C_4 and C_5 with handling quality template cut-off frequency is presented in Fig 8.4a and Fig 8.4b respectively. The conclusions are similar to the ones of section 7.2. The DC gain is loosely dependant on ω_3. The peak gain is continuously increasing with ω_3. The large variation of C_4 with ω_3 should ensure a possible solution for ω_3 at least larger than 0.6 rad/s.

8.3 Co-design with motor failures

8.3.1 Formulation

Upon the observation of the previous section, it is now clear that option 1. discussed in section 8.1.2 can be eliminated since the degrees of freedom brought by allocation are necessary to find a satisfying solution. The decision resumes to know whether the aircraft can keep the same handling qualities with motor failures or if one needs to relax them.
Recalling the constraint (7.3) relating the motor saturation and gain:

$$\bar{d}_{x,i} \geq |d_{x,i}(s)| = \left|\mathrm{T}_{\beta_r \to d_{x,i}}(s)\beta_r(s)\right| .$$

The first saturation limit is replaced by the second saturation limit $\underline{d}_{x,i}$ for transient manoeuvres and the equation is generalized by summing over each operational motor:

$$\sum_{i=1}^{10} \underline{d}_{x,i} \geq \sum_{i=1}^{10} \left|\mathrm{T}_{\beta_r \to d_{x,i}}(s)\beta_r(s)\right| , \tag{8.3}$$

$$1 \geq \left| \sum_{i=1}^{10} \mathrm{T}_{\beta_r \to d_{x,i}}(s) \beta_r(s) \right| \frac{1}{\sum_{i=1}^{10} \underline{d}_{x,i}} \,. \tag{8.4}$$

Taking the maximum norm of equation (8.4) when $\beta_r(s)$ is a Diract impulse of amplitude $\beta_{\text{req}} > 0$:

$$\sum_{i=1}^{10} \left\| \mathrm{T}_{\beta_r \to d_{x,i}}(s) \right\|_\infty \frac{\beta_{\text{req}}}{\sum_{i=1}^{10} \underline{d}_{x,i}} \leq 1 \,, \tag{8.5}$$

$$\sum_{i=1}^{10} \left\| \mathrm{T}_{\beta_r \to d_{x,i}}(s) \right\|_\infty \leq \sum_{i=1}^{10} \frac{\underline{d}_{x,i}}{\beta_{\text{req}}} \,. \tag{8.6}$$

The maximum control power $\sum_{i=1}^{10} \underline{d}_{x,i}$ weighted by β_{req} can hence be compared to the criterion C_4 to know if the handling quality frequency template cut-off frequency should be relaxed. In a similar fashion the maximum control power before reaching the first saturation weighted by β_{req} is:

$$\sum_{i=1}^{10} \frac{\bar{d}_{x_i}}{\beta_{\text{req}}} \,, \tag{8.7}$$

it can be used for comparison with the symmetric thrust conditions in which case the twelve motors are operational: $\sum_{i=1}^{12} \frac{\bar{d}_{x,i}}{\beta_{\text{req}}}$.

Table 8.2 presents the trim position of each motor for the aircraft with motor failure and Table 8.3 shows the value of the factor $\sum_{i=1}^{10} \frac{\underline{d}_{x_i}}{\beta_{\text{req}}}$ corresponding to this trim level. According to these data, the sum of the peak gain C_4 can be increased

Table 8.2 – Aircraft with motor failures, trim power level.

$\delta_{x,1}$	$\delta_{x,2}$	$\delta_{x,3}$	$\delta_{x,4}$	$\delta_{x,5}$	$\delta_{x,6}$	$\delta_{x,7}$	$\delta_{x,8}$	$\delta_{x,9}$	$\delta_{x,10}$	$\delta_{x,11}$	$\delta_{x,12}$
0.26	0.32	0.38	0.43	0.48	0.52	0.64	0.71	0.78	0.82	0.0	0.0

up to $\sum_{i=1}^{10} \frac{\underline{d}_{x_i}}{\beta_{\text{req}}} = 0.44\,(1/°)$. From Fig 8.4a, it is possible to maintain the same handling quality requirements even in presence of motor failure. Option 2 will therefore be used for the co-design strategy.

The problem now consist of expressing the motor frequency templates for each of the ten motors of the aircraft with asymmetric thrust $\mathrm{T}_F(s, \bar{d}_{x,i}, \underline{d}_{x,i})$. The same template definition as in equation (7.10) is used and the subscript $_F$ will be employed to differentiate between the nominal and failure case. The main difference is that each motor will be constrained by a unique frequency template defined by

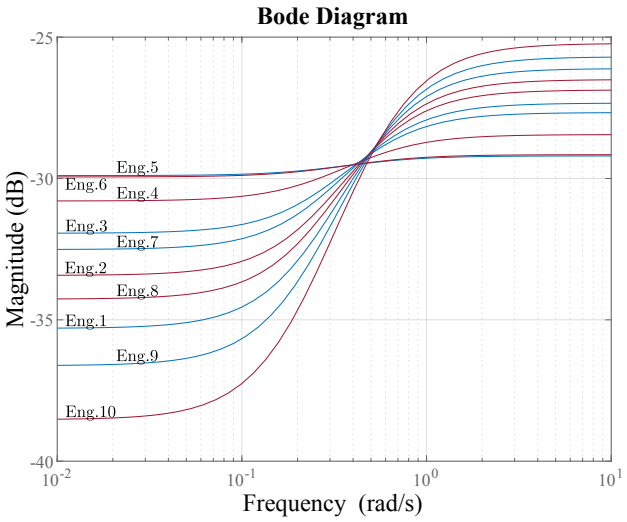

Figure 8.5 – Engine frequency templates for the asymmetric thrust.

the corresponding motor trim power level. The motor frequency templates for the failure case are represented in Fig 8.5.

Table 8.3 – Case study for parallel co-design

Aircraft nominal		Aircraft degraded	
Engines	All operative	Motors	Two outer right inoperative
β_{req} (°)	15	β_{req} (°)	15
$d_{x_i,\text{trim}}$ (-)	0.436		see 8.2
$\sum_{i=1}^{12} \frac{\bar{d}_{x_i}}{\beta_{\text{req}}}$ (1/°)	0.35	$\sum_{i=1}^{10} \frac{\bar{d}_{x_i}}{\beta_{\text{req}}}$ (1/°)	0.23
$\sum_{i=1}^{12} \frac{d_{x_i}}{\beta_{\text{req}}}$ (1/°)	0.45	$\sum_{i=1}^{10} \frac{d_{x_i}}{\beta_{\text{req}}}$ (1/°)	0.44
ω_3 (rad/s)	0.7	ω_3 (rad/s)	0.7
$\varepsilon_{V,\gamma}$	0.15	$\varepsilon_{V,\gamma}$	0.15
Flight condition			
Airspeed	$1.3V_{\text{sr}}$		
Flight path angle	3%		
Altitude	Sea level		

The parameters used to construct the co-design constraints are summarised in Table 8.3. One may notice the similar values for the two factors $\sum_{i=1}^{12} \frac{d_{x_i}}{\beta_{\text{req}}}$ and $\sum_{i=1}^{10} \frac{d_{x_i}}{\beta_{\text{req}}}$ for the symmetric and asymmetric thrust case respectively, despite the different number of operational motor. This shows the dependency of the maxi-

mum control power on the trim level. Additionally, in asymmetric thrust condition, the second saturation limit $\underline{d}_{x,i}$ is valid when the aircraft is required to yaw towards the failed motors. For a yawing action towards the operational motors, the maximum control power is limited by the first saturation limit. In this condition, one can expect a noticeable performance degradation due to motor saturation in transient manoeuvres. This particular manoeuvre will be investigated through time simulation after co-design.

The codesign workflow is described in Table 8.4.

Table 8.4 – Direct Co-design workflow

1.1. Initialisation Symmetric			
Variables	$\mathcal{K}_1 = [\mathbf{H}_L, \mathbf{H}_D, \mathbf{K}_L, \mathbf{K}_D, K_\alpha, K_q, \mathbf{L}_L, \mathbf{L}_D]$		$\arg\min_{\mathcal{K}_1} J_1$
Objective	$J_1 = T_{\mathbf{w}\to\tilde{d}_{x_i}}$	Solve	Such that:
Constraints	Flight handling qualities		$\left\|\frac{\mathbf{S}_0(i,j)}{\mathbf{S}_{0,des}(i,j)}\right\|_\infty \leq 1$
1.2. Initialisation Asymmetric			
Variables	$\mathcal{K}_2 = [\mathbf{H}_L, \mathbf{H}_D, \mathbf{K}_L, \mathbf{K}_D, K_\alpha, K_q, \mathbf{L}_L^F, \mathbf{L}_D^F]$		$\arg\min_{\mathcal{K}_2} J_1$
Objective	$J_1 = T_{\mathbf{w}\to\tilde{d}_{x_i}}$	Solve	Such that:
Constraints	Flight handling qualities		$\left\|\frac{\mathbf{S}_0(i,j)}{\mathbf{S}_{0,des}(i,j)}\right\|_\infty \leq 1$
2. Co-design			
Variables	$\mathcal{K}_3 = [\mathbf{H}_L, \mathbf{H}_D, \mathbf{K}_L, \mathbf{K}_D, K_\alpha, K_q, \mathbf{L}_L^F, \mathbf{L}_D^F, \delta_v, \omega_p]$		$\arg\min_{\mathcal{K}_3} J_{\text{co}}$
Objective	$J_{\text{co}} = \delta_v + \frac{\omega_p}{\omega_{p_0}}$		Such that:
	Flight handling qualities	Solve	$\left\|\frac{\mathbf{S}_0(i,j)}{\mathbf{S}_{0,des}(i,j)}\right\|_\infty \leq 1$
Constraints	Directional flight envelop		$\left\|\frac{\mathbf{T}_{\tilde{\beta}_r,\,\tilde{\phi}_r\to\tilde{d}_{x_i}}(s)}{\mathrm{T}(s,\tilde{d}_{x,i},\underline{d}_{x,i})}\right\|_\infty \leq 1$
	Engine saturation		$\left\|\frac{\mathbf{T}_{\tilde{\beta}_r,\,\tilde{\phi}_r\to\tilde{d}_{x_i,F}}(s)}{\mathrm{T}_F(s,\tilde{d}_{x,i},\underline{d}_{x,i})}\right\|_\infty \leq 1$
	Longitudinal gain relaxation		$\left\|\frac{1}{\varepsilon_{V,\gamma}}\mathbf{T}_{\widetilde{V}_r,\,\widetilde{V}_{z_r}\to\tilde{d}_{x_i}}(s)\right\|_\infty \leq 1$

8.3.2 Application of the co-design with motor failure

The resulting design is presented in Table 8.5. A trade-off has been found with a VT size reduced to $\delta_v = 0.5$ and an motor bandwidth of $\omega_p = 10.4\,\text{rad/s}$. Both variables have increased noticeably when compared to the values obtained at the end of Chapter 7 when only symmetric thrust is considered. The aircraft is unstable but close to neutral.

Table 8.5 – Constraint γ_1 and objective function values during optimization process.

step	γ_1	δ_v	$\omega_p\,(rd/s)$
1	2.532	1.0	20
2	0.9986	0.50	10.4

The final allocations are presented in Fig 8.6b for the symmetric and Fig 8.6a for the asymmetric case.

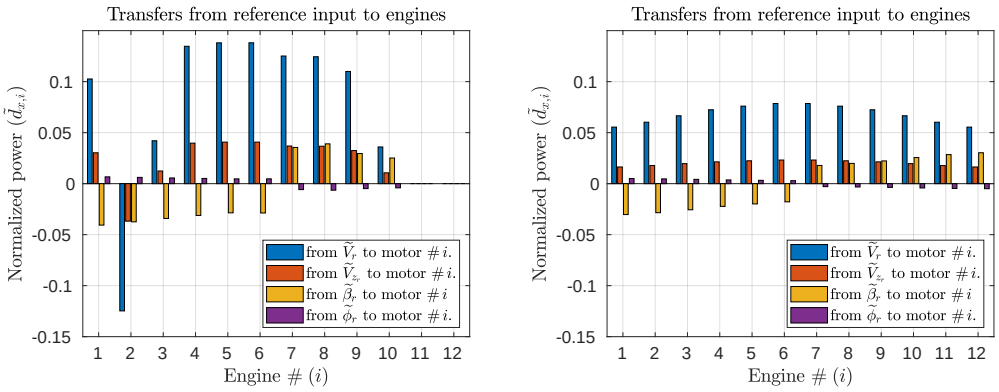

(a) Solution for the allocation in asymmetric thrust conditions.

(b) Solution for the allocation in nominal thrust conditions.

Figure 8.6 – Solution for the allocation after co-design.

The allocation for the symmetric case has the same shape as the one obtained in section 7.4 since the allocation is fixed but the amplitude is lower probably due to the fact that the control law is common with the asymmetric thrust case (see section 6.4.3 explaining the formulation behind Fig 8.6).

The resulting allocation for the asymmetric thrust case takes an atypical form. A positive longitudinal reference input translates as a reduction of thrust for motor two. This allocation tends to symmetrize the thrust by progressively switching off motor two and reducing the level of thrust of motor three. Another way of doing this is simply to switch off motor one and two. The explanation for conserving motor

one operational can be found in the aero-propulsive interaction rendering the inner motors less efficient to generate thrust.

The 50% reduction in VT results in an unstable aircraft. The handling qualities in closed loop are evaluated by time simulations for a doublet input in the reference side slip angle. A first step of $\beta_r = -15°$ (nose toward the failed motors), followed by a positive step of 15° to go back to $\beta_r = 0°$. The doublet input reference toward the failed motors is the most difficult manoeuvre for an unstable aircraft (inversely to what has been said for a stable aircraft in section 8.3.1).

The side slip angle and external motor responses are shown in Fig 8.7 for the symmetric and asymmetric thrust conditions.

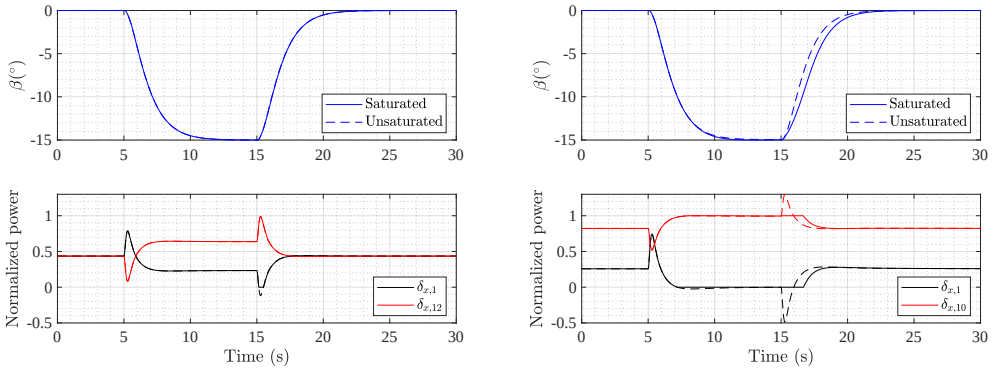

(a) Nominal conditions.

(b) Asymmetric conditions.

Figure 8.7 – Response to a $\beta_r = -15°$ doublet in nominal conditions. Dashed line: with unsaturated actuators, continuous line: with saturated actuator.

The results for the symmetric case (see 8.7a) are close to the ones obtained in section 7.4 and the focus will be put on the asymmetric case at first. The differences between the symmetric and asymmetric conditions can be seen in Fig 8.7. The aircraft with asymmetric thrust makes use of the outer motors very close the minimum $\delta_{x,i} = 0$ and maximum $\delta_{x,i} = 1$ power levels. However, once again, the fact that not all motors saturate at once (see Fig 8.10) gives still sufficient margin to the flight control system to operate the manoeuvre with a small performance degradation when returning from $\beta = -15°$ to $\beta = 0°$.

The doublet manoeuvre does however represent a maximum limitation since just the inner left motor is not saturated during the transient to return to $\beta = 0°$ as shown by Fig 8.10. A high frequency oscillation is visible in the aileron deflection and the roll rate indicating a badly damped pole. This is confirmed by analysis of the poles presented in Fig 8.8.

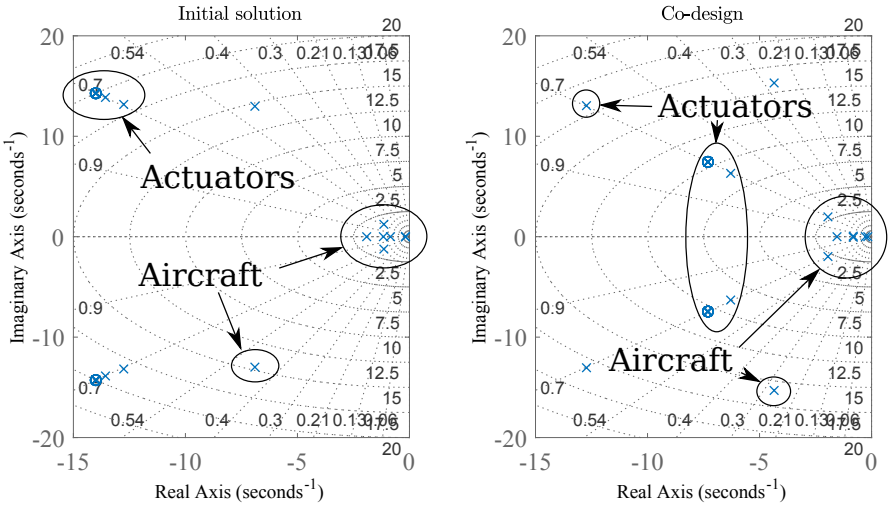

(a) Symmetric thrust.

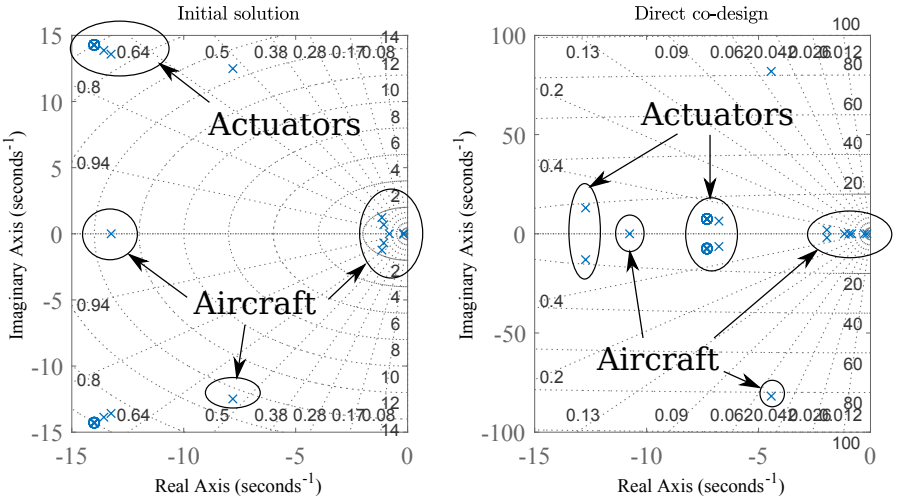

(b) Asymmetric thrust.

Figure 8.8 – Poles at initialisation and after co-design.

The aircraft in both symmetric and asymmetric conditions fails to maintain a good damping for one pair of complex conjugate poles. It is probably more difficult to maintain a good damping of this mode knowing that the ailerons are less efficient with asymmetric thrust due to the fact the right aileron is not blown. In this case, the addition of a constraint on the aircraft poles appears to be the solution.

Compared to the aircraft with symmetric thrust, the longitudinal axis is more impacted by the side slip doublet input with a variation of airspeed of $V = -0.5\,\mathrm{m/s}$. The cause being more saturated motors as visible in Fig 8.9.

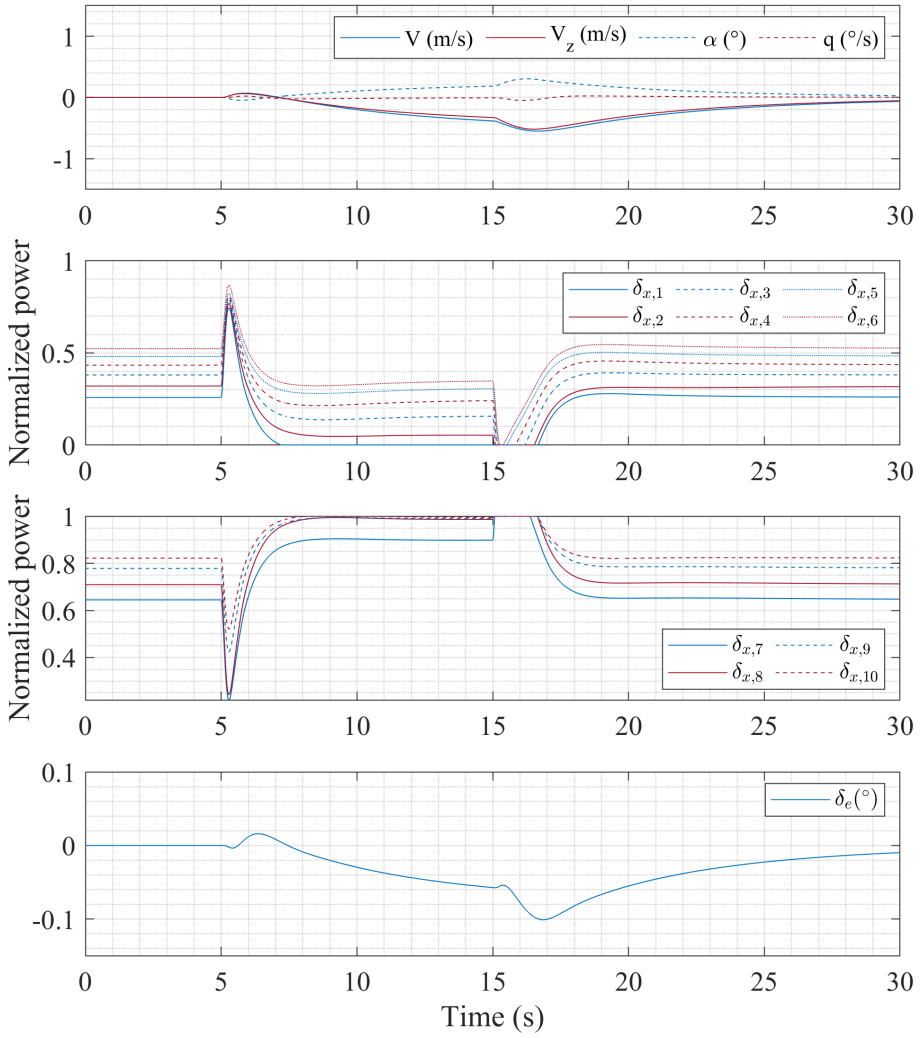

Figure 8.9 – Longitudinal state responses to a $\beta_r = -15°$ doublet in asymmetric thrust conditions.

Additionally, the response to a forward velocity step input with the aircraft with asymmetric thrust is simulated in order to estimate the perturbation on lateral states due to motor saturations. Fig 8.11a and Fig 8.11b compare the responses between a saturated and unsaturated simulation for a step of reference airspeed $V_r = 5\,\mathrm{m/s}$ ($\approx 10\,\mathrm{KTS}$) and highlight the important motor saturations. Fig 8.12 shows in more detail the important motor saturations on motors seven to ten that last for several seconds.

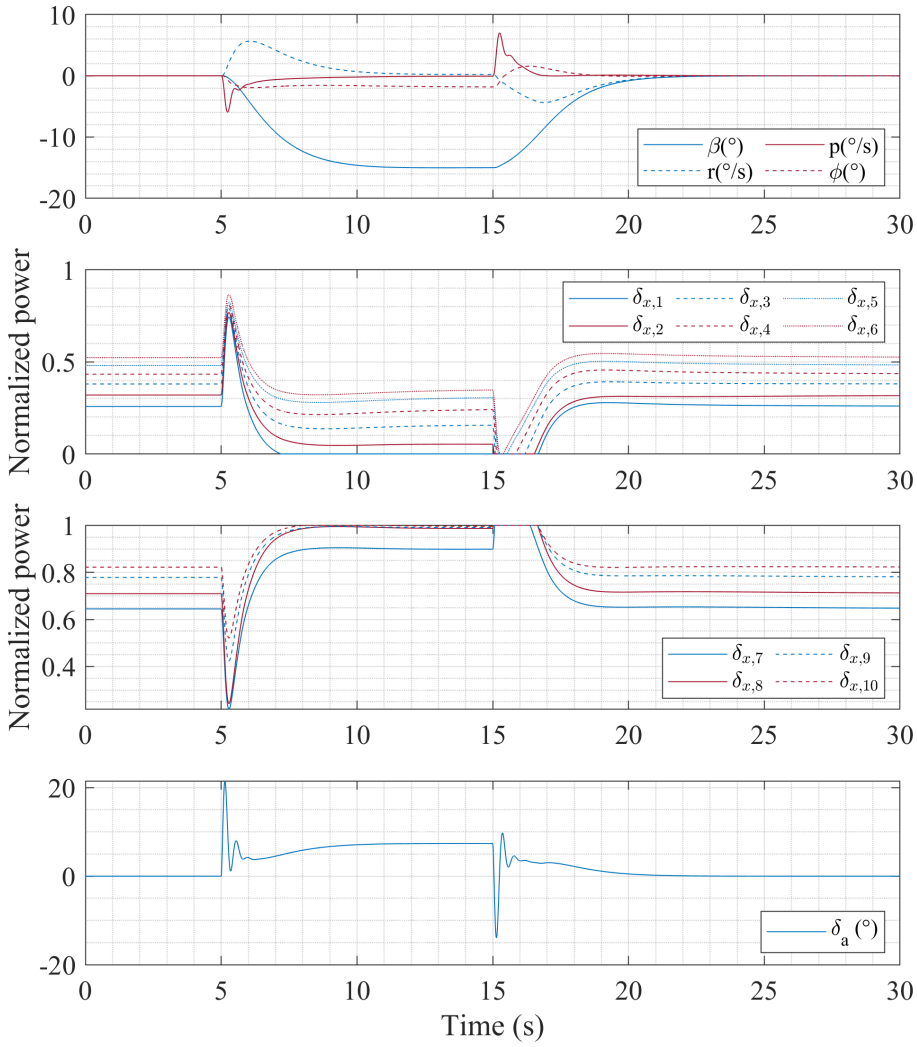

Figure 8.10 – Lateral state responses to a $\beta_r = -15°$ doublet in asymmetric thrust conditions.

Consequently, the impact on the lateral axis can be important with an maximum induced side slip of 3.8° as shown by Fig 8.11b. This perturbation remains reasonable but a small steady state error remains on the side slip.

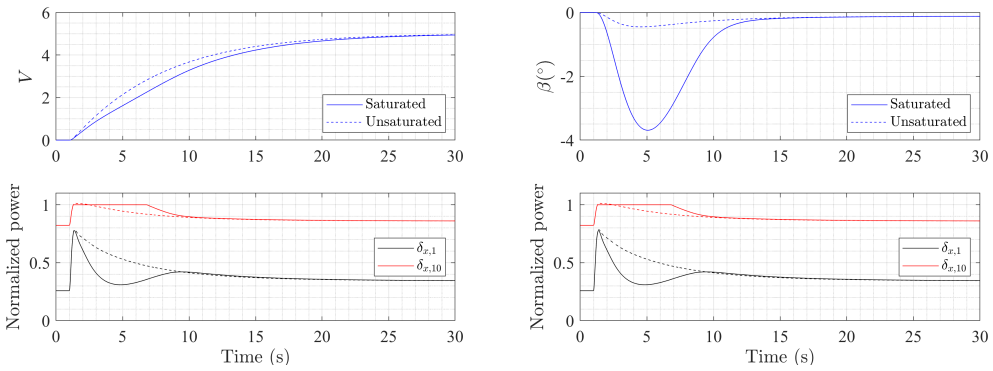

(a) Airspeed response.

(b) Perturbation in side slip.

Figure 8.11 – Response to a $V_r = 5\,\mathrm{m/s}$ step input in asymmetric conditions. Dashed line: with unsaturated actuators, continuous line: with saturated actuator.

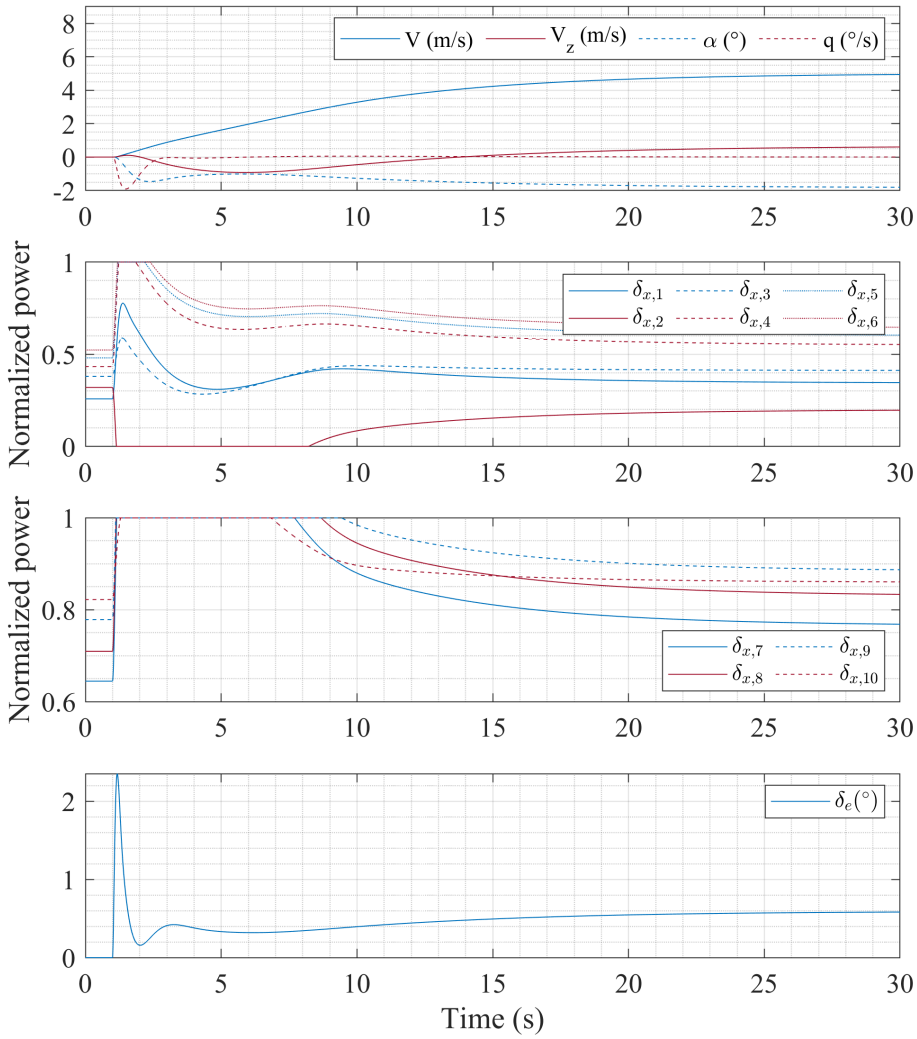

Figure 8.12 – Longitudinal state responses to a $V_r = 5\,\mathrm{m/s}$ step in asymmetric conditions.

8.4 Conclusion

This chapter represents the final development of the co-design framework to size the VT surface area, motor bandwidth and to compute the control laws. The co-design is solved with both nominal and degraded flight conditions represented by symmetric and asymmetric thrust. These two cases are solved in parallel, while sharing the design variables and control law gains. Only the allocation is allowed to change between the two flight conditions (see section 8.1 and section 8.2). The aircraft with asymmetric thrust has mostly the same sensitivity to design or control variables but with a higher control effort consecutive to the loss of two motors.

A trade-off is found with a VT reduced by 50% and motor bandwidth $\omega_p = 10.4\,\text{rad/s}$ that are suitable for both nominal flight and critical motor failure conditions. Identical flight handling qualities and directional flight envelop between nominal and degraded conditions are obtained by a thrust reallocation. Motor saturations are however hit more often for the aircraft with asymmetric thrust leading to small performance degradation with respect to reference tracking. Noticeable couplings between longitudinal and lateral axis (see section 8.3) and a badly damped poles are also observed. The perturbations on the lateral axis due to longitudinal inputs are appearing due to motor saturations and may be lowered by relaxing the longitudinal flight handling qualities. Additionally, it is possible to add a constraint on the aircraft poles during H_∞ synthesis to maintain sufficient damping.

The same limitation as formulated in Chapter 7 hold, namely the lack of delay, rate saturation and atmospheric perturbations in this preliminary design stage. The results may be too optimistic.

Part III Conclusion

The main focus of Part III was the determination and the evaluation of design trade-offs. To be viable a trade-off should satisfy the flight certification regulations which necessitates the inclusion of handling qualities and flight envelop constraints. Co-design under design constraints is rendered possible with multiple objectives, non smooth optimization tools introduced in Chapter 6.

Being interested in a novel flight control system where the rudder control surface is fully replaced by differential thrust, the work consisted in formulating compatible and achievable design constraints. In this objective, a series of sensitivity analysis revealed the key design parameters: the thrust allocation and the motor bandwidth. These two parameters have the most influence on the control effort to satisfy a prescribed flight handling quality. Interestingly enough, the VT has almost no influence on the control effort in transient manoeuvres for the class of aircraft studied. Given the results obtained in Chapter 7 and Chapter 8, for an aircraft of the class of the ATR72, the main purpose of the VT is to give the appropriate static stability.

The final trade-off between VT surface area and motor bandwidth after taking into account the critical motor failure was obtained in Chapter 8 for a slightly unstable aircraft. The associated motor bandwidth remains low at 10 rad/s. Motor saturations are avoided by imposing directional flight handling qualities with a response time of 1.43 s. It was found possible to maintain the same handling qualities in symmetric and asymmetric flight conditions by reallocation only.

Time simulations highlighted the coupling appearing between longitudinal and lateral motion when the motors hit saturation. The motors have to be chosen such that their saturations offer enough power margins because the maximum directional control depends on the trim state. This remark already made in the conclusion of Part II was emphasized again in this part.

In regard to the results obtained in Part II and Part III, it seems that the VT can be sized for neutral static stability on a DEP aircraft utilizing differential thrust. Relying solely on differential thrust for yawing control on an aircraft of the class of an ATR72 is discouraged but can remain interesting for aircraft having lower inertia.

These conclusions have been drawn without considering atmospheric perturbations, rate saturations and delays in the electronics.

Now, it is possible to also issue recommendations for directional control with a

combined rudder and differential thrust. It seems natural in regards to the design sensitivities to allocate the high frequency directional control effort to a small and fast rudder, while the slow and steady manoeuvres can be taken care of by the motors. In this case, more important VT reduction can be expected together with smaller motor bandwidth.

Part IV

Experimental research with Distributed Electric Propulsion

Introduction

DEP being a new emerging technology in the field of aerospace, a number of recent experimental studies are contributing to the understanding of highly distributed propulsive architectures with important aero-propulsive interactions like the project Ampere [Hermetz 2016] but also [Borer 2016], [Fredericks 2017], [Stoll 2015], [Baris 2017], [Ma 2020].

Data are gathered in wind tunnel and/or flight tests to validate the tools able to compute DEP aircraft performances at low airspeed but also in term of range or speed. These studies complement the theoretical work undertaken to calculate the resulting thrust, lift and drag arising from the combination of a propulsion system and a lifting surface with strong aero-propulsive interactions. The determination of these aerodynamics efforts with sufficient accuracy within a reasonable computational time for conceptual aircraft design remains an open problem [Bohari 2018], [Borer 2017].

Among the previously cited studies, the Ampere project discusses the handling qualities of a DEP aircraft on the basis of data collected during wind-tunnel tests [Liaboeuf 2018], [Dilinger 2018]. The Greased Lightning project [Fredericks 2017], is a V/STOL aircraft investigating mainly the transition manoeuvre from hover to horizontal flight. The rest of the studies focus on performance prediction. Data available to study and model the flight dynamics of a DEP aircraft remain sparse and the main motivation for conducting experimental work with DEP. The project Ampere being extensively studied in wind-tunnel, kinematic tests were identified as the next step. Dynamic rigs in wind tunnel such as in [Pattinson 2013] or flight tests are two possible solutions. The latter has been selected to leave the possibility to implement control laws for flight testing.

The two major sources of uncertainty in simulating DEP aircraft flight dynamics arise from:

— the aerodynamic complexified by the fact that a large portion of the wing is immersed in the propeller slipstreams,

— for an active use of differential thrust, induced forces due to aero-propulsive interaction are generated.

The development and flight testing of a DEP demonstrator called DEmonstrateur COntrol Latéral, (Lateral Control Demonstrator) (DECOL) came as an at-

tempt to reduce these uncertainties and to validate the modeling and the co-design principle realized in Part II and Part III. To this end, the aircraft was developed with the following goals:

— characterise the aircraft lateral flight dynamics when a large portion of the wing is immersed in the propeller slipstream,

— characterise the induced aero-propulsive effects at play when differential thrust is used,

— evaluate the feasibility to implement the control laws and VT reduction obtained in Part III with the knowledge obtained from the first two objectives.

The experimental platform, its key design aspect, equipment and instrumentation as well as theoretical exploration is presented in a first Chapter 9. The flight experimentation and identification work, with key findings and the identified aerodynamic models are discussed in Chapter 10.

Chapter 9

DEP flight demonstrator

Contents

This chapter describes the construction of the experimental DEP aircraft DECOL. The objectives of the experimental research are briefly recalled:

— characterise the aircraft lateral flight dynamics when a large portion of the wing is immersed in the propeller slipstream,

— characterise the induced aero-propulsive effects at play when differential thrust is used,

— evaluate the feasibility to implement the control laws and VT reduction obtained in Part III with the knowledge obtained from the first two objectives.

The development of the aircraft aimed at producing a platform able to fulfil these objectives with the constraints associated with practical work, namely aircraft operation, commercial availability of the equipment, available time and resources. These

constraints induced a number of trade-offs that prioritised the functions associated with the objectives at the cost of global aircraft performances.

The design choices, key characteristics and instrumentation are described in this chapter. Section 9.1 describes the overall aircraft geometry, mass properties and key design characteristics. Section 9.2 describes the equipment necessary for flight operation, especially the propulsion systems and power distribution. Section 9.3 describes the instrumentation, acquisition system and flight controller. Finally, section 9.4, presents a theoretical study of the demonstrator with the aerodynamic tools developed in Chapter 2 and in Chapter 3.

9.1 Aircraft characteristics

The reference aircraft throughout this work is the ATR72, a turbo-propeller, regional transport aircraft. The demonstrator was constructed with the idea to represent this class of aircraft and integrate design constraints related to aircraft operation and flight regulations. Some of the strongest constraints are: manual piloting only, operability from a hobby model runway of 100m long and a weight lower than 25kg.

With these constraints in mind, the design of the demonstrator started with the consideration of similarity rules. To be able to transpose the findings made with a small scale demonstrator to the scale of the reference aircraft, the demonstrator should comply with the Froude similarity principle. A Froude scaling guarantees similar inertial and gravitational effects on vehicles with geometric similitude [Wolowicz 1979], [Chambers 2015].

A $n = 1/12$ Froude scaling applied to the reference ATR72 geometry, airspeed and masses is presented in table 9.1.

The immediate limitation is the wing loading of 37.3kg.m^{-2} that would result from this Froude scaling and the associated lift coefficient in cruise, almost 0.9, which are both high values for a small scale demonstrator. The risks associated with such wing loading were judged too high for the project and the Froude scaling was abandoned. It follows from this that the inertias are scaled according to Froude either.

Therefore, the findings made with the demonstrator can hardly be transposed to larger scale without caution but they will remain valid for most Unmanned Aerial Vehicle (UAV)s.

Table 9.1 – Geometry of a 1/12 scaled model of the ATR72 using Froude scaling rules. The ATR72 is assumed to fly at 2500m and is designated by the subscript $_A$ in the table. The scaled model is supposed to fly at sea level and is designated by the subscript $_m$.

Quantity	Scaling rule	ATR72	Scaled model
Wingspan (m)	$n = \frac{b_m}{b_A}$	$b_A = 27.05$	$b_m = 2.254$
Wing area (m^2)	$n^2 = \frac{S_m}{S_A}$	$S_A = 61$	$S_m = 0.4236$
Fuselage length (m)	$n = \frac{l_{f,m}}{l_{f,A}}$	$l_{f,A} = 27.17$	$l_{f,m} = 2.26$
Maximum airspeed of interest ($m.s^{-1}$)	$\frac{V_m}{V_A} = n^{0.5}$	$V_A = 90$	$V_m = 26.0$
Mass (kg)	$\frac{m_m}{m_A} = \frac{\rho_m}{\rho_A} n^3$	$m_A = 21350$	$m_m = 15.8$

9.1.1 Geometry and mass

A sequential design was used starting from what could be considered a safe approach velocity in combination with a reasonably high aspect ratio. The process was iterated with refinement of weight projection and workshop capability until convergence. The main drivers for the layout were the distributed propulsion continuously positioned on the wing leading edge and a fuselage with a large cross-section both to accommodate the instrumentation and to be representative of a transport aircraft.

The aircraft overall geometry is represented in Fig 9.1 and a picture of the assembled model is given in Fig 9.3. Its detailed geometry is available in Annex C.1, Table C.1. The aircraft has a high wing with a low Reynolds airfoil S3010, for which wind-tunnel data exist [Selig 1989]. The aircraft is equipped with plain flaps and ailerons. The distributed propulsion system is composed of eight identical motors symmetrically placed on the wingspan. The detailed equipment is further discussed in section 9.2.1.

The horizontal tail surface area and level arm are sized to obtain the same tail volume as the ATR72. The geometry is kept simple on purpose to ease the construction and the integration of the equipment. The wing and tail surface are built from polystyrene foam and carbon composite. The fuselage is a wood and carbon composite truss structure covered with a plastic film. Finally the front cone and the fixed main landing gear are made of fiber-glass.

The final weight amounts to 8.25 Kg and the inertia terms presented in Table 9.2

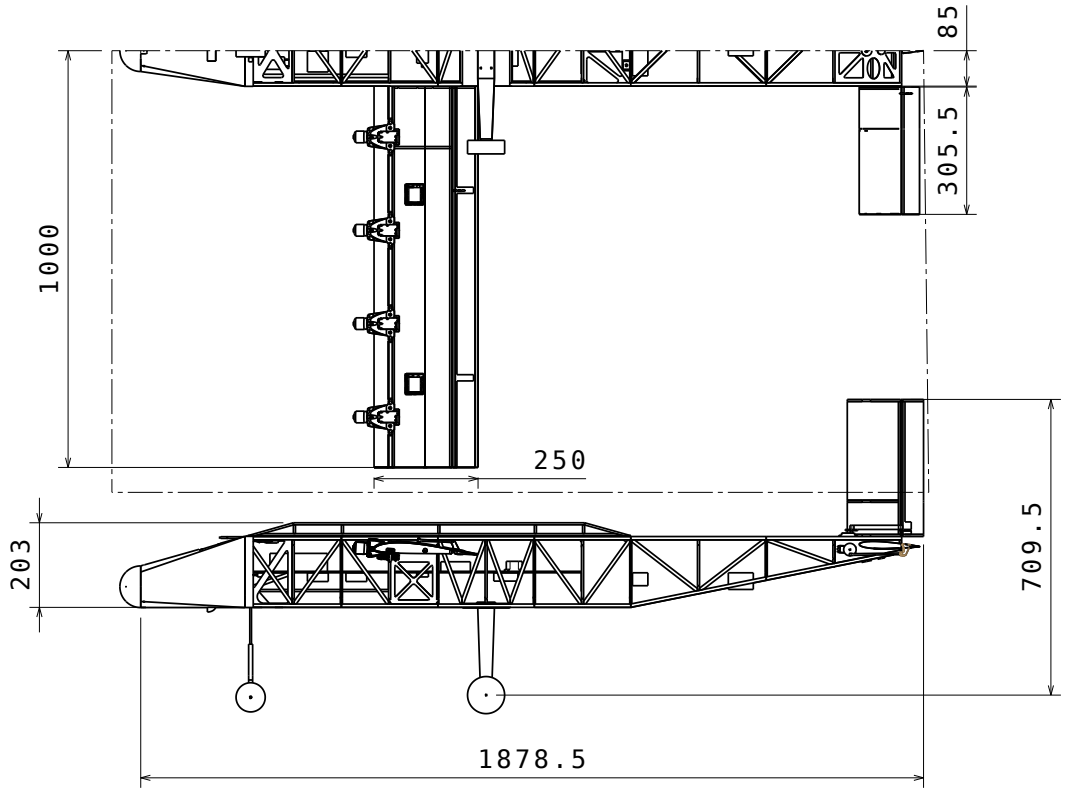

Figure 9.1 – DECOL external dimensions.

are measured by the pendulum technique [Jardin 2009]. At this mass, the cruise airspeed is 23.5 m/s and the stall velocity was measured at 14.5 m/s with flaps deployed at 15°.

Table 9.2 – DECOL mass and inertia characteristics (Normal operating condition)

Mass	8.25kg
I_x	1.1 kg.m^2
I_y	1.2 kg.m^2
I_z	2.0 kg.m^2

9.1.2 Key design properties

The aircraft features unique design properties to study aircraft stability and control with DEP. The directional static stability was calculated in the OEI condition and the vertical tail designed accordingly. Additionally, the fuselage is built with a large cross section on purpose, to have a naturally unstable body. To be able to test the static stability reduction discussed in Part III, the VT is made removable. The level arm between the wing leading edge and vertical tail remains fixed but the surface area and aspect ratio can be changed to obtain the desired directional static stability.

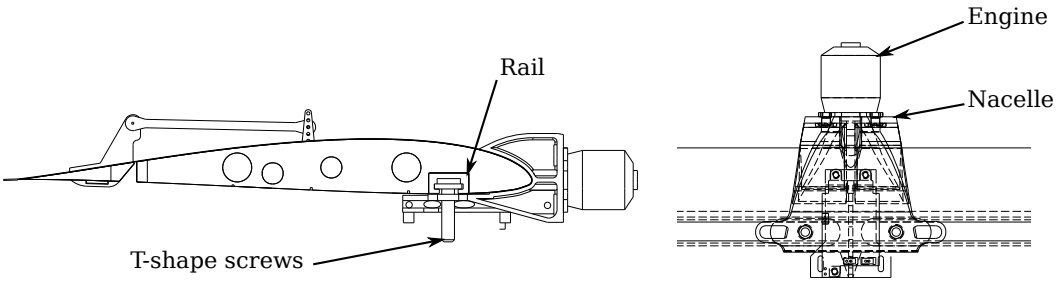

Figure 9.2 – Embedded rail and nacelle positioning on the wing.

A second key characteristic is the possibility to position the engine nacelle continuously on the wingspan thanks to an aluminium rail embedded in the airfoil (see Fig 9.2). This allows to re-configure the aircraft with an arbitrary number of engines of various size, power and position. The nacelles are built by 3D printing and can hence adapt a large variety of engine positioning with respect to the wing chord.

The propulsion cannot be moved in flight nor in between flights as the wiring must be modified in between each version. The idea is that after the first flight campaign, the same platform can be easily re-employed to test a more optimized power distribution. The aluminium rail also provides structural strength to the wing.

Finally, the fuselage answers more practical convenience rather than aerodynamics performances. The rectangular cross section renders the construction, integration and accessibility of equipment easy. A one meter long service hatch provides a large access to all equipments without compromising structure integrity. Additionally, the on-board electronics is fixed to a single rack that slides into the fuselage. The entire electronic system can be exchanged on the field within minutes or removed from the structure if an intervention is required.

Figure 9.3 – DEmonstrateur COntrol Latéral, (Lateral Control Demonstrator) (DECOL) at the airfield.

9.2 Equipment

A difference is made between the equipment mandatory for flight operation and the instrumentations used to log aircraft flight parameters, although the same equipment may fulfil both functions. The aircraft Remote Controlled (RC) equipment, its propulsion and actuation system are described here.

9.2.1 Propulsion system

The distributed propulsion system had to comply with one requirement: to cover a majority of the wing leading edge. However placing an engine in the wingtip vortex was not of interest since this specific interaction is not modelled in this

work. An important power distribution being prioritised, this led the propellers to be the main design driver.

9.2.1.1 Propellers

The choice of propeller was conveniently oriented toward a reference for which a thrust and power model was available. The rich small propeller database created by Brandt and Selig [Brandt 2015] provides a baseline choice of fixed pitch propellers. The second constraint was market availability which was limited by the fact that both left and right rotation propellers should be available. The final trade off was propellers with a diameter D_p of 8 inches and 6 inches in pitch (see propeller characteristics in Fig 9.4). This allowed to fit a maximum of eight engines on the wing with a propeller spacing of $0.1D_p$ and reach the cruise airspeed with a reasonable engine rotation rate of approximately 10 000RPM. The propeller rotation directions are alternating with the outer most engines rotating against the wingtip vortex.

The propeller thrust is retrieved from the motor rotation speed ω_m (in rotation per second), the airspeed and the propeller model of Fig 9.4 using propeller thrust coefficient C_p, power coefficient C_t and the advance ratio defined as:

$$J = \frac{V_a}{\omega_m D} \tag{9.1}$$

$$C_t = \frac{T}{\rho \omega_m^2 D^4} \tag{9.2}$$

$$C_p = \frac{P}{\rho \omega_m^3 D^5} \tag{9.3}$$

9.2.1.2 Electronic Speed Controller (ESC)

The ESC Zubax Orel 20 was selected for its ability to provide data about the engine and power bus. In addition, the ESC uses a well documented, open source firmware [Kirienko 2019b] giving the possibility to adjust the engine acceleration rate, set the RPM controller and also to know the type of engine control performed by the ESC. Each ESC is able to measure and send through the digital UAVCAN bus [Kirienko 2019a], the engine RPM, the intensity drawn from the power bus and the power bus voltage at the location of the ESC. These features are most often not available for ESC aimed at hobby models or small UAVs.

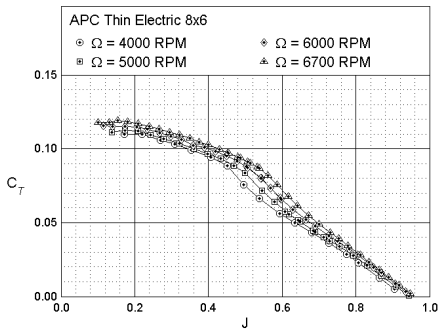

(a) C_t

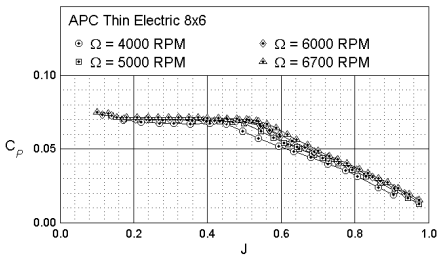

(b) C_p

Figure 9.4 – Propeller APC thin electric 8"x6" thrust and power coefficients [Brandt 2015].

The limit of this ESC was the 19V maximum voltage operation [1] which limited the choice of battery to a 4S lithium polymer battery which provides a voltage between 16.8V and 14.5V. This low bus voltage translated in a high intensity demand and the wires had to be sized to lower resistive losses and local overheating.

The engine, a XPower XC2816/16 [xpo] with maximum current 19A and speed constant $k_v = 1100\,\mathrm{RPM/V}$ was chosen in consequence to accommodate the voltage and rotation speed constraints. The engine operates below its maximum continuous power such that flight operation with 6 engines is possible.

9.2.1.3 Power distribution and power control system

A redundant parallel power distribution, robust to single component failure was designed. The propulsion chain is made of two parallel systems each comprising a 4S1P 5000 mAH lithium battery, a fuse, an electronic safety switch and power board dispatching power to four engines symmetrically placed on the wing.

With this architecture, the failure of one of the critical component (battery, fuse, switch or power board) would result in losing half of the power and the thrust would remain symmetric.

The communication between each ESC and the flight controller is ensured through the digital UAVCAN bus [Kirienko 2019a]. This serial bus allowed significant simplification of the wiring.

1. The manufacturer has discontinued this ESC. It is replaced by a reference accepting up to 50V operation.

9.2.1.4 Actuation system

The aircraft has the following control surfaces: two ailerons, two flaps, a rudder and an elevator. They are actuated by hobby grade servomotors communicating via a Pulse Width Modulation (PWM) link. As these servomotors don't provide position feedback, they are placed at the closest from the control surfaces and the mechanical links are made rigid to be able to approximate the pilot inputs directly as surface deflection.

The RC material is a generic hobby material coupled to a Pixhawk flight controller to manage the link between the RC receiver, the servomotor and the ESC. The Pixhawk is set as 'manual pass-through', which signifies that the input of the pilot are directly passed to the actuators and distributed to the engines. The flight control capability of the Pixhawk is not utilized.

9.3 Instrumentation

The components providing data measurements in parallel to their primary function, the ESC and the Pixhawk, were described previously. This section describes the avionics dedicated to on-board flight data measurement and recording.

9.3.1 Acquisition system

The Pixhawk unit is used with an O-droid companion computer operating Robotic Operating System (ROS) [ros], version melodic under Linux-Ubuntu. The O-droid is directly connected to each component providing data measurements. Data is recorded on-board the aircraft using the ROS function `rosbag` which handles data packaging and time-stamping. A redundant radio link allows the transmission of flight parameters from both the O-droid and the Pixhawk to a ground-station for flight monitoring.

9.3.2 Inertial and Global Navigation Satellite System (GNSS) measurements

A commercially available miniature navigation system from SBG-systems© [SBG] is used to provide orientation, inertial velocity and position. The unit performs internal data fusion with a Kalman filter based on inertial, magnetic, pressure and GNSS measurements. The sensor is calibrated by the manufacturer. It is installed

on the aircraft using a machining template to ensure alignment with the fuselage principal axis and know precisely its position with respect to the centre of gravity. A list of measurement given by the unit is available in Table C.3 in the bloc named *Ellipse2*.

9.3.3 Air data measurement

Upon collaboration with the Laboratoire d'Aérologie of Toulouse, the aircraft benefited from the experience that this Laboratory made with multi-hole sphere probes [Alaoui-Sosse 2018]. The laboratory team kindly provided the mechanical drawings of a custom made five-holes sphere and accompanying electronics. This probe was adopted to furnish the air data measurements (see Fig 9.5).

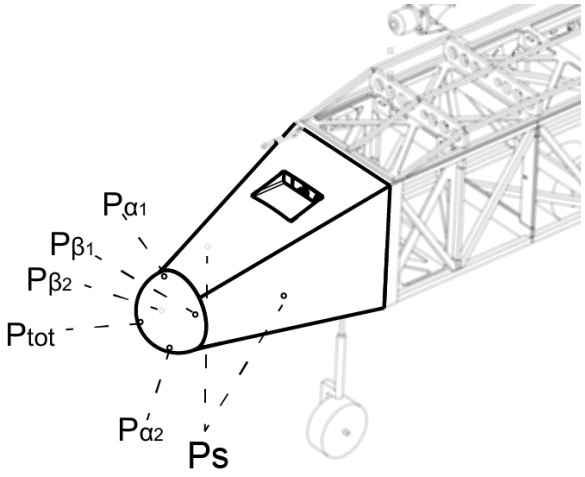

Figure 9.5 – Five-holes sphere integrated in the aircraft nose, reproduced from [Al-Nahhas 2020].

Multi-hole probes have been studied and tested as an alternative to Pitot tubes and air-flow vanes. Their main advantage being the absence of moving parts [Sahin 1985], [Brown 1983]. Multi-hole probes provide differential pressure measurement at known locations on a sphere. Using potential flow theory, it is possible to retrieve the angle of attack and the side slip angle. Theoretical description and development of this type of sensor is available in [Brown 1983]. The baseline relation between the sensor measurements and the airflow angles at the location of the sphere α_s and β_s are given by equation (9.4) and (9.5):

$$\alpha_s = \frac{\Delta P_\alpha}{k_\alpha \bar{q}}, \tag{9.4}$$

$$\beta_s = \frac{\Delta P_\beta}{k_\beta \bar{q}}, \tag{9.5}$$

with ΔP_α, ΔP_β, the differential pressure measurement in the $X_b - Z_b$ plane ($\Delta P_\alpha = P_{\alpha_2} - P_{\alpha_1}$ in Fig 9.5) and $X_b - Y_b$ plane ($\Delta P_\beta = P_{\beta_2} - P_{\beta_1}$ in Fig 9.5). k_α, k_β are the calibration constants for angle of attack and side slip and $\bar{q}$ is the dynamic pressure.

In addition, the sphere measures a pressure differential ΔP_{V_a} between a central hole and static pressure ports located on the side of the cone ($\Delta P_{V_a} = P_{\text{tot}} - P_{\text{s}}$ in Fig 9.5). This dynamic pressure measurement is then used to retrieve the airspeed:

$$V_a = \sqrt{\frac{\Delta P_{V_a}}{0.5\rho}} \tag{9.6}$$

9.4 Aircraft theoretical study

Estimating the aerodynamic coefficients of the aircraft with and without the influence of the propulsion is possible with the VLM software, VeDSC method and aero-propulsive interaction model presented in section 2.2 and section 3.3 respectively. This section proposes an overview of the key aerodynamic coefficients of the aircraft and predicted thrust effects. The thrust coefficient of equation (3.22) is utilized as non-dimensional variable to characterise the thrust effects. Its definition was made in section 3.3 and is recalled here:

$$T_{c_i} = \frac{T_i}{2\rho S_p V_{a_i}^2},$$

where the subscript $_i$ referrers to the engine number, S_p is the propeller disc area and V_{a_i} is the airspeed at the location of the i$^{\text{th}}$ engine:

$$V_{a_i}^b = V_a^b + \begin{pmatrix} p \\ q \\ r \end{pmatrix} \times \begin{pmatrix} x_i \\ y_i \\ z_i \end{pmatrix}.$$

To characterize the global effect of the propulsion with a uniform propulsion, the average thrust coefficient can be utilized. To lighten the notation in this work, T_c always refers to the averaged thrust coefficient: $T_c = \frac{1}{8}\sum_{i=1}^{8} T_{c_i}$.

9.4.1 Longitudinal coefficients

The baseline lift, drag and pitching moment derivatives are obtained with VLM simulations using VSPaero [Gloudemans 1996]. The aero-propulsive interaction model developed in section 3.3 is then employed to compute the lift and drag increase due to blowing. This is illustrated in Fig 9.6 where the lift versus the angle of attack and the lift versus drag polar are plotted with increasing thrust coefficient.

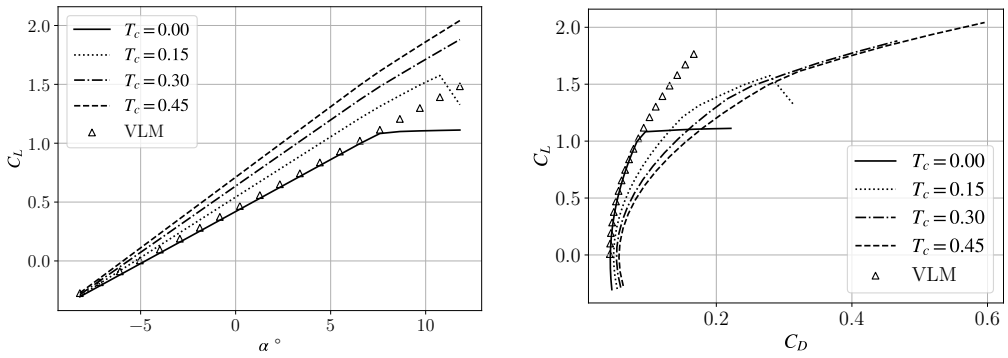

(a) Lift versus angle of attack.

(b) Lift versus drag coefficient.

Figure 9.6 – Aircraft lift and drag polars with increasing thrust settings. The drag includes a zero lift term C_{D_0} found from flight data. The stall angle is set to 11° for unblown case, according to [Brandt 2015].

The primary interest is the lift increase because aero-propulsive forces follow from this. Fig 9.6a shows that both the lift slope coefficient C_{L_α} and the alpha zero lift term C_{L_0} become a function of the thrust coefficient. C_{L_α} can be well approximated by a second order polynomial as shown in Fig 9.7.

The lift coefficients C_{L_α} and C_{L_0} are plotted for an interval of T_c corresponding to what has been observed in flight $T_c \in [0.0; 0.6]$. Within this interval, the non-linear behaviour can be well approximated by a second order polynomial, as illustrated in Fig 9.7a and of the form:

$$C_{L_\alpha} = C_{L_{\alpha T_c^2}} T_c^2 + C_{L_{\alpha T_c}} T_c + C_{L_{\alpha_0}} \,. \tag{9.7}$$

Knowing this kind of information will later facilitate the identification of the model's structure from flight data.

The drag being quadratic in lift, it can be estimated by a function of the angle

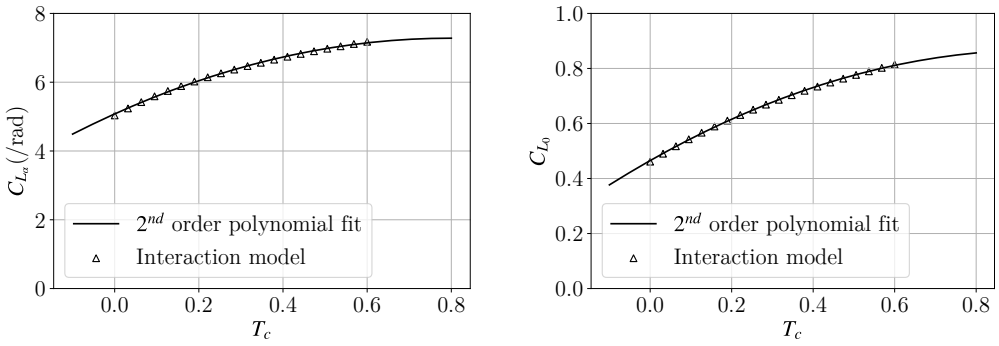

(a) Lift slope coefficient as a function of thrust coefficient.

(b) Alpha zero lift coefficient as a function of thrust coefficient.

Figure 9.7 – Lift coefficients C_{L_α} and C_{L_0} as a function of the thrust coefficient.

of attack as a second order polynomial:

$$C_D = C_{D_{\alpha^2}}\alpha^2 + C_{D_\alpha}\alpha + C_{D_0}\,. \tag{9.8}$$

Each of the coefficients of equation (9.8) can be modified by the thrust coefficient. These changes can be anticipated in the same manner as the lift slope coefficient. The evolution of $C_{D_{\alpha^2}}$, C_{D_α} and C_{D_0} as a function of the thrust coefficient are calculated and shown in Fig 9.8.

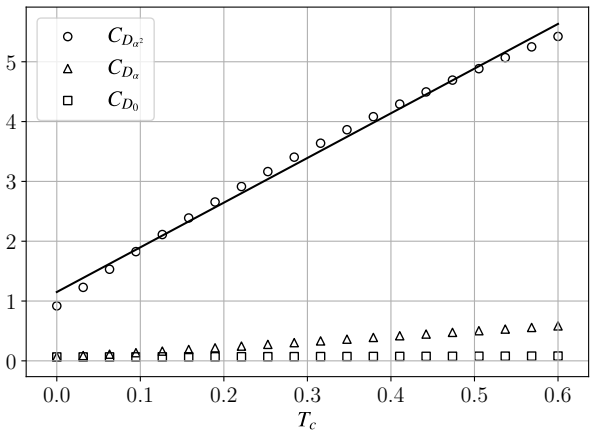

Figure 9.8 – Coefficients of the drag polynomial equation (9.8) as a function of thrust coefficient, calculated evolution.

It appears that $C_{D_{\alpha^2}}$ and C_{D_α} are functions of the thrust coefficient. Although their evolution seem quadratic with T_c, a linear fit can be used with sufficient accu-

racy to describe this evolution.

The pitching moment coefficient C_M will be influenced by T_c through the variation of C_{L_α}. This is illustrated by the pitching moment derivative C_{m_α} that can be expressed as [Etkin 2012]:

$$C_{m_\alpha} = C_{L_\alpha} \frac{x_{\mathrm{CG}} - x_{\mathrm{n}}}{\bar{c}} - V_H C_{L_{t,\,\alpha}} \left(1 - \frac{\partial \varepsilon}{\partial \alpha}\right), \tag{9.9}$$

where V_H is the horizontal tail volume ratio (see Annex C.1), $C_{L_{t,\,\alpha}}$ is the horizontal tail lift slope coefficient, ε is here the downwash angle at the tail, x_{n} and x_{CG} are the neutral point and centre of gravity location from the wing leading edge and $\bar{c}$ is the mean chord.

Since the horizontal tail is at the same height as the wing, it is embedded in the propeller slipstreams. The coefficients related to the horizontal tail can become function of the thrust coefficient. Introducing equation (9.7) into equation (9.9) and neglecting terms of second order in T_c, one obtains:

$$C_{m_\alpha} = \left[C_{L_{\alpha T_c}} T_c + C_{L_{\alpha_0}}\right] \frac{x_{\mathrm{CG}} - x_{\mathrm{n}}}{\bar{c}} - V_H \left[C_{L_{t,\,\alpha T_c}} T_c + C_{L_{t,\,\alpha_0}}\right] \left(1 - \frac{\partial \varepsilon}{\partial \alpha} + \frac{\partial^2 \varepsilon}{\partial \alpha \partial T_c} T_c\right), \tag{9.10}$$

which after developing and neglecting again terms of second order in T_c can be factorized to:

$$C_{m_\alpha} = C_{m_{\alpha_0}} + C_{m_{\alpha\, T_c}} T_c\,, \tag{9.11}$$

with

$$C_{m_{\alpha\, T_c}} = C_{L_{\alpha T_c}} \frac{x_{\mathrm{CG}} - x_{\mathrm{n}}}{\bar{c}} - V_H C_{L_{t,\,\alpha T_c}} \left(1 - \frac{\partial \varepsilon}{\partial \alpha} + \frac{\partial^2 \varepsilon}{\partial \alpha \partial T_c}\right). \tag{9.12}$$

$$C_{m_{\alpha_0}} = C_{L_{\alpha_0}} \frac{x_{\mathrm{CG}} - x_{\mathrm{n}}}{\bar{c}} - V_H C_{L_{t,\,\alpha_0}} \left(1 - \frac{\partial \varepsilon}{\partial \alpha}\right). \tag{9.13}$$

This shows that the thrust can have either a stabilizing ($C_{m_{\alpha T_c}} < 0$) or destabilizing effect ($C_{m_{\alpha T_c}} > 0$) on the pitching moment coefficient. The aerodynamic tool developed to estimate aero-propulsive interactions being limited to the propeller-wing interactions, the coefficient $C_{L_{t,\,\alpha T_c}}$ cannot be estimated before hand.

9.4.2 Lateral coefficients

The lateral force coefficient can be modified by the lateral force developed by propellers in side slip (see section 3.1.1). This contribution can be calculated with

equations (3.1) to (3.5) and is illustrated in Fig 9.9a.

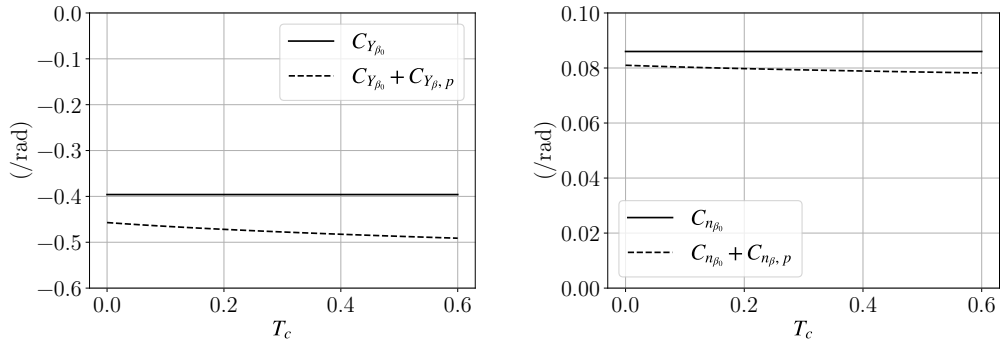

(a) Side force derivative with and without propeller side forces.

(b) Restoring yawing moment derivative. With and without the contribution of the propeller.

Figure 9.9 – Propeller forces and moment coefficients as a function of the thrust coefficient.

The baseline side force derivative $C_{Y_{\beta_0}}$ of the aircraft, as calculated with the VLM simulation and VeDSC method is also represented. Most of the propeller effect is a constant contribution to the side force derivative and a small variation with T_c.

Most of the vertical tail being outside of the propeller slipstream (see Fig 9.1), the lateral force due to the VT is assumed to be independent of the thrust coefficient. Once again, the aero-propulsive interaction module being limited to propeller-wing interactions, any slipstream-empennage interaction cannot be calculated before hand.

The propellers being located in front of the centre of gravity, the side force due to propeller discs creates a destabilizing yawing moment derivative $C_{n_{\beta},p}$. The effect of this derivative is represented in Fig 9.9b along with the baseline restoring moment derivative $C_{n_{\beta_0}}$ calculated with VLM simulations and the VeDSC method.

As for the lateral force, most of the propellers contribution to $C_{n_{\beta}}$ is a constant term with a small dependence on T_c.

Finally, with the actual model, the contribution of the propulsion on the rolling moment is essentially manifested with the aileron efficiency. The ailerons are fully embedded in the propeller slipstream and their efficiency can be extracted for small deflections. The rolling moment coefficient and induced yawing moment coefficient due to aileron deflection as a function of the thrust coefficient is presented in Fig 9.10.

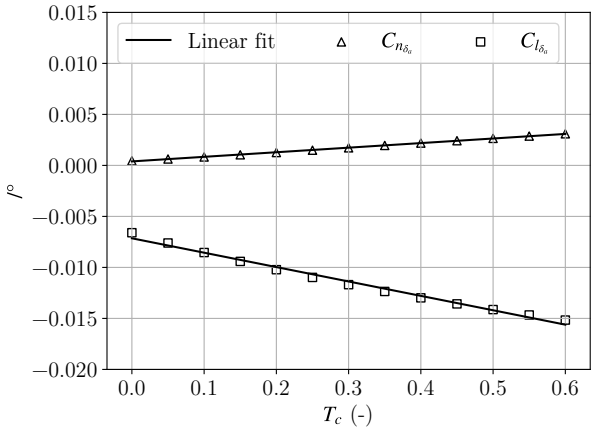

Figure 9.10 – Rolling and yawing moment derivatives due to an aileron deflection as a function of T_c

The adverse yaw with increasing T_c illustrated in Fig 9.10 is given for a case where aileron differential is not used. The aileron efficiency is largely impacted by the thrust and although the variation is not linear, with the interval of T_c encountered in flight, it can be well approximated by a linear relationship.

9.4.3 Efforts induced by differential thrust

Differential thrust is realised with the four outer engines 1, 2 and 7, 8. It is measured as a difference of thrust coefficient between symmetric engines: $\Delta T_c = (T_{c_1} - T_{c_8}) = (T_{c_2} - T_{c_7})$. With this convention, and the level of differential thrust observed in flight, it is possible to compute:

— the induced rolling moment coefficient due to ΔT_c, illustrated in Fig 9.11a

— the total yawing moment coefficient that takes into account the local induced drag increase, illustrated in Fig 9.11b.

The two graphics of Fig 9.11 have been obtained for a steady flight at cruise velocity. Since the source of these induced forces are the lift increase due to blowing, they depend heavily on the angle of attack. The induced rolling moment due to differential thrust is compared with the rolling moment of the ailerons at the same reference thrust coefficient ($\Delta T_c = 0.15$) but without differential thrust. It gives an idea of the effort necessary to counter the rolling moment induced by differential thrust.

Fig 9.11b shows the yawing moment due to engine thrust alone and when the

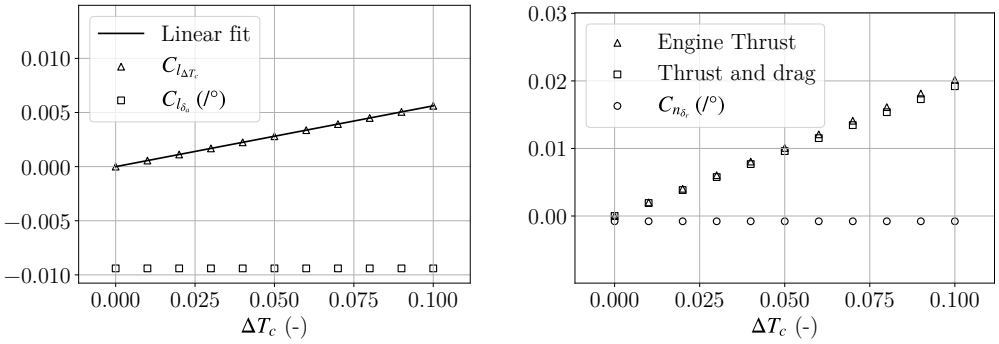

(a) Rolling moment induced by differential thrust compared with a 1° aileron deflection.

(b) Yawing moment produced by differential thrust compared with a 1° rudder deflection.

Figure 9.11 – Induced rolling and yawing moment due to differential thrust at a reference $T_c = 0.15$.

local induced drag is taken into account. In these cruise conditions, the local induced drag is small and the engines remain efficient. The yawing moment due to a one degree deflection of the rudder is shown for comparison. It should be noted that $\Delta T_c = 0.1$ is quite an extreme value for cruise conditions and the rudder can reach 30° of deflection. At the maximum deflection the rudder would produce slightly more yawing moment than differential thrust at $\Delta T_c = 0.1$.

9.5 Conclusion

This chapter introduced the flight demonstrator DEmonstrateur COntrol Latéral, (Lateral Control Demonstrator) (DECOL) designed to answer the three following goals:

— characterise the aircraft lateral flight dynamics when a large portion of the wing is immersed in the propeller slipstream,

— characterise the induced aero-propulsive effects at play when differential thrust is used,

— evaluate the feasibility to implement the control laws and VT reduction obtained in Part III with the knowledge obtained from the first two objectives.

The geometry and key design aspects of this eight engines aircraft were introduced in section 9.1. The notable design characteristics are a rail allowing to continuously position the engines on the wing or interchange the engine nacelle to modify the

propeller position with respect to the wing. The vertical tail is removable to allow a reduction of directional static stability.

The propulsion system and instrumentation were summarized in section 9.2 and section 9.3. Key technologies and component such as the UAVCAN and the ESC facilitated greatly the communication between components and on-board computer on such a distributed architecture. The on-board computer operating system ROS Melodic gathers all data and manages on-board logging.

Finally, the tools developed in Part II of this work were used to analyse the aircraft. It gave the expected changes in aerodynamics and actuator induced forces with the thrust coefficient and an initial idea of how the aero-propulsive interactions can be modelled in the identification process. Except for the lift coefficients, most of the changes in aerodynamic derivatives should be correctly approximated by a linear dependence on the thrust coefficient. This analysis represents a baseline against which the identified model can be compared to put in light unexpected behaviours.

Chapter 10

Identification of aero-propulsive model

Contents

The flight test campaign consisted of 8 flights of a duration of 7 minutes in average. The members of the hobby model club of Revel were so kind to welcome the aircraft and the team on their airfield located on the private airfield of Revel (France). This airfield had the advantage of having a runway allowing safe excursion without damaging the aircraft.

The objective of the first four flights were to acquire a good knowledge of the aircraft handling qualities at low speed, its behaviour toward stall and create a procedure to safely operate the aircraft, especially for landing. Two additional flights were used to get more knowledge about the climb rate.

The two last flights were used to identify the longitudinal and lateral aerodynamic models as well as the aero-propulsive effects. Data used for identification of

the models presented in this chapter come from these two flights which were realized the same day.

The chapter starts with the methodology used for calibration of the multi-hole sphere and wind estimation in section 10.1.

The equation error is used for identification, this methodology and theoretical background for identification is presented in section 10.2.

The identified longitudinal and lateral models are presented in section 10.3. For both longitudinal and lateral models, two model structures were created: the first one ignores the aero-propulsive effect and the second one uses the thrust coefficient to account for the aero-propulsive effects. The two models are presented in parallel to appreciate the pertinence of explicit thrust derivatives.

10.1 Instrumentation calibration

Sensors were calibrated from the factory or on the ground with the exception of the five-holes probe. This sensor is calibrated directly with flight data. This section explains the dynamic pressure calibration (section 10.1.1), wind estimation (section 10.1.2) and the calibration of the airflow angles reading (section 10.1.3).

10.1.1 Dynamic Pressure

The dynamic pressure ΔP_{V_a} is measured by the five-holes sphere as the pressure differential between the sphere central hole P_T and the static pressure ports P_s located on the side of the nose: $\Delta P_{V_a} = P_T - P_s$ (see Fig 9.5 section 9.3.3).

From this measurement, the airspeed V_a is retrieved through the equation of the dynamic pressure:

$$\Delta P_{V_a} = \frac{1}{2}\rho V_a^2 (1 - C_{p_s}) \,, \tag{10.1}$$

$$V_a = \sqrt{\frac{\Delta P_{V_a}}{\frac{1}{2}\rho(1 - C_{p_s})}} \,, \tag{10.2}$$

where $C_{p_s} = \frac{P_s - P_\infty}{0.5\rho V_a^2}$ is the pressure coefficient at the location of the static port. If the static port is ideally located on the aircraft, then $P_s = P_\infty$ and equation (10.1) reduces to $\Delta P_{V_a} = \frac{1}{2}\rho V_a^2$. This is generally not the case [Klein 2006] and it was anticipated with DECOL given the shape of the nose. Potential flow simulations gave a preliminary value for C_{p_s} but the constant was estimated again with ground

and flight data.

The sphere's central hole is not sensitive to small variations of angle of attack or side slip angle and it can be assumed that the total pressure is well measured [Brown 1983].

To find C_{p_s}, the aircraft is flown in rectangular circuits around the field at cruise velocity and altitude in calm weather conditions. The rectangular circuits cancel the mean effect of the wind such that in average the five-holes dynamic pressure measurement can be calibrated with the kinematic velocity. C_{p_s} is found by minimizing the residual error between the kinematic velocity V_k and the airspeed ε_{dyn}:

$$\varepsilon_{dyn} = \sum_{i=1}^{N} \left[V_{k_i}^2 - \frac{\Delta P_{V_a,\,i}}{\frac{1}{2}\rho(1 - C_{p_s})} \right] , \tag{10.3}$$

for a data sequence comprising N measurements. Diverse runs resulted in small values of C_{p_s}, the reference pressure coefficient used in this work is $\widehat{C}_{p_s} = 0.0034$. This value is then used to correct the dynamic pressure reading by manipulating equation (10.1):

$$\bar{q} = \frac{\Delta P_{V_a}}{(1 - \widehat{C}_{p_s})} = \frac{1}{2}\rho V_a^2 \, . \tag{10.4}$$

10.1.2 Wind Estimation

Although the flight tests were carried out as much as possible in calm conditions, the wind has to be estimated as it is needed for the calibration of the airflow angle measurements.

Turbulent conditions and thermals were avoided by flying only in the morning. The wind is assumed to be constant and uniform, and the vertical component of the wind speed w_w^o was assumed to be negligible as vertical components of wind are assumed to be short-lived at the location of the flight tests..

Under these hypotheses it is possible to expressed the magnitude of the airspeed as:

$$\|\mathbf{V}_a^o\| = \|\mathbf{V}_k^o - \mathbf{V}_w^o\| \, , \tag{10.5}$$

$$V_a^2 = (u_k^o - u_w^o)^2 + (v_k^o - v_w^o)^2 + w_k^{o2} \, . \tag{10.6}$$

The kinematic velocity being given by the IMU and the airspeed being deduced from the calibrated dynamic pressure readings from the five-holes sphere, u_w and

v_w are found by minimizing the residual error ε_w:

$$\varepsilon_w = \sum_{i=1}^{N} [V_{a_i}^2 - (u_{k_i}^o - u_w^o)^2 - (v_{k_i}^o - v_w^o)^2 - {w_{k_i}^o}^2] = 0\,. \tag{10.7}$$

This minimisation resulted in a constant estimate for wind in the North u_w^o and East v_w^o directions for each flight. An example of wind estimation is given in Fig 10.1.

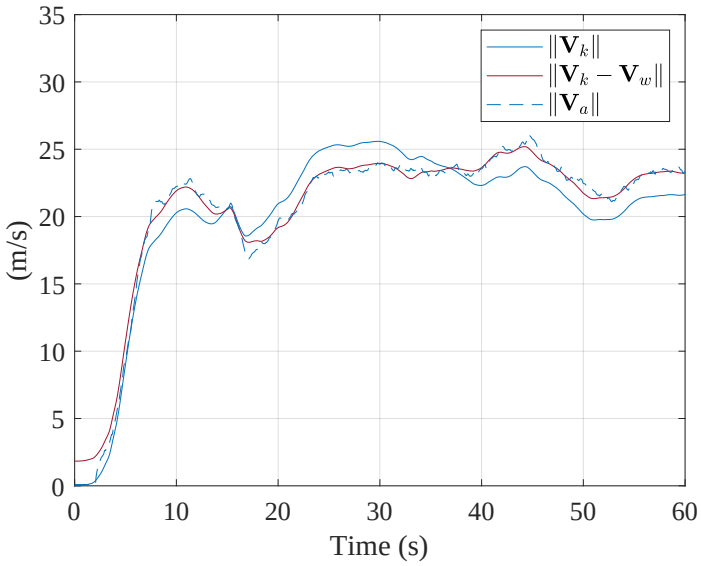

Figure 10.1 – Example of estimation of a constant wind. First minute of the flight including take-off.

10.1.3 Calibrating Airflow Angles

The goal of this section is to calibrate the multi-holes sphere with flight data. Recalling equation (9.4) and (9.5), a model linking the probe's measurements and the local airflow angles α_s, β_s is:

$$\alpha_s = \frac{\Delta P_\alpha}{k_\alpha \bar{q}} + \alpha_0\,, \tag{10.8}$$

$$\beta_s = \frac{\Delta P_\beta}{k_\beta \bar{q}} + \beta_0\,, \tag{10.9}$$

where ΔP_α, ΔP_β are respectively the vertical, horizontal pressure differential and $\bar{q}$ the calibrated dynamic pressure. The constants to estimate during calibration are k_α, k_β the proportionality coefficients and α_0, β_0, two constant bias accounting

for misalignments. The model is calibrated using the equation error method and reconstructed airflow angles from inertial and GNSS measurements and the constant wind field.

The local airflow angles α_s and β_s can be found by expressing the airflow velocity vector at the location of the sphere $V_{a,\,s}$ with the hypothesis of uniform wind:

$$\mathbf{V}^b_{a,\,s} = \mathbf{V}^b_{k,\,s} - \mathbf{V}^b_w \,, \tag{10.10}$$

with $\mathbf{V}^b_{k,\,s}$ the kinematic velocity vector at the location of the sphere, expressed with the distance between the aircraft centre of gravity to the sphere **os**:

$$\mathbf{V}^b_{k,\,s} = \mathbf{V}^b_{k,\,s} + \mathbf{\Omega}^b \times \mathbf{os}^b \,. \tag{10.11}$$

Combining the two previous equation gives:

$$V_{a,\,s} \begin{pmatrix} \cos\alpha_s \cos\beta_s \\ \sin\beta_s \\ \cos\beta_s \sin\alpha_s \end{pmatrix} = \begin{pmatrix} u^b_k \\ v^b_k \\ w^b_k \end{pmatrix} + \begin{pmatrix} p \\ q \\ r \end{pmatrix} \times \begin{pmatrix} x^b_{os} \\ y^b_{os} \\ z^b_{os} \end{pmatrix} - \mathcal{T}_{bo} \begin{pmatrix} u^o_w \\ v^o_w \\ 0 \end{pmatrix} \,, \tag{10.12}$$

with $(x^b_{os},\, y^b_{os},\, z^b_{os})^T = \mathbf{os}$ and $\mathcal{T}_{bo}$ the rotation matrix from NED to body frame (see equation 1.1). Selecting the two last rows of equation (10.12), one obtains [Boiffier 1998]:

$$\sin\beta_s = \frac{1}{V_{a,\,s}} (v^b_k - v^b_w + r x^b_{os} - p z^b_{os}) \,, \tag{10.13}$$

$$\sin\alpha_s = \frac{1}{V_{a,\,s}\cos\beta_s} (w^b_k - w^b_w + p y^b_{os} - q x^b_{os}) \,. \tag{10.14}$$

The constants $\hat{k}_\alpha$, $\hat{k}_\beta$, $\hat{\alpha}_0$, $\hat{\beta}_0$ are obtained after solving the ordinary least square problems:

$$\boldsymbol{\alpha}_s = \left[\frac{\Delta\mathbf{P}_\alpha}{\Delta\mathbf{P}_{dyn}} \quad \mathbf{1_n} \right] \begin{pmatrix} \frac{1}{k_\alpha} \\ \alpha_0 \end{pmatrix} \,,$$

$$\boldsymbol{\beta}_s = \left[\frac{\Delta\mathbf{P}_\beta}{\Delta\mathbf{P}_{dyn}} \quad \mathbf{1_n} \right] \begin{pmatrix} \frac{1}{k_\beta} \\ \beta_0 \end{pmatrix} \,, \tag{10.15}$$

where $\boldsymbol{\beta}_s$, $\boldsymbol{\alpha}_s$ are the vector of $\mathbf{n}$ measurements determined with equations (10.13) and (10.14).

After calibration of the probe, the airflow angles at the location of the sphere are obtained with the identified model:

$$\hat{\alpha}_s = \frac{\Delta P_\alpha}{\hat{k}_\alpha \bar{q}} + \hat{\alpha}_0 \,, \tag{10.16}$$

$$\hat{\beta}_s = \frac{\Delta P_\beta}{\hat{k}_\beta \bar{q}} + \hat{\beta}_0 \,. \tag{10.17}$$

The aircraft airflow angles, α_a, β_a and airspeed V_a are computed from the calibrated model of the probe by removing the rotation terms:

$$\mathbf{V}_a^b = \mathbf{V}_{a,\,s}^b - \boldsymbol{\Omega} \times \mathbf{os} \,,$$

$$V_a = \left\| \begin{array}{c} V_{a,\,s} \cos\hat{\alpha}_s \cos\hat{\beta}_s - (qz_{os}^b - ry_{os}^b) \\ V_{a,\,s} \sin\hat{\beta}_s - (rx_{os}^b - pz_{os}^b) \\ V_{a,\,s} \cos\hat{\beta}_s \sin\hat{\alpha}_s - (py_{os}^b - qx_{os}^b) \end{array} \right\| , \tag{10.18}$$

$$\sin\beta_a = \frac{V_{a,\,s}}{V_a} \sin\hat{\beta}_s + \frac{pz_{os}^- rx_{ob}^b}{V_a} \,, \tag{10.19}$$

$$\sin\alpha_a = \frac{V_{a,\,s}}{V_a \cos\beta_a} \sin\hat{\alpha}_s \cos\hat{\beta}_s + \frac{qx_{os}^b - py_{ob}}{V_a \cos\beta_a} \,. \tag{10.20}$$

Flight periods with a good estimation of the wind field and dynamic manoeuvres are chosen for calibration of the sphere. The least square estimate of the constants is given in Table 10.1.

Table 10.1 – Multi-hole sphere calibration parameters

$\hat{k}_\alpha$ (rad^{-1})	6.481
$\hat{k}_\beta$ (rad^{-1})	4.817
$\hat{\alpha}_0$ (rad)	0.0377
$\hat{\beta}_0$ (rad)	0.0089

The resulting calibration is shown in Fig 10.2 where the reconstructed angles α_s, β_s, the model of the probe $\hat{\alpha}_s$, $\hat{\beta}_s$ and the aircraft airflow angles α_a, β_a are compared.

There may be a deviation between the reconstructed airflow angles α_s, β_s and

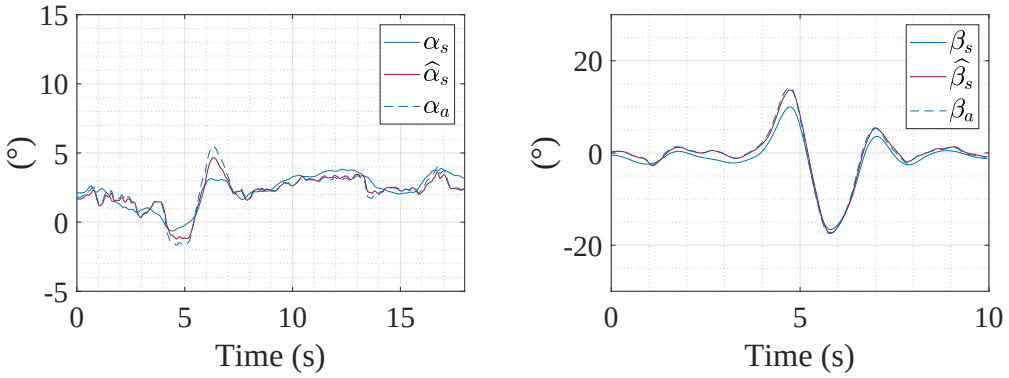

(a) Angle of attack. (b) Side slip.

Figure 10.2 – Calibration of multi-holes probe with flight data.

the model $\hat{\alpha}_s$, $\hat{\beta}_s$. It is believed to be due to the reconstruction of α_s and β_s from inertial and GNSS data because the acceleration vector correlates better with the angles deduced from the probe (see Fig 10.3). The error in the reconstructed airflow angles α_s, β_s may originate from the static wind estimation.

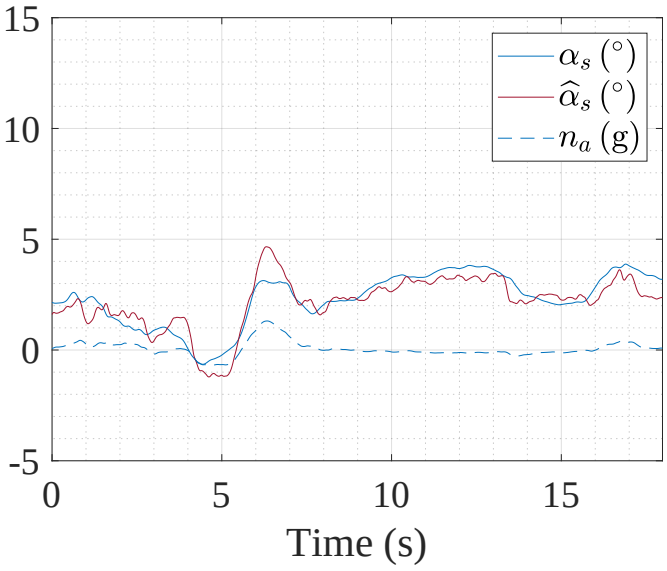

Figure 10.3 – Angle of attack and acceleration factor. Here $n_a = \frac{\|\mathbf{a}^b\| - g}{g}$.

10.2 Methodology

Forces and moments coefficients are calculated from the inertial measurements a_x, a_y, a_z, p, q and r provided by the on-board IMU. The mass m, and inertia terms I_x, I_y, and I_z are measured prior to flight and given in Table 9.2. I_{xz} could not be correctly approximated and is taken as zero. The centre of gravity is measured prior to flight and remains constant during flight and in between flights. The dynamic pressure is measured during flight. All these parameters are supposed well known. The force and moment coefficients for the lateral model are calculated as [Klein 2006]:

$$C_Y = \frac{ma_y^b}{\bar{q}S} \tag{10.21}$$

$$C_l = \frac{I_x}{\bar{q}Sb}\left[\,\dot{p} \;-\; \frac{I_{xz}}{I_x}\,(pq + r) + \;\frac{I_z - I_y}{I_x}\,qr\,\right] \tag{10.22}$$

$$C_n = \frac{I_z}{\bar{q}Sb}\left[\,\dot{r} \;-\; \frac{I_{xz}}{I_z}\,(\dot{p} - qr) + \;\frac{I_y - I_x}{I_z}\,pq\,\right]. \tag{10.23}$$

With this convention, the yawing moment due to differential thrust is supposed unknown and is part of the parameters to identify. The force and moment coefficients for the longitudinal model are:

$$C_X = \frac{(ma_x^b - \sum_{i=1}^{N_m} T_i \cos(i_{p_i}))}{\bar{q}S}\,, \tag{10.24}$$

$$C_Z = \frac{ma_z^b + \sum_{i=1}^{N_m} T_i \sin(i_{p_i})}{\bar{q}S}\,, \tag{10.25}$$

$$C_m = \frac{I_y}{\bar{q}S\bar{c}}\left[\,\dot{q} \;+\; \frac{(I_x - I_z)}{I_y}\,pr + \;\frac{I_{xz}}{I_y}\,(p^2 - r^2)\,\right], \tag{10.26}$$

where the thrusts T_i are estimated from the engine rotation rates, the propeller model and the airspeed, i_{p_i} in the case of DECOL is the wing tilt angle (see C.2) The lift C_L and drag C_D coefficients will be compared with the lift and drag calculated by the aero-propulsive interaction model. They are deduced by projecting the body force coefficients onto the aerodynamic frame using the airflow angles measured by the multi-holes sphere:

$$C_L = -C_Z \cos\alpha + C_X \sin\alpha\,, \tag{10.27}$$

$$C_D = -C_X \cos\alpha \cos\beta + C_Y \sin\beta - C_Z \sin\alpha \cos\beta \,. \tag{10.28}$$

The manoeuvres for longitudinal and lateral identification were separated, such that we used small angle approximations when possible.

The derivatives are calculated with respect to non-dimensional rates. The convention used in this work is the following:

$$\hat{p} = p\frac{b}{2V_a} \tag{10.29}$$

$$\hat{q} = q\frac{\bar{c}}{2V_a} \tag{10.30}$$

$$\hat{r} = r\frac{b}{2V_a} \tag{10.31}$$

10.2.1 Equation Error Method

The state of the aircraft can be calculated with the available measurements without a state observer such that the equation error method can be easily used for identification [Klein 2006], [Bucharles 2012]. Its simplicity and fast execution gives an advantage for an initial phase when the thrust dependent terms are not well known. It allows a rapid trial and error phase to identify the coefficients of interest.

Each force and moment coefficient is identified separately on a flight sequence containing N_f measurements. For example, the equation error method for an arbitrary coefficient C_w, can be formulated as follows:

$$\mathbf{z} = \mathbf{\Phi}\boldsymbol{\theta} + \boldsymbol{\varepsilon} \,, \tag{10.32}$$

where,

$$\mathbf{z} = [C_w(1) \quad C_w(2) \quad ... \quad C_w(N_f)]^T \,, \tag{10.33}$$

$$\boldsymbol{\theta} = [C_{w_a} \quad C_{w_b} \quad C_{w_c}]^T \,, \tag{10.34}$$

$$\mathbf{\Phi} = [\mathbf{a} \quad \mathbf{b} \quad \mathbf{c}] \,, \tag{10.35}$$

$$\boldsymbol{\varepsilon} = [\varepsilon(1) \quad \varepsilon(2) \quad .... \quad \varepsilon(N_f)]^T \,, \tag{10.36}$$

where $\mathbf{z}$ is the $N_f \times 1$ vector force or moment coefficient estimated with the equation (10.21) to (10.26). $\boldsymbol{\theta}$ is the $n \times 1$ vector of unknown parameters to be estimated. $\mathbf{\Phi}$ is the $N_f \times n$ regression matrix which the $N_f \times 1$ columns $\mathbf{a}$, $\mathbf{b}$ and $\mathbf{c}$ are the

regressors. $\boldsymbol{\varepsilon}$ is the $N_f \times 1$ vector of error, n is the number of parameters to identify.

The solution is found using Ordinary Least Square technique where the cost function to minimize is the square of the norm of the error vector $\boldsymbol{\varepsilon}$:

$$I(\boldsymbol{\theta}) = \frac{1}{2} \left(\mathbf{z} - \boldsymbol{\Phi\theta} \right)^T \left(\mathbf{z} - \boldsymbol{\Phi\theta} \right). \tag{10.37}$$

The least squares estimate of $\boldsymbol{\theta}$ is:

$$\widehat{\boldsymbol{\theta}} = (\boldsymbol{\Phi}^T \boldsymbol{\Phi})^{-1} \boldsymbol{\Phi}^T \mathbf{z}. \tag{10.38}$$

The associated model fit error variance estimate, $\hat{\sigma}^2$, is calculated as follows:

$$\hat{\sigma}^2 = \frac{(\mathbf{z} - \boldsymbol{\Phi}\hat{\boldsymbol{\theta}})^T (\mathbf{z} - \boldsymbol{\Phi}\hat{\boldsymbol{\theta}})}{(N - n)}. \tag{10.39}$$

The covariance matrix is calculated using the associated model fit error variance:

$$\boldsymbol{\Sigma}(\hat{\boldsymbol{\theta}}) = \hat{\sigma}^2 (\boldsymbol{\Phi}^T \boldsymbol{\Phi})^{-1}. \tag{10.40}$$

The standard errors of the estimated parameters are given by the square root of the diagonal elements of the covariance matrix:

$$\sigma_{\widehat{\theta}_j} = \sqrt{\Sigma_{jj}} \quad j = 1, 2, ..., n. \tag{10.41}$$

A series of checks was conducted to ensure consistency [Bucharles 2012]:

— The regressors of matrix $\boldsymbol{\Phi}$ are linearly independent, that is $\text{rank}(\boldsymbol{\Phi}) = n$,

— The observation matrix $\boldsymbol{\Phi}$ is not statistically correlated with the error vector $\boldsymbol{\varepsilon}$, that is: $E(\boldsymbol{\Phi}^T \boldsymbol{\varepsilon}) < \nu$, where ν is small, in the order of 10^{-9} or lower.

To further verify the estimated parameters and the identified model, the global model standard error $\hat{\sigma}$ and the one associated with each parameter $\sigma_{\widehat{\theta}_j}$ is tracked. Identification was performed for a selected portion of the flight. Once a model was deemed accurate on the first flight portion, a validation step was performed on a different flight portion.

10.2.2 Input sequences

Input manoeuvres were selected to be able to identify a maximum of parameters at once. In [Bucharles 2012], a series of efficient input signals covering a wide

frequency range are presented. Based on this example, we used an efficient signal resembling a doublet input to excite the longitudinal motion with elevator input and lateral motion with a combination of rudder and differential thrust input. The input sequences were repeated multiple times. An example of the raw input sequences can be seen in Fig 10.4.

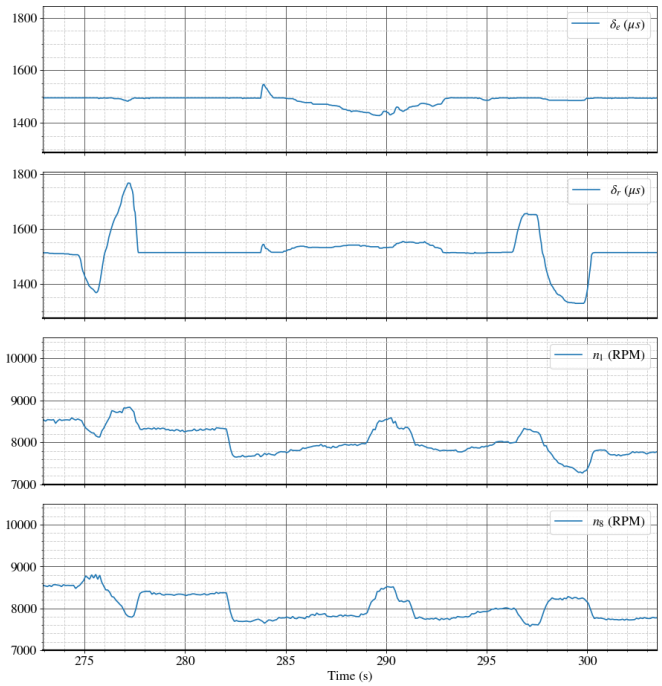

Figure 10.4 – Input sequence for lateral model identification. δ_e: elevator and δ_r: rudder input, both in PWM. n_1 and n_8 : engines rotation rates, used for differential thrust.

10.3 Identified aero-propulsive models

The identified aerodynamic models are presented in this section. They are separated between longitudinal and lateral models in section 10.3.1 and section 10.3.2 respectively.

The structure of the models describing aero-propulsive interactions is initially guessed from the theoretical study realized in section 9.4. Then, the structure is adjusted based on the global standard error and the errors associated with each derivative. The main differences are discussed and illustrated in figures when the aero-propulsive terms brought a significant change.

10.3.1 Longitudinal models

10.3.1.1 Lift coefficient

The identified lift models are given in Table 10.2. The first column, labelled 'standard derivatives', refers to the identified model without explicit thrust derivatives. The second column refers to the model with explicit thrust derivatives.

Table 10.2 – Identified lift models. Derivatives are per radians when applicable.

Parameter	Standard derivatives $\widehat{\theta}_j \pm \sigma_{\widehat{\theta}_j}$	Explicit thrust terms $\widehat{\theta}_j \pm \sigma_{\widehat{\theta}_j}$
$C_{L_{\alpha=0}}$	$0.32 \pm 7.9 \cdot 10^{-4}$	$0.31 \pm 4.9 \cdot 10^{-4}$
$C_{L_{0,\,T_c}}$	(-)	0.54 ± 9.10^{-3}
$C_{L\alpha}$	$7.6 \pm 2.1 \cdot 10^{-2}$	$5.8 \pm 2.1 \cdot 10^{-2}$
$C_{L_{\alpha T_c^2}}$	(-)	$-2.4 \pm 6.6 \cdot 10^{-1}$
$C_{L_{\alpha T_c}}$	(-)	$5.9 \pm 2.4 \cdot 10^{-1}$
$C_{L\dot{\alpha}}$	$-0.26 \pm 7.2 \cdot 10^{-3}$	$-0.39 \pm 4 \cdot 10^{-3}$
$C_{L\hat{q}}$	$-36.1 \pm 4.7 \cdot 10^{-1}$	$6.7 \pm 5.4 \cdot 10^{-1}$
$\hat{\sigma}$	$34.3 \cdot 10^{-3}$	$17.7 \cdot 10^{-3}$

As seen in section 9.4, the variation of C_{L_α} and C_{L_0} with T_c can be described by a second order polynomial. In the identification process, the degree of T_c was gradually increased and it was found that polynomials of order higher than two do not increase the accuracy of the model. The resulting polynomials used for the model are of the form:

$$C_{L_\alpha} = C_{L_{\alpha T_c^2}} T_c^2 + C_{L_{\alpha T_c}} T_c + C_{L_{\alpha_0}} \,, \tag{10.42}$$

$$C_{L_0} = C_{L_{0,\,T_c}} T_c + C_{L_{\alpha=0}} \,. \tag{10.43}$$

Most of the improvement comes from the first order terms $C_{L_{\alpha T_c}}$ and $C_{L_{0,\,T_c}}$. In fact the coefficients associated with higher powers of T_c have a larger uncertainty as it can be noticed with the term $C_{L_{\alpha T_c^2}}$ in Table 10.2.

The significant reduction in the model error justifies the introduction of the thrust dependent derivatives. This improvement is illustrated in Fig 10.5 where the two models are compared on a push down pull up manoeuvre. The aircraft longitudinal states and pilot inputs during the manoeuvre are represented in Fig 10.6.

The difference between the two models appear for a large thrust coefficient,

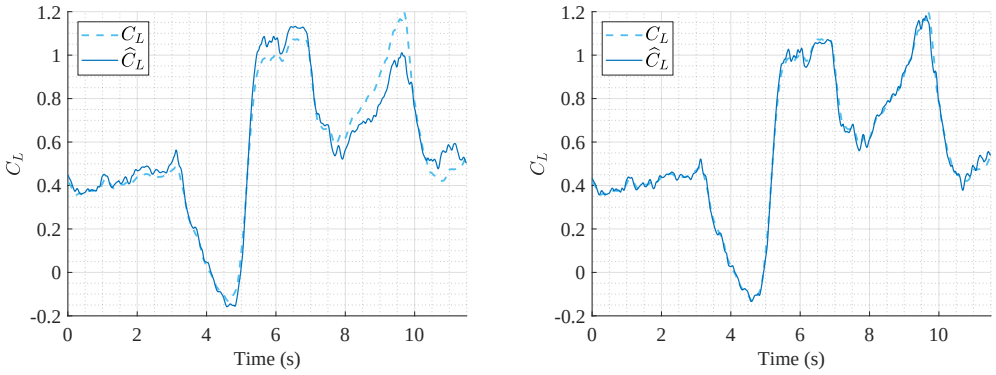

(a) $\widehat{C}_L$ with the standard derivatives. (b) $\widehat{C}_L$ with explicit thrust derivatives.

Figure 10.5 – Evaluation of the two models for estimating the lift coefficient.

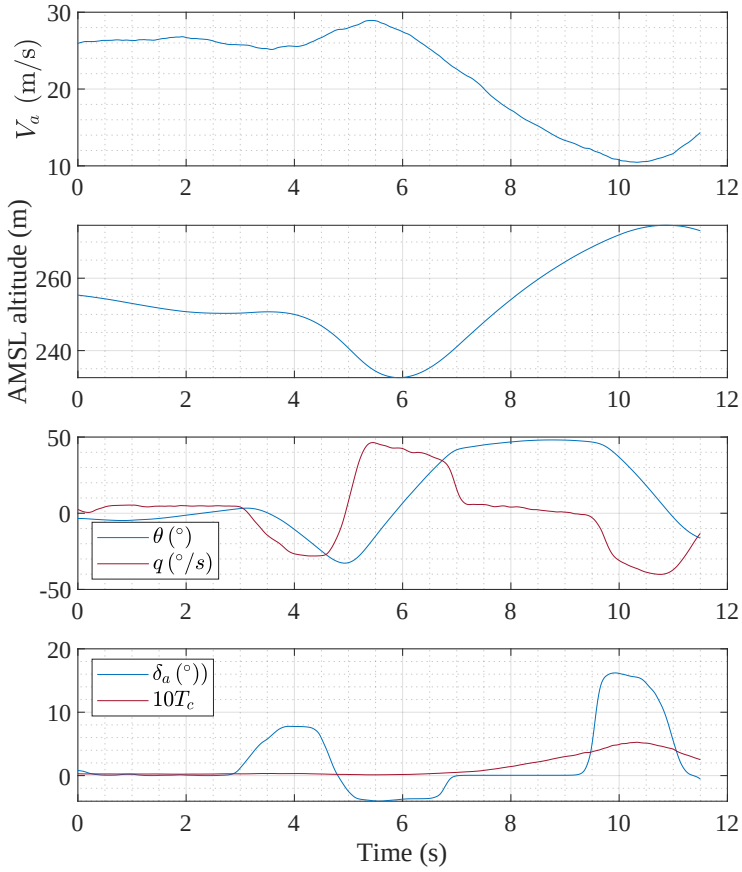

Figure 10.6 – Aircraft state during the phugoid manoeuvre associated with the lift coefficient estimation of Fig 10.5

between 8s and 11s in Fig 10.5, when the thrust coefficient reaches its maximum. Prior to this, the explicit thrust derivatives bring little to the estimation.

The unusually high lift slope coefficient $C_{L_\alpha} = 7.6$ of the model with standard derivatives also justifies the inclusion of thrust explicit derivatives. The use of standard derivatives is sufficiently accurate to describe the cruise flight conditions and variation of lift around a constant thrust coefficient. The value of C_{L_α} is however not physically realistic as it is greater than the maximum theoretical value of 2π [Pope 2009]. This illustrates the approximation that can be commonly made when ignoring thrust derivatives. The estimate made with the standard derivatives is an average of what is observed during the manoeuvre.

10.3.1.2 Drag coefficient

The identified drag models are presented in Table 10.3. The introduction of thrust explicit derivatives are significantly reducing the global model error as well. However, only the term $C_{D_{\alpha T_c}}$ could be identified with sufficient accuracy. The quadratic term $C_{D_{\alpha^2 T_c}}$ came with an associated standard error of 50% with little to no improvements in the model error. This term was hence discarded, although it was shown in section 9.4 that $C_{D_{\alpha^2}}$ was largely impacted by the thrust coefficient.

Table 10.3 – Identified drag models. Derivatives are per radians when applicable.

Parameter	Standard derivatives $\widehat{\theta}_j \pm \sigma_{\widehat{\theta}_j}$	Explicit thrust terms $\widehat{\theta}_j \pm \sigma_{\widehat{\theta}_j}$
C_{D_0}	$0.075 \pm 3.0 \cdot 10^{-4}$	$0.077 \pm 1.6 \cdot 10^{-4}$
$C_{D\alpha}$	$0.63 \pm 9.4 \cdot 10^{-3}$	$0.25 \pm 6.1 \cdot 10^{-3}$
$C_{D_{\alpha^2}}$	$2.13 \pm 6.4 \cdot 10^{-2}$	$2.76 \pm 3.3 \cdot 10^{-2}$
$C_{D_{\alpha T_c}}$	(-)	$2.68 \pm 2.7 \cdot 10^{-2}$
$C_{D\hat{q}}$	$-6.8 \pm 1.5 \cdot 10^{-1}$	$-2.6 \pm 9.0 \cdot 10^{-2}$
$\hat{\sigma}$	$11.8 \cdot 10^{-3}$	$5.8 \cdot 10^{-3}$

10.3.1.3 Pitching moment coefficient

The identified models for the pitching moment coefficient are presented in Table 10.4. The pitching moment coefficient does not show the same increase in accuracy as for the lift and drag coefficient when thrust dependent derivatives are included. It is more delicate to conclude on the effect of thrust in the pitching stability. It seems that for this particular aircraft, the thrust coefficient has a stabilizing

Table 10.4 – Identified pitching moment model. Derivatives are per radians when applicable except for the control surface derivatives which are per degree.

Parameter	Standard derivatives $\widehat{\theta}_j \pm \sigma_{\widehat{\theta}_j}$	Explicit thrust terms $\widehat{\theta}_j \pm \sigma_{\widehat{\theta}_j}$
C_{m_0}	$0.013 \pm 2.6 \cdot 10^{-4}$	$0.004 \pm 3.5 \cdot 10^{-4}$
$C_{m_{T_c}}$	(-)	$0.128 \pm 5.1 \cdot 10^{-3}$
$C_{m\alpha}$	$-0.21 \pm 5.4 \cdot 10^{-3}$	$-0.077 \pm 1.0 \cdot 10^{-2}$
$C_{m\dot{\alpha}}$	$0.079 \pm 2.3 \cdot 10^{-3}$	$0.094 \pm 2.4 \cdot 10^{-3}$
$C_{m_{\alpha T_c}}$	(-)	$-2.06 \pm 5.6 \cdot 10^{-2}$
$C_{m\hat{q}}$	$-9.24 \pm 1.9 \cdot 10^{-1}$	$-6.34 \pm 2.7 \cdot 10^{-1}$
C_{δ_e}	$-0.0079 \pm 1.1 \cdot 10^{-4}$	$-0.0049 \pm 1.5 \cdot 10^{-4}$
$C_{\delta_e T_c}$	(-)	$-0.0106 \pm 3.6 \cdot 10^{-4}$
$\hat{\sigma}$	$8.51 \cdot 10^{-3}$	$7.16 \cdot 10^{-3}$

effect with $C_{m_{\alpha T_c}} < 0$. Recalling equation (9.12) of section 9.4:

$$C_{m_{\alpha\, T_c}} = C_{L_{\alpha T_c}} \frac{x_{\mathrm{CG}} - x_{\mathrm{n}}}{\bar{c}} - V_H C_{L_{t,\, \alpha T_c}} \left(1 - \frac{\partial \varepsilon}{\partial \alpha} + \frac{\partial^2 \varepsilon}{\partial \alpha \partial T_c}\right),$$

this observation shows that the term $C_{L_{t,\, \alpha T_c}} \left(1 - \frac{\partial \varepsilon}{\partial \alpha} + \frac{\partial^2 \varepsilon}{\partial \alpha \partial T_c}\right)$ is positively impacted by the propeller slipstreams.

Another important observation is the influence of the thrust coefficient on the elevator efficiency. Both results may be explained by the fact that the horizontal tail is immersed in the first two propeller slipstreams (see Fig 9.1).

10.3.1.4 Comparison with theoretical aero-propulsive model

A comparison between the identified and predicted thrust dependent derivatives is made in Table 10.5 for the lift coefficient. The best agreements are obtained for the derivatives with first power of T_c. The coefficient $C_{L_{\alpha T_c^2}}$ presents a large deviation which can be related to the important standard error associated with this derivative. The quadratic evolution of the lift slope coefficient with the thrust requires a large variation of the thrust coefficient in the flight data to be accurately identified. A good flight manoeuvre for this is the phugoid where the thrust coefficient varies with the velocity at nearly constant angle of attack. Unfortunately, the slow evolution of this mode allowed to record only half a period in one field length. It is believed that the recording a full period of the phugoid can be sufficient to well identify the

aero-propulsive effect on the lift coefficient.

Table 10.5 – Comparison between identified and predicted aero-propulsive lift coefficients (see section 9.4)

Parameter	Identified coefficients $\widehat{\theta}_j \pm \sigma_{\widehat{\theta}_j}$	Theoretical estimates
C_{L_0}	$0.31 \pm 4.9 \cdot 10^{-4}$	0.45
$C_{L_{0,\,T_c}}$	0.54 ± 9.10^{-3}	0.58
$C_{L\alpha}$	$5.8 \pm 2.1 \cdot 10^{-2}$	5.08
$C_{L_{\alpha T_c^2}}$	$-2.4 \pm 6.6 \cdot 10^{-1}$	-3.46
$C_{L_{\alpha T_c}}$	$5.9 \pm 2.4 \cdot 10^{-1}$	5.51
$C_{L\dot{\alpha}}$	$-0.39 \pm 4 \cdot 10^{-3}$	(-)
$C_{L\hat{q}}$	$6.7 \pm 5.4 \cdot 10^{-1}$	(-)

The same exercise for the the drag led to important differences which can be expected due to the level of fidelity of the theoretical tools used in section 9.4 and the difficulty associated with estimating the drag coefficients from flight data. The goal here is not to validate the calculation of the drag coefficients but rather to validate the increase of drag due to wing blowing. In this sense, the identified model presented in Table 10.3 confirms this prediction.

10.3.2 Lateral model

The identified models for the lateral coefficients are initially guessed from the analysis of section 9.4 but the theoretical tool ignores the effect of side slip and rotation rates, so these derivatives were looked for by trial and error. When a derivative confirmed an observation made in section 9.4, thus gave an expected behaviour, multiple derivatives were tested to try to replicate this behaviour. This allowed to confirm that the observed behaviour was correctly described by the derivative or inversely, find a better derivative for this purpose. The same procedure was used when an unexpected behaviour was observed.

10.3.2.1 Lateral force coefficient

The identified model for the lateral force is given in Table 10.6. For this coefficient, a good estimation was obtained with the standard derivatives. The lateral force should be mostly impacted by the propeller forces but this hypothesis is countered by the associated coefficient $C_{y_{\beta T_c}}$. This coefficient is low with a high standard

Table 10.6 – Identified models for the side force coefficient. Derivatives are per radians when applicable except for the control surface derivatives which are per degree.

Parameter	Standard derivatives $\widehat{\theta}_j \pm \sigma_{\widehat{\theta}_j}$	Explicit thrust terms $\widehat{\theta}_j \pm \sigma_{\widehat{\theta}_j}$
C_{Y_0}	$0.0063 \pm 9.6 \cdot 10^{-5}$	$0.0068 \pm 9.6 \cdot 10^{-5}$
C_{Y_β}	$-0.94 \pm 1.2 \cdot 10^{-3}$	$-0.95 \pm 2.6 \cdot 10^{-3}$
$C_{Y_{\beta T_c}}$	(-)	$-0.032 \pm 1.7 \cdot 10^{-2}$
$C_{Y_{\hat{p}}}$	$0.11 \pm 9.7 \cdot 10^{-3}$	$0.11 \pm 9.8 \cdot 10^{-3}$
$C_{Y_{\hat{r}}}$	$0.22 \pm 9.1 \cdot 10^{-3}$	$0.22 \pm 9.4 \cdot 10^{-3}$
$C_{Y_{\delta_r}}$	$0.005 \pm 3.2 \cdot 10^{-5}$	$0.005 \pm 3.6 \cdot 10^{-5}$
$\hat{\sigma}$	$6.8 \cdot 10^{-3}$	$6.8 \cdot 10^{-3}$

error and does not contribute to improve the general standard error. However, the thrust coefficient during the lateral manoeuvre does not vary as much as for the longitudinal manoeuvres. The lateral forces due to the propeller may still be included in the coefficient C_{Y_β}.

An observation should however be made here, the identified coefficient C_{Y_β} is twice as high as the theoretical value obtained in section 9.4. Such increase cannot be fully explained by the propeller lateral forces based on Fig 9.9a. It may come from the tail, in which case C_{y_r} and C_{n_β} should follow the unexpected change. It is not the case for C_{y_r} (which is coherent with the predicted value) and neither for C_{n_β}, as will be seen with the yawing moment coefficient in section 10.3.2.2. The preferred hypothesis is the fuselage contributing to lateral force, a contribution which may be badly estimated with VLM simulations due to the rectangular cross-section.

10.3.2.2 Yawing moment coefficient

The identified models for the yawing moment coefficient are presented in Table 10.7. Important preliminary remarks have to be made concerning the differential thrust command and thrust differential due to yaw rate.

Remark 1. The differential thrust and the rudder control surface are coupled to the same stick. When the pilot moves this stick, both are activated at the same time. This was necessary for ground control where the aircraft is guided using differential thrust. Since both commands are coupled, it is complicated to give independent and trusted derivatives for each of them. Therefore, it was decided to keep them

coupled and represented by one term: δ_r.

Remark 2. A thrust differential appears with yaw rate as a result of the difference in local airspeed at the location of engines. One way of accounting for this is to estimate the thrust differential and remove it from the yawing moment coefficient. In this work, the effect is included in the yawing derivatives as an explicit thrust induced effect.

Table 10.7 – Identified yawing moment model. Derivatives are per radians when applicable except for the control surface derivatives which are per degree.

Parameter	Standard derivatives $\widehat{\theta}_j \pm \sigma_{\widehat{\theta}_j}$	Explicit thrust terms $\widehat{\theta}_j \pm \sigma_{\widehat{\theta}_j}$
C_{n_0}	$-0.00033 \pm 3.4 \cdot 10^{-5}$	$-0.00028 \pm 2.7 \cdot 10^{-5}$
C_{n_β}	$0.064 \pm 5.0 \cdot 10^{-4}$	$0.094 \pm 8.0 \cdot 10^{-4}$
$C_{n_{\beta T_c}}$	(-)	$-0.251 \pm 7.1 \cdot 10^{-3}$
$C_{n_{\hat{p}}}$	$-0.038 \pm 3.2 \cdot 10^{-3}$	$-0.055 \pm 2.6 \cdot 10^{-3}$
$C_{n_{\hat{r}}}$	$-0.135 \pm 3.4 \cdot 10^{-3}$	$-0.278 \pm 7.7 \cdot 10^{-3}$
$C_{n_{\hat{r}T_c}}$	(-)	$1.64 \pm 1.0 \cdot 10^{-1}$
$C_{n_{\delta_r}}$	$-0.0013 \pm 1.2 \cdot 10^{-5}$	$-0.0015 \pm 1.0 \cdot 10^{-5}$
$\hat{\sigma}$	$2.02 \cdot 10^{-3}$	$1.62 \cdot 10^{-3}$

The effect of the thrust is clear on the weathercock stability through the coefficient $C_{n_{\beta T_c}}$ and the yawing rate through the derivative $C_{n_{rT_c}}$. It has the effect of lowering natural stability and damping. Inversely, the thrust was found to be loosely impacting the yawing moment due to roll rate and the yawing moment due to combined rudder and differential thrust. Derivatives associated with these effects, $C_{n_{pT_c}}$ and $C_{n_{\delta_r T_c}}$ were rejected due to too large associated standard uncertainty and no significant improvement to the model error. Adverse yawing due to aileron deflection was rejected as well and this is explained by the fact that aileron differential is used on the aircraft to ease the piloting.

The pertinence of the explicit thrust derivative is illustrated in Fig 10.7 where the two models are compared on a flight manoeuvre shown by Fig 10.8.

The important reduction of weathercock stability due to the thrust coefficient is an unexpected behaviour. Recalling Fig 9.9b of section 9.4, the propeller lateral force should reduce the weathercock stability but it was estimated to be a maximum of $C_{n_{\beta,\,p}} = -0.0078$ for a thrust coefficient of $T_c = 0.6$. What is observed in Table 10.7 cannot be fully explained by the propeller lateral forces. This model

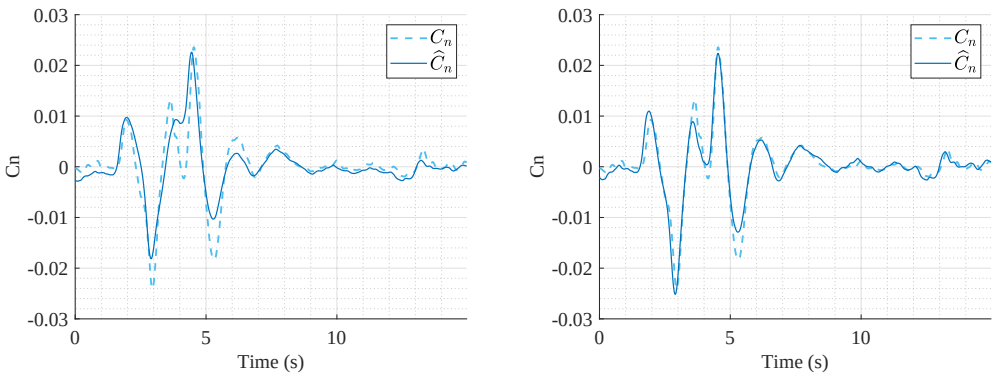

(a) $\widehat{C}_n$ with standard derivatives. (b) $\widehat{C}_n$ with explicit thrust derivatives.

Figure 10.7 – Evaluation of two models for estimating the yawing moment coefficient.

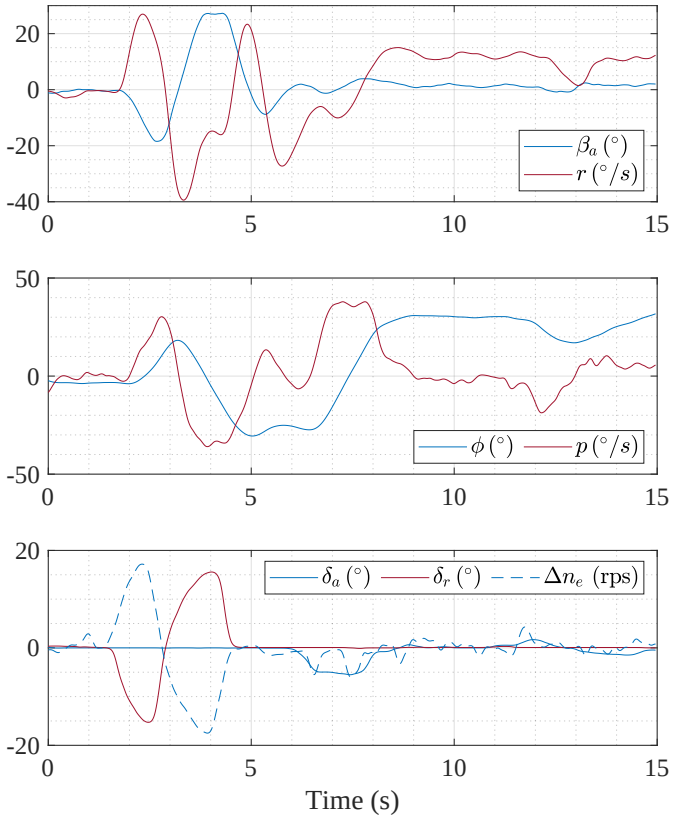

Figure 10.8 – Aircraft state during the manoeuvre associated with the yawing moment coefficient estimation in Fig 10.7. Here Δn_e is the engine rotation rate differential between engine number 1 and engine number 8.

raises an important observation and is further tested in non-linear simulations in section 10.4.

10.3.2.3 Rolling moment coefficient

The identified model for the rolling moment coefficient is presented in Table 10.8. The improvement brought by the inclusion of thrust terms is less significant than for the yawing moment coefficient. Nevertheless, it is possible to see the influence of the thrust on the rate derivatives C_{l_p} and C_{l_r}. The derivative associated with the influence of the thrust on the dihedral effect $C_{l_{\beta T_c}}$ was rejected. The fact that the aircraft has no geometric dihedral and that the whole wing is embedded in the propeller slipstream may explain this result.

Table 10.8 – Identified rolling moment model. Derivatives are per radian when applicable except for the control surface derivatives which are per degree.

Parameter	Standard derivatives $\widehat{\theta}_j \pm \sigma_{\widehat{\theta}_j}$	Explicit thrust terms $\widehat{\theta}_j \pm \sigma_{\widehat{\theta}_j}$
C_{l_0}	$-0.0004 \pm 2.7 \cdot 10^{-5}$	$-0.0004 \pm 2.6 \cdot 10^{-5}$
C_{l_β}	$-0.016 \pm 4.0 \cdot 10^{-4}$	$-0.019 \pm 4.1 \cdot 10^{-4}$
$C_{l_{\hat{p}}}$	$-0.209 \pm 4.1 \cdot 10^{-3}$	$-0.125 \pm 6.2 \cdot 10^{-3}$
$C_{l_{\hat{r}}}$	$0.115 \pm 2.3 \cdot 10^{-3}$	$0.068 \pm 6.6 \cdot 10^{-3}$
$C_{l_{\hat{p}T_c}}$	(-)	$-1.28 \pm 7.2 \cdot 10^{-2}$
$C_{l_{\hat{r}T_c}}$	(-)	$0.71 \pm 9.3 \cdot 10^{-2}$
$C_{l_{\delta_a}}$	$-1.8 \times 10^{-4} \pm 3.0 \cdot 10^{-5}$	$-0.24 \times 10^{-4} \pm 7.2 \cdot 10^{-5}$
$C_{l_{\delta_a T_c}}$	(-)	$-0.026 \pm 1.1 \cdot 10^{-3}$
$\hat{\sigma}$	$1.61 \cdot 10^{-3}$	$1.51 \cdot 10^{-3}$

Thrust seems to increase the rolling moment induced by yaw. This remains counter intuitive since a yawing action would lower the thrust level of the advancing wing, causing less induced rolling moment and inversely on the receding wing.

Rolling moment due to differential thrust and rudder input which remain coupled, was found irrelevant. This can arise from the fact that a positive rudder deflection induces a negative rolling moment while a positive differential thrust should induce a positive rolling moment: they are cancelling each other.

10.4 Model validation

In the previous section, the use of explicit thrust derivative was justified by a lower standard error and illustrated for the key coefficients that are C_L and C_n. The identified model for the yawing moment coefficient raised an unexpected behaviour and further validation through non-linear simulation was sought before interpreting this result.

In this section, the identified models are implemented in the software JSBsim and evaluated against flight data in non-linear simulation to show the differences the aero-propulsive interactions can have on the aircraft flight dynamics. For these simulations, the aircraft is modelled with the propulsion gathered at the centre of gravity since the identified model includes all moments due to thrust and thrust differential.

The lateral aircraft dynamics and more particularly the yawing moment model will be mainly discussed, although longitudinal flight dynamics is available in Annex C.2

10.4.1 Lateral manoeuvre

The lateral manoeuvre was a rudder and differential thrust doublet to excite the Dutch-roll mode of the aircraft. The results are spread between side slip oscillation in Fig 10.9 and roll mode in Fig 10.10.

It is clear that the best model is the one using explicit thrust derivatives. The model with standard derivatives shows a slower side-slip oscillation than what is measured in flight. This is explained by the low value of C_{n_β} describing the weathercock stability of the aircraft. The model with standard derivatives being an average estimate, it means that the aircraft stability is lowered for a transient period of time.

On the contrary, the model with explicit thrust derivatives is validated as it reproduces well the aircraft lateral dynamics.

The final value of the bank angle is not well estimated with both models despite the good estimation of the roll rate. This is explained by the identification method that does not take the bank angle as an input. Additionally the aileron input being a rate input, deviation from the flight data is rapidly obtained. The roll model would benefit from an output error method to improve the identified model.

The interrogation is hence, why does the thrust reduce the natural static stability

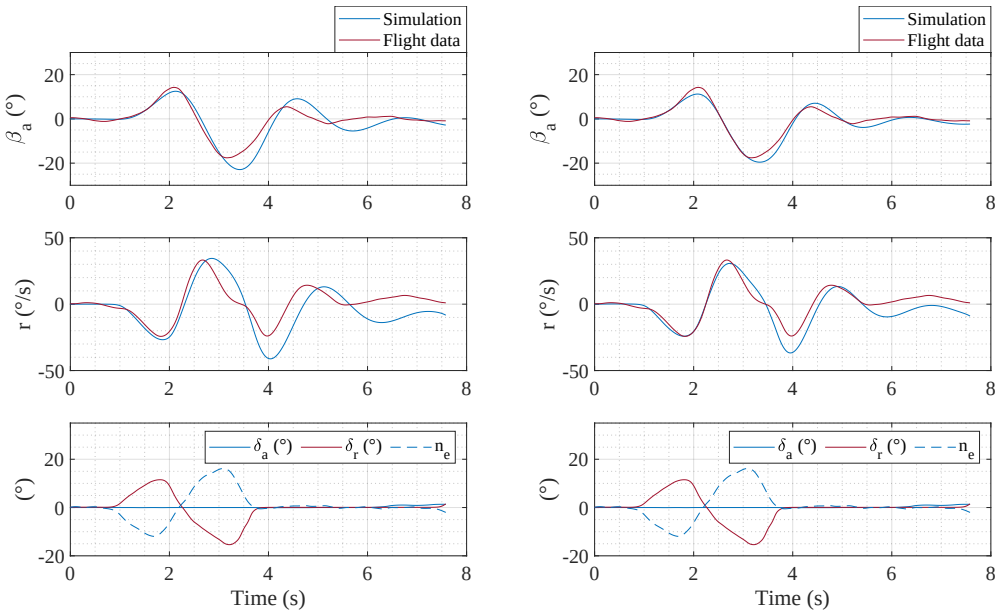

(a) Standard derivatives

(b) Explicit thrust derivatives.

Figure 10.9 – Evaluation of standard derivatives and explicit thrust derivative model in non linear simulation, lateral side slip oscillation.

and damping, represented by the derivatives C_{n_β} and C_{n_r}? Two hypotheses are currently considered:

— the VT is 'shadowed' by the propulsion. The propagation of the propeller-wing interaction to the tail and the combined propeller slipstreams could reduce the side slip at the location of the VT,

— the inner engines are masked by the fuselage in side slip.

Since the lateral force is not impacted by the thrust coefficient (see Table 10.6), the second hypothesis is preferred. However, since the fuselage seems to produce an important lateral force, an interaction between the the propeller slipstreams and the fuselage may be considered as well. An interaction between the propeller slipstreams, the fuselage and the vertical tail may resolve in no observable modifications in lateral force and a significant reduction of yawing moment coefficient.

No strong argument was found to approve one of these hypotheses at the current level of knowledge. A reproduction of this phenomenon should be attempted in simulation to be able to argue in favour of one explanation.

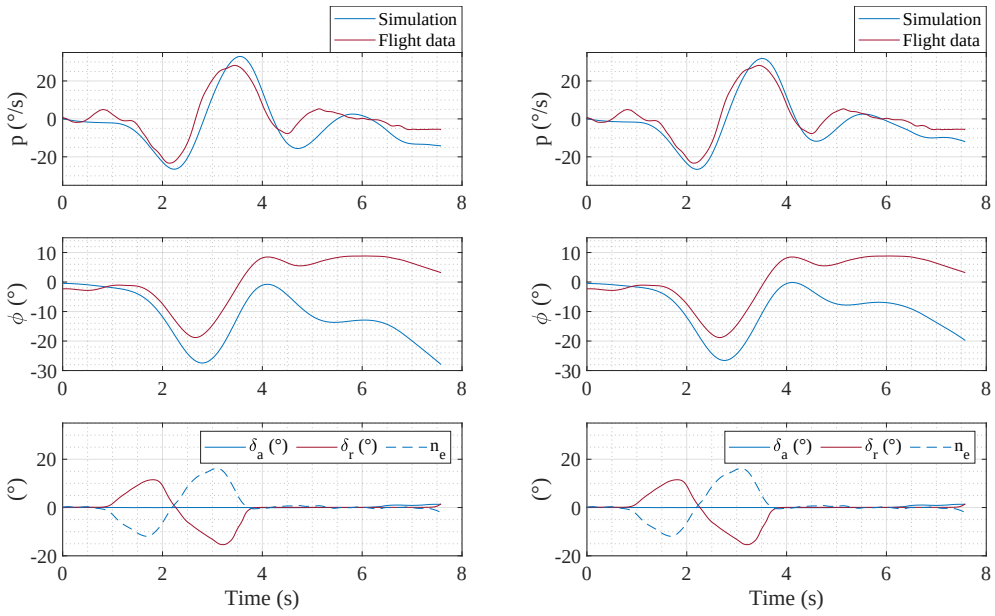

(a) Standard derivatives

(b) Explicit thrust derivatives.

Figure 10.10 – Evaluation of standard derivatives and explicit thrust derivative model in non linear simulation, lateral Dutch Roll.

10.5 Conclusion

Two sets of aerodynamic models could be identified from flight data with the equation error method presented in section 10.2. A model with standard derivatives, ignoring the effect of propulsion and one including explicit thrust derivatives. This last model was found more accurate at estimating the lift, drag, rolling and yawing moment coefficients (see section 10.3).

A comparison between flight data and non-linear simulations confirmed that the aircraft lateral flight dynamic is correctly reproduced with the explicit thrust derivatives. A model with standard derivatives has the effect of averaging the derivatives. Such a model should not be used to simulate the aircraft dynamics as emphasized in section 10.4. The aero-propulsive interactions with this aircraft have been found to significantly lower the natural stability and damping of the aircraft. Two hypotheses have been formulated in section 10.4 as an attempt to explain this phenomenon but neither could be confirmed.

The validity of the physical interpretation of the identified models is limited without a reproduction of the phenomenon in aerodynamic simulations and/or more flight test analysis. As was seen with the lift slope coefficient in section 10.3.1.1,

it may be possible to find a good average solution with the equation error method even if this solution is physically incorrect.

Part IV Conclusion

An experimental research campaign has been realized with a small scale DEP aircraft designed and build to study the flight dynamics of an aircraft with a blown wing. The objective of the experimental campaign was to meet the following goals:

— characterise the aircraft lateral flight dynamics when a large portion of the wing is immersed in the propeller slipstream,

— characterise the induced aero-propulsive effects at play when differential thrust is used,

— evaluate the feasibility to implement the control laws and VT reduction obtained in Part III with the knowledge obtained from the first two objectives.

The first objective has been fulfilled and it was demonstrated that an identified model describes better the lateral aircraft flight dynamics when thrust explicit derivatives are present. It was also shown a significant reduction of natural directional stability and damping with the thrust. The current knowledge is insufficient to fully explain this phenomenon.

The second objective suffered from a lack of testing. Flight tests with decoupling of the rudder input and the differential thrust input could not be realised.

Finally, with the knowledge acquired in Chapter 10, it is clear that a VT reduction cannot be implemented with the current level of knowledge. The source of directional stability and damping reduction with the thrust should be better understood before considering a VT reduction.

Part V

General Conclusions and Perspectives

General conclusions

The principal information and knowledge gained throughout the analysis of a regional transport aircraft utilizing differential thrust and distributed electric propulsion to relax the directional static stability can now be summarised.

The main advantage of DEP in regard to directional stability and control is the ability to reallocate the thrust so as to avoid thrust unbalance in presence of motor failures. This ability allows a reduction of vertical tail surface area without compromising the trim capability of the aircraft during one or many motor failures.

As long as the propulsion system is able to compensate for thrust unbalance, the sizing flight conditions of the vertical tail are defined by the $\pm 15°$ of available side slip, at low speed with motor failures as defined by the certification specification paragraph CS25.147. This controllability requirement necessitates a certain control power that may be brought by a rudder and/or differential thrust. If the latter is the only means of directional control, it is advantageous to size the vertical tail for neutral static stability. If a rudder is used in combination with differential thrust, or if enough excess power is available for differential thrust, the aircraft may be designed naturally unstable.

On a configuration utilizing the differential thrust only, flight handling qualities have been shown to depend more on the actuator bandwidth rather than the VT surface area. Motor saturations are a strong limitation to reach the prescribed handling quality and flight envelope requirements. A realizable trade-off satisfying static and handling quality requirements in presence of unbalanced thrust was found with a vertical tail reduction of 50% and an associated motor bandwidth of 10.4 rad/s. The solution results in an aircraft having a relatively slow reaction time to a side slip command, with a time constant of 1.43 s.

The aero-propulsive interactions, limited to propeller-wing interaction, can significantly lower the efficiency of differential thrust and reduce the directional flight envelope at low airspeeds and large thrust coefficients. Although of less importance for the control laws design, their non linear evolution with airspeed can be problematic for gain scheduling. In addition, when using differential thrust only, the available directional control power is a function of the longitudinal trim. Finally, the aerodynamic model identified from flight tests showed an important dependency of the directional stability and damping on the thrust coefficient which suggests an interaction between the propeller slipstream, the vertical tail and the fuselage as well.

Recommendations and perspectives

Based on the knowledge and the analysis presented in this thesis, the following recommendations are issued for future research projects and similar applications:

- The high inertia of the subsonic transport aircraft encourages the use of a combination of differential thrust and a small rudder to obtain a sufficiently fast directional response. This solution can be regarded as a serious candidate to obtain an important reduction of vertical tail with a robust and redundant directional control system. In the effort to do so, the primary focus should be given to the allocation between the rudder and the motors.
- The co-design results have been obtained while ignoring delays in the electronics, the actuator rate saturation, atmospheric perturbations and variation of the centre of gravity. Additionally, only one flight condition has been used for the control laws design, while aero-propulsive interactions have a quadratic evolution with the thrust coefficient. In an effort to validate the feasibility of an unstable aircraft or an aircraft with neutral static stability, future analysis should address these limitations.
- In the construction of the aerodynamic model of a DEP aircraft for stability and control design, the use of multi-fidelity tools seems appropriate to increase the level of accuracy at a reasonable cost. It is advised to:
  - use a high fidelity method including aero-propulsive interactions to determine the trim power since the available directional control power depends on this position.
  - the aerodynamic derivatives and their dependence on the thrust may be determined with faster methods and the following advice:
    - consider aero-propulsive interactions on the overall aircraft and not on a limited part,
    - increase the level of fidelity to methods able to solve airflow pressure field around 3D bodies.
- In the definition of the co-design methodology, it was assumed that the propulsion system was an input. However, the actuator dynamics being of primary importance over the VT surface area for aircraft control, it can be tempting to install more powerful and heavier motors and power systems to satisfy a set of prescribed handling qualities using differential thrust. This may negatively

impact the inertia of the aircraft and its performances due to the increase in weight. This is why, to fully benefit from the co-design methodology, it should be embedded in an overall aircraft design environment to allow interactions with the disciplines that were left on the side for this study.

- In order to validate the co-design methodology on the demonstrator DECOL, three steps are missing:
  - Additional flight tests with decoupled rudder and differential thrust input via a new channel mixing.
  - The reduction of directional rigidity and damping should be replicated in simulations to be validated, understood and modelled.
  - After these two steps, an enhanced aero-propulsive module or the identified model extended with the results of the first recommendation could then be utilized within the co-design framework to compute a set of control law gains and resize the VT of DECOL.

Part VI

Appendices

Appendix A

Continuous propulsion model

A.1 Convergence study: number of basis functions

For the flight conditions described in section 5.2.3, Table 5.1, the results on the total installed power over each flight P'_T (equation (5.26)) and vertical tail ratio for increasing number of basis functions is given below in Tables A.1 and A.2.

Table A.1 – Convergence study with $\bar{Y} = 0.5$ for increasing number of basis function N_g at $\bar{Y}_c = 0.5$.

	No rudder		Rudder	
N_g	$\hat{P}'_T$ (MW)	$\frac{\hat{S}_v}{S_{v,0}}$	$\hat{P}'_T$	$\frac{\hat{S}_v}{S_{v,0}}$
10	4.598	0.652	4.277	0.385
20	4.595	0.65	4.394	0.395
40	4.771	0.647	4.442	0.395
80	4.485	0.656	3.969	0.395
120	4.352	0.656	3.759	0.396
160	4.111	0.65	3.667	0.396

Table A.2 – Convergence study with $\bar{Y} = 0$ and for increasing number of basis function N_g at $\bar{Y}_c = 0.0$.

	Rudder	
N_g	$\hat{P}'_T$	$\frac{\hat{S}_v}{S_{v,0}}$
10	6.279	0.452
20	5.150	0.872
40	4.820	0.892
80	4.086	0.91
120	4.708	0.918
160	4.732	0.922

The aircraft with rudder control surface shows an important step in the total power at $N_g = 80$ and slowly converging behavior at $N_g > 80$. We selected a slightly

higher value for N_g for the study of Chapter 5 but better converged results can be obtained with higher number of basis function.

A.2 Power and VT co-design with differential thrust and rudder control surface

The same study as in section 5.3 has been conducted when considering differential thrust and the rudder control surface.

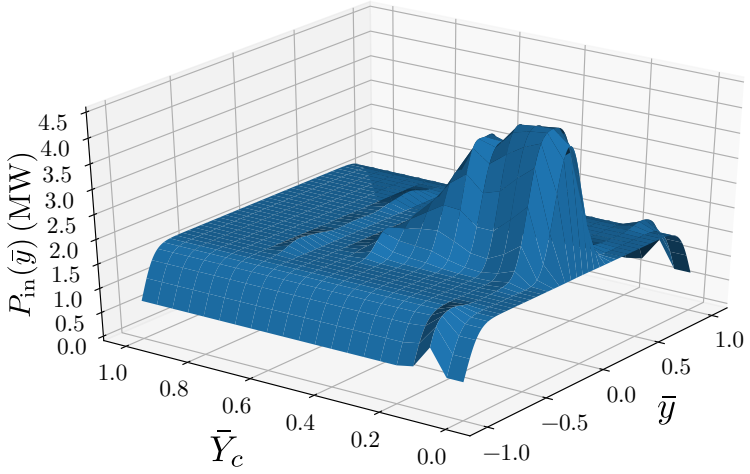

Figure A.1 – Power distribution along the wingspan as a function of the level of failure $\bar{Y}_c$.

The power distribution for varying severity of failure (Fig A.1), has a uniform power distribution for an initial value of $\bar{Y}_c = 0$. As soon as $\bar{Y}_c \geq 0$, power is gathered at the centre of the wing and the vertical tail size drops from 0.87 to 0.38 at $\bar{Y}_c = 0.2$. This is interpreted as a minimization of thrust asymmetry, allowing to reduce drastically the directional control power from the rudder and therefore the vertical tail size. For a global flight operation, it is disadvantageous as the total installed power remains high for $0.0 \leq \bar{Y}_c \leq 0.3$. As $\bar{Y}_c$ is increased beyond 0.3, power is progressively removed from the wing centre part and eventually becomes uniformly distributed for $\bar{Y}_c > 0.6$. Fig A.2 shows a decrease in installed power between $\bar{Y}_c = 0.3$ and $\bar{Y}_c = 0.6$. The remaining power ratio after failure shows a flatter increase in the same interval $0.3 < \bar{Y}_c < 0.5$. The vertical tail surface ratio decreases very rapidly between $0 < \bar{Y}_c < 0.2$ and remains constant at $\frac{S_v}{S_{v_0}} = 0.39$ afterwards.

The results for $\bar{Y}_c = 0$ reflect the twin engine configuration. The power is sized

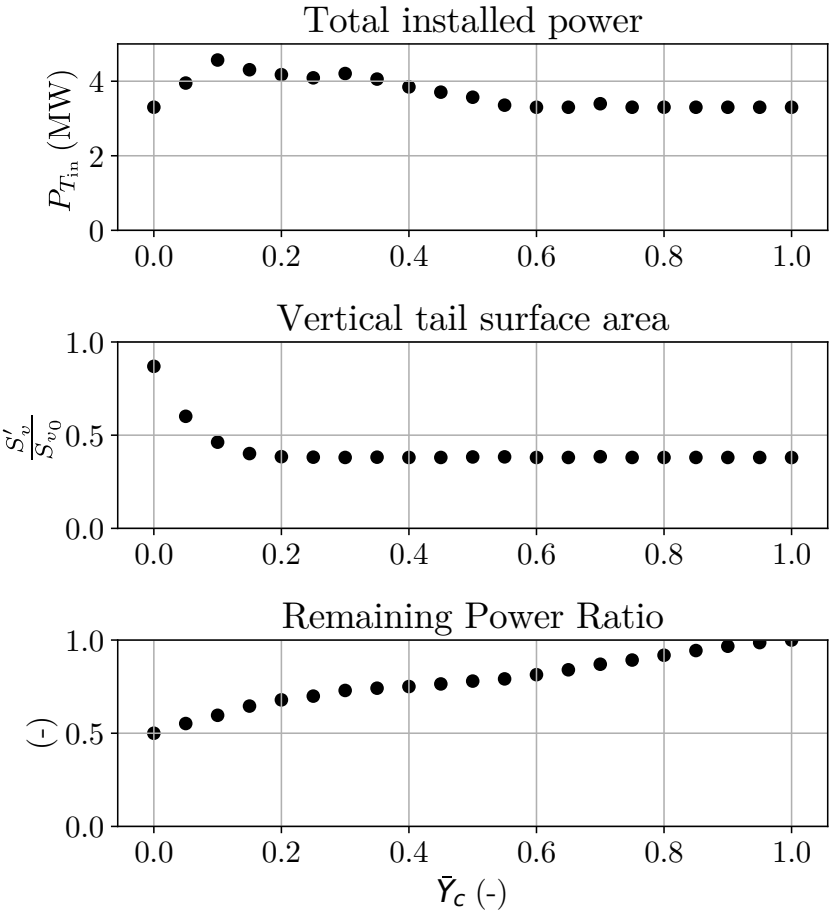

Figure A.2 – From top to bottom: Total installed power P'_T, vertical tail ratio $\frac{\tilde{S}_v}{S_{v_0}}$, power ratio remaining after failure $\frac{P}{P'_T}$.

for OEI at take off and the vertical tail follows this sizing point.

The limiting flight conditions for power distribution and total on board power are:

— FP 1 and 3, for $0 < \bar{Y}_c < 0.6$, representing an asymmetric thrust condition,

— FP 7 for $\bar{Y}_c > 0.6$, representing a nominal flight condition.

For the vertical tail ratio, the limiting flight conditions are:

— FP 1, ($\beta > 0$) for $0 < \bar{Y}_c < 0.1$, representative of directional requirements at take-off,

— FP 5 and 6 for $\bar{Y}_c > 0.1$, representative of directional requirements at landing.

The main result is the fact that distributed propulsion does change the sizing

point for both power systems and vertical tail if the severity of failure or the ultimate power/thrust asymmetry can be relaxed. At $\bar{Y}_c = 0.15$ and a remaining power ratio of $\frac{P}{P_T'} = 0.6$, the vertical tail size design point changes to landing conditions and can be reduced to 39% of its original size leading to a naturally unstable aircraft.

Appendix B

Co-design

B.1 Aircraft lateral dynamics evolution with varying VT

Figure B.1 represents the evolution of the aircraft dynamics in flight condition $[V, \beta, \gamma, \Omega] = [1.13V_{\text{sr}}, 0°, 3\%, 0°/s]$ defined at the end of Chapter 4.

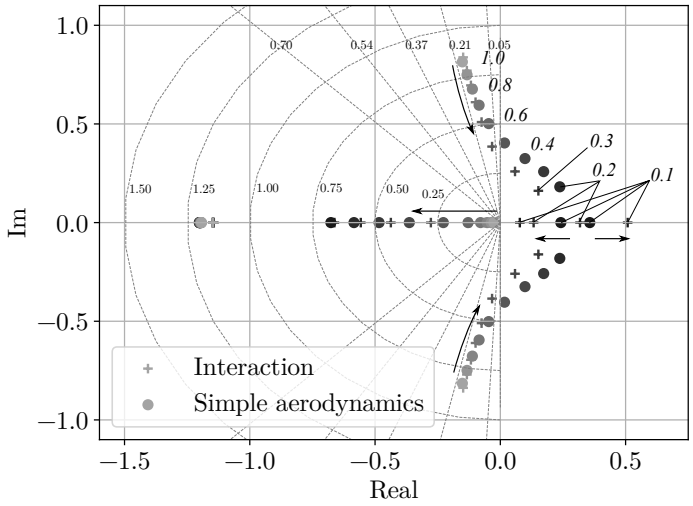

Figure B.1 – Evolution of lateral modes of the reference aircraft with the reduction of the VT surface area, from $S_{\text{v}}/S_{\text{v}_0} = 1$ to $S_{\text{v}}/S_{\text{v}_0} = 0.1$. The number in italic next to an eigenvalue indicates the corresponding $S_{\text{v}}/S_{\text{v}_0}$. Regular numbers next to radial and circumferential dashed line refer to damping and natural frequency respectively.

B.2 Sensitivity analysis: additional information

Additional graphics obtained during design exploration and co-design are given in this annex.

B.2.1 Aircraft with asymmetric thrust

Figure B.2 shows the results of the sensitivity analysis with the initial allocation fixed. The reduction of decision variables translated in a large number of solutions with unsatisfied constraints, resulting in large spikes on the surface. Although when one zooms into the surface, this one seems smooth, the loss of reliability argues in favor of leaving the allocation as a free variable.

The explanation for this behaviour is not clear but it may be that the initial solution is too specific. One may obtain better exploration results with a less optimal solution. The global optimality of the exploration remaining non-guaranteed.

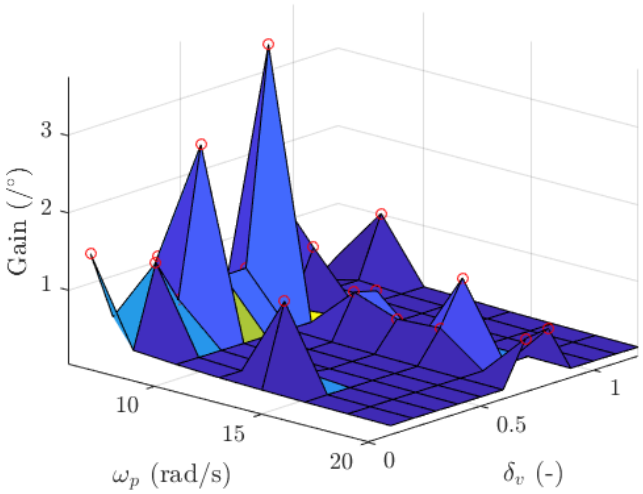

Figure B.2 – Evolution of the H_∞ norm C_2, with engine bandwidth, ω_p and VT size, δ_v. Red circles indicate solutions with unsatisfied constraints.

Appendix C

DECOL

C.1 Aircraft detailed geometry

The demonstrator's detailed geometry is given in Table C.1. Complementary information about the cruise velocity and trim is available in Table C.2.

Parameter	Value	Parameter	Value
Wingspan (m)	2.000	Wing area (m^2)	0.5000
Wing chord (m)	0.250	Wing AR	8
Flaps chord (% of c)	25	Flaps span total (m)	0.450
Ailerons chord (same as flaps) (m)	0.63	Ailerons span (m) each	0.450
Horizontal tail design			
Area (m^2)	0.0877	Span (m)	0.611
Aspect ratio	4.25	Taper ratio	1.00
Root chord (m)	0.144	Distance from wing LE (m)	1.167
V_H	0.80	Elevator Chord (full span) (%)	30
Vertical tail design			
Area (m^2)	0.0600	Span	0.329
Aspect ratio	1.80	Taper ratio	1.00
Root chord (m)	0.183	Distance to wing LE (m)	1.137
Swept angle (°)	0.000	Rudder Chord (full span) (%)	30
V_V	0.37		

Table C.1 – DECOL geometry.

Quantity	Model	Quantity	Model
Design CL	0.45	Design velocity m/s	23.5
Wing tilt angle (°)	3.2	H tail tilt angle (°)	2.1
CG location (% of MAC)	41.6	CG location from LE (mm)	104
CG max forward (% of MAC)	23.1	CG max rear (% of MAC)	56.6
CG max forward (mm)	58	CG max rear from LE(mm)	142
Static margin	15%	Elevator deflection to reach Max CL (°)	-7.6

Table C.2 – DECOL longitudinal stability and trim values. Note that the tilt angles are given relative to fuselage center line.

C.1.1 Measurements available on DECOL

Table C.3 – List of measurements logged on-board the aircraft and used in identification.

Ellipse2 by SBG-systems©[SBG]		
Filtered Accelerations	a_x^b, a_y^b, a_z^b	$\pm 8g$ (m/s^2)
Filtered Rotation rates	p, q, r	(rad/s)
EKF Euler angles	ϕ, θ, ψ	(rad), error $< 0.5°$
EKF Velocities	V_N, V_E, V_D	(m/s), accuracy $0.1m/s$
EKF Position	Latitude, Longitude, altitude	(°) and (m), accuracy $2m$ and $2.5m$
Static pressure	$P_{s,b}$	(Pa)
Multi-hole sphere		
AoA differential pressure	ΔP_α	(Pa)
Side slip differential pressure	ΔP_β	(Pa)
Dynamic pressure	ΔP_{V_a}	(Pa)
Temperature	T_a	(°C)
Pixhawk		
Pilot input	d_a, d_e, d_R, d_x	PWM signal (μs)
Command input	δ_a, δ_e, δ_R, $\delta_{x,i}$	PWM signal (μs) or rawcommand for engine [0,8191]
ESC		
Engine rotation rates	ω_{m_i}	(rpm)
Engine currents	I_i	(A)
Bus voltage at ESC	U_i	(V)
Power boards		
Battery current	I_1, I_2	(A)

C.2 DECOL : identified model validation

C.2.1 Longitudinal manoeuvre

A comparison between the model with standard derivatives and the one with thrust derivatives is given in Fig C.1 and in Fig C.2.

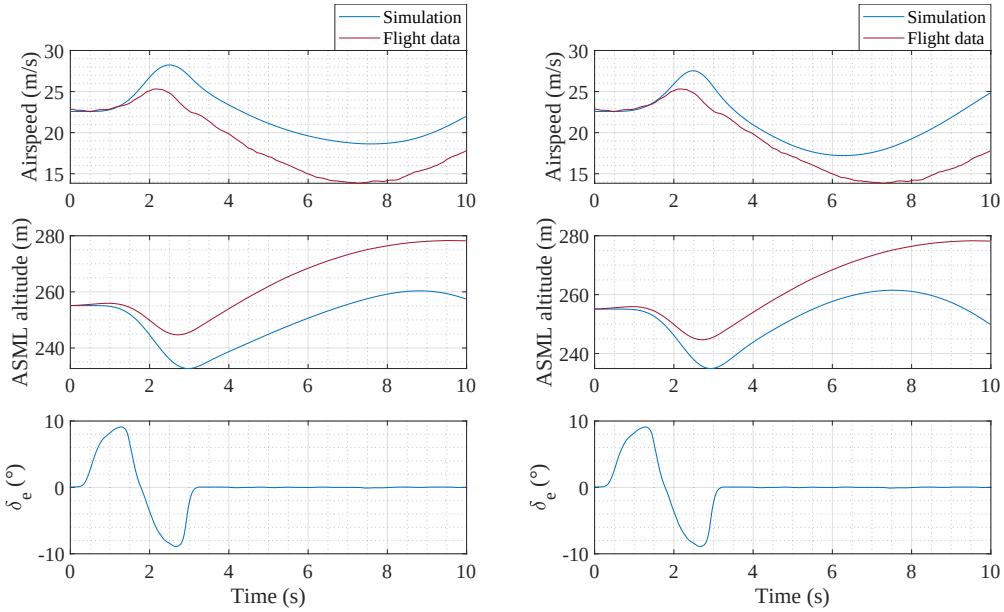

(a) Standard derivatives

(b) Explicit thrust derivatives.

Figure C.1 – Evaluation of simple model and explicit thrust derivative model in non linear simulation, longitudinal Phugoid.

The phugoid shown in Fig C.1 is not well captured by the two models. The model with thrust derivatives seems faster than what is observed in the flight data. The model with standard derivatives seems more in phase but a large error in the velocity remains. Both models give a poor estimate of the Phugoid and it was observed that the pitch rate was the source of the problem for the model with explicit thrust derivatives. The pitching moment coefficient is the longitudinal coefficient that showed the least improvement after the introduction of thrust derivatives which explains in part the results. The Phugoid is also a penalizing manoeuvre for validation due to the impossibility to record a full period in flight.

For the short period oscillation shown in Fig C.2 both models are reasonably correct. However, the introduction of explicit thrust derivatives seems to penalize the accuracy of the flight simulations. This is essentially visible on the evolution of the pitch rate. The model with standard derivatives performs better during the

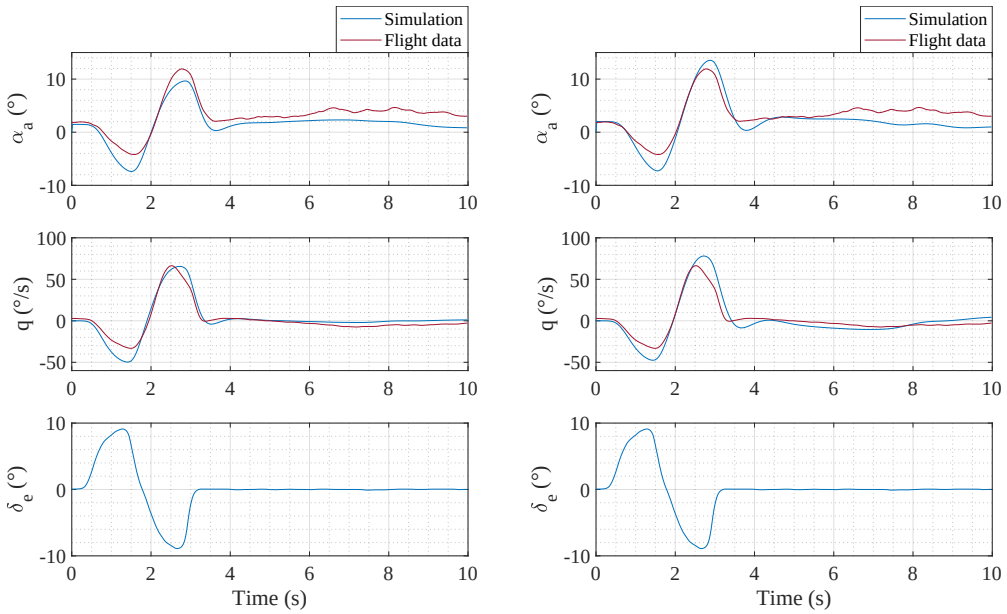

(a) Simple model

(b) Explicit thrust derivatives.

Figure C.2 – Evaluation of simple model and explicit thrust derivative model in non linear simulation, longitudinal short period oscillation.

rapid oscillation and seems also closer to the flight data during the phugoid. Based on these results, it would be beneficial to rely on the model with standard derivatives for the pitching moment coefficient.

Synthèse en Français des travaux de recherche

Cette partie présente une synthèse en français des travaux de recherche obtenus pendant cette thèse. Chaque chapitre de ce manuscrit est résumé par une section reprenant les contributions et principaux résultats présentés dans les chapitres en question.

10.3 Modèle de la dynamique du vol

Le but de ce chapitre est d'introduire les outils mathématiques, notations et hypothèses utilisés par la suite. La plupart des outils est standard à l'étude de la mécanique de vol d'un avion. La contribution de ce chapitre est de présenter un algorithme de trim permettant de prendre en compte (voir section 1.3 et Fig 10.3) :

— un nombre arbitraire N_m de moteurs électriques répartis symétriquement sur l'aile,

— l'utilisation de la poussée différentielle,

— la panne d'un ou de plusieurs moteurs.

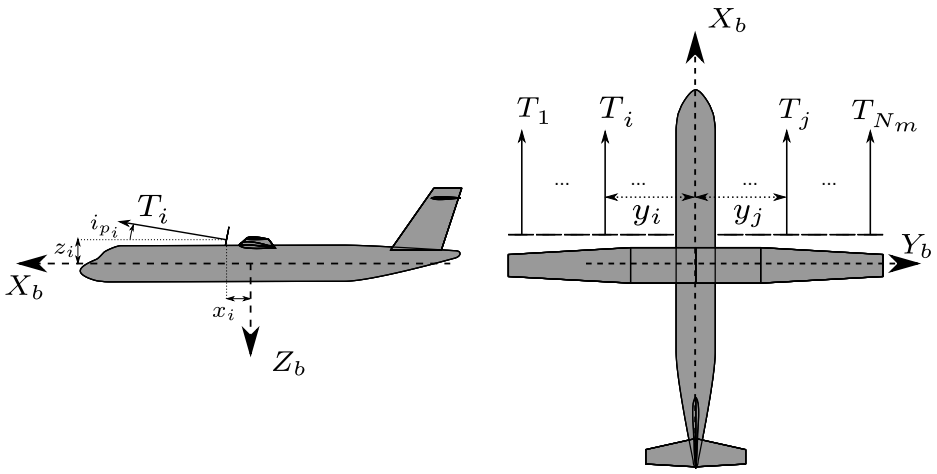

FIGURE 10.3 – Illustration d'une propulsion distribuée symétriquement le long du bord d'attaque de l'aile avec $y_j = -y_i$, $j = N_m + 1 - i$.

Les commandes des moteurs rendant le problème sous-contraint, l'algorithme de trim fait appel à une routine d'optimisation par gradient pour trouver une solution (voir section 1.5).

Enfin, le système est linéarisé en préparation de l'analyse de stabilité et de la synthèse des lois de commande (voir section 1.6).

10.4 Base de données aérodynamiques

Le but du chapitre 2 est la création d'un module d'aérodynamique capable de déterminer les dérivées des coefficients de forces et moments issus des efforts aérodynamiques. Un avion de référence, l'ATR72, un avion de transport régional est d'abord présenté. Cet avion restreint l'étude à une aérodynamique subsonique. Son équivalent équipé d'une propulsion distribuée de douze moteurs répartis au bord d'attaque de l'aile est également présenté dans la section 2.1.

Le choix a été fait de séparer l'aérodynamique de l'avion en deux parties. Un module de base qui estime les dérivées aérodynamiques en fonction de la taille de la dérive. Un second module s'occupe des interactions aéro-propulsives qui peuvent apparaître lorsqu'une aile est immergée dans le sillage d'une hélice. La construction du module de base est détaillée dans ce chapitre alors que les interactions aéro-propulsives sont traitées dans le chapitre 3.

Le module de base se devait d'être compatible avec l'algorithme de trim qui utilise une méthode d'optimisation par gradient tout en conservant un niveau de fidélité suffisant. En effet, l'écoulement au niveau de l'empennage vertical peut être soumis à d'importantes perturbations provenant des interférences avec les autres parties de l'avion (aile et fuselage).

La solution a consisté à créer un module composite qui utilise une méthode numérique VLM fournie avec le logiciel OpenVSP [Gloudemans 1996] pour évaluer les dérivées aérodynamiques du fuselage, de l'aile et de l'empennage horizontal. La contribution de l'empennage vertical incluant les perturbations causées par le reste de l'avion est obtenue par une méthode semi-empirique VeDSC créée spécifiquement pour les avions de transport régional (voir section 2.2 et [Ciliberti 2017] pour la méthode VeDSC).

Ce module permet l'évaluation des dérivées aérodynamiques de l'avion en fonction de la taille de l'empennage vertical présentée en section 2.2.2.

10.5 Interactions aéro-propulsives

Une étude approfondie des interactions aéro-propulsives est proposée dans le chapitre 3. Le sujet d'étude est centré sur le type d'interactions lorsqu'une aile est soufflée par une hélice placée en bord d'attaque. Le but de ce chapitre est de décrire les phénomènes physiques en jeu dans ce type d'interactions et d'en donner une estimation afin de déterminer comment cela peut modifier l'analyse statique et la

synthèse des lois de commande de l'avion.

Il y est montré que deux phénomènes sont à l'œuvre dans ce type d'interaction :

— les forces créées par le disque d'hélice lorsque l'écoulement n'est pas perpendiculaire à celui-ci,

— le soufflage de l'aile à proprement dit.

Les forces d'hélices ont été écartées en faisant l'hypothèse que les hélices seront de faible solidité, ce qui diminue ce type de force. Seul le soufflage de l'aile est retenu car celui-ci peut facilement doubler le coefficient de portance d'une aile isolée et une étude portant sur des essais en vol d'un bi-moteur suggère que la dynamique latérale est significativement impactée par le soufflage. Ces interactions étant plus importantes à faible vitesse comme le montre la figure 10.4 et donc proche du point de dimensionnement de l'empennage vertical, il a été décidé d'inclure ces efforts dans l'analyse (voir section 3.1).

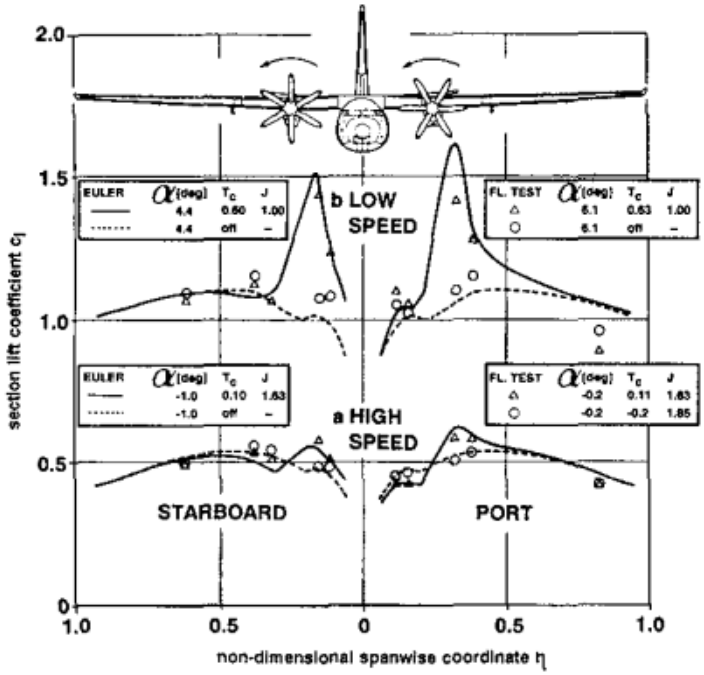

FIGURE 10.4 – Effet du soufflage sur la distribution de portance d'un Fokker 50 mesuré en vol à haute et faible vitesse. Reproduit à partir de [den Borne 1990].

Une revue des modèles capables de modéliser ce type d'interactions est donnée et une méthode directe de basse fidélité a été sélectionnée principalement pour sa rapidité d'exécution. Cette méthode a néanmoins dû être complétée pour donner une estimation de la traînée d'une aile soufflée ainsi que l'inclusion d'ailerons et des

volets (voir section 1.3 et 3.3).

Ce modèle étendu a été évalué avec des données expérimentales disponibles dans la littérature ainsi qu'avec les données mesurées en vol par le démonstrateur DECOL. Il a été montré que la précision de ce modèle n'est pas satisfaisante pour une évaluation des performances d'un avion à propulsion distribuée surtout en présence de volet, ceci est aussi confirmé dans le chapitre 4. Néanmoins il donne des estimations suffisamment précises pour l'étude de la dynamique du vol. Il permet notamment d'estimer les interactions découlant de l'utilisation de la poussée différentielle (voir section 3.4).

10.6 Étude des enveloppes de vol

Le chapitre 4 apporte une contribution tant technique que méthodologique. Une approche séquentielle est utilisée pour déterminer la configuration et les conditions de vol dans lesquelles, la stabilité latérale d'un avion à propulsion électrique distribuée, soumis à des interactions aéro-propulsives doit être étudiée.

Lorsque la stabilité et le contrôle d'un avion repose sur une utilisation active des systèmes de poussée, l'idée suivie dans ce chapitre est de démarrer par une analyse des efficacités moteurs, en terme d'accélération et de moment de lacet, en présence d'interactions aéro-propulsives.

La raison est illustrée dans la figure 10.5 tirée de la section 4.4 ou les efficacités moteur sont comparées entre le modèle aérodynamique simple et le modèle d'interactions aéro-propulsives.

La présence d'interactions diminue de manière significative les efficacités moteur à faible vitesse et/ou à fort coefficient de poussée. Cette caractéristique impose de trouver une configuration avion qui préserve au mieux les efficacités moteur et/ou la perte d'un moteur ne doit pas déboucher sur des conséquences catastrophiques. Dans le cas de la figure 10.5, il s'agit d'une configuration sans volets.

À son tour cette configuration peut avoir des conséquences sur les vitesses de référence et essentiellement sur la vitesse de décrochage V_{sr}. Pour un avion à propulsion électrique distribuée qui emploie le soufflage comme moyen hypersustentateur, la définition de V_{sr} telle que donnée par la certification CS25.103 n'est plus adaptée. Celle-ci est trouvée par l'étude des enveloppes de vol en vitesse et pente $(V_a - \gamma_a)$ en considérant plusieurs pannes moteurs.

Il se trouve que l'ATR72 avec propulsion distribuée et sans volets peut utiliser

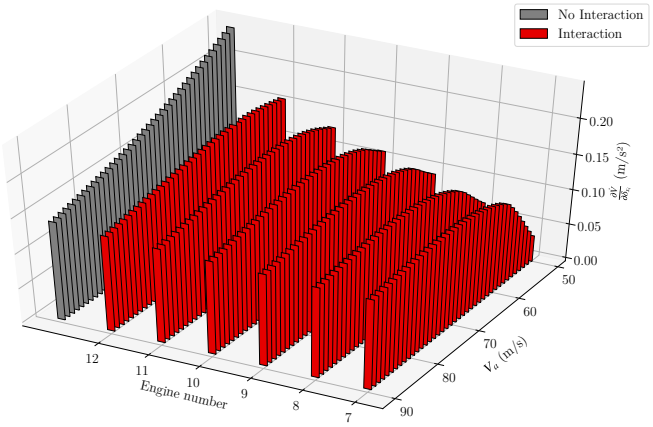

(a) $\frac{\partial \dot{V}}{\partial \delta_{x,i}}$.

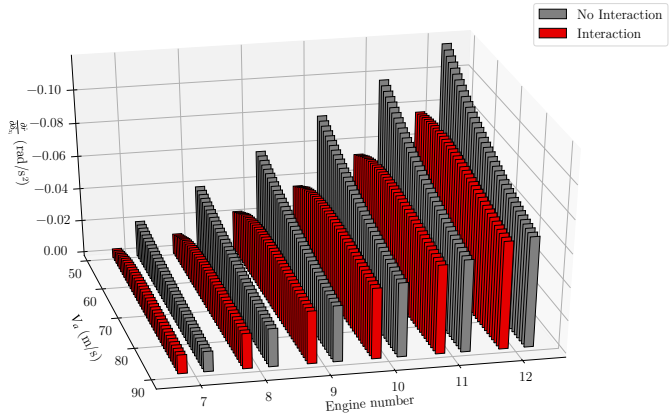

(b) $\frac{\partial \dot{r}}{\partial \delta_{x,i}}$.

FIGURE 10.5 – Efficacités des moteurs droits (moteur n°7 à 12).

la même vitesse de décrochage de référence que l'avion original et cela jusqu'à la perte de cinq moteurs (voir section 4.4). Ce résultat peut paraître surprenant et il est permis de mettre en doute la validité du modèle d'interactions aéro-propulsives dans l'estimation des performances de vol car celui-ci n'a pas été développé dans ce but.

Ce modèle a par ailleurs produit des résultats étonnants lorsqu'il a été appliqué à la version bi-moteur de l'ATR72. Il a par la suite été conclu que cette application ne faisant pas partie des essais de validation du modèle d'interactions, les résultats ne peuvent être considérés comme sérieux. Lorsque le modèle est appliqué à une version de l'avion avec propulsion distribuée, les performances longitudinales sont bien plus en accord avec le modèle aérodynamique simple, le modèle a donc été conservé pour l'étude de la propulsion distribuée (voir section 4.2 et section 4.3). Ceci illustre

un paradoxe qui veut que les performances de vol de l'avion soit complètement déterminées avant de pouvoir évaluer les caractéristiques latérales de l'avion.

Une fois les performances longitudinales de l'avion à propulsion distribuée connues, il est possible d'identifier les conditions de vol dimensionnant l'empennage vertical. Il a été trouvé que le cas de panne moteur au décollage reste le plus limitant. L'étude des enveloppes de vol en $\beta_a - V_a$ montre qu'une vitesse minimum de contrôle apparaît tout en restant inférieure à la limite de $1.13V_{\text{sr}}$ (voir section 4.4). Dans le cas où la poussée différentielle est utilisée seule, sans la gouverne de direction, l'élément qui semble diriger cette vitesse minimum de contrôle est la capacité à symétriser la poussée après une panne moteur. Si cette capacité est maintenue, la taille de l'empennage vertical ne semble pas influencer cette vitesse minimum de contrôle.

À l'inverse, la taille de l'empennage vertical influence la capacité à atteindre un dérapage de $\pm 15°$ à la vitesse de $1.3V_{\text{sr}}$. Dans le cas de l'utilisation de la poussée différentielle, il a été montré qu'une réduction de la surface de l'empennage était bénéfique.

La configuration de référence pour le dimensionnement de l'empennage vertical est finalement déduite comme étant la perte de deux moteurs extérieurs du même côté pendant le décollage (voir Tableau 10.4). Dans ce cas, il est possible de se passer complètement de gouverne de direction et il a été décidé d'explorer cette idée dans le reste de l'étude (voir section 4.5).

10.7 Distribution continue de propulsion pour le co-design des systèmes de propulsion et de la dérive

L'idée principale du chapitre 5 est tirée de l'analyse séquentielle des modes de défaillance d'un avion à propulsion distribuée telle que présentée dans le chapitre 4. Le nombre important et discret de moteurs fait rapidement augmenter le nombre de cas de panne à envisager et à étudier jusqu'à pouvoir isoler le cas de panne dimensionnant.

Le but de ce chapitre est de formuler une fonction continue de distribution de puissance le long de l'envergure. Cette fonction inclut une variable continue qui permet de simuler la perte d'une partie de la puissance. Cette formulation doit pouvoir rendre l'étude des modes de défaillance plus simple et permettre le design des systèmes de propulsion pour un cas de panne connu d'avance.

La fonction de distribution de puissance $P(\bar{y})$, où $\bar{y}$ est la position adimension-

nelle sur l'envergure, est approximée par un réseau de fonctions radiales $h_i(\bar{y})$:

$$P(\bar{y}) = \frac{P_0}{N_g} \sum_{i=1}^{N_g} w_i h_i(\bar{y}), \tag{10.1}$$

où les poids w_i sont calculés en trimant l'avion à des points de vol particulièrement dimensionnant (voir section 5.1).

Deux modèles de masse et de traînée de surface simples paramétrisés par la surface de l'empennage vertical sont ajoutés à l'analyse. Cela permet en minimisant la puissance et la taille de l'empennage vertical de trouver un compromis entre réduction de l'empennage et installation de puissance (voir section 5.2).
Les interactions aéro-dynamiques ne sont pas considérées dans ce chapitre.

Les conclusions générales qui peuvent être tirée de ce chapitre sont (voir section 5.3) :

— La distribution optimale de puissance est celle qui évite l'apparition d'une asymétrie de poussée après la panne critique.

— Si la poussée différentielle est le seul moyen de contrôle directionnel, alors c'est l'exigence de contrôlabilité ($\beta_a = \pm 15°$ à $1.3V_{\text{sr}}$) qui est dimensionnant pour l'empennage indépendamment du cas de panne.

TABLE 10.4 – Configuration de référence pour le dimensionnement de l'empennage vertical pour un avion à propulsion électrique distribuée.

Paramètre de design	
Puissance continue	4.1MW
Moteurs	12
Efficacité dérive	Dérive non autorisée.
Efficacité hélices	0.8
Hélices	En drapeau si inopérante.
Poussée différentielle	Activée.
Conditions de vol	
Moteurs inopérants	11 et 12
Angle de montée	3%
Taux de virage, Ω (rad/s)	0
Masse	21.5 T
Volets	0°
V_{sr}	51 m/s
$1.13V_{\text{sr}}$	57.6 m/s
$1.3V_{\text{sr}}$	66.3 m/s

Ces résultats ne peuvent être généralisés à l'ensemble des configurations de propulsion distribuée sans une étude plus approfondie. En revanche, ils confirment le principal avantage d'une propulsion distribuée, à savoir la possibilité de maintenir une poussée symétrique après un cas de panne.

10.8 Architecture de co-design

Le chapitre 6 représente le début de l'étude du comportement dynamique de l'avion à petite dérive et avec elle la mise en place de l'architecture de co-design qui permettra de calculer en parallèle les lois de commande et la taille de l'empennage vertical. La configuration retenue pour cette étude est un avion à propulsion électrique distribuée auquel on aura supprimé la gouverne de direction. La poussée différentielle est le seul moyen de contrôle directionnel.

Le calcul de lois de commande basée sur la norme H_∞ est d'abord introduit dans la section 6.1, puis le co-design est illustré dans un exemple simplifié mais représentatif de l'application prévue sur l'avion de référence.

La dynamique de l'avion à petite dérive est présentée avec et sans interactions aéro-propulsives et est discutée dans la section 6.2. Le principal résultat, l'évolution des pôles de l'oscillation de dérapage avec la taille de l'empennage vertical est reproduite ici dans la figure 10.6.

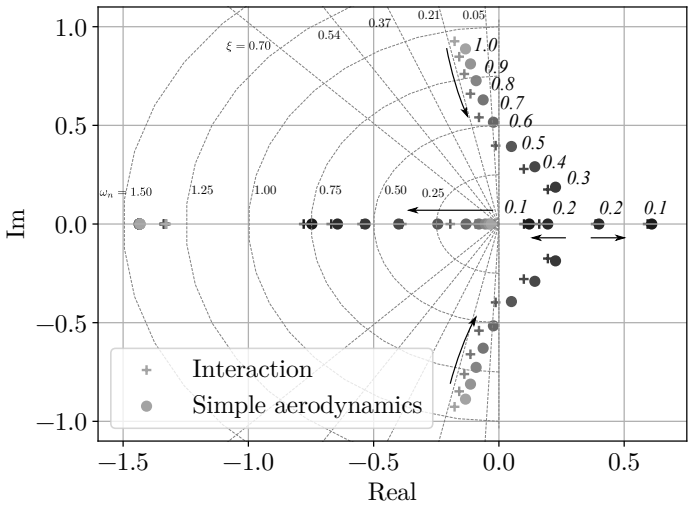

FIGURE 10.6 – Évolution des pôles de l'oscillation de dérapage avec la réduction de l'empennage vertical de $S_{\mathrm{v}}/S_{\mathrm{v}_0} = 1$ à $S_{\mathrm{v}}/S_{\mathrm{v}_0} = 0.1$.

Les interactions aéro-propulsives ne modifient pas de façon très importante la dynamique propre de l'avion et ont surtout tendance à rendre l'oscillation de dérapage mieux amorti (décalage vers la gauche du plan complexe). Il serait donc possible d'utiliser une aérodynamique standard comme pire cas. Enfin les modèles linéarisés de l'avion avec différentes tailles d'empennage vertical sont mis sous forme LFR pour le co-design (voir section 6.2.2).

L'architecture des lois de commande est discutée dans la section 6.3 et reproduite dans la figure 10.7. Cette architecture a été choisie pour réaliser un suivi de

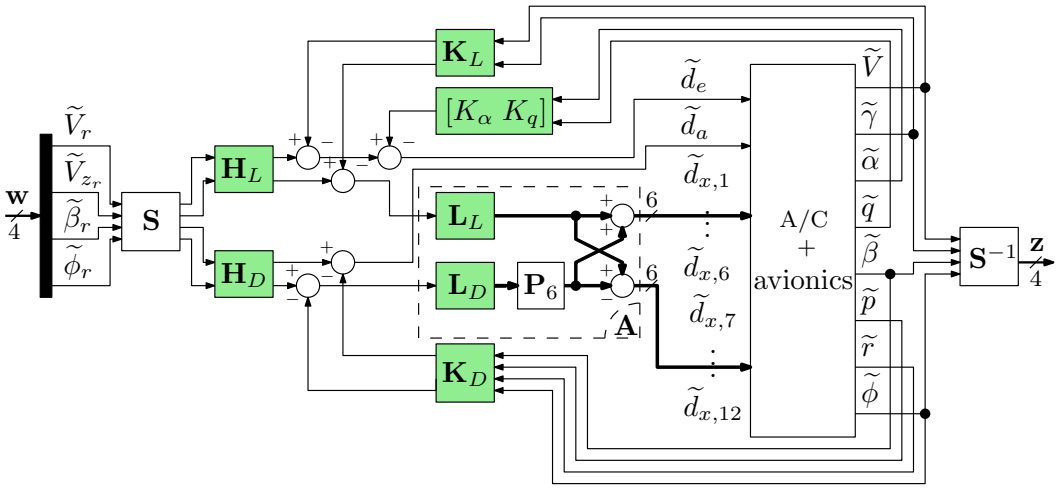

FIGURE 10.7 – Architecture des lois de commandes.

consigne donnée par le pilote : $\mathbf{w} = [V_r,\ V_{z_r},\ \beta_r,\ \phi_r]^T$. Des retours d'états latéraux et longitudinaux sont effectués par l'intermédiaire des gains statiques $\mathbf{K}_L$ pour fixer la phugoïde, K_α et K_q pour fixer l'oscillation d'incidence et la matrice de gain $\mathbf{K}_D$ pour fixer la dynamique latérale. Deux pré-commandes $\mathbf{H}_L$ et $\mathbf{H}_D$ sont utilisées pour réduire l'erreur statique à zéro.

Les matrices d'allocation $\mathbf{L}_L$ et $\mathbf{L}_D$ distribuent les efforts aux moteurs de façon symétrique pour des consignes longitudinales et anti-symétrique pour les consignes latérales par l'intermédiaire d'une matrice de permutation $\mathbf{P}_6$.

Les outils d'optimisation non lisse fournissant un optimum local, la solution de co-design dépend de la solution initiale. De façon à influencer le solveur vers un design réalisable, les lois de commande sont initialisées par une technique de placement de pôles.

Un co-design préliminaire est finalement présenté en section 6.4. Ce co-design séquentiel repose sur un compromis manuel car les valeurs de relâchement des gains et des variables de design sont fixées par l'utilisateur. Une marge de progression im-

portante est cependant découverte car il est possible d'éliminer l'empennage vertical tout en maintenant des contraintes de qualités de vol satisfaisantes.

10.9 Méthodologie de co-design avec contraintes d'enveloppe de vol

Les principales limitations du co-design tel que présenté dans le Chapitre 6 sont le compromis manuel et la non prise en compte des exigences de trim et des saturations moteurs. Le chapitre 7 propose de résoudre ces problèmes en traduisant les limites de saturation et les exigences de trim en contraintes (voir section 7.1).

Il est possible de définir ces contraintes de façon simple, en revanche peu d'informations sont disponibles pour transformer ces contraintes en expression numérique. Une étude de sensibilité est donc conduite en section 7.2 pour pouvoir définir des contraintes réalisables. Les paramètres qui sont variés sont :

— la surface de l'empennage vertical,

— la bande passante moteur,

— les qualités de vol exigées,

— la pression dynamique.

Pour chaque configuration, les lois de contrôle sont calculées pour minimiser leurs gains. Trois grandeurs sont ensuite mesurées sur la fonction de transfert entre une consigne pilote de dérapage et les consignes moteurs :

— le gain statique maximal,

— la norme H_∞ maximale,

— la fréquence du pic H_∞.

L'évolution de la norme H_∞ avec la surface relative de l'empennage vertical δ_v et la bande passante moteur est reproduite dans les figures 10.8a pour le modèle aérodynamique standard et dans la figure 10.8b pour le modèle d'interaction aéro-propulsive.

La figure 10.8 illustre deux résultats importants de ce chapitre. L'influence de la surface de l'empennage vertical est relativement faible par rapport à la bande passante moteur. Les interactions aéro-propulsives n'augmentent pas forcément la norme H_∞ mais donnent une surface moins lisse à cause de la variation d'efficacité des moteurs.

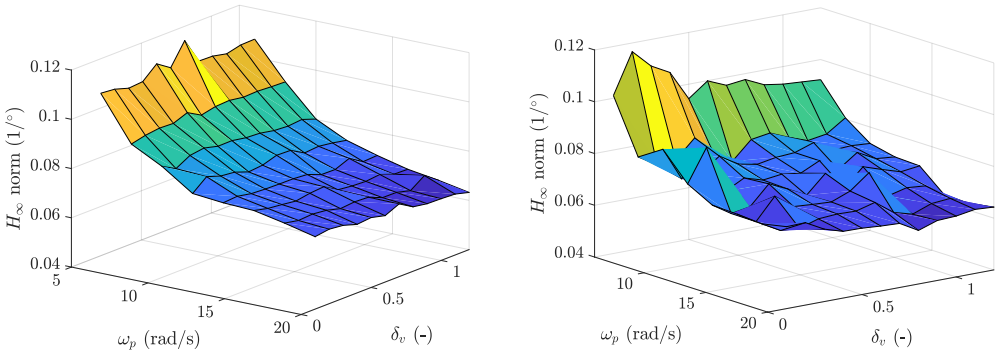

(a) Aérodynamique standard.

(b) Modèle d'interaction aero-propulsive

FIGURE 10.8 – Évolution de la norme H_∞ avec la bande passante moteur ω_p et la surface relative de l'empennage vertical δ_v.

L'étude de sensibilité débouche sur des contraintes qui sont rassemblées sous la forme d'un gabarit fréquentiel à imposer aux fonctions de transferts entre les consignes en latéral du pilote et les entrées moteurs (reproduit dans la figure 10.9).

Ce gabarit définit deux limites de gain : la plus sévère permet d'assurer qu'aucun moteur ne soit saturé en régime permanent, l'autre limite autorise une saturation transitoire des moteurs pour les manœuvres dynamiques qui se répercuteront en perturbation sur l'axe longitudinal (voir section 7.3).

Le schéma de définition du problème de co-design est ensuite établi où les matrices d'allocation $\mathbf{L}_L$ et $\mathbf{L}_D$ sont calculées dans une première étape pour minimiser les gains, puis le problème de co-design est résolu pour obtenir un compromis par optimisation. L'empennage vertical est diminué de 72%, ce qui représenterait un avion naturellement instable, avec une bande passante moteur de 7.66 rad/s. Les qualités de vol ont dû être modifiées pour satisfaire toutes les contraintes ce qui résulte en une constante de temps en réponse à une consigne en dérapage de $\tau = 1.43$s.

10.10 Co-design avec panne moteur

L'étape manquante est l'introduction du cas de panne moteur critique dans le co-design, c'est le but du chapitre 8. La stratégie retenue pour cela est le design de l'empennage vertical et la bande passante moteur en parallèle pour un cas de poussée symétrique et pour le cas de panne critique. Les seules variables étant autorisées à changer étant les matrices d'allocation $\mathbf{L}_L$ et $\mathbf{L}_D$. Une étude de sensibilité similaire

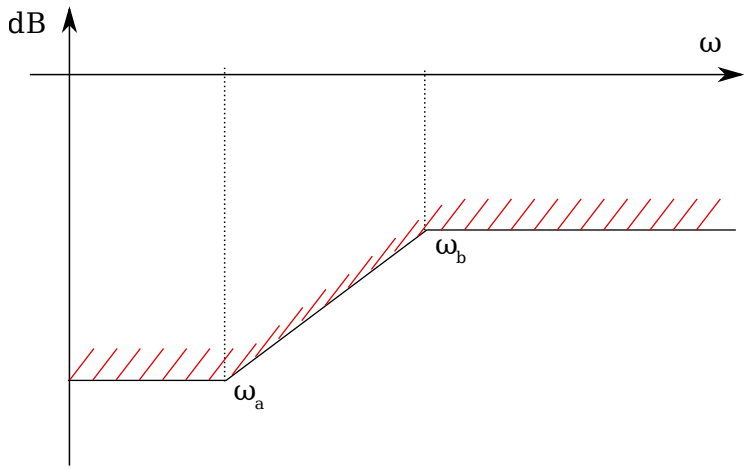

FIGURE 10.9 – Gabarit fréquentiel pour les fonctions de transfert entre consignes du pilote en latéral et les entrées moteurs.

à celle présentée dans le chapitre précédent est conduite pour définir les contraintes de co-design (voir section 8.1 et section 8.2). Les mêmes tendances se dégagent de cette étude, seuls les gains sont plus élevés du fait de la perte de poussée.

Le co-design donne un compromis avec un empennage vertical diminué de 50% et une bande passante moteur de 10.4 rad/s avec des qualités de vol identiques même dans le cas de panne critique.
Il doit cependant être rappelé que cette étude néglige :

— les perturbations atmosphériques,

— les saturations en vitesse des moteurs,

— un délai dans l'électronique de commande.

10.11 Recherche expérimentale : démonstrateur de vol à propulsion électrique distribuée

La propulsion électrique distribuée est un domaine de recherche récent dans lequel plusieurs études expérimentales sont actuellement en cours ou ont eu lieu récemment (voir le projet Ampere [Hermetz 2016] mais aussi [Borer 2016], [Fredericks 2017], [Stoll 2015], [Baris 2017], [Ma 2020]). Les données expérimentales sont utilisées pour développer et valider des modèles aérodynamiques pour le calcul de performances. Ces modèles sont ensuite utilisés en conception préliminaire avion. Á l'exception des projets Ampere dans [Dilinger 2018] et Greased Lighting [Fredericks 2017], la dynamique de vol est un sujet de préoccupation secondaire dans

ces projets et un intérêt a été identifié pour étudier l'impact des interactions aero-propulsives sur la dynamique de vol. Un segment de recherche expérimentale a donc été mis en place pendant cette thèse pour contribuer à combler ce manque. Un démonstrateur de vol nommé DECOL a donc été développé pour répondre aux trois objectifs suivants :

— caractériser la dynamique de vol latéral de l'avion lorsqu'une importante partie de l'aile est immergée dans les flux d'hélices,

— caractériser les effets aéro-propulsifs induits par l'utilisation de la poussée différentielle.

— évaluer la possibilité d'implémenter des lois de contrôle et la réduction de dérive obtenue par co-design avec le retour d'expérience des objectifs précédents.

Le chapitre 9 décrit le démonstrateur construit pour répondre à ces objectif.

Le démonstrateur est développé en intégrant des contraintes opérationelles ce qui a eu pour effet de favoriser des fonctions pratiques au détriment des performances de l'avion. Néanmoins, des caractéristiques de design uniques sont présentes comme la possibilité de positionner les moteurs de manière continue sur l'aile ou de remplacer l'empennage vertical (voir section 9.1). L'avion a une envergure de 2m pour une masse de 8.25 Kg.

La propulsion de ce démonstrateur est constituée de huit moteurs électriques qui couvrent l'ensemble du bord d'attaque mais laissent les saumons d'aile libres. Des briques technologiques clés comme le bus UAVCAN ont permis de faciliter grandement la circulation de données et simplifier l'architecture du système de propulsion distribuée. Un ordinateur de bord recueille et enregistre les mesures effectuées à bord dont les mesures inertielles, de position satellite, les mesures aéro-clinométriques ainsi que les régimes moteurs (voir section 9.2 et section 9.3).

Une étude théorique de l'avion est effectuée avec les outils aérodynamiques développés au chapitres 2 et 3. Les effets attendus des interactions aéro-propulsives sur les dérivées aérodynamiques sont mis en évidence et permettent d'établir une structure de base pour identifier un modèle à partir des données de vol. Hormis le coefficient de portance, la majorité des changements peut être modélisée par une relation linéaire par rapport au coefficient de poussée définis comme suit :

$$T_c = \frac{T}{4(\frac{\rho}{2} S_p V_a^2)}\,, \tag{10.2}$$

où T est la poussée d'un moteur, S_p est la surface du disque d'hélice, V_a la vitesse

air de l'avion et ρ la densité de l'air.

10.12 Identification des modèles aérodynamique et aéropropulsif de DECOL

Le chapitre 10 présente dans un premier temps la méthode basée sur l'erreur de prédiction qui est utilisée pour l'identification de modèles depuis les données de vol et la calibration des mesures aéro-clinométriques effectuées directement en vol (voir section 10.1 et section 10.2).

Ensuite, pour chaque coefficient, deux modèles sont identifiés (voir section 10.3) :

— le premier se basant sur un jeu de dérivées aérodynamiques standards,

— le deuxième incluant des dérivées par rapport au coefficient de poussée.

Les deux modèles sont ensuite évalués dans leur capacité à reproduire les forces et moments observés en vol. La pertinence de l'introduction des dérivées par rapport au coefficient de poussée est justifiée par l'augmentation de précision non-négligeable qu'elles apportent. Cela est reproduit ici dans la figure 10.10 où le coefficient de portance est estimé par les deux modèles pendant une phugoïde.

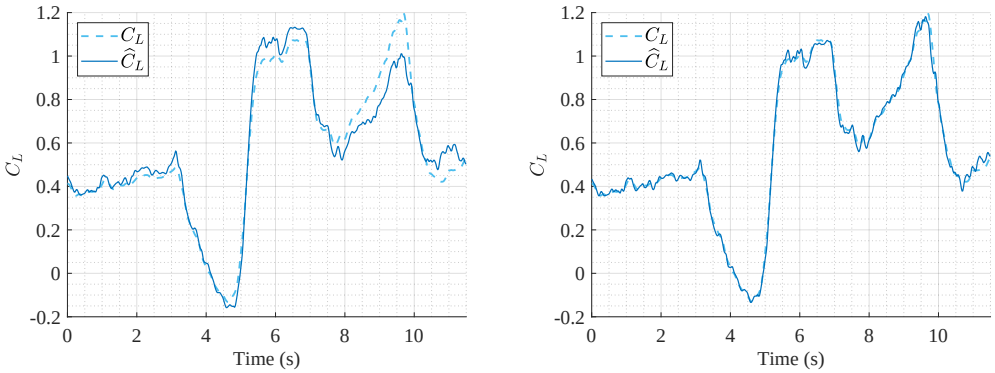

(a) $\widehat{C}_L$ avec les dérivées standards. (b) $\widehat{C}_L$ avec les dérivées par rapport à T_c.

FIGURE 10.10 – Évaluation des deux modèles pour l'estimation du coefficient de portance pendant une phugoïde.

Il est possible que les dérivées par rapport au coefficient de poussée soient rejetées comme dans le cas du coefficient de force latérale ou bien qu'elles n'apportent que peu d'amélioration comme dans le cas du coefficient du moment de tangage.

Les modèles identifiés des coefficients latéraux ont donné des résultats inattendus car il est apparu que la stabilité latérale et l'amortissement, donnés par les

coefficients C_{n_β}, C_{n_r} étaient fortement diminués par le coefficient de poussée (voir section 10.3.2). Ce constat est apparu sans explication et a donné lieu à une vérification des modèles par simulation de vol non-linéaire (voir section 10.4). Les simulations ont confirmé cette observation car les modèles incluant les dérivées par rapport au coefficient de poussée permettent de mieux reproduire les manœuvres réelles que les modèles se reposant sur les dérivées standards.

Deux hypothèses ont été formulées pour expliquer ce phénomène mais aucune ne peut être validée par manque d'information. Il apparaît cependant que les interactions aéro-propulsives se propagent et impactent l'avion dans son ensemble (fuselage et empennage) et ne peuvent être réduites à des interactions entre les hélices et la voilure.

Ce dernier point compromet la réduction de dérive envisagée comme troisième objectif avec le niveau actuel de connaissance.

10.13 Conclusion générale et perspectives

Ces travaux de recherches ont montré que l'avantage principal de la propulsion électrique distribuée concernant la stabilité et le contrôle sont la capacité de pouvoir ré-allouer la poussée afin d'éviter un déséquilibre de poussée après une panne moteur. Cette possibilité permet de réduire la surface de l'empennage vertical sans compromettre les capacités de trim de l'avion.

Pour autant que le système de propulsion permette de symétriser la poussée, la condition de vol dimensionnant l'empennage vertical reste l'exigence de $\pm 15°$ de dérapage à faible vitesse, avec panne moteur critique, définie par la spécification de certification CS25.147. Cette exigence de contrôlabilité demande une certaine puissance de contrôle qui peut être délivrée par la poussée différentielle, la gouverne de direction ou les deux. Si la poussée différentielle est le seul moyen de contrôle directionnel, il est avantageux de dimensionner l'avion pour une stabilité latérale neutre. Si suffisamment de puissance est disponible ou si un volet de dérive est utilisé en parallèle, il est possible d'envisager un avion naturellement instable.

Les qualités de vol sont principalement dépendantes de la bande passante des actionneurs et sur une configuration n'utilisant que la poussée différentielle, sont contraintes par les limites de saturation des moteurs. Le compromis déduit du co-design avec panne moteur donne une taille d'empennage réduite de 50% pour une bande passante des moteurs de 10.4 rad/s. L'avion ayant une réaction plutôt lente

avec une constante de temps de $1.43\,s$.

Les interactions aéro-propulsives peuvent réduire de manière significative l'efficacité de la poussée différentielle et réduire l'enveloppe de vol directionnelle de l'avion à basses vitesses, lorsque le coefficient de poussée atteint des valeurs importantes. Ce phénomène est moins pénalisant pour le comportement dynamique et le calcul des lois de contrôle mais ce phénomène étant non linéaire avec la vitesse, il peut poser problème lors d'un séquencement de gains. Á cela s'ajoute le phénomène observé lors des essais en vols : la réduction de stabilité et de l'amortissement en latéral avec le coefficient de poussée.

En se basant sur les connaissances acquises lors de ce travail, les recommandations suivantes sont formulées :

- L'importante inertie d'un avion de transport régional encourage la combinaison de la poussée différentielle et d'une gouverne de direction pour améliorer les qualités de vol. Cette solution peut être vue comme une candidate sérieuse pour obtenir une réduction importante de l'empennage vertical (au moins jusqu'au point de neutralité) tout en conservant un système de contrôle latéral robuste et redondant. Dans cet effort, la priorité devrait être donnée au problème d'allocation d'effort entre la poussée différentielle et la gouverne de direction.
- Le co-design a été réalisé en ignorant la présence de délais, de saturations en vitesse des actionneurs ou de perturbations atmosphériques. De plus, seule une configuration de vol a été explorée. Afin de renforcer l'argumentaire en faveur d'un avion instable ou neutre sur l'axe latéral, il est nécessaire de prendre ces limitations en compte.
- La construction du modèle aérodynamique d'un avion à propulsion électrique distribuée pour l'étude de la stabilité et du contrôle peut être abordée par une approche multi-fidélité. Il est conseillé de :
  - utiliser une méthode haute fidélité pour calculer la puissance aux équilibres
  - les dérivées aérodynamiques avec effet aéro-propulsif peuvent être calculées par des méthodes plus basse fidélité, à ce moment il est conseillé de :
    - considérer les interactions autour de la géométrie complète de l'avion,
    - augmenter le niveau de fidélité à des méthodes capables de résoudre un champs de pression autour d'objet en 3 dimensions.

— la bande passante des actionneurs étant un paramètre bien plus important que la taille de l'empennage vertical pour les qualités de vol, il peut être tentant d'installer des systèmes propulsifs plus puissants et plus lourds. Cela devrait entraîner une baisse des performances de l'avion et une augmentation de son inertie. C'est pourquoi, afin de pleinement tirer avantage de la méthode de co-design, celle-ci devrait être incluse dans un environnement global de conception avion afin de la faire interagir avec les disciplines qui ont été laissées de côté pour cette étude.

— Trois étapes manquent pour l'implémentation des résultats de co-design sur le démonstrateur DECOL :

  — Découpler la gouverne de direction et la poussée différentielle actuellement en place afin d'identifier les dérivées de contrôles directionnelles de façon indépendante.

  — Répliquer la réduction de stabilité de route et d'amortissement par simulation afin de la comprendre et de la modéliser.

  — Après ces deux étapes, un nouveau modèle d'interactions aéro-propulsives incluant le modèle de dynamique de vol identifié et augmenté avec les résultats du premier point, peut être utilisé avec la méthode de co-design afin d'optimiser la taille de l'empennage vertical.

Bibliography

[Abzug 2005] M.J. Abzug and E.E. Larrabee. Airplane stability and control: A history of the technologies that made aviation possible. Cambridge Aerospace Series. Cambridge University Press, 2005. (Cited in pages 3, 8, and 139.)

[Aerospace-Technology 2017] Aerospace-Technology. *Extra 330LE Electric Aircraft*, 2017. https://www.aerospace-technology.com/projects/extra-330le-electric-aircraft/. (Cited in page 13.)

[Aerostories 2002] Aerostories. *Breguet 941 in approach*, 2002. http://aerostories.free.fr/appareils/Br941/index.html. (Cited in pages ix and 10.)

[Airbus 2019] Airbus. *E-fan X*, 2019. https://www.airbus.com/innovation/future-technology/electric-flight/e-fan-x.html. (Cited in page 13.)

[aircraft 2000] ATR aircraft. *ATR72 Flight Crew Manual*, 2000. (Cited in pages xvii, 43, 97, and 98.)

[Al-Nahhas 2020] Cedra Al-Nahhas. *Flight Tests and System Identification Applied to a Small-Scale Demonstrator*, 2020. Master Thesis pursued at ISAE-SUPAERO. (Cited in pages xiii and 224.)

[Alaoui-Sosse 2018] Sara Alaoui-Sosse, Philippe Pastor, Pierre Durand, Patrice Medina, Michel Gavart, José Darrozes and Marie Lothon. *Development and Qualification of Instrumented Unmanned Planes for Turbulence Observations in the Atmospheric Surface Layer*. In 23rd Symposium on Boundary Layers and Turbulence, pages 1–10, Oklahoma City, US, 2018. (Cited in page 224.)

[Alazard 2013] Daniel Alazard, Thomas Loquen, Henry De Plinval and Christelle Cumer. *Avionics/Control co-design for large flexible space structures*. In AIAA Guidance, Navigation, and Control (GNC) Conference, pages 1–15, Boston, US, 2013. (Cited in page 145.)

[Ameyugo 2006] Gregorio Ameyugo, Mark Taylor and Riti Singh. *Distributed propulsion feasibility studies*. ICAS2006, 2006. (Cited in page 9.)

[Anderson 1996] M. R. Anderson and W. H. Mason. *An MDO Approach to Control Configured Vehicle Design*. AIAA Meeting Papers on Disc, no. 96-4058, pages 734–743, 1996. (Cited in page 8.)

[Angrand 2020] Antony Angrand. *City a réalisé son premier vol*, 2020. https://www.air-cosmos.com/article/cityairbus-a-ralis-son-premier-vol-22392. (Cited in page 13.)

[Apkarian 2006] P. Apkarian and D. Noll. *Nonsmooth H_∞ Synthesis*. IEEE Transactions on Automatic Control, vol. 51, no. 1, pages 71–86, 2006. (Cited in page 146.)

[Apkarian 2012] Pierre Apkarian. *Tuning Controllers Against Multiple Design Requirements*. In System Theory, Control and Computing (ICSTCC), 2012 16th International Conference on, pages 1–6. IEEE, 2012. (Cited in page 146.)

[Arne W 2006] Stuermer Arne W. *Unsteady Simulation of Propeller Installation Effects*. AIAA 42^{nd} Joint Propulsion Conference & Exhibit, no. 4969, 2006. (Cited in page 68.)

[Aviation-Week 2017] Aviation-Week. *German Startup Unveils Electric Air Taxi*, 2017. https://aviationweek.com/business-aviation/german-startup-unveils-electric-air-taxi. (Cited in page 13.)

[Baris 2017] Engin Baris and Drew Landman. *An Investigation into the Potential Benefits of Distributed Electric Propulsion on Small UAVs at Low Reynolds Numbers*. In 35th AIAA Applied Aerodynamics Conference, 2017. (Cited in pages 213 and 294.)

[Bohari 2018] Baizura Bohari, Quentin Borlon, Perla B. Mendoza-Santos, Alessandro Sgueglia, Emmanuel Benard, Murat Bronz and Sebastien Defoort. *Conceptual Design of Distributed Propellers Aircraft: Non-Linear Aerodynamic Model Verification of Propeller-Wing Interaction in High-Lifting Configuration*. In AIAA Scitech 2018, 2018 AIAA Aerospace Sciences Meeting, pages eISBN: 978–1–62410–524–1, Kissimmee, United States, Janvier 2018. AIAA. (Cited in pages 67, 70, 75, 76, and 213.)

[Boiffier 1998] J.L. Boiffier. The dynamics of flight, the equations. The Dynamics of Flight. Wiley, 1998. (Cited in pages 7, 22, 32, and 237.)

[Borer 2016] Nicholas K Borer, Michael D Patterson, Jeffrey K Viken, Mark D Moore and al. *Design and Performance of the NASA SCEPTOR Distributed Electric Propulsion Flight Demonstrator*. 16^{th} AIAA Aviation Technology, Integration, and Operations Conference, no. 3920, 2016. (Cited in pages 56, 213, and 294.)

[Borer 2017] Nicholas K. Borer, Joseph M. Derlaga, Karen A. Deere, Melissa B. Carter, Sally Viken, Michael D. Patterson, Brandon Litherland and Alex Stoll. *Comparison of Aero-Propulsive Performance Predictions for Distributed Propulsion Configuration.* In 55th AIAA Aerospace Sciences Meeting, numéro AIAA 2017-0209, 2017. (Cited in page 213.)

[Brandt 2015] J.B. Brandt, R.W. Deters, G.K. Ananda and M.S. Selig. *UIUC Propeller Database*, 2015. http://m-selig.ae.illinois.edu/props/propDB.html. (Cited in pages xiii, 221, 222, and 226.)

[Brown 1983] E. N. Brown, C. A. Friehe and D. H. Lenschow. *The Use of Pressure Fluctuation on the Nose of an Aircraft for Measuring Air Motion.* Journal of Climate and Applied Meteorology, vol. 22, January 1983. (Cited in pages 224 and 235.)

[Bucharles 2012] A. Bucharles, C. Cumer, G. Hardier, B. Jacquier, A. Janot, T. Le Moing, C. Seren, C. Toussaint and P. Vacher. *An overview of relevant issues for aircraft model identification.* Journal Aerospace Lab, 2012. (Cited in pages 241 and 242.)

[Byrd 1996] Richard H. Byrd, Jean Charles Gilbert and Jorge Nocedal. *A Trust Region Method Based on Interior Point Techniques for Nonlinear Programming*, 1996. Projet PROMATH, INRIA, https://hal.inria.fr/inria-00073794. (Cited in page 36.)

[Casadei 2006] D. Casadei, G. Serra, A. Tani and L. Zarri. *Assessment of direct torque control for induction motor drives.* Bulletin of the Polish Academy of Sciences. Technical Sciences, vol. Vol. 54, nr 3, pages 237–254, 2006. (Cited in page 14.)

[Catalano 2004] F.M. Catalano. *On the Effect of an Installed Propeller Slipstream on Wing Aerodynamic Characteristics.* Acta Polytechnica, no. Vol. 44 No. 3/2004, 2004. (Cited in pages 63, 77, and 78.)

[Chambers 2015] J. Chambers. Modeling flight : The role of dynamically scale free flight models in support of nasa aerospace programs. NASA. US National Aeronautics and Space Admin, 2015. (Cited in page 216.)

[Chen 1991] S. Chen, C. F. N. Cowan and P. M. Grant. *Orthogonal least squares learning algorithm for radial basis function networks.* IEEE Transactions on Neural Networks, vol. 2, no. 2, pages 302–309, March 1991. (Cited in page 125.)

[Chudoba 2001] Bernd Chudoba. *Stability and Control of Conventional and Unconventional Aircraft Configuration.* Phd thesis, Cranfield University, 2001. (Cited in page 45.)

[Chudoba 2003] B. Chudoba and H. Smith. *A Generic Stability and Control Methodology for Novel Aircraft Conceptual Design.* AIAA Atmospheric Flight Mechanics Conference, no. 5388, 2003. (Cited in pages 8 and 45.)

[Ciliberti 2013] Danilo Ciliberti, Fabrizio Nicolosi and Pierluigi Della Vecchia. *A New Approach in Aircraft Vertical Tailplane Design.* XXII Conference AIDAA, 2013. (Cited in pages xvii, 8, and 48.)

[Ciliberti 2017] Danilo Ciliberti, Pierluigi Della Vecchia, Fabrizio Nicolosi and Agostino De Marco. *Aircraft directional stability and vertical tail design: A review of semi-empirical methods.* Progress in Aerospace Sciences, vol. 95, pages 140 – 172, 2017. (Cited in pages 47 and 284.)

[Clarke 2017] S. Clarke, M. Redifer, K. Papathakis, A. Samuel and T. Foster. *X-57 power and command system design.* In 2017 IEEE Transportation Electrification Conference and Expo (ITEC), pages 393–400, 2017. (Cited in page 13.)

[Cook 2013] Michael V. Cook. *Chapter 10 - Flying and Handling Qualities.* In Michael V. Cook, editeur, Flight Dynamics Principles (Third Edition), pages 33 – 71. Butterworth-Heinemann, third edition édition, 2013. (Cited in page 181.)

[Cozensa 2017] Dario Cozensa and Roelof Vos. *Handling Qualities Optimization in Aircraft Conceptual Design.* 17$^{\text{th}}$ AIAA AVIATION Forum, no. 3763, 2017. (Cited in page 9.)

[Cybenko 1989] George Cybenko. *Approximation by superpositions of a sigmoidal function.* Mathematics of Control, Signals and Systems, vol. 2, pages 303–314, 1989. (Cited in page 125.)

[De Young 1965] John De Young. *Propellers in Yaw.* Journal of Aircraft, no. Vol. 2, NO. 3, 1965. (Cited in page 57.)

[den Borne 1990] P. C. M. Van den Borne and J. van Hengst. *Investigation of the Slipstream effect on the Fokker 50 through in flight pressure measurements.* AIAA Applied Aerodynamics Conference, no. AIAA-90-3084, 1990. (Cited in pages x, xv, 62, and 285.)

[Denieul 2016] Yann Denieul. *Preliminary Design of Control Surfaces and Laws for Unconventional Aircraft Configurations.* Theses, Institut Supérieur de

l'Aéronautique et de l'Espace (ISAE), Dec 2016. (Cited in pages 8, 14, 139, 146, and 163.)

[Denieul 2017] Yann Denieul, Joël Bordeneuve-Guibé, Daniel Alazard, Clément Toussaint and Gilles Taquin. *Multi-control Surface Optimization for Blended Wing-Body Under Handling Quality Constraint.* Journal of Aircraft, vol. 55, pages 638–651, 2017. (Cited in page 139.)

[Deters 2015] Robert W Deters, Gavin K. Ananda and Michael S. Selig. *Slipstream Measurements of Small Scale Propellers at Low Reynolds Number.* AIAA Aviation, no. AIAA2015-2265, 2015. (Cited in pages ix and 61.)

[Diederich 1951] Franklin W. Diederich. *A planform parameter for correletating certain aerodynamic characteristics of swept wing.* no. NACA-TN-2335, 1951. (Cited in page 47.)

[Dilinger 2018] Edouard Dilinger, Carsten Döll, Romain Liaboeuf, Clément Toussaint, Jean Hermetz, C. Verbeke and M. Ridel. *Handling qualities of ONERA's small business concept plane with Distributed Electric Propulsion.* ICAS18 Bello Horizonte, Brazil, 2018. (Cited in pages 13, 61, 213, and 294.)

[Döll 1997] C. Döll, J.F. Magni and Y. Le Gorrec. *A modal multi-modal approach.* In J.F. Magni, S. Bennani and J. Terlouw, editeurs, Robust flight control — A design challenge, volume 224, chapitre 19, pages 258–277. 1st édition, 1997. (Cited in pages 154 and 158.)

[Döll 2001] Carsten Döll. *La robustesse de lois de commande pour des structures flexibles en aéronautique et espace.* PhD thesis, 2001. Thèse de doctorat dirigée par Magni, Jean-François Systèmes automatiques Toulouse, ENSAE 2001. (Cited in page 156.)

[Drum 1924] Alphonsus L. Drum. *Electrically-Propelled Aircraft*, 1924. Patent US1511448A. (Cited in page 12.)

[EASA 2017] EASA. *Certification Specifications and Acceptable Means of Compliance for Large Aeroplanes CS-25 Amendment 20*, August 2017. (Cited in pages 6 and 34.)

[Etkin 2012] B. Etkin. Dynamics of atmospheric flight. Dover Books on Aeronautical Engineering. Dover Publications, 2012. (Cited in pages 47, 58, and 228.)

[Federal Aviation Administration 2015] Federal Aviation Administration. *Type Certificate data sheet No. A53EU*, 2015. (Cited in pages xvii and 43.)

[Felder 2009] James L Felder, Hyun Dae Kim and Gerald V Brown. *Turboelectric Distributed Propulsion Engine Cycle Analysis for Hybrid Wing Body Aircraft.* 47th AIAA Aerospace Sciences Meeting, no. 1132, 2009. (Cited in pages 12 and 13.)

[Feuersänger 2008] Alexander P Feuersänger. *Control of Aircraft with Reduced Stability.* Phd thesis, ISAE-SUPAERO, ONERA, 2008. (Cited in pages 9 and 139.)

[Fisher 2017] Jan-Sören Fisher. *Simulation and Analysis of the Aerodynamic Interactions between Distributed Propellers and Wings*, 2017. Master Thesis, Delft University. (Cited in pages 67, 68, 73, and 75.)

[Francis 1987] B.A. Francis. A course in h_∞ control theory. Lecture notes in control and information sciences. Springer-Verlag, 1987. (Cited in page 142.)

[Fredericks 2017] William J. Fredericks, Robert G. McSwain, Brian F. Beaton and David W. Klassman. *Greased Lightning (GL-10) Flight Testing Campaign*, 2017. NASA/TM–2017-219643. (Cited in pages 213 and 294.)

[Freeman 2018] Jeffrey L. Freeman and Garrett T. Klunk. *Dynamic Flight Simulation of Spanwise Distributed Electric Propulsion for Directional Control Authority.* In 2018 AIAA/IEEE Electric Aircraft Technologies Symposium, 2018. (Cited in page 15.)

[Gabarrou 2013] Marion Gabarrou, Daniel Alazard and Dominikus Noll. *Design of a flight control architecture using a non-convex bundle method.* Mathematics of Control, Signals and Systems (MCSS), vol. 25, no. 2, pages 257–290, June 2013. (Cited in page 145.)

[Gahinet 2011] P. Gahinet and P. Apkarian. *Structured H_∞ Synthesis in MATLAB.* IFAC Proceedings Volumes, vol. 44, no. 1, pages 1435 – 1440, 2011. 18th IFAC World Congress. (Cited in pages 145 and 146.)

[Gambu 1959] Jacques Gambu and Jean Perard. *Première application pratique de l'aile soufflée: LE BREGUET Br-941.* Aviation Magazine, président-directeur général P. Laureys, no. 277, pages 24–28, 06 1959. http://catalogue.bnf.fr/ark:/12148/cb34415552n. (Cited in page 11.)

[Gloudemans 1996] James R. Gloudemans, James D. Davis and Paul A. Gelhausen. *A rapid geometry modeler for conceptual aircraft.* AIAA, Aerospace Sciences Meeting and Exhibit, 34th, Reno, NV, Jan. 15-18, 1996, 1996. (Cited in pages 49, 73, 226, and 284.)

[Goman 2008] M G Goman, A V Khramtsovsky and E N Kolesnikov. *Evaluation of Aircraft Performance and Maneuvrability by Computation of Attainable Equilibrium Sets*. JOURNAL OF GUIDANCE, CONTROL, AND DYNAMICS, vol. 31, no. 2, 2008. (Cited in pages 33 and 96.)

[Grellet 1996] G. Grellet and G. Clerc. Actionneurs électriques: principes, modèles, commande. Collection Électrotechnique. Eyrolles, 1996. (Cited in page 14.)

[Henke 2018] Markus Henke, Gerrit Narjes, Jan Hoffmann, Constantin Wohlers, Stefan Urbanek, Christian Heister, Joern Steinbrink, Wolf-Rüdiger Canders and Bernd Ponick. *Challenges and Opportunities of Very Light High-Performance Electric Drives for Aviation*. Energies, vol. 11, page 344, 02 2018. (Cited in page 13.)

[Hepperle 2012] Martin Hepperle. *Electric Flight - Potential and Limitations*, 2012. NATO Technical Report STO-MP-AVT-209. (Cited in pages 13, 44, and 45.)

[Hermetz 2016] J. Hermetz, M. Ridel and C. Döll. *Distributed Electric Propulsion for small business aircraft — A concept-plane for key-technologies investigations*. In Proc. 30th ICAS Congress, Daejeon, South Korea, September 2016. (Cited in pages 13, 213, and 294.)

[Hess 1972] J. L. Hess. *Calculation of Potential Flow About Arbitrary Three-Dimensional Lifting bodies*, 1972. Technical Report AD0755480, Douglas Aircraft Co. (Cited in page 67.)

[Hoerner 1958] Sighard F Hoerner. Fluid dynamic drag. 1958. (Cited in page 77.)

[Hoerner 1985] Sighard F Hoerner and Henry V Borst. Fluid dynamic lift. 1985. (Cited in pages ix, 8, 57, 58, 59, and 60.)

[Hunsaker 2006] Douglas Hunsaker and Deryl Snyder. *A lifting line approach to study propeller wing interaction*. AIAA 24^{th} Applied Aerodynamics Conference, no. AIAA2006-3466, 2006. (Cited in page 67.)

[Jackson 2014] P. Jackson. *Jane's All the World's Aircraft: Development and Production : 2014-2015*, 2014. (Cited in pages xvii, 43, and 97.)

[Jameson 1968] Antony Jameson. *Preliminary Investigation of the Lift of a Wing in an Elliptic Slipstream*, 1968. Aerodynamics Report 393-68-6, Grumman. (Cited in page 67.)

[Jameson 1970] Antony Jameson. *Analysis of Wing Slipstream Flow Interaction*. no. NASA CR-1632, 1970. (Cited in pages 67, 74, 80, 81, and 82.)

[Jardin 2009] Matt R. Jardin and Eric R. Mueller. *Optimized Measurements of Unmanned-Air-Vehicle Mass Moment of Inertia with a Bifilar Pendulum.* Journal of Aircraft, no. 3, 2009. (Cited in page 219.)

[Kilgore 1949] Lee A. Kilgore, Jr Frank W. Gosey, Bennie A. Rose and Frank B. Powers. *Electrical Airplane Propulsion*, 1949. Patent US2462201A. (Cited in pages ix and 12.)

[Kim 2010] Hyun Dae Kim. *Distributed Propulsion Vehicles.* ICAS, 2010. (Cited in pages 3 and 10.)

[Kim 2018] Hyun D. Kim, Aaron T. Perry and Phillip J. Ansell. *A Review of Distributed Electric Propulsion Concepts for Air Vehicle Technology.* In 2018 AIAA/IEEE Electric Aircraft Technologies Symposium, EATS 2018, 2018 AIAA/IEEE Electric Aircraft Technologies Symposium, EATS 2018. Institute of Electrical and Electronics Engineers Inc., Novembre 2018. (Cited in page 13.)

[Kimberlin 2003] Ralph D. Kimberlin. Flight Testing of Fixed Wing Aircraft. AIAA Education Series. AIAA, Inc, 2003. (Cited in page 86.)

[Kirienko 2019a] Pavel Kirienko. *UAVCAN: a highly dependable publish-subscribe protocol for real-time intravehicular networking*, 2019. https://forum.uavcan.org/t/uavcan-a-highly-dependable-publish-subscribe-protocol-for-real-time-intravehicular-networking/557. (Cited in pages 221 and 222.)

[Kirienko 2019b] Pavel Kirienko. *Zubax SAPOG BLDC motor control solution*, 2019. https://kb.zubax.com/display/MAINKB/Zubax+Orel+20. (Cited in page 221.)

[Klein 2006] V. Klein and E.A. Morelli. Aircraft system identification: Theory and practice. AIAA education series. American Institute of Aeronautics and Astronautics, 2006. (Cited in pages 234, 240, and 241.)

[Klunk 2018a] Garrett T Klunk. *Vertical Tail Reduction Using Spanwise Distributed Electric Propulsion.* AIAA, no. 2018-5022, 2018. (Cited in page 95.)

[Klunk 2018b] Garrett T. Klunk and Jeffrey L. Freeman. *Vertical Tail Area Reduction for Aircraft with Spanwise Distributed Electric Propulsion.* In 2018 AIAA/IEEE Electric Aircraft Technologies Symposium, 2018. (Cited in page 15.)

[Ko 2003] Andy Ko, J A Schetz and William H Mason. *Assessment of the Potential Advantages of Distributed Propulsion for Aircraft.* ISABE-2003-1094, 2003. (Cited in page 13.)

[Köning 1934] C. Köning. Aerodynamic theory. Springer, Berlin, Heidelberg, 1934. Influence of the Propeller on Other Parts of the Airplane Structure. (Cited in page 66.)

[Kraft 1988] D. Kraft. A software package for sequential quadratic programming. Numéro DFVLR-FB 88-28 de Forschungsbericht / Deutsche Forschungs- und Versuchsanstalt für Luft- und Raumfahrt. Wissenschaftl. Berichtswesen d. DFVLR, 1988. (Cited in page 36.)

[Kuhn 1959] Richard E. Kuhn. *Semi-empirical Procedure for Estimating Lift and Drag Characteristics of Propeller-Wing-Flap Configurations for Vertical-and Short-Take-Off-and-Landing Airplanes*, 1959. NASA-MEMO-1-16-59L, L-144. (Cited in page 67.)

[Lan 2005] C. Edward Lan and Michael Guan. *Flight Dynamic Analysis of a Turboprop Transport Airplane in Icing Accident.* AIAA Atmospheric Flight Mechanics Conference and Exhibit, no. AIAA 2005-5922, 2005. (Cited in pages xvii and 43.)

[Liaboeuf 2018] Romain Liaboeuf and Edouard Dilinger. *ONERA's small business concept plane with Distributed Electric Propulsion longitudinal handling qualities evaluation.* In ODAS Symposium 2018, DLR Bonn, 2018. (Cited in pages 13 and 213.)

[Lin 2016] John C Lin and al. *Innovative Flow Control Concepts for Drag Reduction.* 2016 AIAA SciTech Forum and Exposition, no. NASA ID 20160007668, 2016. (Cited in page 9.)

[Lu 2018] Long K. Lu and Kamran Turkoglu. *Adaptive Differential Thrust Methodology for Lateral/Directional Stability of an Aircraft with a Completely Damaged Vertical Stabilizer.* Hindawi International Journal of Aerospace Engineering, no. 8654031, 2018. (Cited in page 14.)

[Ma 2020] Yiyuan Ma, Wei Zhang, Yizhe Zhang, Xingyu Zhang and Yujiang Zhong. *Sizing Method and Sensitivity Analysis for Distributed Electric Propulsion Aircraft.* Journal of Aircraft, Articles in Advance, 2020. (Cited in pages 213 and 294.)

[Mannée 1962] J. Mannée, National Aero and Astronautical Research Institute. Windtunnel investigation of the influence of the aircraft configuration on the yawing- and rolling moments of a twin-engined, propeller-driven aircraft with one engine inoperative. Report Nationaal Luchtvaartlaboratorium. Failli, 1962. (Cited in page 64.)

[Marvin 1964] P. Fink Marvin, G. Mitchell Robert and White Lucy C. *Aerodynamic data on large semi-span tilting wing with 0.6-diameter chord, single slotted flap, and single propeller rotating up a tip*, 1964. NASA Technical Report TN D-1586. (Cited in page 81.)

[McCormick 1999] B.W. McCormick. Aerodynamics of v/stol flight. Dover Publications, 1999. (Cited in pages 59, 73, and 124.)

[Miley 1988] Stan J Miley, Richard M Howard and Bruce J Holmes. *Wing Laminar Boundary Layer in the Presence of a Propeller Slipstream.* Journal of Aircraft, vol. 25, no. 7, 1988. (Cited in pages 63 and 77.)

[Miranda 1977] Luis R Miranda, Robert D Elliott and William M Baker. *A Generalized Vortex Lattice Method for Subsonic and Supersonic Flow Applications*, 1977. NASA Contractor Report. (Cited in page 67.)

[Miranda 1986] Luis R Miranda and James E Brennan. *Aerodynamic Effect of Wingtip Mounted Propellers and turbines.* AIAA 4^{th} Applied Aerodynamic Conference, no. 1986-1802, 1986. (Cited in pages 62 and 67.)

[Mooney 2014] Helen P Mooney, John B Brandt, Douglas S Lacy and Edward A Whalen. *AFC-Enabled Vertical Tail System Integration Study.* NASA ID 20140003900, 2014. (Cited in page 9.)

[Moore 2014] Mark D Moore and Bill Fredericks. *Misconception of Electric Propulsion Aircraft and their Emergent Aviation Market.* 52^{nd} AIAA Aerospace Sciences Meeting, no. 0535, 2014. (Cited in pages 13 and 42.)

[Morris 2013] Craig C Morris. *Flight Dynamic Contraints in Conceptual Aircraft Design Analysis and Design Optimization.* Phd thesis, Virginia Polytechnic Institute, 2013. (Cited in pages 6, 8, 9, and 139.)

[Nguyen 2018] Nhan T. Nguyen, Kevin Reynolds, Eric Ting and Natalia Nguyen. *Distributed Propulsion Aircraft with Aeroelastic Wing Shaping Control for Improved Aerodynamic Efficiency.* Journal of Aircraft, vol. 55, no. 3, pages 1122–1140, 2018. (Cited in pages 3 and 9.)

[Nicolosi 2013] Fabrizio Nicolosi, Perluigi Della Vecchia and Danilo Ciliberti. *An investigation on vertical tailplane contribution to aircraft sideforce.* Aerospace Science and Technology, vol. 28, no. 1, pages 401 – 416, 2013. (Cited in page 46.)

[Nicolosi 2016] Fabrizio Nicolosi, Pierluigi Della Vecchia, Danilo Ciliberti and Vincenzo Cusati. *Fuselage aerodynamic prediction methods.* Aerospace Science and Technology, vol. 55, pages 332 – 343, 2016. (Cited in page 50.)

[Nicolosi 2017] Fabrizio Nicolosi, Pierluigi Della Vecchia, Danilo Ciliberti, Salvatore Corcione and Vincenzo Cusati. *A Comprehensive Review of Vertical Tail Design.* 6th Symposium on Collaboration in Aircraft Design, At Warsaw, 2017. (Cited in pages 47 and 95.)

[Nita 2008] Mihaela Florentina Nita. *Aircraft Design Studies Based on the ATR 72*, 2008. Master Thesis, Hochshule für Angewandte Wissenschaften Hamburg. (Cited in pages 6, 8, and 97.)

[Noetinger 2001] J. Noetinger. Non à l'oubli!: L'incroyable aventure française dans le ciel. Nouvelles éditions latines, 2001. (Cited in pages 11 and 12.)

[Obert 2009] Ed. Obert. Aerodynamic design of transport aircraft. Forschungsbericht / Deutsche Forschungs- und Versuchsanstalt für Luft- und Raumfahrt. IOS Press, 2009. (Cited in pages x, 3, 5, 8, 48, 59, 63, 64, and 95.)

[Ope 2020] *OpenVSP publication list*, 2020. `http://openvsp.org/wiki/doku.php?id=papers`. (Cited in page 49.)

[Oppenheimer 2006] Michael W Oppenheimer and Ph.D. David B Doman. *Control allocation for overactuated systems.* 4th Mediterranean Conference on Control Automation proceedings, no. 321, 2006. (Cited in page 34.)

[Park 1991] J. Park and I. W. Sandberg. *Universal Approximation Using Radial-Basis-Function Networks.* Neural Computation, vol. 3, no. 2, pages 246–257, June 1991. (Cited in pages 123 and 125.)

[Patterson 2015] Michael D Patterson and Brian J Germany. *Simplified Aerodynamics Models to Predict the Effects of Upstream Propellers on Wing Lift.* AIAA SciTech, no. 1673, 2015. (Cited in pages 59, 67, and 70.)

[Patterson 2016] Michel D Patterson. *Conceptual Design for High Lift Propeller Systems for Small Electric Aircraft.* Phd thesis, Georgia Institute of Technology, 2016. (Cited in pages x, 68, 70, 71, and 72.)

[Pattinson 2013] J. Pattinson, M. H. Lowenberg and M. G. Goman. *Multi-Degree-of-Freedom Wind-Tunnel Maneuver Rig for Dynamic Simulation and Aerodynamic Model Identification.* Journal of Aircraft, vol. 50, no. 2, pages 551–566, 2013. https://doi.org/10.2514/1.C031924. (Cited in page 213.)

[Perez 2006] Ruben E Perez, H T Liu and Kamran Behdinan. *Multidisciplinary Optimization Framework for Control Configuration Integration in Aircraft Conceptual Design.* Journal of Aircraft, vol. 43, no. 6, 2006. (Cited in page 8.)

[Pope 2009] A. Pope. Basic wing and airfoil theory. Dover Books on Aeronautical Engineering Series. Dover Publications, 2009. (Cited in pages 75, 77, 78, and 246.)

[Quigley 1964] Hervey C. Quigley, Robert C. Innis and Curt A. Holzhauser. *A flight investigation of the performance, handling qualities and operational characteristics of a deflected slipstream STOL transport airplane having four interconneted propellers*, 1964. NASA Technical Report TND2231, https://ntrs.nasa.gov/search.jsp?R=19640007812. (Cited in pages ix and 11.)

[Raymer 1989] P Daniel Raymer. Aircraft Design: A Conceptual Approach. AIAA Education Series. American Institute of Aeronautics and Astronautics, Inc, 1989. (Cited in pages 3 and 6.)

[Rediess 1980] Herman A Rediess. *Impact of Advanced Control Concepts on Aircraft Design.* 12$^{\text{th}}$ ICAS Congress, no. Paper 80 - 0.4, 1980. (Cited in page 8.)

[Ribner 1945] Herbert S. Ribner. *Propellers in Yaw.* no. NACA report 820, 1945. (Cited in page 57.)

[Roos 2014] C. Roos, G. Hardier and J. Biannic. *Polynomial and rational approximation with the APRICOT Library of the SMAC toolbox.* In 2014 IEEE Conference on Control Applications (CCA), pages 1473–1478, 2014. (Cited in page 152.)

[ros] *ROS.* (Cited in page 223.)

[Sachs 2012] G Sachs. *Flight Performance Issues of Electric Aircraft.* AIAA Atmospheric Flight Mechanics Conference, no. 4727, 2012. (Cited in pages 29 and 30.)

[Sahin 1985] Besir Sahin and A. Ward-Smith. *The measurement of air-flow characteristics using a five-hole Pitot probe in conjunction with a microcomputer.*

Transactions of The Institute of Measurement and Control - TRANS INST MEASURE CONTROL, vol. 7, pages 110–116, 06 1985. (Cited in page 224.)

[Saied 2015] M. Saied, B. Lussier, I. Fantoni, C. Francis and H. Shraim. *Fault tolerant control for multiple successive failures in an octorotor: Architecture and experiments*. In 2015 IEEE/RSJ International Conference on Intelligent Robots and Systems (IROS), pages 40–45, 2015. (Cited in page 192.)

[Samuelsson 1987] Ingemar Samuelsson. *Low speed wing tunnel experimentation of propeller slipstream aerodynamic effects on different nacelle wing combinations*, 1987. Technical Report 1263, FFA, Aeronautical Research Institute of Sweden, FFA TN 1987-22. (Cited in page 68.)

[SBG] *SBG systems*. (Cited in pages 223 and 277.)

[Schmollgruber 2019] Peter Schmollgruber, Olivier Atinault, Italo Cafarelli, Carsten Döll, Christophe François, Jean Hermetz, Romain Liaboeuf, Bernard Paluch and Michael Ridel. *Multidisciplinary Exploration of DRAGON: an ONERA Hybrid Electric Distributed Propulsion Concept*. AIAA SciTech Forum, no. AIAA2019-1585, 2019. (Cited in pages 13, 14, and 56.)

[Schroijen 2010] M. J. T. Schroijen, L. L. M. Veldhuis and R. Slingerland. *Propeller Empennage Interaction Effects on the Vertical Tail Design of Multiengine Aircraft*. Journal of Aircraft, vol. 47, no. 4, pages 1133–1140, 2010. (Cited in pages 67 and 70.)

[Selig 1989] M. S. Selig, J. F. Donovan and D. B. Fraser. Airfoils at low speeds. 1989. https://m-selig.ae.illinois.edu/uiuc_lsat/Airfoils-at-Low-Speeds.pdf. (Cited in page 217.)

[Smelt 1937] R Smelt and H Davies. *Estimation of increase in lift due to slipstream*. no. ARC TN 1788, 1937. (Cited in page 66.)

[Stein 2003] G. Stein. *Respect the unstable*. IEEE Control Systems Magazine, vol. 23, no. 4, pages 12–25, 2003. (Cited in page 148.)

[Stoll 2015] Alex M. Stoll. *Comparison of CFD and Experimental Results of the LEAPTech Distributed Electric Propulsion Blown Wing*. In 15th AIAA Aviation Technology, Integration, and Operations Conference, 2015. (Cited in pages 213 and 294.)

[Stoll 2016] Alex M. Stoll and Gregor Veble Mikic. *Design Studies of Thin-Haul Commuter Aircraft with Distributed Electric Propulsion*. In 16th AIAA Avi-

ation Technology, Integration, and Operations Conference, 2016. (Cited in page 67.)

[Stückl 2015] Stefan Stückl. *Methods for the Design and Evaluation of Future Aircraft Concepts Utilizing Electric Propulsion Systems*. Phd thesis, Technische Universität München, 2015. (Cited in page 42.)

[Torenbeek 1982] Egbert Torenbeek. Synthesis of Subsonic Airplance Design. Delft University Press. Kluwer Academic Pulishers, 1982. (Cited in pages 3, 5, 6, 7, 40, 48, 50, 95, and 127.)

[Tucker 1999] Tom Tucker. *Touchdown : The Developement of Propulsion Controlled Aircraft at NASA Dryden*, 1999. (Cited in page 14.)

[V Robert 1968] Page V Robert, O.Dickinson Stanley and Wallace H. Deckert. *Large-Scale Wind-Tunnel Tests of a Deflected Slipstream STOL Model with Wings of Various Aspect Ratios*, 1968. NASA Technical Report TN D-4448. (Cited in page 81.)

[van Rooyen 1981] R. S. van Rooyen and M. E. Eshelby. *Assessment of propeller influence on lateral-directional stability of multiengine aircraft*. Journal of Aircraft, vol. 18, no. 5, pages 364–371, 1981. (Cited in page 64.)

[Veldhuis 2004] LLM Veldhuis. *Review of Propeller Wing Aerodynamic Interference*. ICAS, 2004. (Cited in pages 62 and 68.)

[Veldhuis 2005] Leonardus Louis Maria Veldhuis. *Propeller Wing Aerodynamic Interference*. Phd thesis, Delft University, 2005. (Cited in pages 59 and 61.)

[Warwick 2019] Graham Warwick. *Harbour Air and MagniX Claim First for Electric Aircraft*, 12 2019. `https://aviationweek.com/aerospace/harbour-air-magnix-claim-first-electric-aircraft`. (Cited in page 13.)

[Welstead 2014] Jason Welstead and Gilbert L Crouse Jr. *Conceptual Design Optimization of an Augmented Stability Aircraft Incorporating Dynamic Response and Actuator Constraints*. In 52nd AIAA Aerospace Sciences Meeting, numéro AIAA Paper 2014-0187, 2014. (Cited in page 8.)

[W.F. 2000] Phillips W.F. and D.O. Snyder. *Modern Adaptation of Prandtl's Classic Lifting-Line Theory*. Journal of Aircraft, no. Vol. 37 No. 4, 2000. (Cited in page 67.)

[Wildi 2000] T. Wildi and G. Sybille. Electrotechnique. Editions De Boeck Université, 2000. (Cited in page 14.)

[Wir 2010] *Aerospace Standard AS 50881 : Wiring Aerospace Vehicle*, 2010. (Cited in page 30.)

[Witkowski 1989] Dave P. Witkowski, Alex K. H. Lee and John P. Sullivan. *Aerodynamic interaction between propellers and wings.* Journal of Aircraft, vol. 26, no. 9, pages 829–836, 1989. (Cited in page 67.)

[Wolowicz 1979] Chester H. Wolowicz, James S. Jr. Bowman and William P. Gilbert. *Similitude Requirements and Scaling Relationships as Applied to Model Testing*, 1979. NASA Technical Report TP 1435. (Cited in page 216.)

[xpo] *Xpower XC2816/16.* (Cited in page 222.)

[Zhong 1997] L. Zhong, M. F. Rahman, W. Y. Hu and K. W. Lim. *Analysis of direct torque control in permanent magnet synchronous motor drives.* IEEE Transactions on Power Electronics, vol. 12, no. 3, pages 528–536, 1997. (Cited in page 14.)

[Zhou 1998] K. Zhou and J.C. Doyle. Essentials of robust control. Prentice Hall Modular Series for Eng. Prentice Hall, 1998. (Cited in pages 142 and 145.)